12-2020

Experimental and Computational Analysis of Progressive Failure in Bolted Hybrid Composite Joints

John S. Brewer

EXPERIMENTAL AND COMPUTATIONAL ANALYSIS OF PROGRESSIVE FAILURE IN BOLTED HYBRID COMPOSITE JOINTS

DISSERTATION

John S. Brewer Jr., Major, USAF

AFIT-ENY-DS-20-D-057

DEPARTMENT OF THE AIR FORCE
AIR UNIVERSITY

AIR FORCE INSTITUTE OF TECHNOLOGY

Wright-Patterson Air Force Base, Ohio

AFIT-ENY-DS-20-D-057

EXPERIMENTAL AND COMPUTATIONAL ANALYSIS OF PROGRESSIVE FAILURE IN BOLTED HYBRID COMPOSITE JOINTS

DISSERTATION

Presented to the Faculty

Department of Aeronautics and Astronautics

Graduate School of Engineering and Management

Air Force Institute of Technology

Air University

Air Education and Training Command

In Partial Fulfillment of the Requirements for the

Degree of Doctor of Philosophy

John S Brewer Jr., BS, MS

Major, USAF

December 2020

AFIT-ENY-DS-20-D-057

EXPERIMENTAL AND COMPUTATIONAL ANALYSIS OF PROGRESSIVE FAILURE IN BOLTED HYBRID COMPOSITE JOINTS

DISSERTATION

John S. Brewer Jr., BS, MS,

Major, USAF

Approved:

PALAZOTTO.ANTHONY.N.1228660813 Digitally signed by PALAZOTTO.ANTHONY.N.1228660813 Date: 2020.12.09 14:35:22 -05'00'

Dr. Anthony Palazotto (Chairman) — 9-Dec-2020 — Date

RUGGLES-WRENN.MARINA.B.1267711514 Digitally signed by RUGGLES-WRENN.MARINA.B.1267711514 Date: 2020.12.10 11:00:28 -05'00'

Dr. Marina B. Ruggles-Wrenn (Member) — 10-Dec-2020 — Date

HERR.NICHOLAS.CONRAD.1274803297 Digitally signed by HERR.NICHOLAS.CONRAD.1274803297 Date: 2020.12.07 15:51:53 -07'00'

Maj Nicholas C. Herr, PhD (Member) — 7-Dec-2020 — Date

Accepted:

BADIRU.ADEDEJI.B.1293329580 Digitally signed by BADIRU.ADEDEJI.B.1293329580 Date: 2020.12.10 16:23:39 -05'00'

Dr. Adedeji B. Badiru
Dean, Graduate School of
Engineering and Management — 10-Dec-2020 — Date

Abstract

Composite materials are strong, lightweight, and stiff making them desirable in aerospace applications. However, a practical issue arises with composites in that they behave unpredictably in bolted joints, where damage and cracks are often initiated.

This research investigated a solution to correcting the problem with composite bolted joints. A novel hybrid composite material was developed, where thin stainless steel foils were placed between and in place of preimpregnated composite plies during the cure cycle to reinforce stress concentrations in bolted joints. This novel composite was compared to control samples experimentally in quasi-static monotonic loading in double shear configuration in 9-ply and 18-ply layups. It was also investigated in quasi-static loading in single shear configuration using 18-ply samples in both protruding head and countersunk head configurations. Progressive failure samples were compared to stress-strain curves to explain which phenomenon in the material caused certain features in experimental curves. The final goal of the experimental effort was to perform an initial cycle fatigue comparison between the novel hybrid and control materials. The parallel research effort explored creating finite element models that could correctly represent and predict the behavior of this hybrid system. This was the first effort employing numerical failure criterion alongside a rigorous experimentation across multiple configurations.

Hybridizing the composite material increased yield load capacity by as much as 25% and increased ultimate load capacity as much as 42%. The finite element models employed Hashin failure criteria and proved the ability to predict the yield load capacity to within 6.5% error.

Acknowledgements

All praise be to Christ our King who holds all wisdom and knowledge. He has put many people in my life to make this work possible.

To my advisor, Distinguished Professor, Dr. Anthony Palazotto, thank you for all the time you have spent with me. I have learned wisdom from you that I will carry with me the rest of my life. To Dr. Marina Ruggles-Wrenn and Maj Nicholas Herr, thank you for serving on my committee and providing advice throughout this research.

To Mr. John Feie, your tireless efforts and friendship have been invaluable to keeping my research moving. To the machinists and staff of the AFRL/RQ FIRST lab and the AFRL/RX materials team, thank you for the countless hours you spent supporting my research. The hands-on education you provide officers and engineers is priceless. To the late Michael Falugi, thank you for trusting me to continue your work. Rest in peace. To Mr. Michael Gran, thank you for believing in me and always supporting this work. To Dr. Casey Holycross, thank you for the time spent trudging through testing and data with me. Your ability to bridge the gap between theory and practice was immensely helpful.

To my wife, you are my friend and my teammate. You are bone of my bone and flesh of my flesh. I cherish you. To my son, you are an answer to prayer. My hope for you is that you confidently go where the Lord leads. Too all my family and Church family, thank you for loving us so well.

Table of Contents

Page

List of Figures

Page

List of Tables

Page

Nomenclature

Variables and Operators

- A – bearing area
- B_{sd} – strain-displacement matrix
- C – constitutive matrix
- C_d – damage elasticity matrix for composite damage and failure
- d – damage variable
- d_h – hole elongation
- d_f – fiber damage variable
- d_f^t – fiber tension damage variable
- d_f^c – fiber compression damage variable
- d_m – matrix damage variable
- d_m^c – matrix compression damage variable
- d_m^t – matrix tension damage variable
- D – bolt diameter
- D_d – damage evolution variable
- E – elastic modulus
- E_C – composite elastic modulus
- E_{chord} – bearing chord stiffness
- E_m – metal composite elastic modulus
- f_n – normal force
- f_t – tangential force

- F – Force
- F_b – bolt clamping force
- g_n – the normal penetration
- g_t – the tangential penetration
- G^C – mixed mode fracture energy
- G_n^C – normal mixed mode fracture energy
- G_s^C – mixed mode fracture energy
- H_0 – null hypothesis
- H_a – alternative hypothesis
- I – Internal Forces
- K_{fric} – torque frictional constant
- k_n – normal penalty stiffness
- k_t – the tangential penalty stiffness
- K – cohesive interaction stiffness
- L - length
- L_c – element characteristic length
- L_{CI} – confidence interval length
- L_w – torque wrench length
- L_{ext} – torque extension length
- M – lumped mass matrix
- M_d – damage matrix in composite damage and failure criteria
- n – sample size (number of samples)

- n_{comp} – number of composite plies in hybrid layup
- n_{foil} – number of foils in hybrid layup
- N_{life} – in fatigue step test method, assigned cycle count being investigated
- N_{fail} – in fatigue step test method, number of cycles complete in the block in which the failure criterion was met
- n_y – normal to yield surface
- P – External Forces
- P_{lc} – applied load (measured from load cell)
- P_{ult} – estimated ultimate bearing strength
- P_{yield} – estimated bearing yield of the hybrid
- sgn – the sign operator which takes the sign of the parenthetical quantity
- tr( ) – Trace of a matrix. Sums the diagonal values of a matrix.
- u – position
- u- displacement
- $\bar{u}_f^{pl}$ – effective plastic displacement at failure
- v – degrees of freedom
- V – volume
- S – sample standard deviation
- S^L – Hashin Criteria longitudinal shear strength
- S^T – Hashin Criteria transverse shear strength
- t – time
- t_{avg} – average ply thickness

- t_c – coupon thickness
- t_n – normal cohesive stress
- t_s – shear cohesive stress
- t_t – transverse cohesive stress
- t_n^0 – peak normal cohesive stress
- t_s^0 – peak shear cohesive stress
- t_t^0 – peak transverse cohesive stress
- T_0 – original thickness in a cohesive layer
- T_{des} – desired torque on the fastener
- T_{eff}^0 – effective cohesive traction at damage initiation
- T_r – temperature, ambient
- T_{sf} – temperature, stress free
- T_{set} – torque wrench set value
- T_C – temperature, cure
- T – temperature
- T_b – applied
- $\bar{x}$ – sample mean
- x^0 – initial positions
- X^T – Hashin Criteria longitudinal tensile strength
- X^C – Hashin Criteria longitudinal compressive strength
- Y^T – Hashin Criteria transverse tensile strength
- Y^C – Hashin Criteria transverse compressive strength

- α – statistical significance level
- α_b - coefficient of thermal expansion, bolt
- α_C – coefficient of thermal expansion, composite
- α_M - coefficient of thermal expansion, metal
- α_{shear} – shear component waiting factor in composite damage and failure
- δ_{eq}^{0} – equivalent fracture relative displacement for a given composite failure mode
- δ_{eq}^{fc} – composite fiber compression equivalent relative displacement
- δ_{eq}^{ft} – composite fiber tension equivalent relative displacement
- δ_{eq}^{mc} – composite matrix compression equivalent relative displacement
- δ_{eq}^{mt} – composite matrix tension equivalent relative displacement
- δ_{ij} – Kronecker Delta. When $i = j, \delta = 1. When\ i \neq j, delta = 0.$
- δ_m – cohesive effective displacement
- $\delta_m^{\max}$ - maximum cohesive effective displacement
- δ_n – normal relative displacement in cohesive element
- δ_s – shear relative displacement in cohesive element
- δ_t – transverse relative displacement in cohesive element
- ε – strain
- ε_c – thermal strain, composite
- ε_{cf} – strain correction factor
- ε^e – elastic strain
- ε_g – Green strain
- ε_m – thermal strain, metal

- ε^p – plastic strain
- $\bar{\varepsilon}^{pl}$ – equivalent plastic strain
- $\dot{\bar{\varepsilon}}^{pl}$ – equivalent plastic strain rate
- ε^{tot} – total strain
- ε_{hyd} – hydrostatic strain
- ε_{eff} – hydrostatic strain
- ε_{raw} – raw strain, uncorrected
- $\varepsilon_{ref_{hi}}$ – strain at high reference point
- $\varepsilon_{ref_{low}}$ – strain at low reference point
- μ_d – the coefficient of friction
- μ – mean of a probability distribution
- v_c - volume fraction of the composite with respect to the hybrid thickness
- σ – Cauchy, true stress
- σ' – deviatoric stress
- σ – Von Mises Stress
- $\bar{\sigma}$ – Von Mises Stress (also σ_{vm})
- $\hat{\sigma}$ – effective stress employed in Hashin Criteria
- σ_{br} – bearing stress
- σ_e – fatigue limit stress
- $\sigma_{ref_{hi}}$ – stress at high reference point
- $\sigma_{ref_{low}}$ – stress at low reference point

- σ_0 – in accelerated fatigue step method, stress for the block in which the failure criterion is met
- $\Delta\sigma$ – stress increase between blocks in fatigue step test method
- σ_{eq}^{ft} – composite fiber tension equivalent stress
- σ_{hyd} – Hydrostatic Stress
- $\sigma_{br_{comp}}$ – yield stress of a pinned composite sample from Falugi and Knoth
- $\sigma_{foil_{yield}}$ – published yield value for foil
- σ_{vm} – Von Mises Stress (also $\bar{\sigma}$)
- τ – shear stress

Acronyms and Abbreviations

- 3D – Three Dimensional
- AFRL/RX – Air Force Research Laboratory, Materials and Manufacturing Directorate
- AFRL/RQ – Air Force Research Laboratory, Aerospace Systems Directorate
- ASTM – American Society for Testing and Materials
- CALE – Composite Airframe Life Extension
- ESL – Equivalent Single Layer
- FIRST – Facility for Innovative Research in Structures Technology
- FML – Fiber Metal Laminates
- in – Inch
- ksi – one thousand pounds per square inch

- Lbf – Pounds Forced
- LW – Layerwise
- m – Meter
- MPa – megapascal – one million newtons per square meter
- msi – one million pounds per square inch
- N – Newton
- psi – Pounds Per Square Inch
- PVC – Peak-Valley Control
- SEM – Scanning Electron Microscopy/Microscope

EXPERIMENTAL AND COMPUTATIONAL ANALYSIS OF PROGRESSIVE FAILURE IN BOLTED HYBRID COMPOSITE JOINTS

I. Introduction and Background

1.1 Motivation

Composite materials are being used in ever increasing quantities as aerospace and automotive applications demand lighter and stronger structures. However, a major issue that plagues composite materials is the process of attaching them to other structural elements. Fasteners are often solely employed to create a serviceable joint or to allow access to another component. These fastener sites create stress concentrations and crack initiation sites in the brittle composite materials which can lead to unpredictable failure. The STeel Reinforced Advanced Thin Unitized Structure (STRATUS) Program led by the Air Force Research Lab Aerospace Systems Directorate (AFRL/RQ) proposes the addition of stainless steel foils between and in place of layers of carbon fiber composite near fastener sites as shown in Figure 1. This technology seeks to combine the high strength to weight ratio and stiffness of carbon fiber composites with the predictable toughness and ductile failure nature of stainless steel.

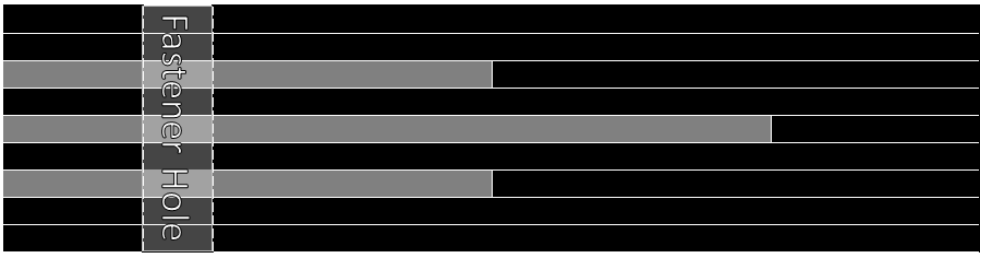

Figure 1: Example Hybrid Structure

1.2 Research Objective

The objective of this work was to investigate the strength and failure characteristics of the proposed unique carbon fiber/stainless steel hybrid material in three bolted joint configurations as an improvement to standard composite layups. Additionally, this research sought to establish preliminary fatigue data for this novel material for comparison to standard composite joints. Finally, this work sought to establish efficient finite element methods to characterize the failure phenomena observed in experimentation and to predict the strength and failure behavior of bolted joints in this hybrid material.

1.3 Approach

This research sought to fulfill the objectives through experimentation and computation. Experimentally, this study sought to characterize a hybrid material comprised of preimpregnated carbon fiber and 301 stainless steel in monotonic quasi-static bolted bearing loading per ASTM D5961-17 and cyclic loading via ASTM D6873-08[1], [2]. Computational modeling was evaluated using Abaqus Finite Element (FE) software [3].

1.4 Background

Valued for light weight and stiffness, composite materials have become commonplace in aerospace design. Over a third of the F-35 Joint Strike Fighter is made of composite materials [4], [5]. The current Boeing 787 and Airbus A350XWB are both made from over 50% composite materials [6]–[8]. Boeing touts a 20% weight savings over traditional aluminum construction [6]. Weight savings allows for decreased fuel

consumption and can also allow increased payload capacity. Airbus expects a 25% fuel efficiency increase in the A350XWB [9]. As composites have increased in use, considerable efforts have been focused on applying composite materials into design roles previously filled with metals. Composites have also allowed engineers to explore new design approaches that take advantage of their unique properties and manufacturing methods. For example, composites are not only well suited to molding to complex geometries, technology exists to enable fiber tow direction optimization through fiber steering and automated tape laying (ATL) capabilities [10]–[12]. Despite the flourishing development of composite technology, a problem persists that engineers are forced to face. At some point a composite structure ends and must be joined to some other structure or have something affixed to it so that the airframe can complete the prescribed mission. Despite all the work to optimize and take advantage of the outstanding properties of composite materials, joints in composites highlight their brittle failure nature and anisotropy. There are many situations that cause joints in composites. The skin of an aircraft must be somehow joined to a substructure. Aircraft essential systems must be attached to the structure. Manufacturability is a major cause of composite joints. For instance, in autoclave cured parts, which are still often preferred over out-of-autoclave methods, the size of the part is limited by the dimensions of the autoclave. Even in out of autoclave processing, the material is typically oven cured, where the dimension of an oven governs part size which lead to joints [13], [14]. Scaled Composites tackled this problem when they constructed Stratolaunch, the world's largest composite airframe. They used traveling ovens to cure the 204 foot (62m) long wing spars [15], [16]. However, this technology is far from being applied to full scale aircraft manufacturing

and mass certification. As large and complex as modern continuous parts are, they still must be joined with other structural elements to create a complete airframe. Joints are such an ever present concern that the US Air Force has an ongoing series of programs largely focused on composite joints and as of 2020, The American Institute of Aeronautics and Astronautics hosts a special session on Structural Joints and Repairs at its annual SciTech conference [17], [18]. As engineers push the bounds of composite manufacturing, the challenge of composite joints seems to remain ever present.

Engineers have approached composite joints in a myriad of ways. Composite joining may be performed with adhesives, but adhesive only joints prove to be difficult to certify. Thus, engineers tend toward joints with fasteners or joints that include both fasteners and adhesives [19]–[21]. In many cases, a joint needs to be removable, so that a part can be replaced or removed to service another aircraft component. In this case, a joint with removable fasteners is required.

Semi-permanent and removable fasteners in aerospace structures are as old as aviation itself, and much technology has been developed on fastened joints in metals. However, the brittle failure nature and anisotropy of composites amplify the challenges of fastened joints. The problem arises in how fastened joints fail. Fastener sites create high stress concentrations in brittle composites and are prone to fatigue due to flight dynamics and cyclical cabin pressurization. Figure 2 shows the three failure modes expected in a fastened composite joint: shear-out, net tension, and bearing. Bearing is the most desirable failure mode since shear-out and net tension tend to be catastrophic failures, while hole elongation due to bearing is likely to be discovered upon inspection.

Studies have shown that current methods of predicting fatigue life in composite bolted joints are lacking [18].

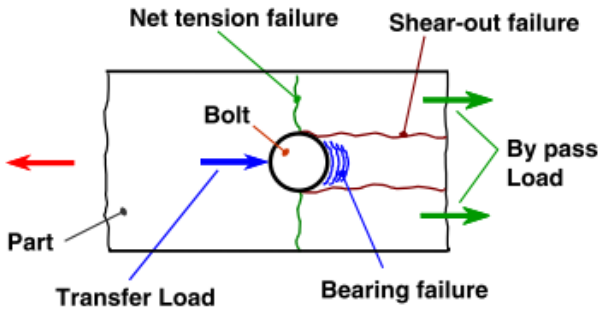

Figure 2: Joint Failure Modes [22]

Engineers have addressed fastened joints in composites in a number of ways. A common method is known as a "pad-up" where the layup is locally thickened near the fastener. While this does increase the strength of the material locally, it does not address the perceived shortcomings of the material when analyzed at a stress concentration such as a fastener. It also creates load eccentricities and often increases the complexity of underlying substructures and can even adversely affect aerodynamics by forcing changes to the shape of the vehicle [23]. Other factors have been explored such as addressing the hole manufacturing, the fastener to hole fit, and the fastener itself [24]–[26]. However, none of these methods specifically address the material properties of the layup at the fastener site. Camancho et al demonstrated an improvement in joint efficiency by using a metal sleeve insert bonded into a bearing hole. While this aided in spreading stress concentration, this required a secondary bonding step and after adhesive failure, the joint failed similarly to a joint with no insert [27].

The focus of this research is to specifically address the layup near the fastener site by adding metal foils between and in place of carbon fiber plies near a fastener site. The idea of uniting metals and composites is not new. Hybrids comprised of metals and composites can be traced back to the 1970s in the Netherlands. These materials have come to be known as Fiber Metal Laminates (FML). FML were pursued because the laminated nature slowed fatigue crack growth by causing cracks to grow in individual layers and transfer load into the adjacent composite fibers [28], [29]. FML have transitioned into modern manufacturing where much of the Airbus A380 fuselage is composed of GLARE (GLAss REinforced) which is composed of glass fiber and aluminum. However, these more historic materials tend to be homogenous over their area [30], [31]. When looking for the ultimate in light weight and stiffness, engineers turn to carbon fiber composites. In an effort to preserve these properties while still addressing bolted joints, engineers have focused efforts on improving bearing properties at regions near fastener sites.

Working with carbon fiber presents its own unique issues compared to other composite materials such as glass fiber and aramid fibers. While aluminum is prized in aerospace applications and has proven successful in GLARE applications, the combination of carbon fiber and aluminum leads to a high risk of galvanic corrosion which could lead to large scale delamination and structural catastrophe [32]. Some work has shown promise in sealing the aluminum with chemical treatments or coatings, but many choose to avoid the combination due to the corrosion dangers [33], [34].

Instead of aluminum, many have turned to titanium as a solution to locally hybridize with carbon fiber at fastener sites. While titanium does not offer the same

plasticity and toughness as other materials, it is strong, light weight and prized for corrosion resistance. Titanium avoids the galvanic corrosion danger that exists between aluminum and carbon fiber. An additional concern in working with carbon fiber composites is that carbon fiber has a coefficient of thermal expansion (CTE) that is near zero while metals usually respond much more measurably to changes in temperature. This difference in CTE means that with any temperature change, thermally induced stresses are imparted into the structure. This difference is magnified in hybrid composites since composites are typically cured at elevated temperatures. When the metallic and composite components are joined at elevated temperatures, thermally induced stresses set in as the part returns to room temperature. In consideration of an aircraft, a structure might see temperatures in excess of 100°F (38°C) on the ground and then experience temperatures cooler than -60°F (-51°C) while airborne. When compared to other common metals, titanium demonstrates a fairly low CTE of around $5x10^{-6}$/°F ($5x10^{-6}$/ °C) [35]. Thus, titanium minimizes thermal expansion. For these reasons, much of the contemporary research in fiber metal laminate bolted joints focuses on titanium-carbon fiber composite hybrids [22], [23], [36]–[38]. Yamada et al demonstrated that a titanium-carbon fiber FML in a bolted joint would delay crack propagation through the thickness of the material. They noted the best results when titanium foils were placed on either side of internal 0° plies. In this configuration, with a 25% metal volume fraction, they noted a 58% load capacity increase. Fink et all demonstrated the testing and modeling of a Titanium-CFRP Hybrid localized to fastener sites. With a 33% metal volume fraction, they showed an over 100% increase in ultimate bearing strength using a stepped

transition zone. They applied this methodology to construction of a spacecraft payload adapter and predicted that steel would be promising for these applications [37].

Despite the difference in CTE, steel has been successfully applied to FML localized to address bolted joints. Petersen et al employed spring steel 1.4310 (301SS) in their investigation of the transition zone, which is the region where the fiber metal laminate localized near a fastener transitions into the pure composite. They determined that a transition zone staggered by at least 10mm (0.39in) provided the highest load capacity when compared to other transition methods [39]. Lopes et al examined a hybrid structure comprised of 301 stainless steel with a Hexcel 8552/AS4 preimpregnated composite. They noted over 100% increase in pinned bearing stress and fatigue cycle lives that were two orders of magnitude greater than pure composite samples [40].

Most applicably, work at the Air Force Research Laboratory Aerospace System Directorate as published by Falugi and Knoth demonstrated the efficacy of a carbon fiber-stainless steel hybrid to improve the bearing strength of a bolted joint. Through double cantilevered beam (Mode I fracture toughness) testing, they concluded that an adhesive was necessary to achieve the most reliable bond between the carbon fiber plies and the stainless steel. They demonstrated that a stepped transition zone allowed the bolted joint to fail in bearing as opposed to one of the more catastrophic modes such as net-tension or shear out. Most importantly, with a 50% fiber volume fraction they demonstrated a 162% increase in ultimate bearing load in a pinned condition and an 84% increase in the bolted condition [41]. The work presented in this dissertation presents a continuation of this research by experimentally studying the progressive failure nature of

this material in multiple configurations, and by producing efficient finite element models to predict the capabilities of joints comprised of this material.

The research presented here is unique because the hybridization of IM7/977-3 preimpregnated carbon fiber composite with stainless steel does not appear to have been explored in literature outside of the work by Falugi and Knoth. The layup sequences explored here are unique, as is the study of a hybrid material across multiple configurations under one body of work. The fatigue data presented is the first effort to explore cyclical loading in this novel hybrid. Very little modeling exists for this unique hybrid and the approach of conducting analysis completely in the Abaqus environment is a first.

Chapter II of this document describes critical areas of theory that support the remainder of the work presented. Chapter III presents the experimental methodology, and Chapter IV presents the computational methodology. Chapter V presents results and discussion of the double shear experimental data, and Chapter VI presents results and discussion of the computational analysis and a comparison to the double shear experimental data. Results and discussion on the single shear experimental data are presented in Chapter VII, and the fatigue experimental results are presented in Chapter VIII. Finally, Chapter IX presents contributions, conclusions, and recommendations for future efforts based on the entire body of work.

II. Theory on Critical Topics

This chapter seeks to layout the theoretical background needed to support the work described in this document. These topics will not be discussed in an exhaustive nature, but in enough detail that the decisions made in and application to this study are explained and supported. While this chapter lays out the background theory for this work, the specifics of the implementation of these theories are discussed in the chapters on Experimental and Computational Methodology.

A bolted joint in a FML involves many diverse topics. Finite element modeling of this system brings about even more complexity. Since the material includes a composite material, failure mechanisms and failure criteria of composites must be considered. Also, different methods of modeling composites must be considered. For example, a complete layup can be approximated as a shell or, in cases where extreme detail is required, multiple elements through the thickness may be used to represent each individual layer. While addressing the foil, plasticity associated with stainless steel must be considered. Since the load is resisted though the fastener, a complex contact relationship must be developed between the fastener and the FML part. Finally, plasticity in the fastener must be considered to accurately represent bending in the fastener and how this bending affects load capacity in the specimen. This load scenario brings about numerous, complex contact relationships.

In the standard bearing test methods (ASTM D5961 and D6873), the fixture is constrained, and the load is applied to the coupon. Thus, the stress is transferred through the coupon and into the foil/composite transition zone. The fastener hole in the foil-composite zone transfers stress into the bolt via the contact interface between the bolt and

the coupon. This contact relationship creates the bearing stress of concern in this study. A contact interaction also occurs between the coupon and fixture. Contact interactions are required between each stacked layer and to prevent penetration. Furthermore, self-contact must be established to prevent components from penetrating themselves under large deformation. This load scenario is diagramed and discussed in detail in Chapter III.

Egan et al have investigated many of these topics in their work on lapped bolted joints. Figure 3 shows a single lap joint investigated by Egan et al. This joint was comprised of two coupons of unidirectional carbon fiber fastened with a single countersunk fastener. This image displays the strengths of modeling techniques such as advance failure models, layerwise modeling, and contact modeling. These topics and others will be explored in this chapter. The remainder of this chapter seeks to present the theory on these topics and some relevant research in which these theories have been employed. In some cases, a breadth of theory and research are presented to make the case for selecting a certain methodology for this study. This chapter includes a discussion on how these theories are collectively employed. The computational work in this study was carried out using Abaqus software. Thus the computational theory presented is compliant with or referenced from Abaqus [42]–[44]. The end of this chapter includes a discussion of failure modes observed in composites and a discussion on various approaches to cyclic fatigue experimentation.

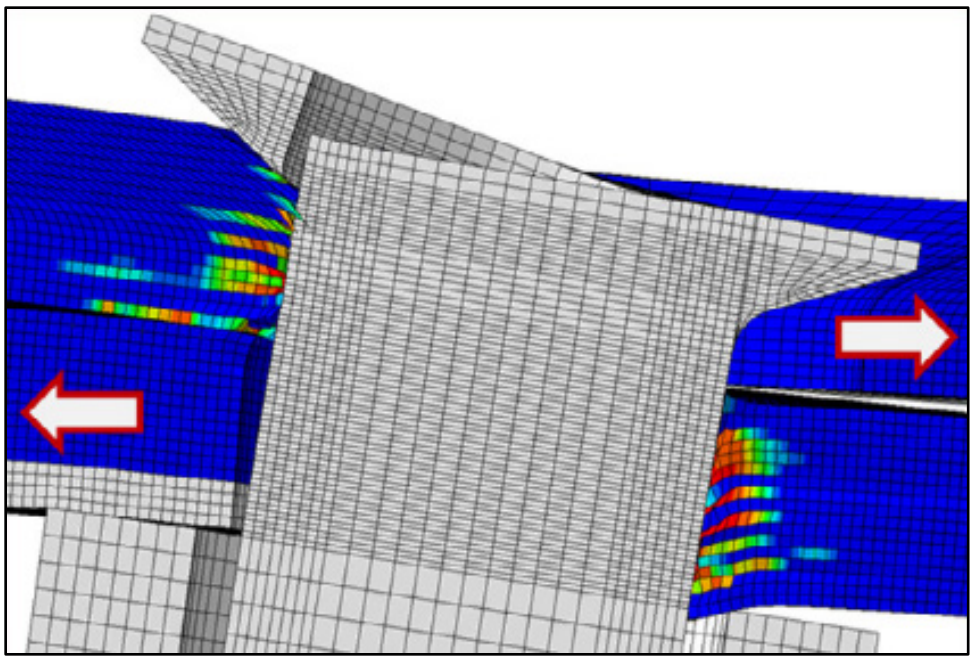

Figure 3: Compressive Fiber Damage in Double Lap Joint [44]

2.1 Stress-Strain Relations and Definitions

Finite element modeling is based in continuum mechanics. In the finite element method, first element strains are calculated using the strain displacement matrix, B_{sd}, as shown in Equation 1. This matrix is comprised of derivatives of admissible shape functions assumed for each type of element. This equation outputs total strain, ε^{tot}, using the strain-displacement matrix, and displacements.

$$\boldsymbol{\varepsilon^{tot} = B_{sd} u} \qquad (\mathbf{1})$$

With total strain calculated, the elastic strain must be calculated so that stress may be determined. This requires a discussion on types of strains. Strain can be divided into two types. Elastic strain is deformation that is fully recoverable and is not dependent on the deformation history. Conversely, plastic strain is not recoverable and is dependent on the

deformation history. The conclusion has been drawn that stress relies completely on elastic strain, and that elastic strain and plastic strain are additive to make total strain. Thus, in order to define elastic strain, ε^e, one need only know the plastic strain, ε^p, and subtract it from the total strain as seen below.

$$\boldsymbol{\varepsilon}^e = \boldsymbol{\varepsilon}^{tot} - \boldsymbol{\varepsilon}^p \quad (2)$$

The issue then becomes knowing the value of this plastic strain. Typically, an equivalent plastic strain is output as a result of the selected plasticity model and then expressed as components. These models are discussed more under Damage and Failure Criteria. With elastic strain known, the stresses can then be calculated using Hooke's Law by relating stress, σ, to elastic strain using the constitutive matrix, C.

$$\boldsymbol{\sigma} = \boldsymbol{C}\colon \boldsymbol{\varepsilon}^e \quad (3)$$

In Equation 3, the double dot operator is the double inner product also known as the dyadic. C is a fourth order tensor and ε^e is a second order tensor, which results in a stress output as a second order tensor.

If damage (discussed in Damage and Failure Criteria) has been initiated, and damage is in the evolution stage, these damage stresses are updated here before the internal forces are calculated.

Finally, internal forces, I, necessary for equilibrium are determined by

$$\boldsymbol{I} = \int_v \boldsymbol{B}_{\boldsymbol{sd}}^{\boldsymbol{T}} \boldsymbol{\sigma} dV \quad (4)$$

where B_{sd}^{T} is the transpose of the strain-displacement matrix and σ is stress determined from Equation 3. In an incremental finite element approach, these values of displacements, strains, and stresses are incremental values instead of total values [45]–[48].

An understanding of types and implications of different stresses and strains are also important to this work. Stress can be divided into two types, hydrostatic stress (also known as pressure stress) and deviatoric stress. Hydrostatic stress can be thought of as stress resulting from submerging an object in water which produces stress equally around the object normal to the surface. Hydrostatic stress causes volumetric strain and is related via the bulk modulus. The naming conventions "hydrostatic stress" and "pressure stress" often differ by a sign since stress is assumed to be tensile when positive, and pressure is assumed to be compressive when positive. Hydrostatic stress is given as the average of the three principal stresses as

$$\sigma_{hyd} = \frac{1}{3} tr(\sigma) \;\; or \;\; \sigma_{hyd} = \frac{1}{3}(\sigma_{kk}) = \frac{1}{3}(\sigma_{11} + \sigma_{22} + \sigma_{33}) \qquad (5)$$

In contrast, the component of stress that causes plastic deformation is known as deviatoric stress. This is simply the total stress with the hydrostatic component subtracted out. It is given by,

$$\boldsymbol{\sigma'} = \boldsymbol{\sigma} - \sigma_{hyd} \;\; or \; \sigma'_{ij} = \sigma_{ij} - \frac{1}{3}\delta_{ij}\sigma_{kk} \qquad (6)$$

$where \; \sigma'$ is the deviatoric stress, and δ_{ij} is the Kronecker delta.

Comparable ideas and values exist for strains where hydrostatic strain is given by

$$\varepsilon_{hyd} = \frac{1}{3} tr(\varepsilon) \;\; or \;\; \varepsilon_{hyd} = \frac{1}{3}(\varepsilon_{kk}) = \frac{1}{3}(\varepsilon_{11} + \varepsilon_{22} + \varepsilon_{33}) \quad (7)$$

And deviatoric strain is given by

$$\boldsymbol{\varepsilon'} = \boldsymbol{\varepsilon} - \; \varepsilon_{hyd} \;\; or \; \varepsilon'_{ij} = \varepsilon_{ij} - \frac{1}{3}\delta_{ij}\varepsilon_{kk} \quad (8)$$

Because three-dimensional loading is complex, there needs to be some effective stress value to predict when a metal fails. Von Mises stress is widely employed in this case. Von Mises stress, which can be derived from deviatoric strain energy, is given by

$$\sigma_{vm} = \sqrt{\frac{3}{2}\boldsymbol{\sigma'}:\boldsymbol{\sigma'}} \; or \; \sigma_{vm} = \sqrt{\frac{3}{2}\sigma'_{ij}\sigma'_{ij}} \quad (9)$$

Here, the double dot operator is the double inner product of two second order tensors. Thus, the output is a scalar value. This is convenient because it gives a one-dimensional equivalent value that can be compared to known experimental values of yield. For this reason, this is also referred to as an equivalent stress [45]–[48].

It is also helpful to have a related effective strain. This value, sometimes known as Von Mises Effective Strain, is given as

$$\varepsilon_{eff} = \sqrt{\frac{2}{3}\boldsymbol{\varepsilon'}:\boldsymbol{\varepsilon'}} \; or \; \varepsilon_{eff} = \sqrt{\frac{2}{3}\varepsilon'_{ij}\varepsilon'_{ij}} \quad (10)$$

These effective stresses and strains are commonly written using a bar notation instead of a subscript notation as seen below [45]–[48].

$$\varepsilon_{eff} \rightarrow \bar{\varepsilon} \quad and \quad \sigma_{vm} \rightarrow \bar{\sigma} \tag{11}$$

In classical plasticity methods, once the yield stress has been exceeded, Abaqus employs associated flow to develop the components of plastic strain from the equivalent plastic strain in a uniaxially defined stress-strain curve. The components of plastic strain for the current increment are given as

$$\Delta\varepsilon_{ij}^{p} = \Delta\bar{\varepsilon}^{p} n_{ij} \tag{12}$$

where $\Delta\bar{\varepsilon}^{p}$ corresponds to the equivalent plastic strain in the user defined curve and n is the normal to the yield surface given as

$$n_{ij} = \frac{3}{2}\frac{\sigma'_{ij}}{\bar{\sigma}} \tag{13}$$

where σ'_{ij} is the tensor form of the deviatoric stress and $\bar{\sigma}$ is the Von Mises stress. This relationship as illustrated by Mendelson is shown in Figure 4. Mendelson uses σ_e (equivalent stress) to denote Von Mises stress. [45], [49]

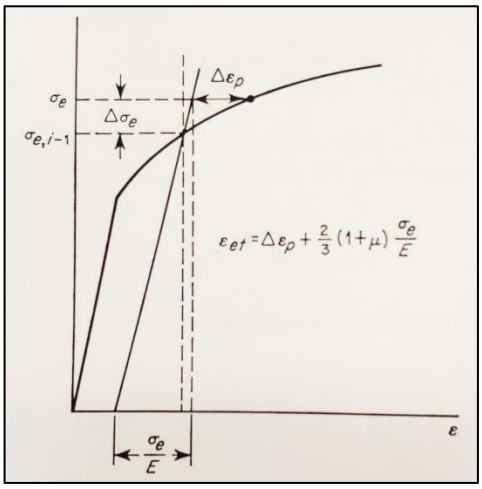

Figure 4: Incremental Stress and Plastic Strain [49]

An additional phenomenon that should be considered is viscoplasticity. Viscoplasticity describes plastic deformation that is dependent on the strain rate. This is commonly experienced in impact settings but may occur in settings where local strain rates are dynamic. The presence of viscoplasticity is heavily dependent on the strain rate and materials properties. The significance of viscoplasticity in this study is presented in the section on foil and bolt damage and the chapter on Computational Methodology [50].

2.2 Explicit vs Implicit Modeling

Many decisions in the modeling process are based on the type of analysis being considered. Since this study included simulation of a dynamic progressive failure, explicit and implicit dynamic analysis methods were both considered. Generally, explicit methods obtain values by solving for a given variable at time $t + \Delta t$ by using only values at time t. Explicit methods are conditionally stable based on a maximum time step based on wave propagation through the system. This stable time step is calculated prior to the first iteration of the explicit analysis. Implicit methods remove the time step constraint,

by solving for a given variable at $t + \Delta t$ by using inputs from both time t and $t + \Delta t$. [45]

2.2.1 Explicit Modeling

Abaqus Explicit, which was employed in this research, relies on central difference integration combined with a "lumped" mass matrix which is mathematically diagonalized. Central difference first satisfies equilibrium at time t. Accelerations at time t are then used to calculate the velocity at time $t + \frac{\Delta t}{2}$ and displacement at $t + \Delta t$. In the central-difference integration theory, the next $(i + 1st)$ position of a given degree of freedom is

$$u_{(i+1)} = u_{(i)} + \Delta t_{(i+1)} \dot{u}_{\left(i+\frac{1}{2}\right)} \quad (14)$$

where u is a displacement or rotation and i is an increment in an explicit step. Half step velocity is given as

$$\dot{u}_{\left(i+\frac{1}{2}\right)} = \dot{u}_{\left(i-\frac{1}{2}\right)} + \frac{\Delta t_{(i+1)} + \Delta t_{(i)}}{2} \ddot{u}_{(i)} \quad (15)$$

Acceleration is given by

$$\ddot{u}_{(i)} = (M)^{-1}\left(P_{(i)} - I_{(i)}\right) \quad (16)$$

M is the lumped mass matrix and $P_{(i)}$ is a vector of applied loads. $I_{(i)}$ is an internal force vector which is assembled from elemental contributions meaning a global stiffness matrix is not required. The construction of the internal force vector is discussed further in Stress-

Strain Relations. This process is *explicit* because values of velocity and acceleration from the previous step are used to calculate the next increment. In order to begin the calculations, Abaqus calculates the initial velocity as

$$\dot{u}_{\left(-\frac{1}{2}\right)} = \dot{u}_{(0)} + \frac{\Delta t_{(0)}}{2}\ddot{u}_{(0)} \qquad (17)$$

where $\dot{u}_{(0)}$ and $\ddot{u}_{(0)}$ are initial values of velocity and acceleration. With these boundary conditions and the initial position defined in the model, calculation is fully defined and the simulation can begin [45]–[47], [51], [52].

Belytschko et al concluded that explicit methods are well suited for complex contact relationships like the ones investigated in this study. Egan et al concluded that for a "simple" model, explicit and implicit methods in Abaqus produced similar results, while the explicit methods took about 3.5 times longer to run. However, they suggest that as damage focused models become more complex, the explicit method is advantageous. Much of Egan's follow-on research on countersunk bolted joints includes explicit modeling. Explicit solution methods also allow for a wide range of contact definitions and automatic or fixed time incrementation [42]–[44].

2.3 Geometric Nonlinearity

Due to the complex nature of the failure modes of these materials and the intention to characterize progressive failure, nonlinearity in both geometry and materials are considered. Materials nonlinearity is covered under damage and failure criteria. Mathematically, the nonlinear terms in strain come from a Tayler Series Expansion employed during the derivation. The equation seen below including the quadratic terms is

commonly known as Green Strain. Here, u terms are displacements and x^0 terms are the undeformed positions. This is the default for shells and beams in Abaqus Standard that assume small strains [46].

$$E_{ij} = \frac{1}{2}\left[\frac{\partial u_i}{\partial x_j^0} + \frac{\partial u_j}{\partial x_i^0} + \sum_n \frac{\partial u_m}{\partial x_i^0}\frac{\partial u_m}{\partial x_j^0}\right] \quad \textbf{(18)}$$

To simplify calculations, engineers often make an assumption of small displacements and rotations and only consider the linear terms. This results in what is known as the small or infinitesimal strain tensor. [53], [54].

$$\epsilon_{ij} = \frac{1}{2}\left(\frac{\partial u_i}{\partial x_j^0} + \frac{\partial u_j}{\partial x_i^0}\right) \quad \textbf{(19)}$$

Functionally, Abaqus Explicit defaults to employing logarithmic strain (true strain) to account for geometric nonlinearity calculated as

$$\boldsymbol{\epsilon}_T = ln\left(\sqrt{\boldsymbol{F}\cdot\boldsymbol{F}^T}\right) \quad \textbf{(20)}$$

Where $\boldsymbol{F}$ is the deformation gradient tensor given as

$$F_{ij} = \delta_{ij} + \frac{\partial u_i}{\partial x_j^0} \quad \textbf{(21)}$$

Where δ_{ij} is the Kronecker delta, u terms are displacements and x^0 terms are the undeformed positions.

Egan, McCarthy, and Frizzell concluded that in a double-lap countersunk joint, it was most efficient to omit geometric nonlinearity in implicit modeling to ensure

convergence and computation efficiency. It is important to note that Egan et al were working with a standard composite panel instead of a hybrid. Thus, they did not face large deformations and plasticity in metals. However, they noted that in an explicit model, the Abaqus default state of including geometric nonlinearity produced stable simulations [43].

2.4 Composite Modeling Methods

One of the first decisions to make when constructing a model containing composites is how to represent the laminate. Numerous methods have been studied and may be placed into four main categories: Three-Dimensional elasticity (3D), Equivalent Single Layer (ESL), Zig-Zag, and Layerwise (LW). 3D theories treat the composite as a solid. Equivalent Singe Layer modeling constructs a representative shell that mimics the properties of a given layup. ESL models effectively create a two-dimensional solution to a three-dimensional problem and are unable to properly represent the transverse stress field. Zig-Zag models employ the superposition of a polynomial displacement field with a Zig-Zag function. These methods still have trouble with transverse stresses. Layerwise modeling constructs individual layers with at least one, but often many elements through the thickness of each layer. This method represents interlaminar relationships, discontinuities and stress concentrations well. For this reason, the layerwise approach is predominant in the study of bolted and countersunk joints [55], [56].

Abaqus contains a “Composite Layup” tool that is a complex ESL-type system. It tends to model macroscopic composite shell parts well. However, it does not provide the

detail and mesh refinement required when the focus is on progressive failure near a loaded discontinuity [45], [46].

2.5 Computational Damage and Failure Criteria

Damage and failure criteria drive modern-day modeling capabilities. In general, there are three phases of damage and failure: initiation, evolution (or stiffness degradation), and element deletion. Damage initiation is typically thought of as the point at which the material has yielded. However, in many cases, the user is allowed to define the exact definition of damage initiation. Damage evolution typically describes how the material behaves through some deformation or degradation resulting in failure. The user is typically able to define failure, and then the user is allowed to delete the element when failure criteria are met if so desired. In the different criteria presented below for specific components, the method by which each criterion fits into these three phases is discussed [45], [46].

2.5.1 Ductile Damage

Since this study examined progressive failure and based on preliminary testing, it was expected that the stainless steel foils would yield. While plasticity in the bolt is undesirable, it was considered a possibility in experimentation and modeling. This section describes the user input and mathematical theory behind damage in ductile materials and concludes with a single element example.

To define a ductile metal, the user is able to define an equivalent stress-strain curve. The user is able to define elasticity by inputting the elastic modulus. Yield and

plasticity are defined tabularly as true stresses and true plastic strains. At yield, the user inputs the yield stress and a zero value for true plastic strain.

2.5.1.1 Damage Initiation and Evolution

For materials exhibiting plastic deformation, damage is initiated at a user defined stress or strain. Then, the damage variable, d, evolves with respect to time as

$$\dot{d} = \frac{L_c \dot{\bar{\varepsilon}}^{pl}}{\bar{u}_f^{pl}} \tag{22}$$

where, L_c is the element characteristic length based on element geometry. For a first order element, it is the typical length of a line across an element. For a second order element, it is half of this length. A first order element is defined by a linear shape function with two nodes on an edge, while a second order element is defined by a quadratic shape function with three nodes along an edge. For membrane and shell elements, it is calculated as the square root of area. Characteristic length is established for each element at the beginning of the analysis and is held as a constant reference throughout the analysis. $\dot{\bar{\varepsilon}}^{pl}$ is the equivalent plastic strain rate which is the strain rate with respect to the time step. $\bar{u}_f^{pl}$ is the user specified effective plastic displacement at failure. Buentello employed a value of $\bar{u}_f^{pl}$ as 1/6th of the characteristic length of critical elements [47]. In this study, due to the extremely thin elements, when a displacement failure criteria was used, it was set to the thickness of the material. Effective stress, which can be thought of as reduced load carrying capacity, is then calculated based on this damage variable as

$$\boldsymbol{\sigma} = (1 - d)\bar{\boldsymbol{\sigma}} \tag{23}$$

Thus, when the damage evolution variable is equal to one, the material is fully degraded. The user may choose to delete the element at a given value of d.

2.5.1.2 Ductile Damage Example

Figure 5 shows a single 3D stress element representing a ductile metal that was loaded in tension until failure. Figure 6 shows the output of the simulation. Figure 6A (upper subplot) displays the stress v. strain while Figure 6B (bottom subplot) displays damage initiation and evolution variables. In this case, the model scenario was a simple bilinear elastic-plastic curve with linear displacement damage. Element deletion was used for demonstration purposes. As the element reaches the defined yield stress, damage is initiated (represented by a solid red line in Figure 6B). As the sample is loaded through the plastic region, the damage initiation variable is defined by normalizing the stress at the current step by the failure stress. When the defined failure stress is reached, the damage initiation variable reaches a value of 1 which initiates damage evolution. This begins calculating a damage evolution variable, d from equation 22 (represented by a dot-dashed green line in the lower subplot). As the damage evolution (or stiffness degradation) variable increases, it linearly degrades the stiffness in the stress-strain plot as defined by equation 23. When damage evolution reaches a value of 1, the stiffness is fully degraded. In this example, element deletion is employed, so that when the stiffness is fully degraded the element is deleted. This is represented by the element status

represented by the blue dashed trace in the lower subplot. When the element is deleted, the status transitions from 1 to 0.

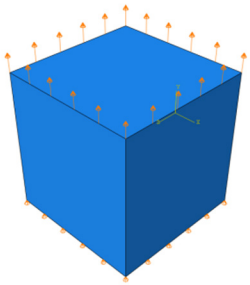

Figure 5: Ductile Damage Single Element Model

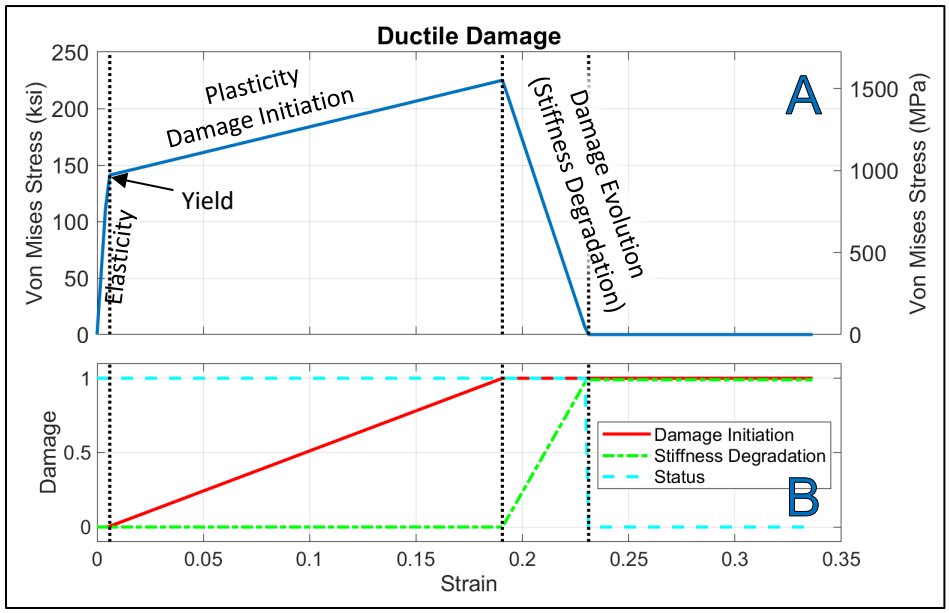

Figure 6: Ductile Damage Single Element Example Output

2.5.1.3 Explicit Step Implementation

In an explicit time step, the equivalent stress in an element is compared to the user input yield stress. If yield has not occurred, equivalent plastic strain is set to zero and the stresses are output. If yield has occurred, the equivalent plastic strain is calculated based

on the user defined stress-strain curve, and damage initiation is checked by comparing the current equivalent plastic strain with the user input damage initiation strain. If no damage has occurred, the stresses and equivalent plastic strains are output. If damage has occurred, the damaged stresses are fed into the central difference approximation. If element deletion is used, the element is deleted, and the status is updated at the user defined value of the damage evolution variable. In the section on Consolidation of Computational Theory, this is integrated into the entire explicit step flow in Block 4 of Figure 20**.**

2.5.2 Composite Damage

Numerous failure criteria have been developed, studied, and applied as composite materials have been developed. A 1996 FAA study performed an exhaustive study on 26 of the most common criteria. These criteria can be split into three main categories: limit, interactive, and separate mode criteria. Limit criteria consider stresses with corresponding materials properties. Interactions are not considered. Interactive criteria employ a polynomial involving all stress components. Separate mode criteria consider matrix and fiber failure separately. The FAA study cites a survey by Burk of AIAA members that showed that at the time, the majority of users employed the limit style criteria of maximum stress and maximum strain criteria. However, this study goes on to say, *"At the lamina level, those criteria (such as the Hashin-Rotem criterion) which separate the fiber failure mode from the matrix failure mode are the most reasonable and accurate*[57]*."* Hashin failure has become the most commonly used set of criteria in unidirectional composite analysis and is built into Abaqus [58].

This section first lays out composite damage initiation and damage evolution criteria then walks through a simple single element example. Finally, the implementation into an explicit step is described.

2.5.2.1 Composite Damage Initiation

2.5.2.1.1 Hashin Failure

Hashin criteria (Hashin and Rotem, 1973 [59]; and Hashin, 1980 [60]) describe damage initiation and failure in unidirectional fiber reinforced composites. These methods have been widely employed in the modeling of polymer matrix composites and have been successfully applied to bolted joints in fiber metal laminates. As discussed in the previously mentioned NASA study, Hashin failure is beneficial because it separately represents failure modes in the fibers and the matrix. It also separates tensile and compressive properties and loading of each [24], [38], [58], [61]–[63]. Thus, four separate criteria are observed, and each may be analyzed separately in finite element software. The Hashin damage initiation criteria, as employed in Abaqus, are given below.

Fiber Tension ($\hat{\sigma}_{11} < 0$):

$$F_f^t = \left(\frac{\hat{\sigma}_{11}}{X^T}\right)^2 + \alpha\left(\frac{\hat{\tau}_{12}}{S^L}\right)^2 \quad (24)$$

Fiber Compression ($\hat{\sigma}_{11} < 0$):

$$F_f^c = \left(\frac{\hat{\sigma}_{11}}{X^C}\right)^2 \quad (25)$$

Matrix Tension ($\hat{\sigma}_{22} \geq 0$):

$$F_m^t = \left(\frac{\hat{\sigma}_{11}}{X^T}\right)^2 + \alpha\left(\frac{\hat{\tau}_{12}}{S^L}\right)^2 \quad (26)$$

Matrix Compression ($\hat{\sigma}_{22} < 0$):

$$F_m^c = \left(\frac{\hat{\sigma}_{22}}{2S^T}\right)^2 + \left[\left(\frac{Y^C}{2S^T}\right)^2 - 1\right]\frac{\hat{\sigma}_{22}}{Y^C} + \left(\frac{\hat{\tau}_{12}}{S^L}\right)^2 \quad (27)$$

In the equations above

X^T is the longitudinal tensile strength

X^C is the longitudinal compressive strength

Y^T is the transverse tensile strength

Y^C is the transverse compressive strength

S^L is the longitudinal shear strength

S^T is the transverse shear strength

α is a coefficient determining the shear stress contribution

$\hat{\sigma}_{11}, \hat{\sigma}_{22}, \hat{\tau}_{12}$ are diagonal components of the effective stress tensor $\hat{\sigma}$

This effective stress tensor is related to the true stress by a damage matrix, M (Equation 28). This diagonal matrix consists of damage variables for the fibers, matrix and shear, as recorded in Equations 29 and 30.

$$\hat{\boldsymbol{\sigma}} = \boldsymbol{M\sigma} \quad (28)$$

Where

$$\boldsymbol{M} = \begin{bmatrix} \frac{1}{(1-d_f)} & 0 & 0 \\ 0 & \frac{1}{(1-d_m)} & 0 \\ 0 & 0 & \frac{1}{(1-d_s)} \end{bmatrix} \quad (29)$$

where d_f, d_m, and d_s are defined from the relationship

$$d_f = \begin{cases} d_f^t & if \quad \hat{\sigma}_{11} \geq 0 \\ d_f^c & if \quad \hat{\sigma}_{11} < 0 \end{cases}$$

$$d_m = \begin{cases} d_m^t & if \quad \hat{\sigma}_{22} \geq 0 \\ d_m^c & if \quad \hat{\sigma}_{22} < 0 \end{cases} \quad (30)$$

$$d_s = 1 - \left(1 - d_f^t\right)\left(1 - d_f^c\right)(1 - d_m^t)(1 - d_m^c)$$

In Equation 30, the specific damage variables are the damage evolution variables presented later (Equation 42). Prior to damage initiation, these damage variables are zero. Thus, M is the identity matrix, meaning effective stress is equal to the actual stress until damage is initiated by one of the four criteria (Equations 24-27) reaching a value of one. As damage occurs, M grows, increasing effective stress. This allows failure in a single mode to affect other modes. [46], [60]

Hashin failure criteria or components thereof are commonly used in composite modeling and have been employed in composite bearing and FML bearing simulation. Zhou et al employed Hashin Criteria to model fiber failure in single-lap multi-bolt joints [25], and Zu et al demonstrated good characterization of a FML bolted joint using Hashin [24]. While Hashin criteria does require a large number of materials properties, several sets of properties are available for the IM7/977-3 material used in this research.

2.5.2.1.2 Puck Failure

Puck proposed that a third matrix failure mode was possible as depicted in Figure 7. Namely, that the matrix may fracture at some angle in addition to the two modes allowed in Hashin criteria.

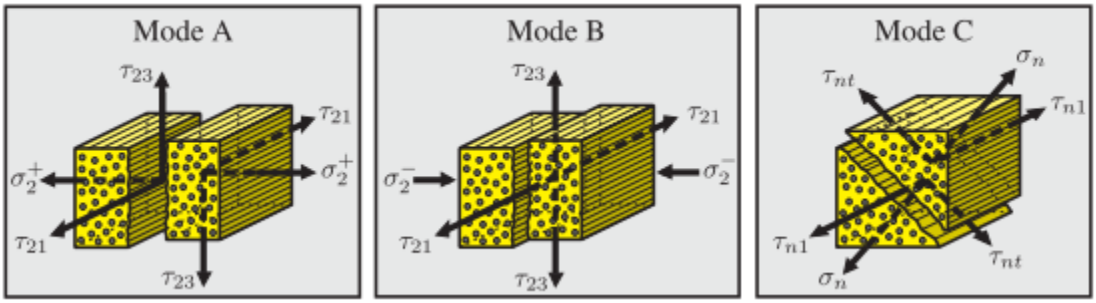

Figure 7: Possible Modes for Hashin (A and B only) and Puck Failure Criteria [64]

This seems like a vast improvement, but has been shown to not significantly change a failure prediction [64]. Working with Puck failure creates some complications. First, much of the related research is published in German. Second, this criterion has not been integrated into the standard Abaqus software package, and thus is not employed in this research [65], [66].

In the last decade, a number of three-dimensional composite failure criteria have been studied by groups like Hundley et al [38], Zhou et al [25] and Donadon et al [63]. However, none appear to be widely accepted or applied to date and none are inherent to Abaqus.

2.5.2.2 Composite Damage Evolution

The proposed damage initiation criteria assume linear elastic behavior up until failure. Then, the load carrying capacity considered during damage evolution is also

assumed to be linear. While these do omit nonlinearity, they are widely accepted as representing brittle composites well [46], [67], [68] .

After damage has initiated via some criterion, such as Hashin, Abaqus uses a damage elasticity relationship where stress is related to strain through a damage elasticity matrix as seen in Equations 31 and 32.

$$\boldsymbol{\sigma} = \boldsymbol{C_d}\boldsymbol{\varepsilon} \tag{31}$$

C_d is the damage elasticity matrix given as

$$\boldsymbol{C_d} = \frac{1}{D}\begin{bmatrix} (1-d_f)E_1 & (1-d_f)(1-d_m)\nu_{21}E_1 & 0 \\ (1-d_f)(1-d_m)\nu_{12}E_2 & (1-d_m)E_2 & 0 \\ 0 & 0 & (1-d_s)GD \end{bmatrix} \tag{32}$$

$$D = 1-(1-d_f)(1-d_m)\nu_{12}\nu_{21}$$

where E is the elastic modulus, G is the shear modulus, ν is the Poisson's Ratio, d_f and d_m are the previously employed damage variables used in failure initiation described in Equation 42. [45], [46]

With the stress-strain relation developed, the damage variable evolves as seen in Figure 8.

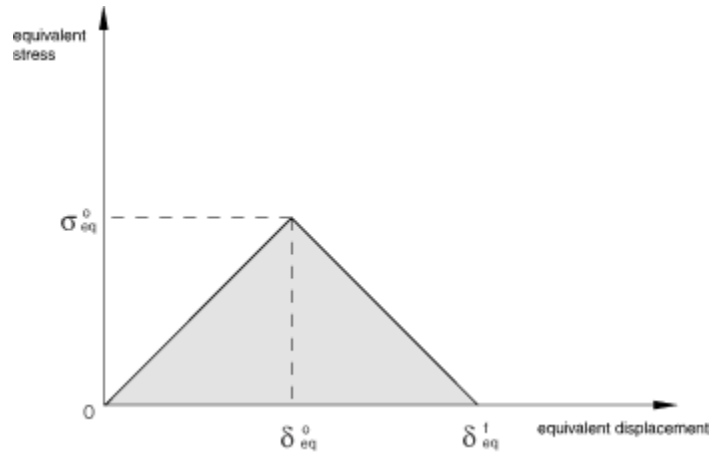

Figure 8: Equivalent Stress vs Equivalent Displacements

It is important to note that the values in Equation 31 are stress and strain matrices. Here, equivalent stresses and strains, as laid out in Equations 33-40, are derived from the components stress and strain matrices of the relationship in Equation 31. It is also important to note that the plot in Figure 8 represents only one mode of the four considered: fiber tension, fiber compression, matrix tension, and matrix compression. Equations 33-40 develop equivalent stresses and strains used to define damage evolution in each of the four described modes. These are calculated based on total stress and strain values accumulated at the current increment. These equations are also used in the calculation of the damage variable described later in Equation 42.

Fiber Tension ($\hat{\sigma}_{11} \geq 0$):

$$\delta_{eq}^{ft} = L^C \sqrt{\langle \varepsilon_{11} \rangle^2 + \alpha \varepsilon_{12}^2} \tag{33}$$

$$\sigma_{eq}^{ft} = \frac{\langle \sigma_{11} \rangle \langle \varepsilon_{11} \rangle + \alpha \tau_{12} \varepsilon_{12}}{\delta_{eq}^{ft} / L^C} \tag{34}$$

Fiber Compression ($\hat{\sigma}_{11} < 0$):

$$\delta_{eq}^{fc} = L^C \langle -\varepsilon_{11} \rangle \tag{35}$$

$$\sigma_{eq}^{fc} = \frac{\langle -\sigma_{11} \rangle \langle -\varepsilon_{11} \rangle}{\delta_{eq}^{fc} / L^C} \tag{36}$$

Matrix Tension ($\hat{\sigma}_{22} \geq 0$):

$$\delta_{eq}^{mt} = L^C \sqrt{\langle \varepsilon_{22} \rangle^2 + \varepsilon_{12}^2} \tag{37}$$

$$\sigma_{eq}^{mt} = \frac{\langle \sigma_{22} \rangle \langle \varepsilon_{22} \rangle + \tau_{12} \varepsilon_{12}}{\delta_{eq}^{mt} / L^C} \tag{38}$$

Matrix Compression ($\hat{\sigma}_{22} < 0$):

$$\delta_{eq}^{mc} = L^C \sqrt{\langle -\varepsilon_{22} \rangle^2 + \varepsilon_{12}^2} \tag{39}$$

$$\sigma_{eq}^{mc} = \frac{\langle -\sigma_{22} \rangle \langle -\varepsilon_{22} \rangle + \tau_{12} \varepsilon_{12}}{\delta_{eq}^{mt} / L^C} \tag{40}$$

where L^C is the characteristic length.

The $\langle\ \rangle$ symbol is the Macaulay operator which is defined for all $a \in \mathbb{R}$ real numbers as

$$\langle a \rangle = \frac{a + |a|}{2} \tag{41}$$

Finally, the damage variable for any given mode is given as seen in Equation 42. By referencing this variable, the user has a quick understanding and characterization of failure in each of the 4 modes in each element. If the damage variable exceeds 1, the element has failed. Abaqus will output the element STATUS which, for a selected mode, displays the elements that have failed with respect to this damage variable.

$$d = \frac{\delta_{eq}^{f}\left(\delta_{eq} - \delta_{eq}^{0}\right)}{\delta_{eq}\left(\delta_{eq}^{f} - \delta_{eq}^{0}\right)} \tag{42}$$

where, δ_{eq}^{0} is the equivalent displacement at which the damage criterion was met and δ_{eq}^{f} is the fracture equivalent displacement for the given mode. Based on this damage variable, the user can decide to delete the element or keep it in place [46], [69],[70].

2.5.2.3 Composite Damage and Failure Example

While this set of equations may seem complex, when considered in each mode (such as fiber tension) separately, they are much simpler to understand. Even in fairly complex load scenarios, for a given element, there is usually only one or two critical modes. To demonstrate the functionality of Hashin damage initiation and composite damage evolution, a single element example model was developed as depicted in Figure 9. The element was loaded in tension with the fiber direction at a 15° angle to the

direction of the applied force. This angle caused both matrix tension and fiber tension in the element.

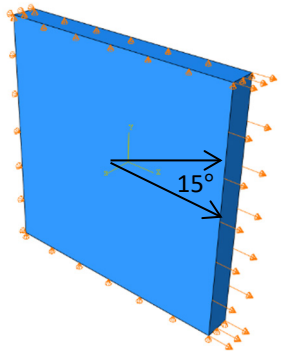

Figure 9: Composite Damage Single Element Model

Figure 10 depicts the output of the composite single element model. The top subplot (Figure 10A) depicts stress v. strain. The center plot (Figure 10B) shows fiber tension damage initiation and evolution and the bottom subplot shows matrix tension criteria. Upon initial loading, the values of both the fiber tension and matrix tension damage initiation variables rise. Fiber tension damage initiation is represented by a solid red line in the middle subplot (Figure 10B). Matrix tension damage initiation is represented by the dashed red line in the bottom subplot (Figure 10B). As loading increases, the fiber tension initiation variable reaches a value of 1 which triggers calculation of the damage evolution variable. As depicted by the green dashed line in the center subplot (Figure 10B), the fiber tension damage evolution variable increases, which in turn drives down the stress capacity of the element. In this case, the element deletion was not employed so the element maintains 1% of its stiffness. Since fiber tension reached a value of 1 and matrix tension did not, this element should be characterized as having failed in fiber tension.

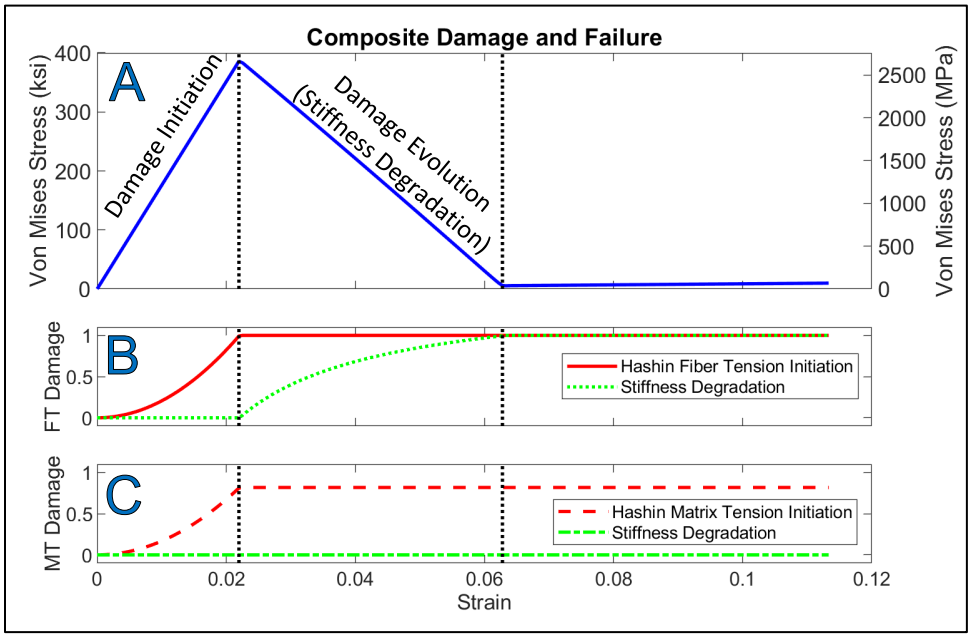

Figure 10: Composite Damage Single Element Example Output

2.5.2.4 Explicit Step Implementation

In an explicit step, stresses from the stress-strain relations are used to calculate an effective stress tensor based on damage (Eq 28 and 29). If no damage has occurred, this is equal to the stress values from the stress-strain relations. Then, these effective stresses are run through the Hashin failure criteria to predict failure (Eq 24-27). If any of the criteria reaches a value of one, failure is initiated in that mode. If failure is not initiated, the elastically derived stresses and strains are output. If damage has occurred, effective stresses and strains are calculated (Eq 33-40), and then the damage evolution variable is calculated (Eq 42). Finally, the damaged stresses (Eq 31) can be calculated using the damage elasticity matrix (Eq 32). These damaged stresses are then used in the calculation of the internal elemental forces. If desired by the user, the element is deleted at a given

value of d and the element status updated [45], [46]. In the section on Consolidation of Computational Theory, this is integrated into the entire explicit step flow in Block 6 of Figure 20. As a comment on the stability of Hashin failure, throughout this work, when coupled with continuum shell elements, the composite layers never drove the critical time step size.

2.5.3 Cohesive Layers and Interactions

When using a layerwise modeling method, one must consider how to define the surface interfaces between stacked plies. This region is known as the interlaminar matrix region. If the composite layers are simply tied together, the system becomes far stiffer than a realistic composite layup. Additionally, ties do not provide a way to describe delamination behavior. For this reason, other methods are required to define this region. The two most common ways to represent this region are to employ cohesive element or cohesive interactions. These are usually covered under the overarching term "cohesive zones." These two methods are also considered in adhesively bonded joints such as the adhesive used in the layup in this study. The main difference is that there is no inherent thickness of a cohesive interaction while the cohesive layer is modeled using a cohesive element of a given representative thickness. Properties of cohesive interactions are defined using interaction properties much like a user would define contact. Cohesive elements are defined by applying materials properties to a set of cohesive elements. As a result, cohesive interactions output values such as contact opening and sliding and contact stresses while cohesive elements output element stresses and strain.

Cohesive zones are typically modeled using traction-separation laws. Similar to the composite damage, cohesive damage involves damage initiation, damage evolution, and element deletion. These definitions are similar for both cohesive interactions and cohesive elements [45], [46].

This section discusses common cohesive damage initiation and cohesive damage evolution methods. Then a single element finite element model is presented as an example. Finally, the implementation into an explicit step is presented.

2.5.3.1 Cohesive Damage Initiation

Using cohesive elements, strains are defined as

$$\varepsilon_n = \frac{\delta_n}{T_0}, \varepsilon_s = \frac{\delta_s}{T_0}, \varepsilon_t = \frac{\delta_t}{T_0} \tag{43}$$

where δ_n, δ_s, and δ_t are relative displacements of the cohesive layer and T_0 is the original thickness of the layer [45], [46].

Elastic behavior for cohesive elements is given as

$$t = \begin{Bmatrix} t_n \\ t_s \\ t_t \end{Bmatrix} = \begin{bmatrix} E_{nn} & E_{ns} & E_{tt} \\ E_{ns} & E_{ss} & E_{st} \\ E_{nt} & E_{st} & E_{tt} \end{bmatrix} \begin{Bmatrix} \varepsilon_n \\ \varepsilon_s \\ \varepsilon_t \end{Bmatrix} = \boldsymbol{E\varepsilon} \tag{44}$$

In cohesive interactions, since thickness is not considered, the elastic behavior is written in terms of relative displacements as,

$$t = \begin{Bmatrix} t_n \\ t_s \\ t_t \end{Bmatrix} = \begin{bmatrix} K_{nn} & K_{ns} & K_{tt} \\ K_{ns} & K_{ss} & K_{st} \\ K_{nt} & K_{st} & K_{tt} \end{bmatrix} \begin{Bmatrix} \delta_n \\ \delta_s \\ \delta_t \end{Bmatrix} = \boldsymbol{K\delta} \tag{45}$$

Figure 11 shows a typical traction-separation response. Below, t_n^0, t_s^0, and t_t^0 represent peak displacement in the normal, shear, and transverse shear directions respectively. Simlary, $\varepsilon_n^0, \varepsilon_s^0$, and ε_t^0 represent peak strains. These values are based on known materials properties. In many cases, these parameters are published by material manufacturers and developed by researchers through experimentation in specific applications. Traction and strain values without the zero superscripts are values measured throughout deformation. [45], [46]

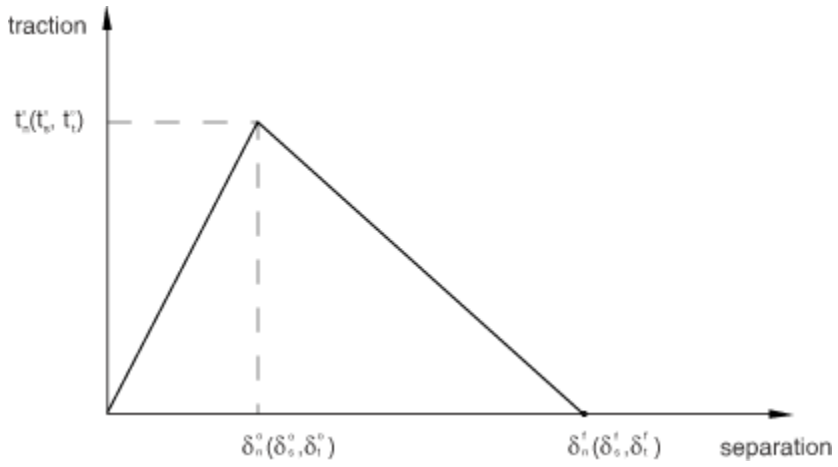

Figure 11: Traction-Separation Response [46]

Damage initiation, the positive sloped portion of Figure 11, is typically modeled using a stiffness and one of the following criteria: maximum strain, maximum stress, quadratic strain, quadratic stress. These are presented below. In all cases, damage is assumed to be initiated when the criteria is equal to one. The ⟨ ⟩ operator is the Macaulay operator as discussed and presented in equation 41. It is used here to show that pure normal compressive stress does not initiate damage in traction-separation methods. As the names imply, maximum stress and strain criteria take the maximum value in any component

direction compared to its peak capacity input by the user. If at any time this value meets or exceeds one for any element, that element has sustained damage. These first two methods do not combine loading directions. The quadratic methods allow damage to grow quadratically and consider the combination of modes [45], [46].

Maximum nominal stress

$$\max\left\{\frac{\langle t_n\rangle}{t_n^0}, \frac{t_s}{t_s^0}, \frac{t_t}{t_t^0}\right\} = 1 \tag{46}$$

Maximum nominal strain

$$\max\left\{\frac{\langle \varepsilon_n\rangle}{\varepsilon_n^0}, \frac{\varepsilon_s}{\varepsilon_s^0}, \frac{\varepsilon_t}{\varepsilon_t^0}\right\} = 1 \tag{47}$$

Quadratic nominal stress

$$\left\{\frac{\langle t_n\rangle}{t_n^0}\right\}^2 + \left\{\frac{t_s}{t_s^0}\right\}^2 + \left\{\frac{t_t}{t_t^0}\right\}^2 = 1 \tag{48}$$

Quadratic nominal strain

$$\left\{\frac{\langle \varepsilon_n\rangle}{\varepsilon_n^0}\right\}^2 + \left\{\frac{\varepsilon_s}{\varepsilon_s^0}\right\}^2 + \left\{\frac{\varepsilon_t}{\varepsilon_t^0}\right\}^2 = 1 \tag{49}$$

2.5.3.2 Cohesive Damage Evolution

To aid in calculation of damage evolution, Abaqus calculates an effective displacement as [71]:

$$\delta_m = \sqrt{\langle \delta_n \rangle^2 + \delta_s^2 + \delta_t^2} \quad (50)$$

This is rolled into the linear deformation-based damage evolution variable as

$$D = \frac{\delta_m^f (\delta_m^{\max} - \delta_m^0)}{\delta_m^{\max} \left(\delta_m^f - \delta_m^0\right)} \quad (51)$$

where $\delta_m^{\max}$ is the maximum value of effective displacement through the deformation history.

Damage evolution can also employ various energy methods as opposed to the stress-strain methods above. These are convenient because many common tests are employed that yield these energies.

The linear energy method employs the same basic equation as in Equation 51. However, in this case, the effective displacement at failure is defined as

$$\delta_m^f = \frac{2G^C}{T_{eff}^0} \quad (52)$$

where T_{eff}^0 is the effective traction at damage initiation and G^C is mixed mode fracture energy calculated differently in different methods. The calculation of this mixed mode fracture energy for various criteria is the subject of much research.

These selected damage variables feed into the following set of equations from which Abaqus calculates the properties of the cohesive zones at the step being considered.

$$t_n = \begin{cases} (1-D)\bar{t}_n \; for \; \bar{t}_n \geq 0 \\ \bar{t}_n \;\; otherwise \; (no \; damage \; to \; compressive \; stiffness) \end{cases}$$
$$t_s = (1-D)\bar{t}_s$$
$$t_t = (1-D)\bar{t}_t \qquad (53)$$

where $\bar{t}_n$, $\bar{t}_s$, and $\bar{t}_t$ are the stress components assuming no damage [45], [46].

Figure 12 shows how energy methods are employed in traction-separation laws in Abaqus. In essence this is a multidimensional version of the plot shown in Figure 11. Here the Benzeggagh-Kenane (B-K) criterion is being used to calculate G^C. This model is geared toward situations where the critical fracture energies in both shear directions are expected to be the same. The B-K criterion are given as

$$G^C = G_n^C + (G_s^C - G_n^C)\left\{\frac{G_s}{G_T}\right\}^\eta \qquad (54)$$

where

$$G_S = G_s + G_t \;\; and \; G_T = G_n + G_s \qquad (55)$$

The user should input the critical energies G_n^C and G_s^C and the material parameter η [45], [46].

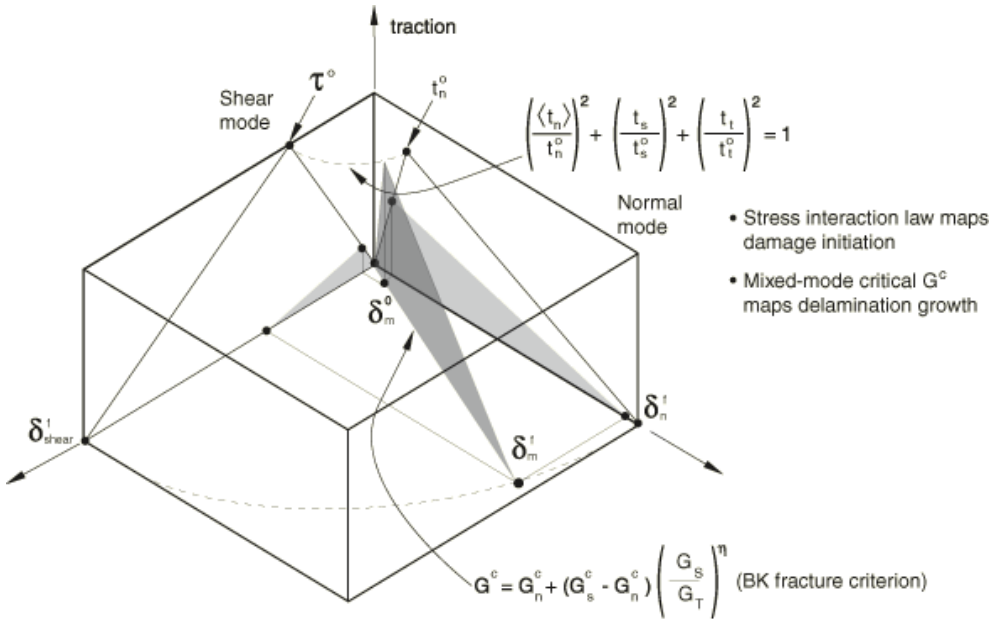

Figure 12: Mixed Mode Response In Cohesive Interactions or Elements [46]

Figure 12 plots the traction mode along the 2 axis and the shear mode along the 1 axis. The damage initiation and progress are plotted in the third direction. The plots lying on the 1-3 plane represent the shear mode independently and the plot in 2-3 plane represents the tensile mode independently. The three-dimensional plot represents the mixed mode damage criterion. In effect, these mixed-mode methods form an equivalent traction-separation behavior much like one would consider an equivalent stress and strain. Here however, fracture energies are the quantities being mixed [45], [46].

The use of cohesive zones is now inherent in much of the current composite fastener research. Frizzel et al employed an optimized cohesive layer shape with Benzeggagh–Kenane criteria in GLARE to model delamination at the critical area near the bolt while preserving computational efficiency [72].

2.5.3.3 Cohesive Single Element Example

Figure 13 depicts a single element model to explain cohesive behavior. A cohesive element is used here since its simplicity provides the clearest example. However, cohesive behavior defined by cohesive interactions functions in much the same way computationally, since both used the same set of equations for traction-separation behavior (equations 46 to 55) after the initial elastic behavior is characterized (equation 44 or 45). This element is loaded in tension over the area of a thin cohesive layer. A clamped boundary condition is placed on the bottom layer and a displacement is commended to the top surface. Figure 14 shows the response of this single element model. Figure 14A (top subplot) shows stress v. strain, while Figure 14B (bottom subplot) shows quadratic stress initiation criteria and linear damage evolution criteria. As the element is loaded, the damage initiation variable (represented by the solid red line) rises. When it reaches a value of 1, the damage evolution variable (green dashed line) rises and begins to degrade the element stiffness. Finally, the element is deleted forcing the status (dotted cyan line) to a value of 0.

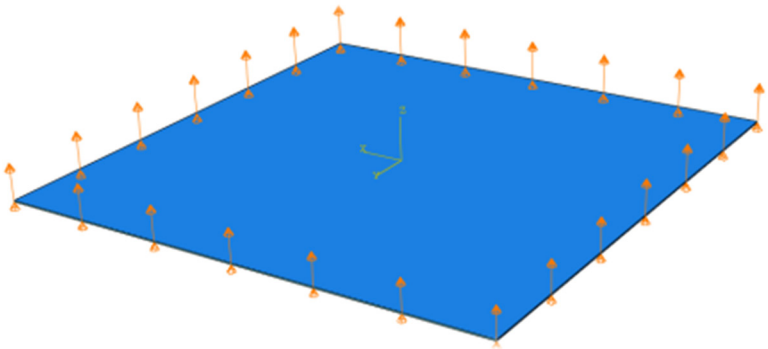

Figure 13: Cohesive Damage Single Element Model

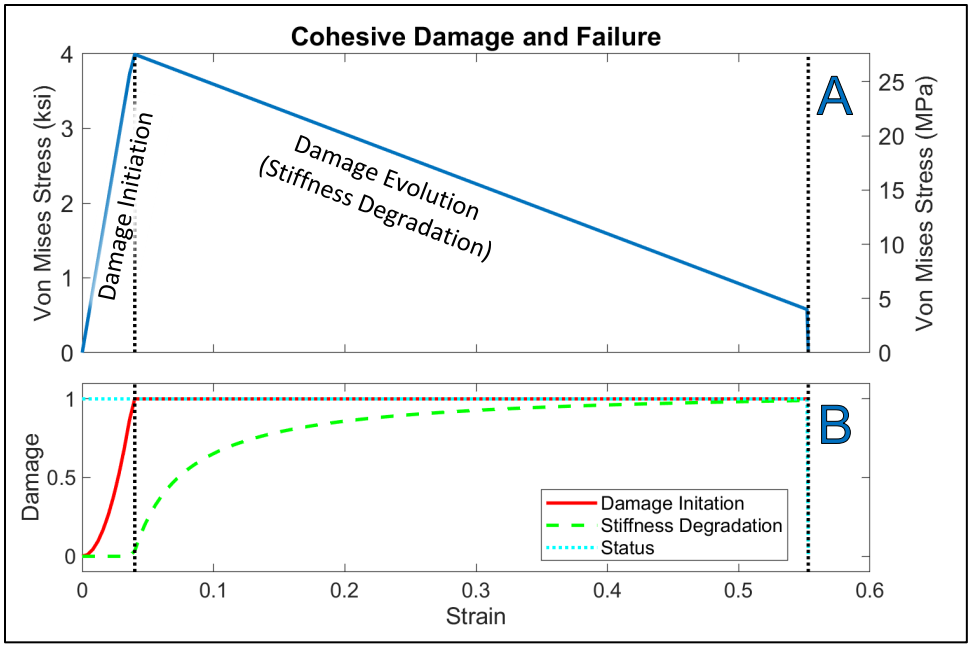

Figure 14: Cohesive Damage Single Element Example Output

2.5.3.4 Explicit Step Implementation

In an explicit step assuming quadratic nominal stress damage initiation and a linear deformation damage evolution (Eq 51), cohesive strains are first calculated by comparing the top and bottom surfaces of the cohesive layer (Eq 43). Then, the cohesive stresses are calculated using a standard elastic relationship (Eq 44 or Eq 45). Next, the quadratic nominal stress damage initiation value is calculated (Eq 48). If this value is less than one, there is no damage and the stresses and strains are output. If damage is initiated (value greater than or equal to one), the effective displacements are calculated (Eq 50). These are then used to calculate the damage evolution variable (Eq 51). The damaged stresses are calculated (Eq 53) and sent to the internal force calculation. If selected, fully degraded elements are removed and the status is output [45], [46]. In the section on

Consolidation of Computational Theory, this is integrated into the entire explicit step flow in Block 5 of Figure 20**.**

2.6 Contact and Interaction

In order to produce the most relevant multi-part models, one must consider how the parts and surfaces relate to one another when they contact and interact. Since explicit modeling methods are advantageous in damage focused models, the methods of contact and interaction definition discussed here are all compatible with the Abaqus explicit modeling environment.

Contact is generally described in pressure-overclosure relationships, where pressure is a function of the distance between two surfaces. If there is a measurable distance between two surfaces, this is known as clearance. The condition of two surfaces moving toward one another to remove this clearance is known as closure. Thus, the tendency for two surfaces to penetrate one another after closure is known as overclosure. This pressure-overclosure relationship is also commonly referred to as the contact stiffness [45], [46], [73].

Contact is still a widely explored field and the exact calculation methods vary greatly depending on the software package and pressure-overclosure relationship. Thus, a general process is presented here [45], [46], [73].

A basic method of representing the pressure-overclosure relationship is called “hard” contact as seen in Figure 15. This assumes no pressure until the surfaces are in contact at which point any possible pressure is allowed. This, however, creates a numerical discontinuity.

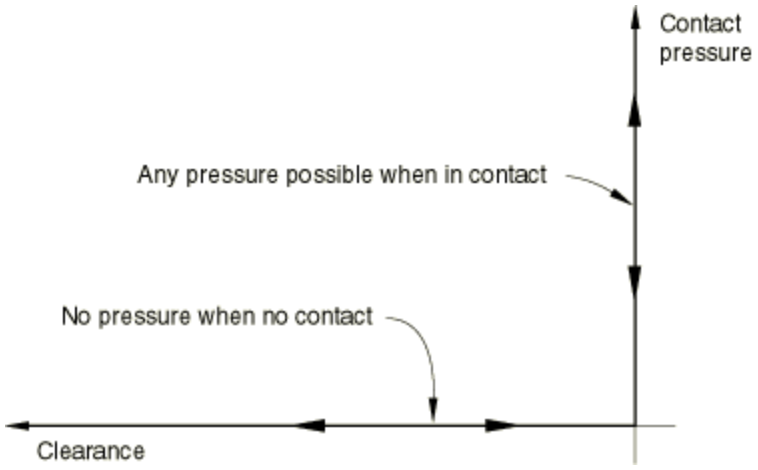

Figure 15: Hard Contact [74]

Thus, it is computationally advantageous for a user to be able to control more details in the pressure-overclosure relationship. The most common method is known as the penalty method.

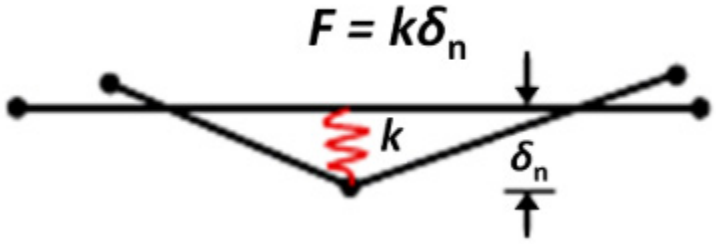

Figure 16: Penalty Method Spring Model [75]

In the penalty method, the stiffness defined by the pressure-overclosure relationship can be thought of as a spring as depicted in Figure 16. In Figure 16, F is the penetration force, k is the penetration stiffness, and δ_n is the normal penetration distance. The penalty method is named as such because it allows this small amount of penetration

and then penalizes the "spring" stiffness based on penetration depth to achieve a stable solution. Abaqus defaults to automatically selecting an optimized penalty stiffness. While Figure 16 depicts a simple example of penalty contact in the normal direction, the penalty method is also able to handle frictional relationships. Based on Figure 17, Stefancu et al present how this is handled in software in the equations that follow [76].

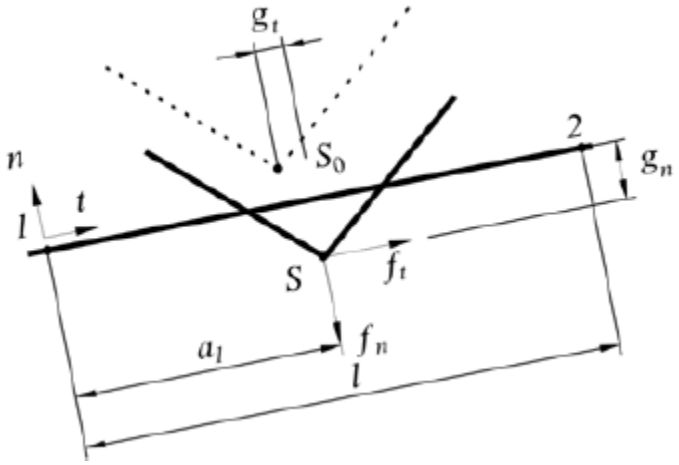

Figure 17: Penalty Method Nodal Penetration [76]

Figure 17 shows a nodal penetration into an element with both normal and tangential components. The potential energy of the pressure-overclosure relationship is minimized using the first variation of potential energy as

$$\delta\Pi_C = f_n\delta g_n + f_t\delta g_t = k_n g_n \delta g_t + sgn(g_t)\mu_d k_n g_n \delta g_t \qquad (56)$$

where

f_n is the normal force

f_t is the tangential force

k_n is the normal penalty term

k_t is the tangential penalty term

g_n is the normal penetration

g_t is the tangential penetration

μ_d is the coefficient of friction

δ is the variational (or functional) derivative

sgn is the sign operator which takes the sign of the parenthetical quantity

(i.e. the last term takes the sign of g_t)

From this relationship, the normal and tangential forces emerge as

$$f_n = k_n g_n \tag{57}$$

$$f_t = -sgn(g_t)\mu_d k_n g_n \tag{58}$$

These forces are distributed to nodes as external nodal forces. Abaqus allows the user to define the coefficient of friction, μ_k, with respect to slip rate and temperature. The slip rate definition allows the user to tailor the relationship based on static and dynamic frictional relationships [47], [73], [75], [76].

Abaqus allows the user to define contact as general contact or by using contact pairs. General contact is aptly named in that it handles most general contact situations well by allowing equal interpenetration between parts. Contact pairs employ a master-slave relationship in which there is no resistance to the master surface penetrating the slave surface, but there is resistance to the slave surface penetrating the master surface. In

some modern versions of software, the “master” surface is referred to as “surface 1” and the “slave” surface is referred to as “surface 2” or the “accessory” surface. These are typically useful in more complex contact situations such as the interaction between a part and a fastener [46], [50].

When using contact, there are special considerations when defining meshes and selecting contact pair surfaces. General convention is to make the stiffer surface master and model it with a coarser mesh. This prevents the master from being able to penetrate the slave surface during the initial kinematic calculation. Figure 18 shows a properly defined mesh relationship on the left and a poorly defined mesh on the right.

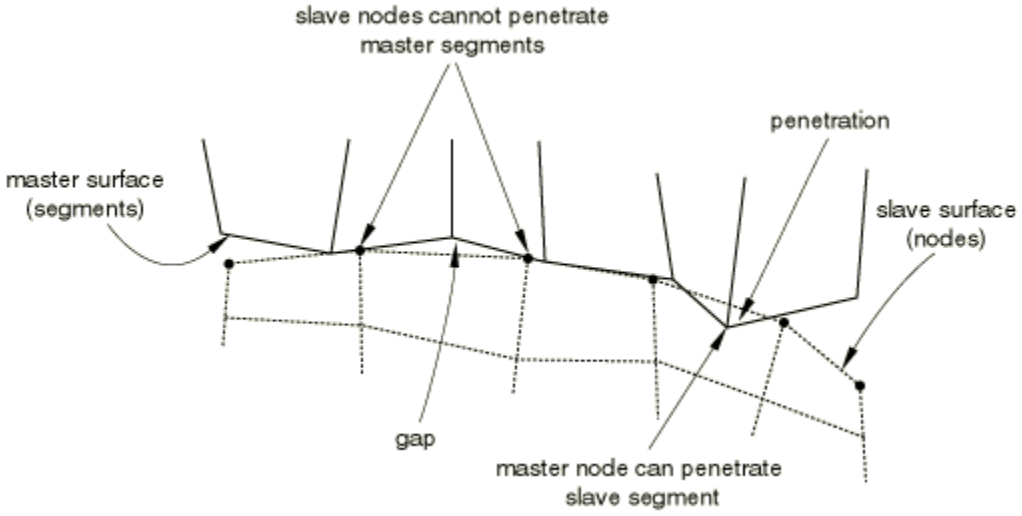

Figure 18: Master-Slave Discretization [45]

2.6.1 Explicit Step Implementation

In general, in an explicit step, the kinematic state of the system is first calculated without considering contact. Then, penetrations are mathematically sought out. Next, based on the penalty stiffness, a local solver is used to minimize the potential energy of the system as the penetrations are corrected so that the contact constraints are enforced.

The results of the minimization are restoring forces which are distributed as external nodal loads and corrected nodal positions. In other words, when penetrations are detected, the forces to correct those penetrations are calculated based on the penalty stiffness. To preserve energy conservation, those forces are distributed to the adjacent nodes [45], [46], [73]. In the section on Consolidation of Computational Theory, this is integrated into the entire explicit step flow in Block 3 of Figure 20.

2.7 Residual Stress and Thermal Expansion

There are multiple sources of residual stress that can be considered in Fiber Metal Laminates. Two are most evident: residual stresses from manufacturing the foil and residual stresses due to mismatched coefficients of thermal expansion (CTE) and high cure temperature.

During metal forming procedures, residual stresses are imparted into materials. This can be seen in many machining operations, where a material deforms during machining due to the release of this residual stress. Despite the presence of these stresses, they are expected to play much less of a role in this study compared to the thermal stresses.

Thermal stresses are imparted during cure cycles. Then, aircraft often see large temperature cycles on each flight which can range from over 100°F on the ground to around -50 °F at altitude. Prussak et al showed the formation of residual stress in FML as seen in Figure 19 [77]. This plot shows the progression of temperatures and resultant strains through the cure cycle. At time t_0 just before the cure cycle begins, the samples are at ambient room temperature, T_r. Then, as temperature increases and the matrix

begins to cure, the materials are joined by the matrix. This cure point is known as the stress-free temperature, T_{sf}. Then, as the cure temperature increases, the compressive and tensile stresses are induced. Finally, as the material cools and exits the cure cycle, the final residual stresses and strains are realized as the comparison between the material at the stress-free temperature,T_{sf}, and the environmental ambient temperature, T_r.

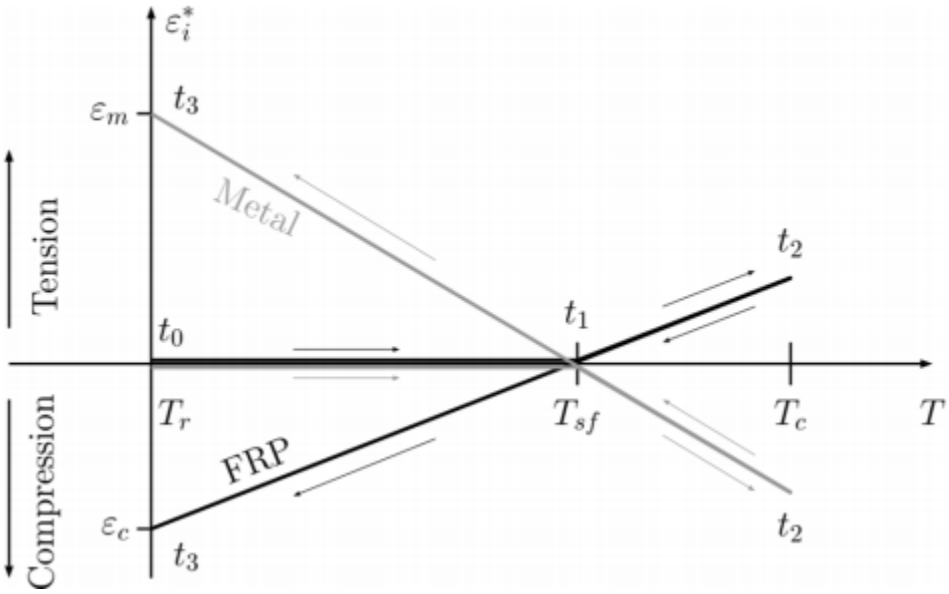

Figure 19: Formation of Residual Stress in Curing [77]

The process described above and shown in Figure 19 can be exacerbated when a large difference in coefficient of thermal expansion exists between materials. Table 1 shows the CTE for some of the materials referenced throughout this document. It is noteworthy that GLARE constituents have closer CTE than those FML with carbon fiber constituents, but the differences are on the same order of magnitude [77].

Table 1: Coefficients of Thermal Expansion

Material	Approximate Coefficient of Thermal Expansion (10^{-6}/°F) [10^{-6}/°C]
Aluminum Alloys [35]	13 [23]
301 Stainless Steel [35]	9.4 [17]
Titanium Alloys [35]	5.0 [9.0]
Hextow IM7 Carbon Fibers [78]	-0.36 [-0.65]
Glass Fibers [79]	5.0 [9.0]

Despite the existence of these cure induced stresses, it seems that they do not have major effects on the structures in operational or experimental settings. Frizzell stated that there were no negative effects from cure induced stresses in a GLARE repair to the C-5 Galaxy [80]. Hosseini-Toudeshky et al showed that varied residual stresses due to different cure cycles did not significantly affect fatigue crack propagation [81]. Da Costa et al showed that up to 2000 temperature cycles to simulate flight did not have significant effects on the tensile strength or interlaminar shear strength of a FML [82]. Fink et al predicted variation in thermal stress due to cure temperatures would have no significant effect on bearing strength in a carbon-titanium FML [37]. While there are studies to show that cure induced stresses in a carbon-steel FML are higher, as one might expect due to the wider difference in CTE [83], there is no evidence to show that these stresses are detrimental. Also there does not seem to be significant work on how to address these thermal stresses, if they indeed need to be addressed at all. Smart cure cycles have been proposed, but this has not been tested with the composite employed in this study [77].

Thus, the main question to be asked with cure induced stresses is, how much does the consideration of thermal stresses drive the ability to model bolted joints in FML properly?

Hausmann et al proposes an analytical solution to predict thermal stresses in a fiber metal laminate based on known materials properties in the following set of equations [83].

$$\sigma_M = \frac{\Delta T(\alpha_C - \alpha_M)}{\frac{1}{E_C} \cdot \frac{1 - v_C}{v_c} + \frac{1}{E_M}} \quad (59)$$

$$\sigma_C = -\frac{1 - v_C}{v_c} \cdot \sigma_M \quad (60)$$

Where

σ_M is the thermal stress in the metal

α_M is the metal coefficient of thermal expansion

$E_M$is the metal elastic modulus

σ_C is the thermal stress in the composite

α_C is the composite coefficient of thermal expansion (longitudinal)

E_C is the composite elastic modulus

ΔT is the temperature change (negative for cooling)

v_c is the volume fraction of the composite with respect to the thickness

Using this calculation method, the thermal stresses in the layup proposed in the study are calculated to peak at 44.6ksi (308MPa) tensile in the metal and 22.6ksi (156) compressive in the composite, which equate to almost 32% of the yield stress of the metal and almost 9% of the ultimate stress of the composite. While these are substantial, they

are high estimates in that they do not consider a compliant adhesive layer between the composite and foil.

In this work residual stresses due to manufacturing are not considered directly, but the computational properties of the foils are developed based on experimentation by Roberts [67]. The computational research evaluates the consideration of thermally induced cure stresses, which are those stresses that results from materials with dissimilar thermal expansion properties bonding at high cure temperatures and then cooling to ambient temperatures.

2.8 Consolidation of Theory for Computation

It is important to understand how the modeling methods explored to represent this scenario will relate to one another computationally. The flow chart in Figure 20 shows the logic flow during each iteration of an explicit dynamic analysis. Logically, at the beginning of each iteration, $time = t$, accelerations, velocities, and locations as well as equivalent plastic strains are coupled with user input materials properties, parameters for failure criteria, and boundary conditions. These values are first used to develop stress-strain relationships. These stress-strain relationships feed the central difference system of equations and are input into failure criterion for Ductile Damage (Block 4), cohesive damage (Block 5), and composite damage (Block 6) (see Figure 20). For cohesive damage (Block 5) assuming traction-separation behavior, the calculation process is the same after the initial stresses are calculated. The failure criteria develop the stress values experienced in the material and process the damage initiation, evolution, and element removal. Meanwhile, the contact algorithm (Block 3) takes in the updated kinematic state

from the central difference calculation and first allows penetration. Once these contact or penetration points are located, the pressure-overclosure relationship is solved using a local solver which minimizes potential energy. Pressures are distributed as external forces to nodes, and element positions for the current iteration are updated. Final outputs are an updated kinematic state, updated equivalent plastic strain, stresses, strains, and element status [45]–[47], [73]. For space efficiency, equations throughout the paper are referenced by the flow chart. Dashed outlines indicate a logical decision point.

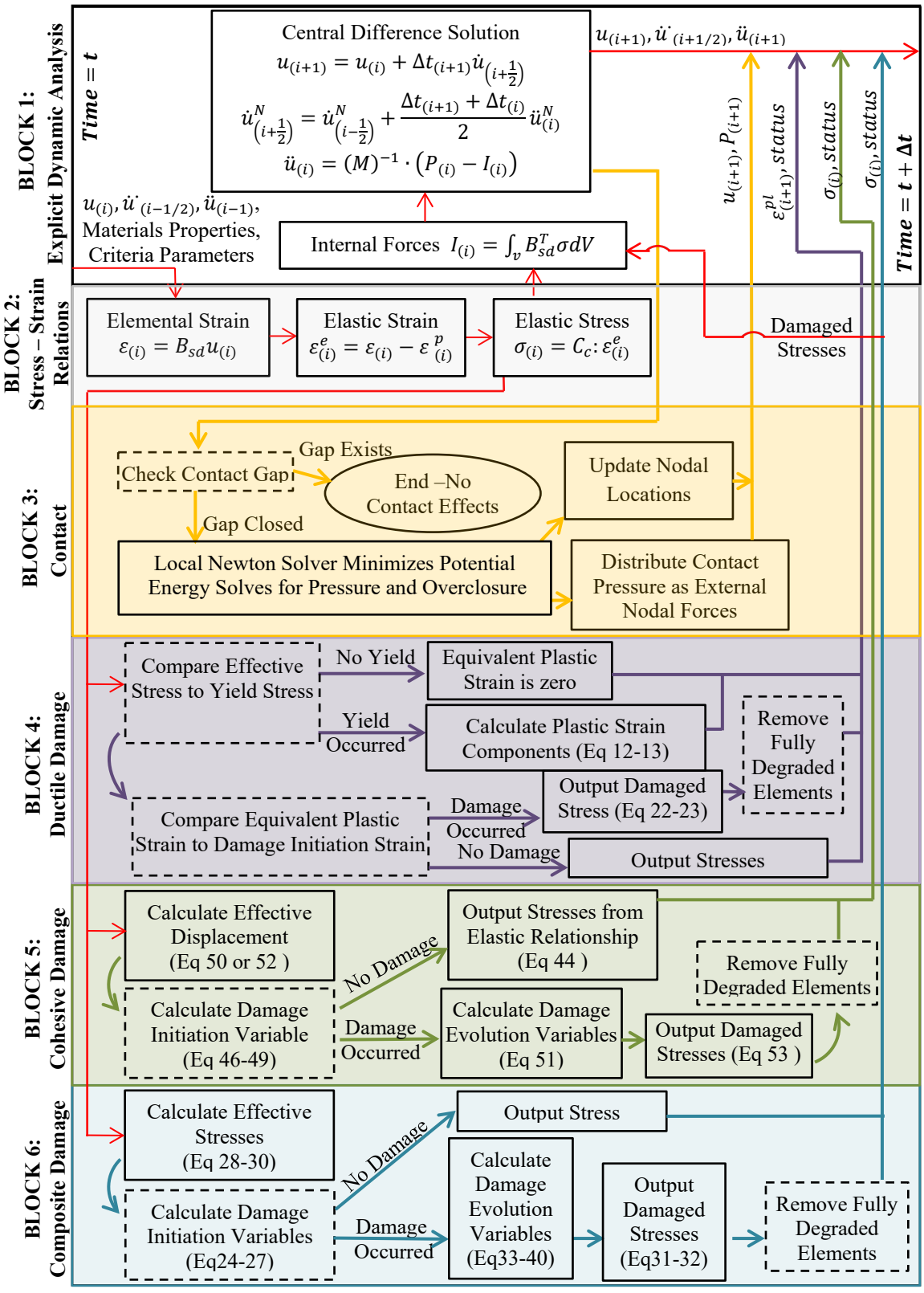

Figure 20: Finite Element Method Logic Flow Chart [45]–[47]

2.9 Composite Failure Modes

In order to interpret results presented in the work, an understanding of phenomenon that occur during bearing failure is necessary. Bearing failure in this study is localized and mostly compressive. It is dominated by two main observable failure modes at the fiber level. The first is fiber kinking. Fiber kinking in brittle carbon fibers is akin to buckling in more ductile materials. While individual fibers can kink, in bearing failure, typically all fibers through the thickness of a given ply kink in a similar region. These are observed as fiber kinking bands. In the optical micrographs included throughout this document, the goal was to capture the behavior through the entire thickness of the layup. Thus, the fiber kinking bands are not observable on the individual fiber level, but rather appear as a band at the ply level. For that reason, Figure 21 shows example Scanning Electron Microscope (SEM) images from samples in this study depicting what is happening at the fiber level to cause fiber kinking bands. Figure 21A shows a typical fiber kinking band across a ply. Figure 21B shows a commonly occurring feature known as a wedge or "V" kink [84].

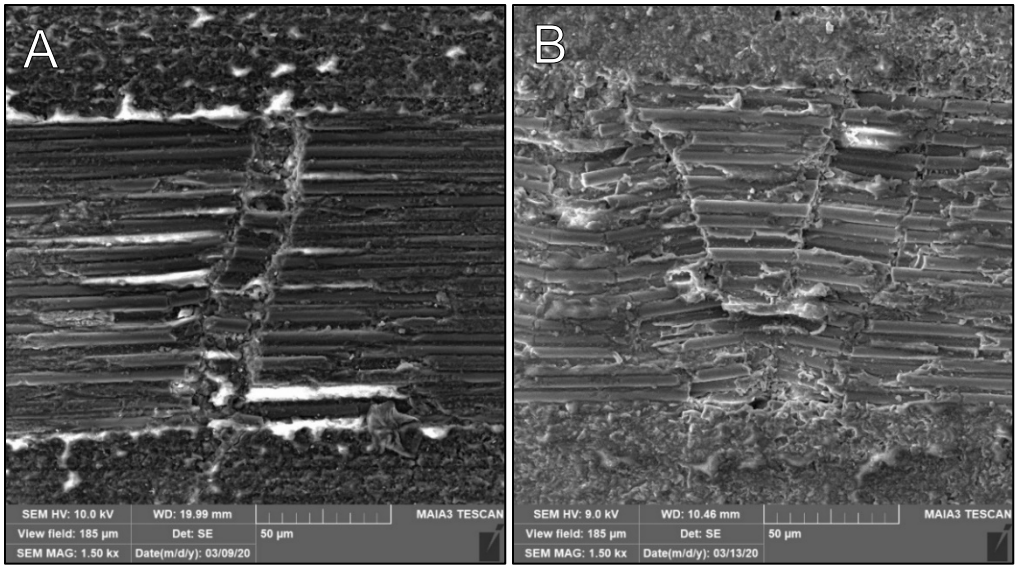

Figure 21: SEM Fiber Kinking Examples A) Typical Kink Band B) Wedge Kink

The second common failure mode is matrix cracking. This is the failure of the matrix between fibers. It is often coupled with fiber kinking in adjacent layers. This is depicted in Figure 22 where fiber kinking is marked with a bright green "FK" and matrix cracking is marked with a white "MC."

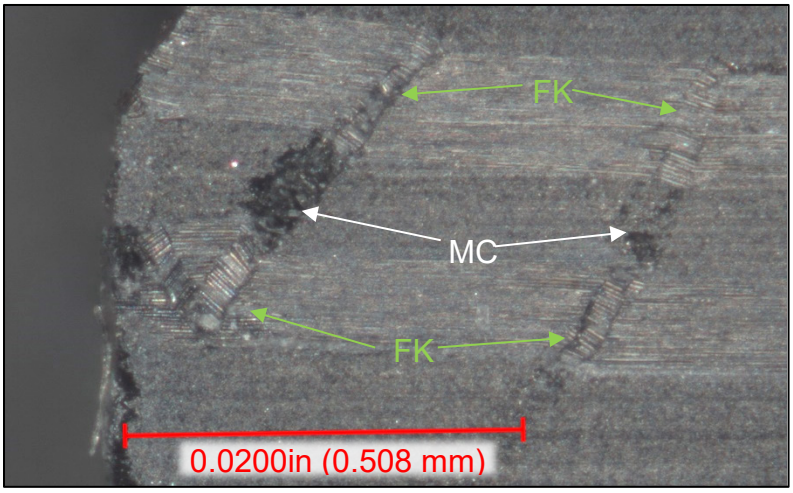

Figure 22: Coupled Fiber Kinking and Matrix Cracking

The final failure type detected in bearing samples is delamination. This occurs when the bond between two layers is broken. In conventional composites, this may be the interlaminar matrix region between two composite plies. In fiber metal laminates, this can also be the interface involving a metallic layer or adhesive layer. Delamination may be localized or spread over a large area. Delamination is especially dangerous in composites that experience compression, because the delamination is often not detectable by visual inspection but can drastically reduce compressive strength [71]. Figure 23 shows several examples of delamination in a composite bearing sample as observed through the thickness of the layup.

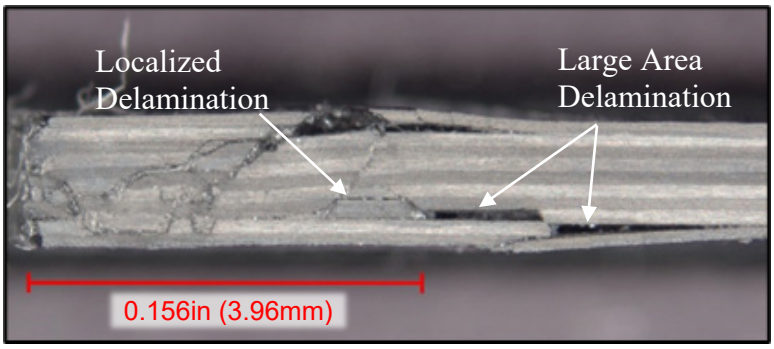

Figure 23: Delamination

2.10 Approaches to Cyclic Fatigue Experimentation

In classical fatigue testing, typically a stress and cyclic rate are set and the experiment results in a number of cycles until failure for the given parameters. These tests can be used to develop a relationship between the stress amplitude (S) and number of cycles (N) commonly known as an S-N curve. A typical S-N curve is depicted in Figure 24. Typically, as the stress amplitude increases, the fatigue life (number of cycles before failure) decreases. In theory, as stress becomes sufficiently low, an infinite fatigue

life is reached. There is likely some limit for these very low stress values, but testing to those high cycle counts is typically deemed unnecessary or overly burdensome. While these classical methods produce useful results, they often require large numbers of samples, intensive statistical analysis, and long run times [85], [86].

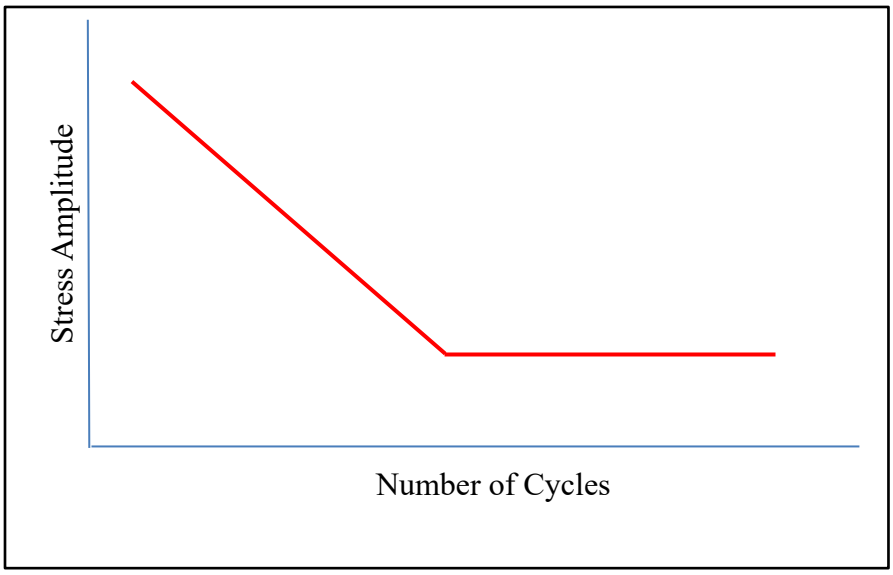

Figure 24: Example S-N Curve

Nicholas and Maxwell proposed an accelerated step test method. Instead of setting a stress and experimentally determining a number of cycles to failure, they proposed setting a number of cycles and determining a stress which they call the fatigue limit stress (FLS). They do this by setting a number of cycles and running that number of cycles at each step in a series of steps at evenly spaced increasing stress amplitudes. Figure 25 shows an example of this approach. To initiate the process, a percentage of a known load is selected. This is usually set as a percentage of yield stress or a similar quantity. Setting a low value for initial stress amplitude is more conservative, but setting

too low of a value for the starting stress will force a larger number of steps, increasing the overall run time. In this example in Figure 25 the stress amplitude begins at 85% of the known stress value, and each step increases by 5% of that value. Maxwell also refers to these steps as “blocks.” Closely spaced steps can provide more fidelity, but they will cause more steps which will increase the overall run time. Steps that are too closely spaced can cause cumulative effects on future steps. Maxwell calls this phenomenon of cumulative effects “coaxing.” The benefits of this method are most realized when the number of cycles is selected based on a specific lifetime of interest, and initial stress and stress step size are carefully chosen to minimize the overall run time. Maxwell points out that a wide statistical variation in cycle life in samples such as composites may require a wide range of steps for similar samples [85], [86].

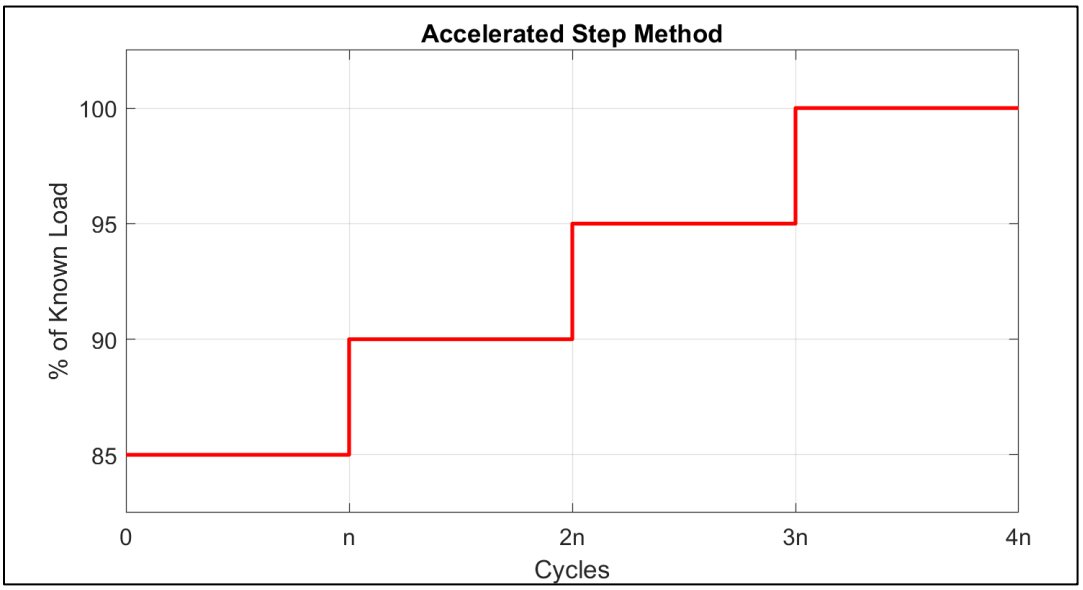

Figure 25: Example Steps for Accelerated Method

To be considered a viable test, a sample must complete one full block and at least one cycle of the next block. Based on these criteria, the sample will reach an established

stop or failure criteria at some number of cycles in the middle of a block. Then a fatigue limit stress can be calculated using a linear interpolation as [85], [86],

$$\sigma_e = \sigma_0 + \Delta\sigma \left(\frac{N_{fail}}{N_{life}} \right) \quad (61)$$

Where

- σ_e is the Fatigue Limit Stress
- σ_0 is the stress for the block in which the failure criterion is met
- $\Delta\sigma$ is the increase in stress after each block is complete
- N_{fail} is the number of cycles complete in the block in which the failure criterion was met
- N_{life} is the assigned cycle count being investigated

This method in effect, allows experimenters to build an S-N curve in reverse of the usual method at a specific life cycle or range of cycle counts that are of specific concern.

III. Experimental Methodology

This chapter explains every aspect of how the experimental portion of this study was executed. It begins with a discussion of the approach which communicates an overview of how the experimentation was undertaken. Then deviations from the ASTM standard and test fixture development are explained. The selection of each process and each material is presented, and the statistical planning and statistical design of experiments is laid out. Specifics about manufacturing are discussed in addition to pre-test characterization and preparation. The specific methodologies used to conduct the quasi-static experimentation and cyclic fatigue experimentation are detailed. The chapter concludes with statistical analysis and post-test characterization techniques. Results are presented in Chapter V: Experimental Results and Discussion.

3.1 Approach

The experimental portion of this study sought to characterize the bearing properties of this hybrid material through monotonic quasi-static testing per ASTM D5961-17 and cyclic loading via ASTM D6873-08. These standards employ test coupons as pictured in Figure 26.

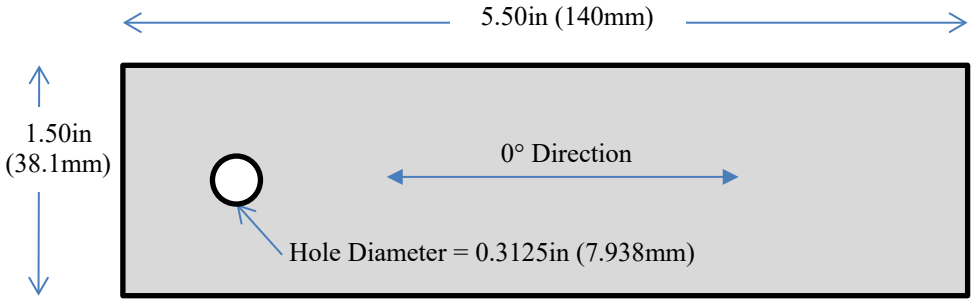

Figure 26: Coupon Configuration

3.1.1 Quasi-Static Experimental Testing Approach

The quasi-static study began with the simplest case in the simplest configuration, which is a 9-ply layup in double shear. Then, complexity was increased to more operationally representative joints. An 18-ply layup was studied in double shear, and then advanced into single shear in both protruding head and countersunk head configurations. The double shear configuration was performed in accordance with ASTM D5961 Procedure A, while the single shear configurations were conducted per Procedure C.

In order to characterize the failure mechanisms that occurred in the bearing samples, both full failure and progressive failure samples were collected. Full failure, as described in this study, are samples that were deformed past 30% hole elongation (bearing strain). The ASTM standard recommends targeting 50% bearing strain (ASTM D5961-17 Para 11.4.7) [2]. However, through the course of this study with the given materials, any deformation past 30% crushed the material so severely that it could no longer be analyzed, or it approached a critical edge distance and failed in net section failure. Halting the sample at 30% hole elongation kept the bearing region intact, so the damage could be observed via post-test evaluation and microscopy. In similar work, Iarve et al halted tests at 10% hole elongation to preserve the bearing region for post-test evaluation [87]. Progressive failure samples were deformed to lesser strains that were targeted to capture the specific failure modes that caused phenomena of interest in data from the full failure samples. For example, Figure 27 shows a stress-strain curve for a given sample. When looking at this chart, one would like to understand what physical phenomenon in the layups are allowing features such as yield, the load redistributions from 5% to 15% strain, and the large load drop around 16% strain. In order to capture

those physical phenomenon, progressive failure samples were displaced until the bearing strain corresponding to that feature was reached, at which point the sample was quickly unloaded (detailed in Quasi-static Experimental Methodology). Example potential progressive failure targets are depicted in Figure 27 as dotted vertical blue lines.

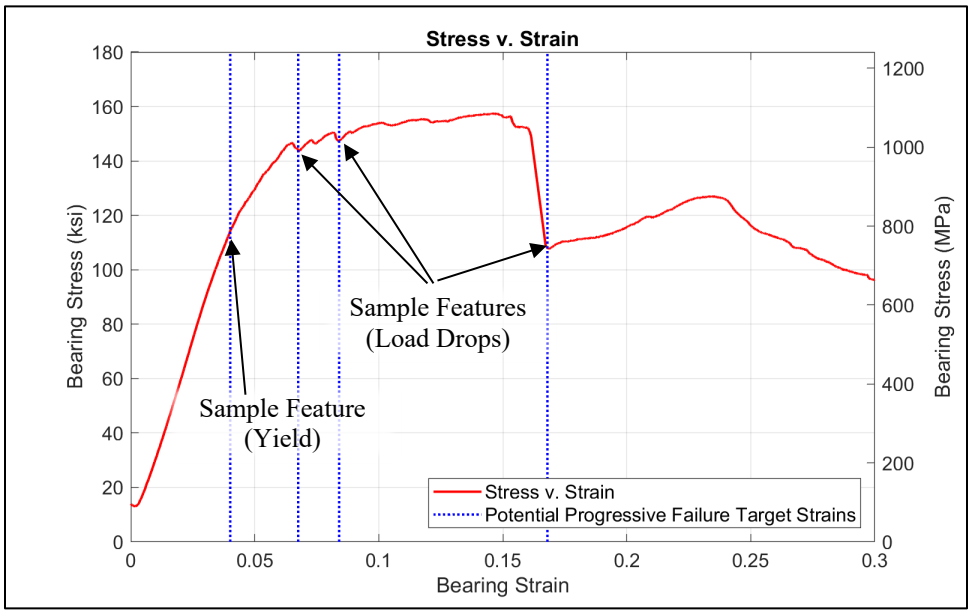

Figure 27: Progressive Failure Description

3.1.2 Fatigue Experimental Testing Approach

For the fatigue portion of the study, 18-ply samples were considered in double shear and single shear protruding configurations also in accordance with Procedures A and C of ASTM D5961.

Fatigue testing was planned which would run samples to low cycle counts ($n = 10, 100, 500, 1000$) at a stress equal to 85% of the quasi-static ultimate stress. The intent was to compare and contrast any failure initiation in the fatigue samples with the failure demonstrated by the quasi-static samples. However, the low cycle counts produced less permanent hole elongation than expected, which limited comparative analysis. Thus, a

more traditional approach was explored that defined a stop criterion at a given hole elongation. The samples were loaded cyclically until this stop criterion was met. The number of cycles was recorded. This method proved to be effective but was extremely time consuming with some tests lasting many days. Finally, due to limited test laboratory availability, an accelerated step method was employed. This step method was proposed by Maxwell and Nicholas [85], [86]. Instead of using a fixed stress and experimentally determining a cycle life, the step method sets a number of cycles and then steps through a series of increasing stress values. Each step at a given stress is referred to as a block. When the failure criteria are met, the failure stress can be calculated based on the number of cycles completed in the block in which the sample failed. This process is detailed in Cyclic Fatigue Experimental Methodology.

3.2 Deviations from ASTM Standard

Pre-test estimates suggested that the peak load of the hybrid material was expected to be around 6.50 kips (28.8KN). These pre-test estimates were calculated using a load capacity estimation iteratively developed in an optimization study by Brewer et al [88] which was based on experimental data by Falugi and Knoth [41]. The estimation was calculated as

$$P_{yield} = 2t_{avg}D(\sigma_{foil_{yield}}n_{foil} + \sigma_{br_{comp}}n_{comp}) \quad (62)$$

$$P_{ult} = 1.1(P_{yield}) \quad (63)$$

where

- P_{yield} was the estimated bearing yield of the hybrid
- P_{ult} was the estimated ultimate bearing strength

- t_{avg} was the average thickness of a foil and composite ply
- D is the bolt diameter
- n_{foil} and n_{comp} were the number of each ply expected
- $\sigma_{foil_{yield}}$ was the published yield value for the foils
- $\sigma_{br_{comp}}$ was the yield stress of a pinned control sample from Falugi and Knoth [41]

The factor of 2 was used to convert values acquired in a pinned condition into a bolted condition. This pre-test estimate of 6.5 kips was remarkably close to the largest stress value of just under 6 kips reached in this research. Assuming pure shear, the standard 0.250in (6.35mm) fastener was expected to yield at 4.66 kips (20.7KN) based on manufacturer specified properties. This shear was calculated by simply dividing estimated load over the cross-sectional area of the bolt. In order to avoid large scale fastener yield and possible fastener fracture when testing was advanced to single shear applications, a 0.3125in (7.938mm) Hi-Lok bolt was employed. This kept the fastener type and diameter consistent throughout all test configurations. Assuming a 0.3125in (7.938mm) diameter Hi-Lok of the same alloy, a yield of 7.29 kips (32.4KN) was expected. This gave confidence that the fastener would not demonstrate large scale plasticity [2], [89]. This resulted in a width to diameter (W/D) ratio of 4.8 versus the standard W/D ratio of 6 [90].

3.3 Test Fixtures

Since a larger bolt was needed and increased loads were expected, new fixtures were locally manufactured from 17-4PH stainless steel. The hole diameter was increased

to 0.3125in (7.938mm). In keeping with the standard, the dimensions of the bosses (pictured in Figure 29) that interface with the samples were increased to maintain their dimensionality at twice the hole diameter. Thus, the nominal diameter of the bosses increased from 0.500in (12.7mm) to 0.625in (15.9mm). Increasing the boss diameter served two purposes. First, it maintained the ratio between the diameter of the hole and the boss, so that future research could make a clear comparison to a test conducted with standard fixtures. Second, since the boss tends to mimic a washer, increasing the boss diameter kept the dimensions of the boss close to the dimensions of a standard washer. The wall thickness of the double shear fixture was increased from 0.120in (3.05mm) to 0.150in (3.81mm) to handle increased loading from the hybrid composite and for robustness in related cyclic testing. This increased the stress capacity of the fixture by 25% while maintaining a boss thickness of 0.0300in (0.762mm) which still allowed it to mimic a standard washer. Similarly, material was added to the stress concentration near the grip area in the single shear fixture. In this case, material was not added to achieve a certain dimensionality, but was simply left at the major dimensions of the material blank. This not only added strength, but it reduced machining time and complexity.

Before machining, finite element analysis in Abaqus was used to verify the loading in the updated fixtures as depicted in Figure 28. Based on coarse conservative models, the double shear model (Figure 28A) showed a factor of safety of around two, while the single shear fixture showed a factor of safety of over five. It is noteworthy that throughout testing with periodic measurements, no plastic deformation was detected in the fixtures.

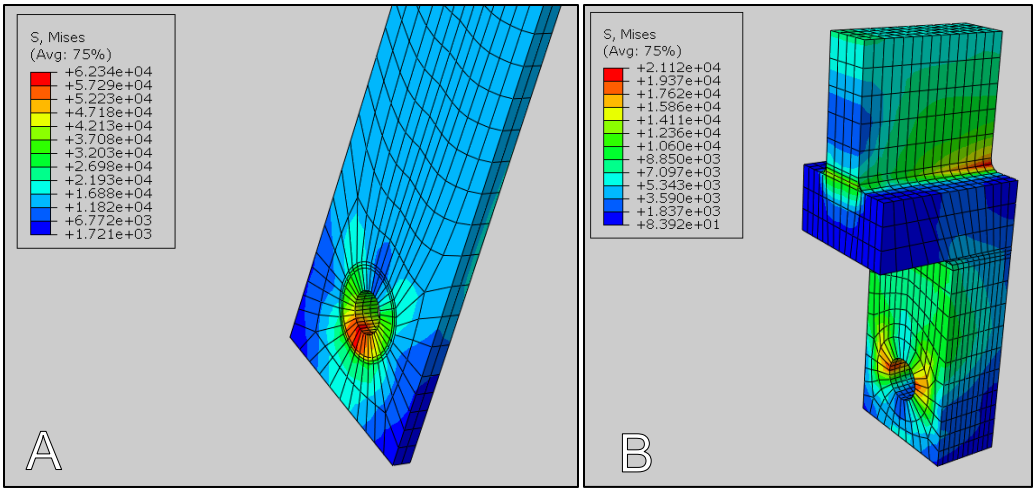

Figure 28: Updated Fixture Finite Element Models

Since new fixtures were being machined, this provided an opportunity to make the task of extension measurement more robust. A knife edge was milled into the rear portion of the fixture, so that a clip-on displacement gauge could be employed. This knife edge was coupled with a locally machined knife edge tab that was bonded to the face of the coupon using Hysol 9394 and cured at 150°F for 1 hour [91]. The theory employed for this knife edge tab was that the fixture remains relatively fixed compared to the bearing surface, and the distance between the two knife edges increases as the hole elongates. Any elastic deformation in the short distance between the bonded knife edge and the hole is assumed to be negligible compared to deformation that happens at the bearing surface causing hole elongation. A post-test comparison showed that the head displacement reached values almost 0.009in (0.2mm) which equates to about 3% strain. Thus, adding the knife edge gave a much more accurate characterization of what was happening at the hole. The bonded knife edge tab was positioned with a jig to ensure that the two knife edges would be in the center of the range of the extension gauge. In the original single shear fixture, a

stress concentration existed where the grip portion transitioned into the body of the fixture. In the updated fixture, material was added back here (not machined away) to make the fixture more robust. Figure 29 shows a modified double shear fixture compared to a conventional fixture. Figure 30 shows an updated single shear fixture as compared to the conventional version. Figure 31 shows both of the updated fixtures and how the clip-on extension gauge is used in conjunction with the integral and bonded knife edges. Dimensioned drawings of the updated fixtures are included in Appendix L.

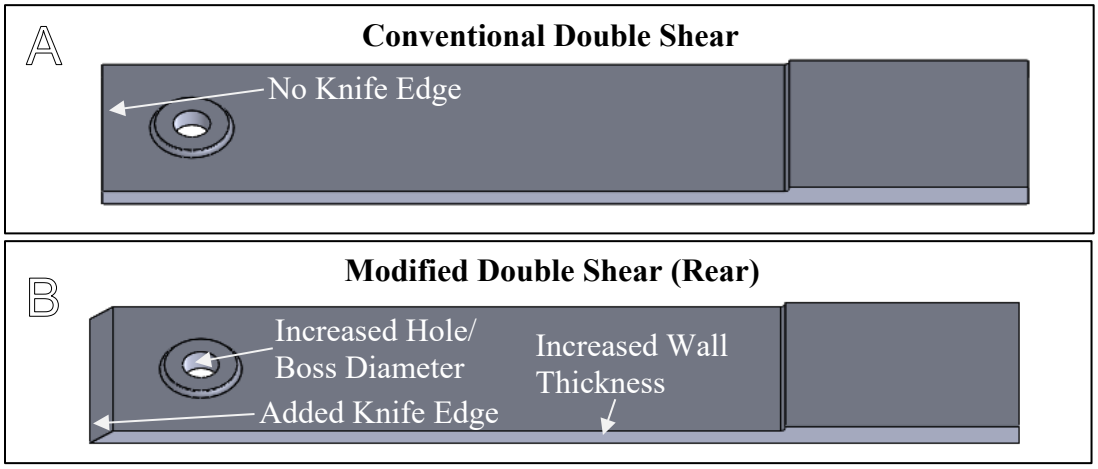

Figure 29: Double Shear Test Fixtures A) Conventional B) Updated

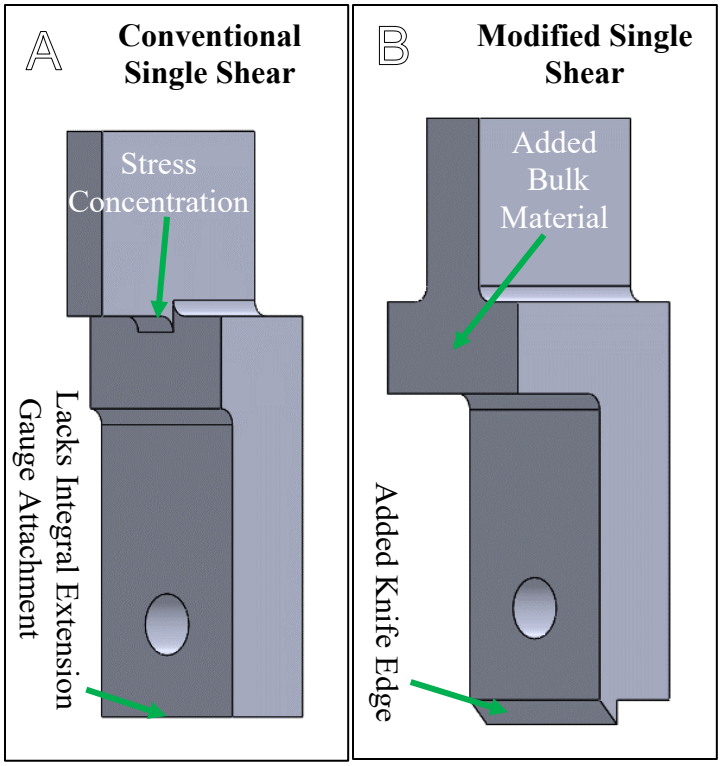

Figure 30: Single Shear Test Fixtures A) Conventional B) Updated

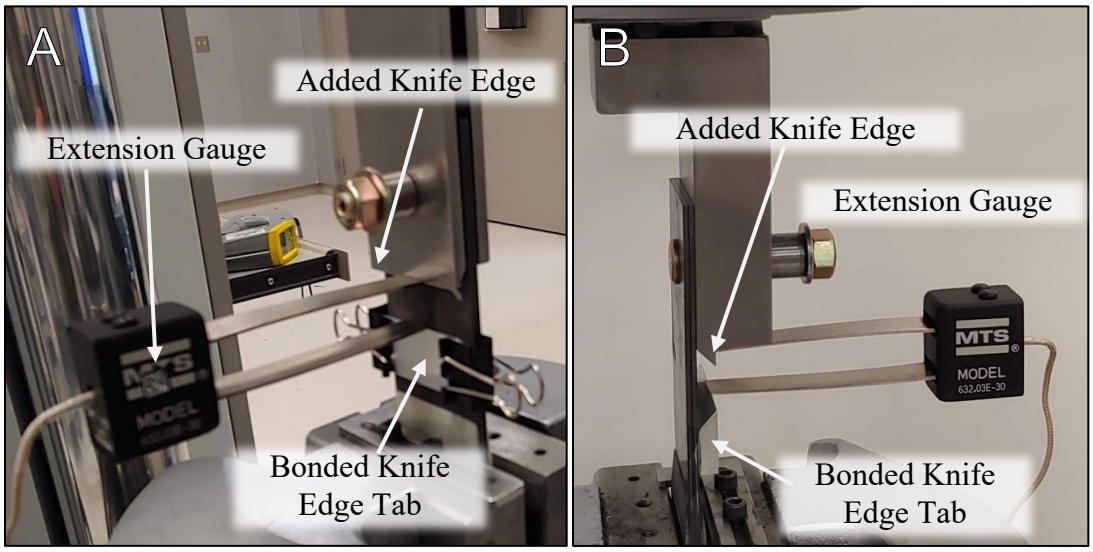

Figure 31: Knife Edge and Clip-on Extension Gauge
A) Double Shear B) Single Shear

3.4 Material and Process Selection

This section explains not only what materials and processes were selected, but also the factors that influenced those selections.

3.4.1 Preimpregnated Carbon Fiber and Epoxy System

IM7/977-3 unidirectional carbon fiber was selected for this study, because it is a state of the art material used on modern aircraft such as the United States Military's F-35 [92]. It has been studied in depth by AFRL in the Composite Airframe Life Extension programs [18]. This material system incorporates unidirectional Hexcel IM7 carbon fiber preimpregnated with CYCOM 977-3 thermoset epoxy resin by Solvay [78], [93]. This system is intended to be autoclave cured at 350°F (177°C) for 6 hours. The material is cold stored at 0°F (-17.8°C) for up to 12 months. An example of the uncured prepreg is shown in Figure 32.

Figure 32: Uncured IM7/977-3 Preimpregnated Carbon Fiber

3.4.2 Stainless Steel Foils

301 stainless steel shim material with a thickness of 0.004 in (0.1016 mm) was chosen for this study. The material was manufactured by Ulbrich Stainless Steels & Special Metals, Inc. and sourced through Trinity Brand Industries. The material has a published yield strength of 167.8ksi (1157MPa) and fracture elongation of 21%, while possessing a Rockwell C hardness of 43 [94]. The selection was made by engineers at AFRL/RQ due to the inherent toughness of stainless steel coupled with its corrosion resistant properties. Also, it avoids the galvanic corrosion effects of introducing aluminum into a carbon fiber structure [95]. For many alloys, titanium has a higher yield strength, but stainless steels demonstrate more ductile failure, enabling detection through inspection or vibration instead of catastrophic failure [96]. The material was also selected because fiber metal laminates have been widely studied with aluminum and titanium alloys, but far less work has included stainless steel. A complete table of properties is provided in Appendix H.

3.4.3 Stainless Steel Preparation

The metal preparation process was that recommended by AFRL/RX. This process has been proven by Kondash et al to provide a consistent surface roughness for bonding while limiting distortion in the material [97]. While much of the research has been done on aluminum bonding, where this process produces an average surface roughness of $24\mu in$ $(610\mu m)$, it has been proven to produce a similarly consistent surface on stainless steel with only slightly reduced surface roughness of $19\mu in$ $(480\mu m)$. This process began by cleaning the surface of the material with 90% isopropyl alcohol and then

blasting with a 240-grit aluminum oxide. This grit-blast procedure was followed by a brush application of 3M™'s AC-130-2 Sol-Gel solution [98]. Finally, the foil was coated with Solvay BR 6747-1 primer to seal and stabilize the surface [99]. During the process, technicians use a sacrificial "traveler panel" that accompanies the main panels being processed. This allows engineers to quantify and quality check the processes without risk of contaminating the main panels. Figure 33 shows a main panel (left) and traveler panel (right) just after application of primer. The specific details of this metal preparation are outlined in Appendix E.

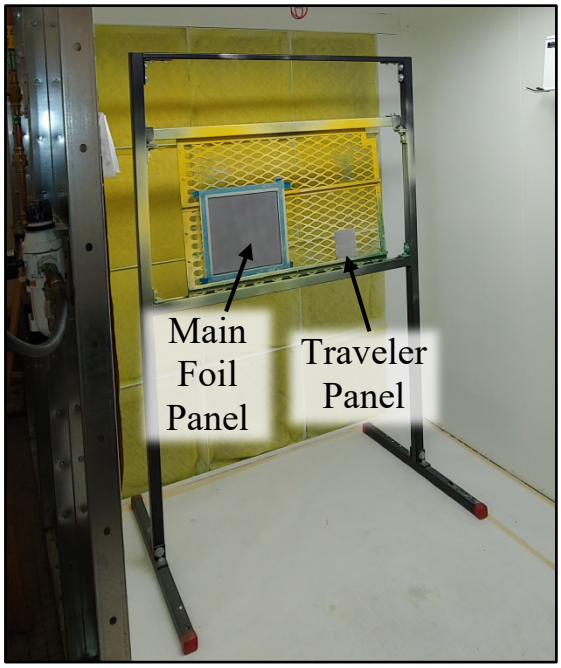

Figure 33: Stainless Steel Priming

3.4.4 Adhesive

Early testing by Falugi and Knoth indicated that an adhesive was necessary to ensure a consistent bond between the composite and metal subjected to mode I delamination (double cantilevered beam) [41]. Thus, the thinnest cure-ready adhesive

was selected. The adhesive, AF191U, is a film adhesive made by 3M commonly used for composite-metal bonding. This material is 0.0025in (0.064mm) thick and is unsupported, meaning it contains no fibrous support material [100], [101].

3.4.5 Layup

The layup chosen for this study includes ± 45°, 0°, and 90° plies arranged symmetrically repeated in multiples of the following stacking sequence: $[45/0/-45/0/90/0/-45/0/45]_n$. This layup has been widely studied by the Air Force Research Laboratory, and similar layups are commonly employed in aircraft skins and structural members. The control layup sequence was [45/0/-45/0/90/0/-45/0/45] for the 9-ply case and $[45/0/-45/0/90/0/-45/0/45]_2$ for the 18-ply case.

Research by Egan et al demonstrated that the majority of the bearing load is carried by the 0° plies. Figure 34 depicts the radial stress in a single lap joint configuration which shows most of the stress in the 0° plies. The 0° plies, represented in blue, show higher stress capacity around more of the bolt hole than the other layers. In multiple studies, Egan et al have used computational models that predict overall bearing behavior well to demonstrate this phenomenon at the ply level [42], [43].

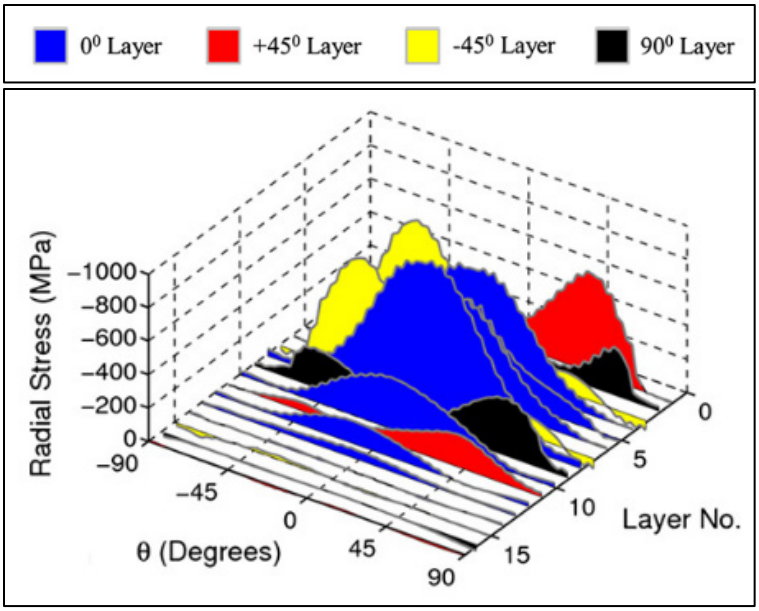

Figure 34: Radial Stress in a Single Lap Joint
(Derived from Egan et al [43])

Thus, for structural efficiency in the hybrid, the 0° plies were kept intact, and the foils replaced the internal -45° and 90° layers. The resulting hybrid layup sequence near the bearing hole was [45/0/|SS|/0/|SS|/0/|SS|/0/45] for the 9-ply case and $[45/0/|SS|/0/|SS|/0/|SS|/0/45]_2$ for the 18-ply case. In this notation, |SS| describes a stainless steel foil with a ply of AF-191 adhesive on either side.

The work by Egan et al not only demonstrated that most of the stress in a lap joint is carried in the 0° plies as shown above, Figure 34 also shows that little of the stress is carried by the head of a countersunk fastener in the single lap joint. In other words, the majority of the stress in a countersunk lap joint is carried by the shank of the fastener. In Figure 34, the plies closest to the viewer contain the countersink. For this reason, a shank-only layup was developed that only hybridized near the shank of the fastener. This

was only considered in the 18-ply layup because the 9-ply layup was not thick enough to accept a countersink. Figure 35 shows a countersunk fastener for reference.

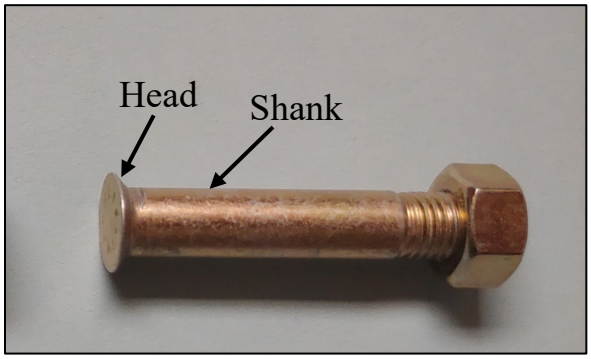

Figure 35: Countersunk Hi-Lok Fastener

The metal foils transition into the composite at 2.00in (5.08cm) and 3.00in (7.62cm) into the layup. These depths are not necessarily optimized, but were demonstrated by Falugi and Knoth to ensure the sample fails in bearing instead of the foil shearing out of the surrounding composite [41]. The 9-ply layup tables are depicted in Figure 36, and the 18-ply layups are shown in Figure 37 [90]. These show the stacking sequence of each material and orientation of each material through the thickness of the laminate near the bearing hole.

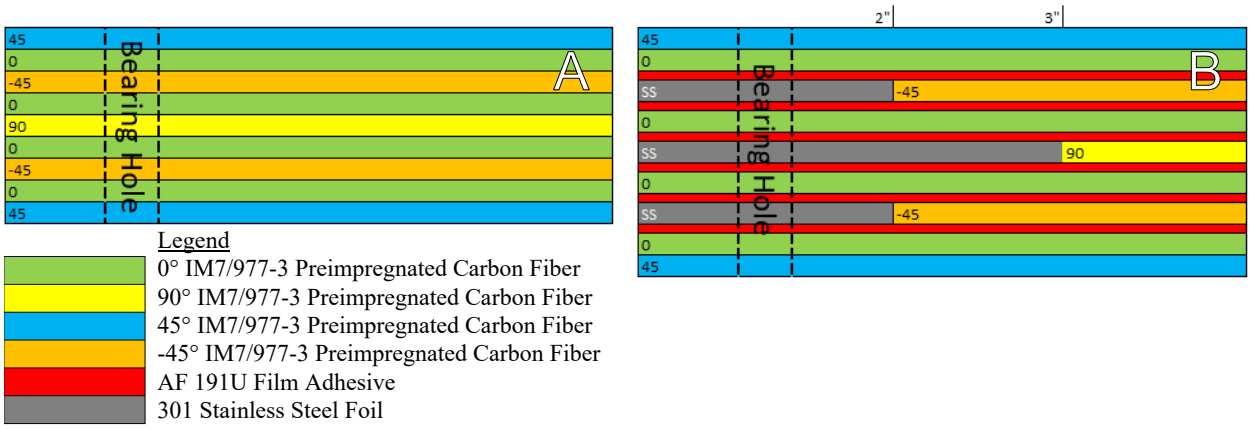

Figure 36: 9-Ply Layup Diagrams A) Control B) Hybrid

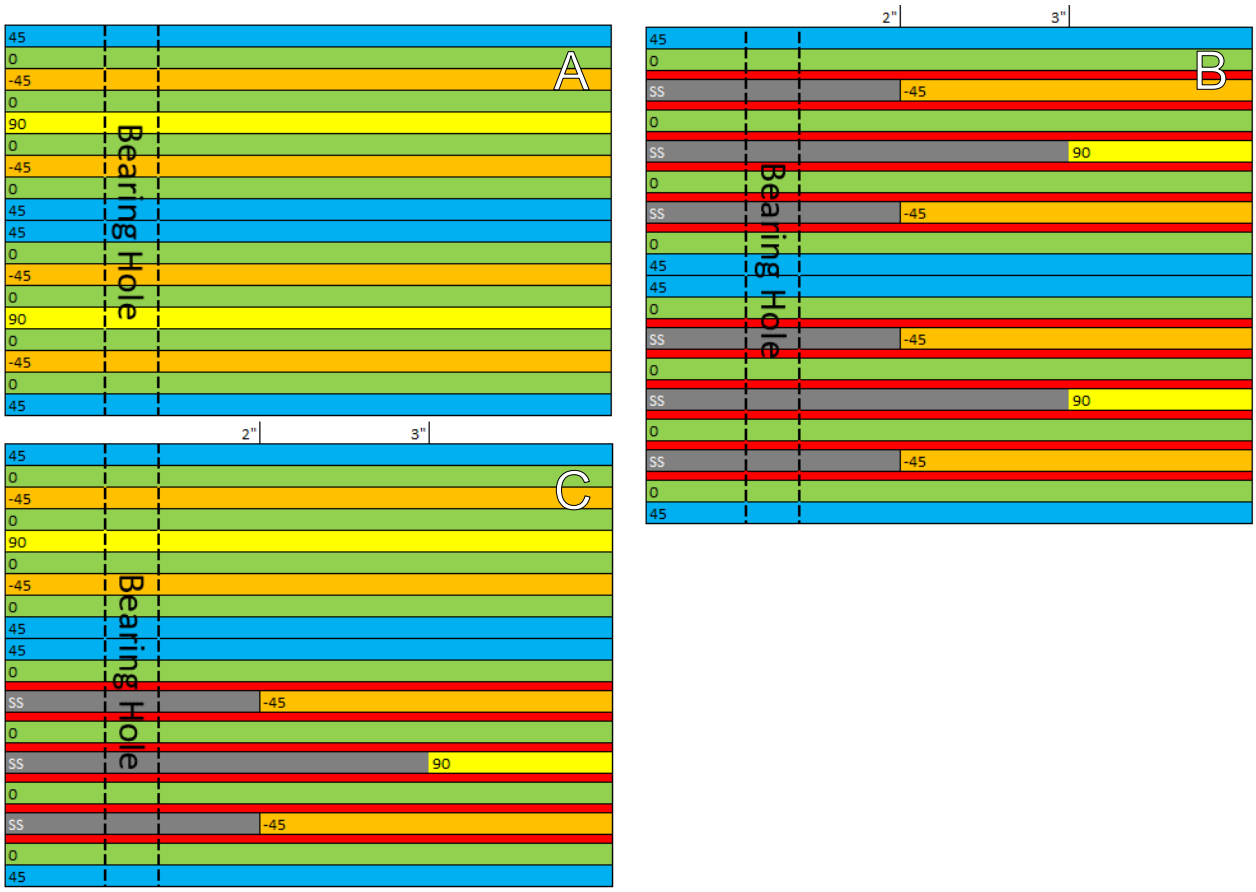

Figure 37: 18-Ply Layup Diagrams A) Control B) Hybrid C) Shank-Only Hybrid

3.4.6 Fasteners and Torque

This study employed three different Hi-Lok fasteners corresponding to the three configurations. All had a diameter of 0.3125in (7.938mm). They were constructed of alloy steel with a tensile strength of 160.0ksi (1103MPa) and a shear strength of 95.0ksi (655MPa). They are depicted in Figure 38 and details are provided in Table 2 [89], [102].

Figure 38: Hi-Loc Fasteners

Table 2: Fastener Details

Hi-Lok Type	Configuration	Head	Grip Length (in) [mm]
HL 18-10-13	Double Shear	Protruding	0.8125 [20.64]
HL 18-10-20	Single Shear Protruding	Protruding	1.250 [31.75]
HL 19-10-20	Singe Shear Countersunk	Countersunk	1.250 [31.75]

In order to apply a specific controlled torque and still allow the joint to be separated easily, a standard 0.3125in (7.938mm) fine thread nut was employed. Though the Hi-Lok system employs a UNJF (Unified National J Series Fine) thread which employs a radius on the thread minimum diameter, no binding from the UNF (Unified National Fine) nuts was noted [103]. Since the Hi-Lok is a 'blind' fastener, meaning it has no head to which a tool may be applied, a torque extension was employed to allow access to the hex socket in the tail, (threaded end) of the fastener. Figure 39 depicts the blind head and hex socket in the tail of the Hi-Lok.

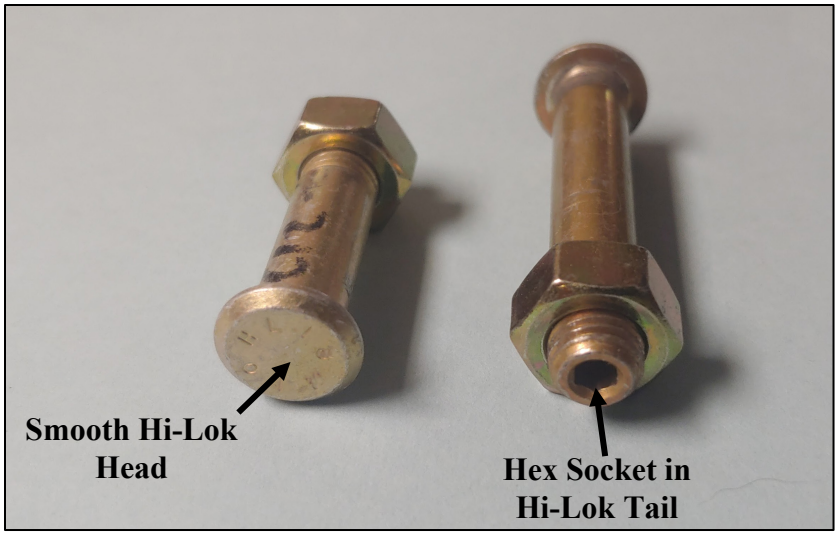

Figure 39: Hi-Lok Fastener Details

The target torque was 60 in-lbs (6.78N). This is about half of the torque targeted by most of the compatible Hi-Lok collars. This value was selected so that it represented a decayed torque value. Torque decay is a phenomenon that has been observed in composites in which torque and bolt preload relaxes during service [70], [104]. Thus, this torque represented a conservative amount of preload decay. Also, this torque corresponds to a bolt preload of around 963lbf (4.28kN) which is in the middle of the range of preload values studied in the Composite Airframe Life Extension programs [18], [105]. The relationship between torque and bolt tension is given by,

$$T = KFD \tag{64}$$

Where

T is applied torque

F is the bolt clamping force

K is the torque friction constant (equals 0.2 for dry fasteners)

D is bolt diameter (0.3115 in for the Hi-Lok fasteners)

Since a torque extension was required, an alternate torque wrench setting had to be calculated. The relationship is given by:

$$T_{set} = T_{des}\frac{L_W}{L_{ext}L_W} \tag{65}$$

Where

T_{set} is the torque wrench setting required to reach the desired torque value

T_{des} is the desired torque on the fastener

L_W is the length of the torque wrench

L_{ext} is the length of the torque extension

Based on this calculation, the final torque wrench setting was 50in-lb. Figure 40 shows the tools that were required to torque the Hi-Lok fastener.

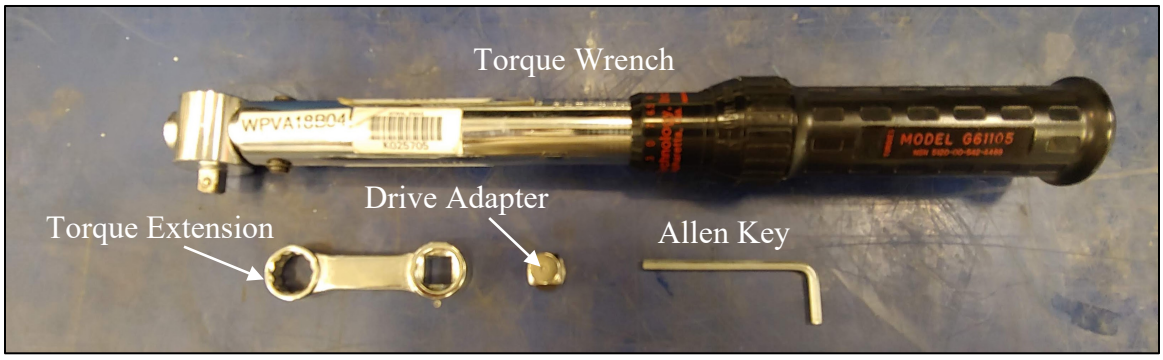

Figure 40: Tools Required for Hi-Lok Fasteners

3.5 Statistical Planning

In the quasi-static experimentation portion of this study, the purpose of three primary samples was to establish a consistent stress-strain curve shape, from which progressive failure test points could be determined. Also, loads were expected to be compared with control samples. Thus, the number of samples of each configuration drove the ability to draw conclusions about the means of two different sample types. ASTM

recommends five samples (replicates) in each configuration [2]. However, discretion is allowed in the test standards to reduce this number if valid test results may be obtained. To estimate the number of samples required prior to any experimentation for this study, previous hybrid bolted test data was explored. Those data demonstrated a standard deviation in ultimate strength of 42.5lbf (189N). That value was expected to be representative in this series of tests. As shown in Table 3, the confidence interval length is also presented as a percentage of what was considered a high conservative estimated maximum load of 10,000bf (44,500N) and then a lower estimated load of 6000lbf (26,700N). This is also seen graphically in Figure 33. These values are presented using the estimated 42.5lbf (189N) estimation and also twice that value at 85.0lbf (378N).

In Table 3, a 95% confidence interval length based on a Student's T distribution was calculated using this estimated standard deviation [106]. Throughout this work, a 95% probability (significance of $\alpha = 0.05$) was employed. The confidence interval about mean $\bar{x}$ is given as

$$\bar{x} \pm t_{(\alpha,n-1)} \frac{S}{\sqrt{n}} \quad \textbf{(66)}$$

Where

$\bar{x}$ is the sample mean

$t_{(a,n-1)}$ is the upper value for the t distribution with $n-1$ degrees of freedom

S is the sample standard deviation

n is the number of samples

Thus, the confidence interval length, $L_{CI,}$ away from the mean is given as,

$$L_{CI} = t_{(\alpha,n-1)}\frac{S}{\sqrt{n}} \quad (67)$$

As an example, for $n = 6$ assuming a 42.5lbf (189N) standard deviation

$$L_{CI} = 2.57\frac{42.5lfb}{\sqrt{6}} = 44.6lbf \quad (68)$$

Table 3: 95% Confidence Interval Width Predictions

	Assuming 42.5lbf (189N) Stdev			Assuming 85.0lbf (378N) Stdev		
n	Confidence Interval Length (lbf) [N]	% of 10 kip Peak	% of 6 kip Peak	Confidence Interval Length (lbf) [N]	% of 10 kip Peak	% of 6 kip Peak
2	382 [1670]	3.82	6.36	764 [3400]	7.64	12.7
3	106 [470]	1.06	1.76	211 [939]	2.11	3.52
4	67.6 [301]	0.68	1.13	135 [602]	1.35	2.25
5	52.8 [235]	0.528	0.880	106 [469]	1.06	1.76
6	44.6 [198]	0.446	0.743	89.2 [397]	0.892	1.49
7	39.3 [175]	0.393	0.655	78.6 [350]	0.786	1.31
8	35.5 [158]	0.355	0.592	71.1 [316]	0.711	1.18
9	32.7 [145]	0.327	0.544	65.3 [291]	0.653	1.09
10	30.4 [135]	0.304	0.507	60.8 [270]	0.608	1.01

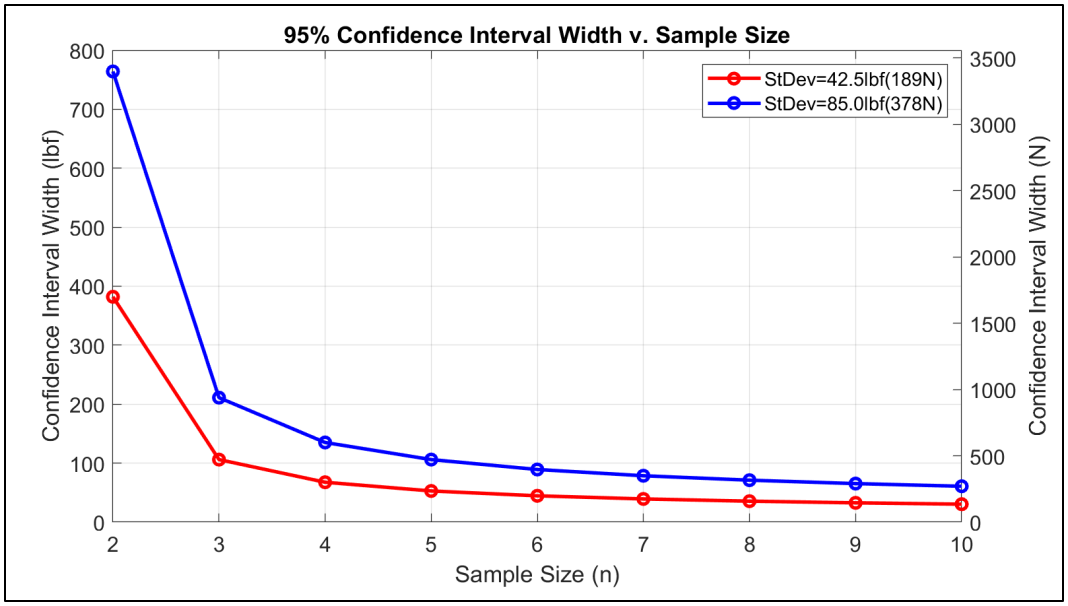

Figure 41: Confidence Width v. Sample Size

From this, it was expected that the three primary samples would allow a confidence interval length just over 200lbf (890N) or around 3.5% of the expected peak load. Furthermore, as the progressive failure samples were processed, the sample size increased each time for the specified load range. For example, by the time the 6th sample was tested over the most narrow load range, the confidence interval was expected to be down to under 100lbf (445N). ASTM E122 has a method of calculating a required number of samples, but in this case, that method provides trivial solutions of less than one required sample [107]. Figure 41 shows graphically that increasing the number of results should return slightly smaller confidence intervals, but it shows a diminishing return on the time and materiel resources to produce those samples.

3.6 Statistical Design of Experiments

3.6.1 Controlled Variables

Controlled variables in this study were ply count, hybridization, and configuration. Ply count and hybridization were controlled via layup. Ply count is the number of layers of material included in each layup. This was tested at 9 plies and 18 plies. Hybridization is the lack or presence of the stainless steel foils. Hybridization was tested as control (no metal), hybrid (metal through the entire thickness) and a shank-only hybrid (metal only near the shank of the countersunk bolt). Configuration was controlled as double shear, single shear protruding head, and single shear countersunk head.

3.6.2 Nuisance Variables

Nuisance variables were coupon panel position, cure cycle, hole diameter, and test environment temperature. Coupon panel position was tracked to test whether or not the source location of a coupon from a given panel was significant. As seen in Figure 42, coupons were assigned integer values as unique identifiers and another integer value representing panel position. If significant differences existed in the properties of coupons from the same panel, this would indicate that an issue occurred during layup or cure. Tracking panel position allowed these differences to be investigated and ruled out to ensure the properties were consistent over the area of the panel. Since six panels could be cured in one cure cycle, three separate cure cycles were required to cure 13 panels. To be able to test for the statistical significance of cure cycle, the control and hybrid panels were spread across the three cure cycles. Ideally, each cure cycle is exactly the same, and

properties do not vary between cure cycles. The panel arrangement in each cure cycle is shown in Table 4.

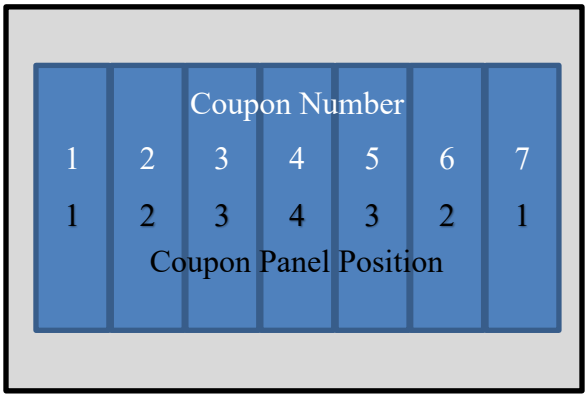

Figure 42: Coupon Panel Position

Table 4: Cure cycles

Cure Cycle A	Cure Cycle B	Cure Cycle C
C-04 H-04 C-06 H-06	C-05 H-05 C-07 H-07 C-12 H-11	C-08 H-08 S-01

Hole diameter was measured using pin gauges graduated in by 0.0010in (.025mm) and undersized by 0.00030in (0.0076mm). The laboratory room temperature, which varied between 69°F and 74°F during testing, was recorded using a desktop thermometer.

The samples were organized across test configurations such that variation from panel position and cure cycle was most widely spread. Additionally, care was taken to be sure this variation was distributed across the full failure and progressive failure samples. In the 9-ply and shank-only panels, only one panel was manufactured, thus variation from source panel and cure cycle could not be distributed. For the naming convention, the first letter “C” or “H” denotes control or hybrid, respectively. The following number identifies

the panel. The final number uniquely identifies the individual coupon. Table 5 lists how the coupons were originally distributed during the planning phase. However, due to careful machining, in many of the panels, seven coupons were able to be machined. Also, during testing, the fatigue testing regime was updated, and more samples were desired at lower strains in double shear. Thus, the coupons were actually distributed and tested as listed in Table 6 where samples that were added to the test plan or transferred to a different test configuration are noted with a dashed underline. This distribution of the coupons is important because it allowed for the testing of the statistical significance of the controlled and nuisance variables. If the coupons were not carefully distributed across test configurations, aliasing could be induced into the statistical analysis making the data less statistically conclusive.

Table 5: Coupon Distribution as Planned

Quasi-Static				Cyclic Loading	
9-Ply Double Shear	18-Ply Double Shear	18-Ply Single Shear Protruding	18- Ply Single Shear Countersunk	18-Ply Double Shear	18-Ply Single Shear Protruding
C-12-1 H-11-1	C-04-1 H-04-1	C-04-2 H-04-2	C-04-3 H-04-3 S-01-1	C-04-4 H-04-4	C-04-5 H-04-5
C-12-2 H-11-2	C-05-4 H-05-4	C-05-5 H-05-5	C-04-6 H-04-6 S-01-2	C-05-2 H-05-2	C-05-3 H-05-3
C-12-3 H-11-3	C-06-2 H-06-2	C-06-3 H-06-3	C-05-1 H-05-1 S-01-3	C-06-5 H-06-5	C-05-6 H-05-6
C-12-4 H-11-4	C-07-5 H-07-5	C-06-6 H-06-6	C-06-4 H-06-4 S-01-4	C-07-3 H-07-3	C-06-1 H-06-1
C-12-5 H-11-5	C-08-3 H-08-3	C-07-1 H-07-1	C-07-2 H-07-2 S-01-5	C-07-6 H-07-6	C-07-4 H-07-4
C-12-6 H-11-6	C-08-6 H-08-6	C-08-4 H-08-4	C-08-5 H-08-5 S-01-6	C-08-1 H-08-1	C-08-2 H-08-2

Notes for quasi-static:

- Black font-Full Failure Samples
- Green font-Progressive Failure Samples

Table 6: Coupon Distribution as Tested

Quasi-Static				Cyclic Loading	
9-Ply Double Shear	18-Ply Double Shear	18-Ply Single Shear Protruding	18-Ply Single Shear Countersunk	18-Ply Double Shear	18-Ply Single Shear Protruding
C-12-1 H-11-1	C-04-1 H-04-1	C-04-2 H-04-2	C-04-3 H-04-3 S-01-1	C-04-4 H-04-4	C-04-5 H-04-5
C-12-2 H-11-2	C-05-4 H-05-4	C-05-5 H-05-5	C-04-6 H-04-6 S-01-2	C-05-2 H-05-2	C-05-3 H-05-3
C-12-3 H-11-3	C-05-7 H-05-7	C-06-1 H-06-3	C-05-1 H-05-1 S-01-3	C-06-5 H-06-5	C-05-6 H-05-6
C-12-4 H-11-4	C-06-2 H-06-2	C-06-3 H-06-6	C-06-4 H-06-4 S-01-4	C-07-3	C-07-4 H-06-1
C-12-5 H-11-5	C-06-7 H-07-3	C-06-6 H-07-1	C-07-2 H-07-2 S-01-5	C-07-6	C-08-2 H-06-7
C-12-6 H-11-6	C-07-5 H-07-5	C-07-1	C-08-5 H-08-5 S-01-6	C-08-1	H-07-4
	C-08-3 H-07-6	C-08-4			H-08-2
	C-08-6 H-08-1				H-08-4
	C-08-7 H-08-3				
	H-08-6				

Notes:

- Underlined-Added or transferred samples

3.7 Manufacturing

For this work, thirteen 6.00in by 8.00in (15.2cm by 20.3cm) composite and hybrid composite panels were constructed in the AFRL/RQ clean room. This facility houses a modern, fully outfitted composite manufacturing operation. A complete list of the materials required to construct the samples used in this research is listed and explained in Appendix A. While much of this manufacturing process may be perceived as standard composite manufacturing, many considerations had to be made to properly construct the novel hybrid material. Thus, much of the process is detailed here to explain the unique considerations required to manufacture the hybrid panels.

3.7.1 Material Preparation

Before layup could begin, the materials had to be prepared to be included in the layup. The preimpregnated composite, stainless steel, and AF-191 adhesive, all had different specific preparation requirements.

Preparation began by processing the 301 stainless steel foils to be included in the layup. First, the foils were cleaned thoroughly with 90% isopropyl alcohol. Then, the foil was affixed to a G10 fiberglass frame so that each side could be grit blasted in a blasting cabinet with 240-grit aluminum oxide pressurized with nitrogen. Figure 43A shows the blasting cabinet that was used to prepare the foils and Figure 43B shows the size of the blasting media compared to a U.S. quarter.

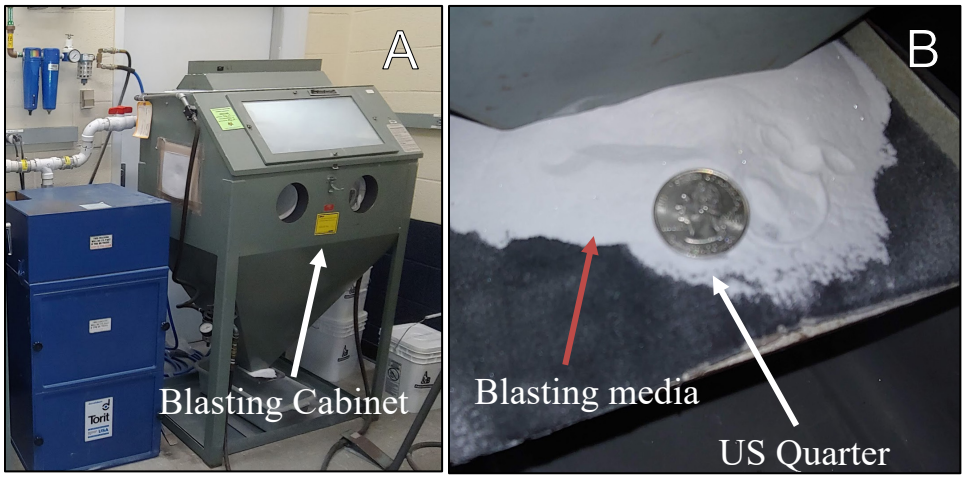

Figure 43: Layup Components A) Blasting Cabinet B) Blasting Media

After blasting, the foil was then fastened to a G10 fiberglass window, so that both sides could be treated in one operation. A Sol-Gel treatment was applied to each surface. Finally, Solvay BR-6747-1 water-based primer was applied to stabilize the surface.

Figure 44 depicts the life of a stainless steel foil through its preparation. Figure 44A shows the foil after being affixed to the fiberglass backing and cleaned. Figure 44B

shows the panel after grit blasting, where the blasted surface shows a stark contrast when compared to the pristine surface which was cover by tape during blasting. Here the prepared area of the sample displays a stark contrast to the unprepared surface near the edge. After grit blasting, the panel was affixed to a G10 fiberglass frame to expose both sides. Figure 44C shows the panel after the Sol-Gel Treatment was applied and Figure 44D shows the panel after primer was applied.

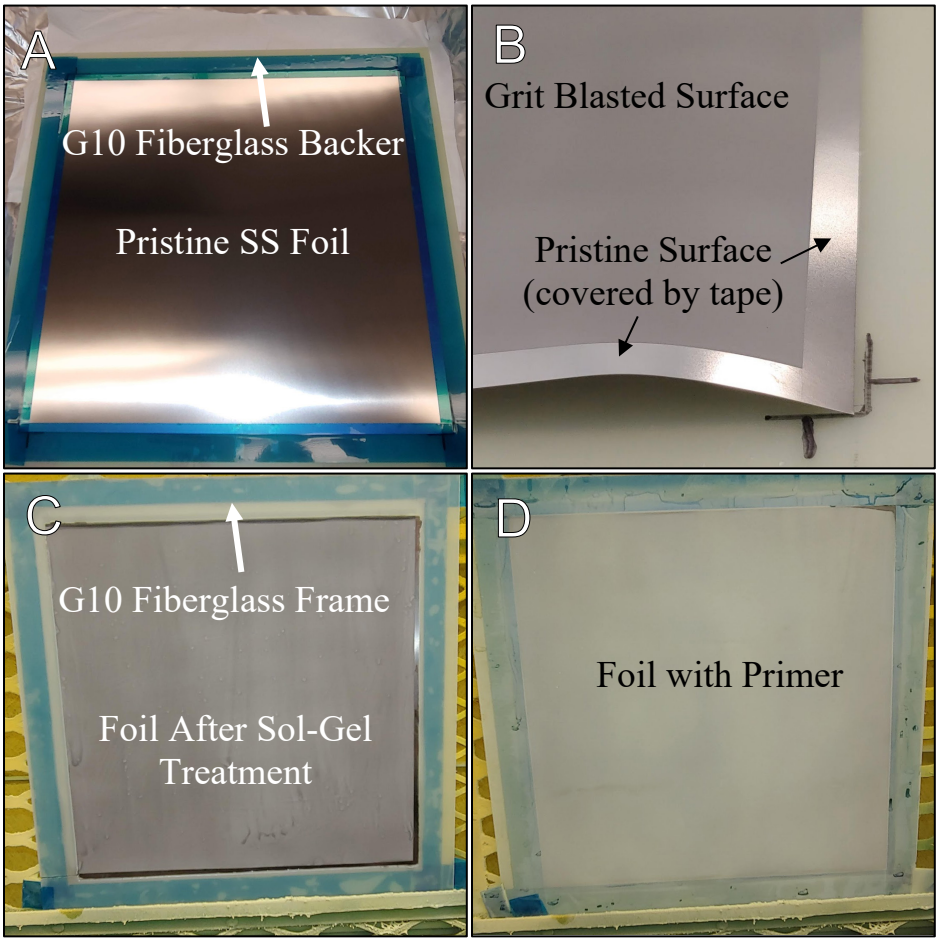

Figure 44: Stainless Steel Foil Preparation
A) After Cleaning B) After Media Blasting
C) After Sol-Gel Solution D) after Priming

The foils were cut using a standard office paper cutter. The process was attempted on numerous sheet metal shears, but the thin gauge of the material caused inconsistent results. In most cases when using a sheet metal shear, the foils would simple fold as if a sheet metal break were employed. The paper cutter gave the most consistent, repeatable, and straight cut of all the options explored.

Preparation of the foils was by far the most labor intensive of all the preparatory processes, with each panel requiring four to six man-hours to prepare. Due to the labor requirement and prioritization amongst other programs, foils were the item requiring the longest lead time.

It is noteworthy that when one side of the foil was grit blasted, stored residual manufacturing induced stresses were released causing the foil to roll as shown in Figure 45. Once the opposite side was grit blasted, the opposing stresses were released, causing the foil to lie flat.

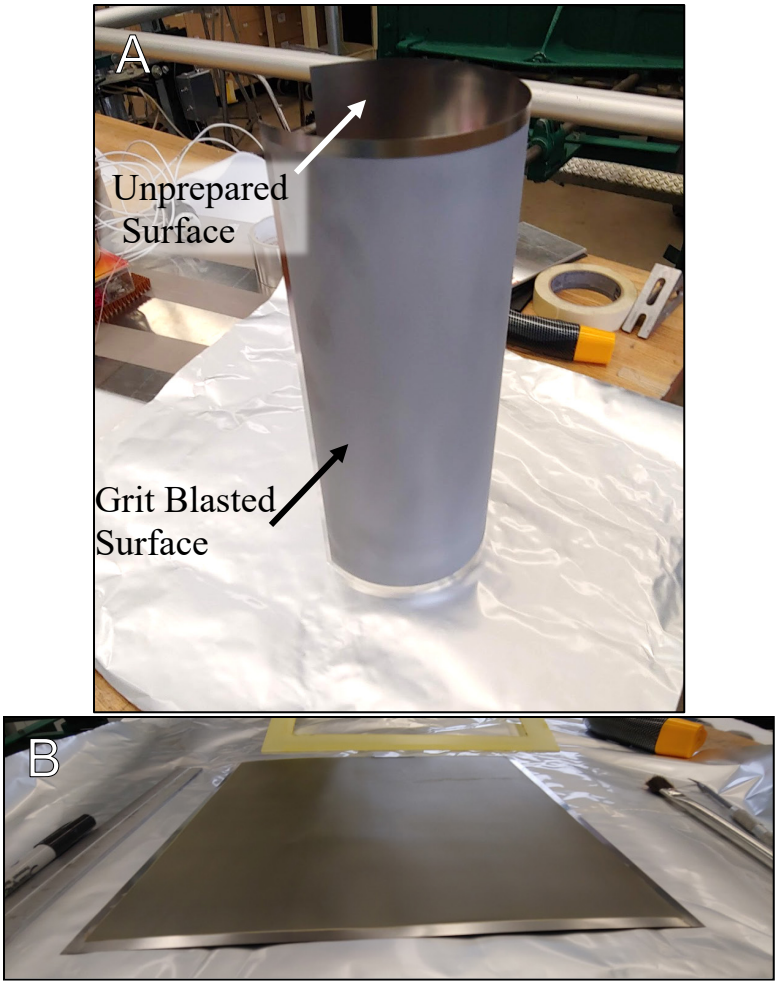

Figure 45: A) Rolled Stainless Steel Due to Released Manufacturing Stresses B) Stainless Steel Lying Flat after Full Grit Blast

The prepreg and adhesive film are maintained in cold storage. For this reason, the material had to be extracted from cold storage for approximately 12 hours to thaw. The material could then be cut using a Gerber 2D plotting cutter (Figure 46). In operation, the composite material was always placed in the same orientation on the table as it came off the roll. The fiber direction was varied by changing the position of the shape being cut with reference to the table. In other words, to cut a 45° ply, the raw material remained in the same configuration and the tool path was rotated by 45°.

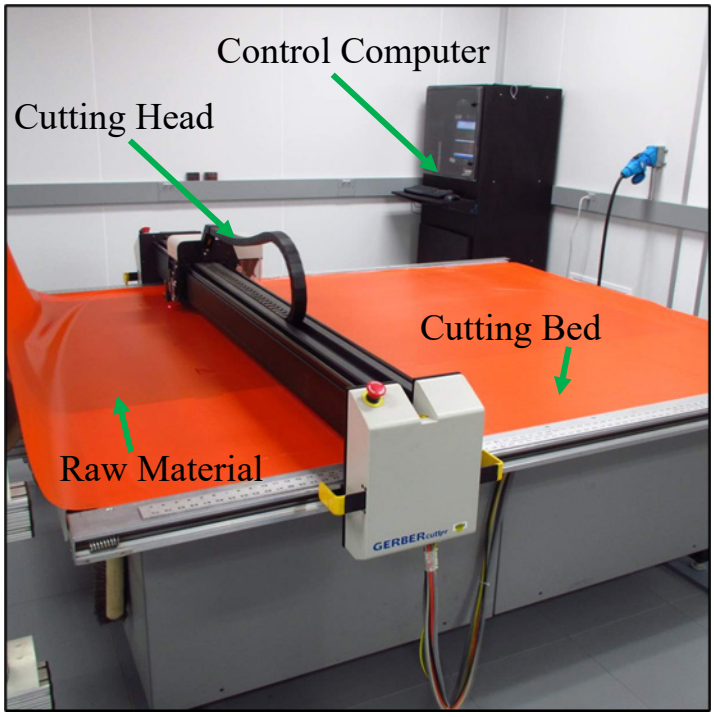

Figure 46: Gerber Cutter

3.7.2 Panel Layup

The layup process began with establishing a right-angle jig at a workstation as depicted in Figure 47A. Fiber directions and transition points were labeled. Each ply was positioned in the jig and initially compressed with a roller. After each layer was applied, the stack was debulked for three minutes under vacuum at 120°F (48.9°C) as shown in Figure 47B. Debulking removes bulk trapped gasses introduced during layup and initially consolidates the plies. Engineers recorded each layer on a layup table to ensure that the prescribed order was followed. After all layers were applied, the panel was debulked for 60 minutes.

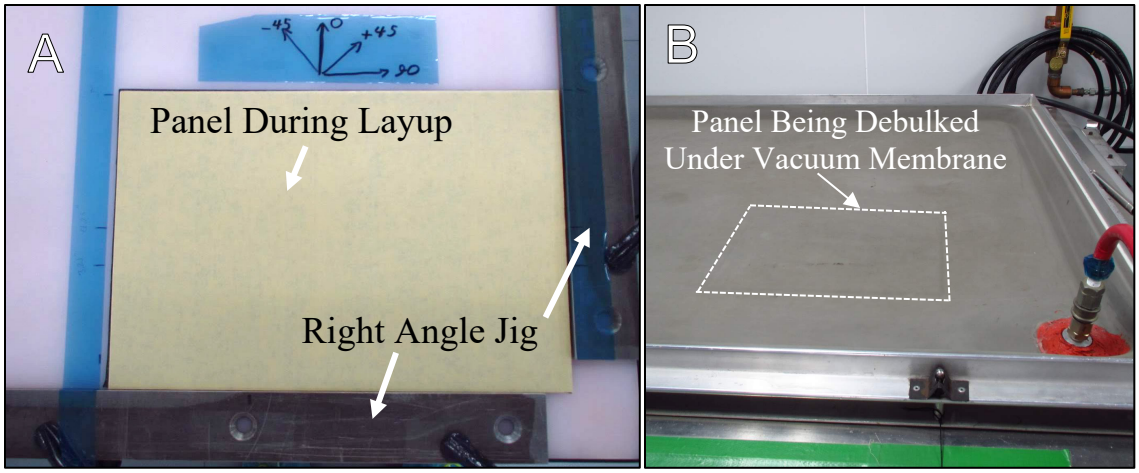

Figure 47: Composite Layup Jig

It is important to note that the stainless steel foils and film adhesive were integral to the layup and were co-cured in the primary cure cycle. Figure 48A depicts the layup of a layer of stainless steel as it transitions into a piece of prepreg. Figure 48B shows the layup process as the protective film is removed from the adhesive which has been applied over a layer of prepreg and stainless steel.

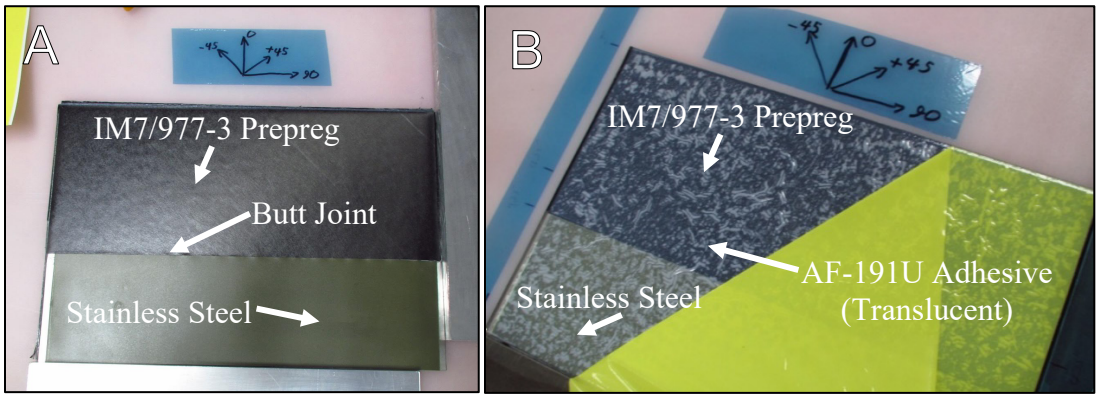

Figure 48: Layup Components

During layup, some difficulties were noted in working with the AF-191U adhesive. Two common defects are shown in Figure 49. The first defect was a tear

(Figure 49A) that rendered the affected adhesive plies unusable. This was not attributable to any material handling error. Second, seams attributed to manufacturing were common (Figure 49B). These seams were placed in the carbon fiber sections of the layup instead of at the critical junction with the stainless steel.

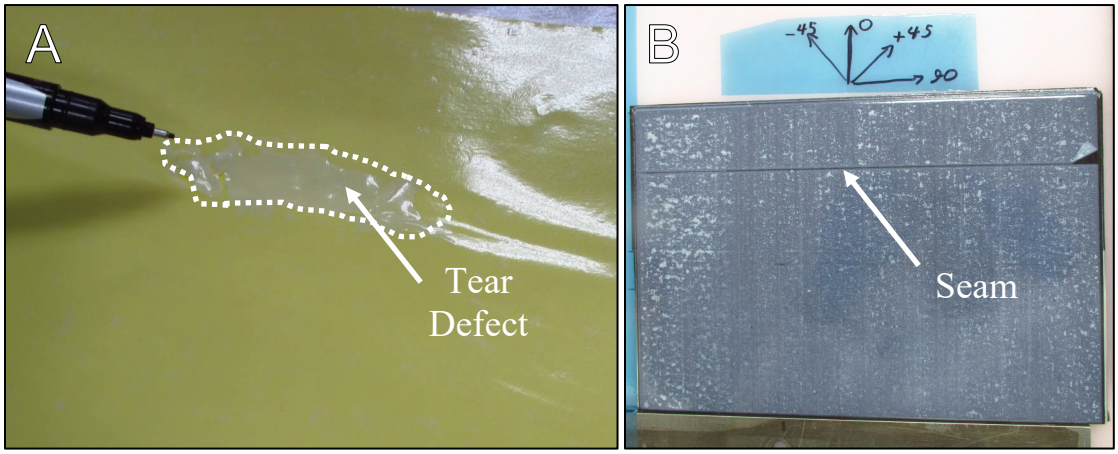

Figure 49: AF-191U Adhesive Defects

It was also noted that at the clean room temperature that remained near 68°F (20°C), the adhesive was brittle. Often, the adhesive would tear when attempting to remove it from the backer material. Heating the adhesive on the bed of the debulk table for one minute (held at 120°F (49°C)) made the material more compliant and easier to work with.

3.7.3 Vacuum Bagging and Cure Considerations

The panels were vacuum bagged and cured using standard procedures for IM7/977-3 composite materials. The processes are described in Appendix B and the cure cycle specific by Hexcel Composites is included in Appendix D.

Of the four cure cycles performed for this research (described in section 3.6.2 and Table 4), two performed nominally as expected and two displayed behavior that gave

cause for concern. Figure 50 shows four cure cycles conducted for this study. The top plot shows the temperature measured at the platen (curing surface) using a thermocouple. The middle plot shows the pressure measured inside the autoclave which is expected to be high throughout most of the cycle. The bottom plot represents the pressure inside the vacuum bag which is expected to be less than or equal to zero throughout most of the cycle indicating vacuum. Cure cycles B and C performed nominally. In cure cycle D, around 70min into the cycle it appears that a slight leak developed in the system allowing a positive pressure of about 3psi (21kPa) inside the vacuum bag. However, this relatively low pressure remained constant through the remainder of the 6hr pressure hold. Further evidence of the leak is demonstrated around the 430min point when vacuum was reintroduced to the vacuum bag. At this point a positive pressure of almost 20psi (138kPa) was reached. Since this vacuum bag had surpassed the leak down test, this leak is attributed to a poor connection between the autoclave vacuum system and the vacuum bag. Per lab technicians, the vacuum connectors inside the autoclave had been problematic in other recent cure cycles. Because the pressure deviation from the prescribed cure cycle was small throughout the 6hr hold time, the panels cured in cure cycle D appeared nominal in ultrasonic scans, and coupons from those panels did not display any measurable difference in mechanical properties.

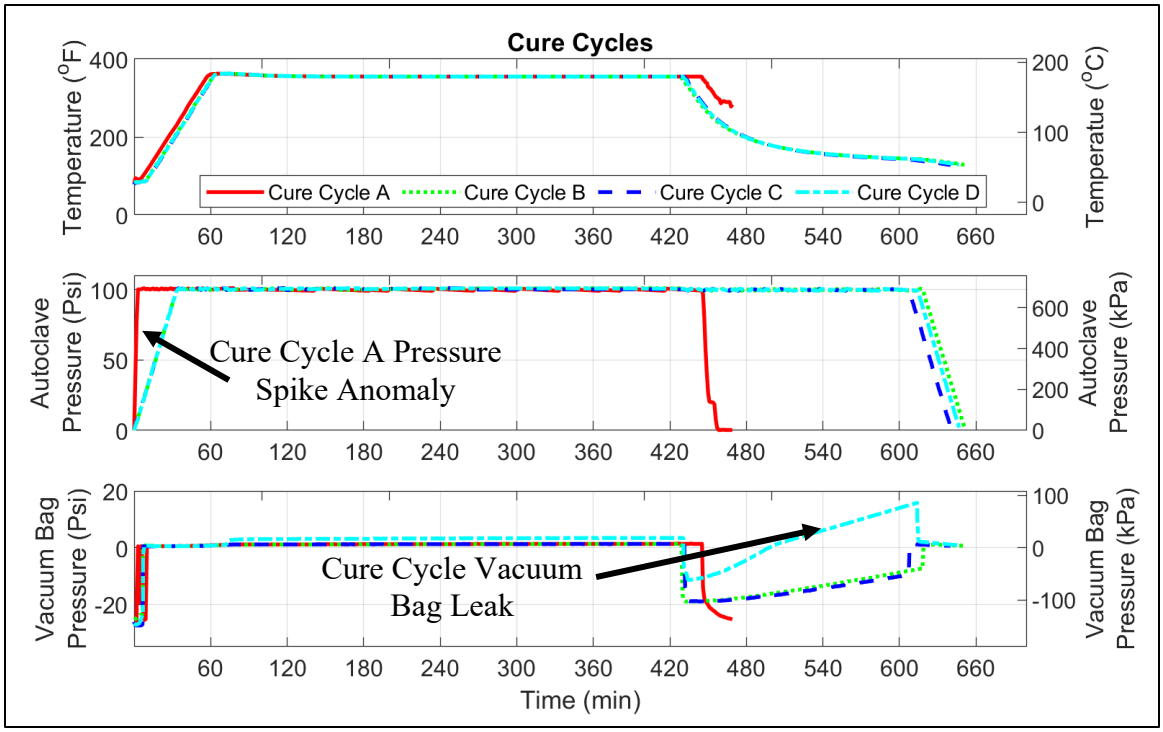

Figure 50: Cure Cycles

What is most noteworthy in Figure 50 is the erroneous behavior of cure cycle A. A computer software crash corrupted the recipe files which control the autoclave system. When the first six panels were cured, instead of ramping temperature and pressure, the system incorrectly commanded the peak temperature and pressure immediately upon initiation of the cure cycle. This effectively clamped down the edges of the panels that were still near room temperature which prevented compaction of the panels. This rendered the affected panels unusable. Evidence of this will be shown in the section on Nondestructive Inspection.

3.7.4 Coupon Machining

The machining processes are critical to the discussion of this research as the addition of the stainless steel complicated machining. These were the current best

practices for machining the hybrid composite material as of the time this research was conducted. Laying out the machining methodology here provides a baseline for future machining optimization efforts. The samples were sectioned from the panels as shown in Figure 51, using a diamond blade set up in a 3-axis mill using a mist coolant (Figure 52). The first precision cut on the panel was to ensure that the shorter foils extended exactly 2.00in (5.08cm) into the part. The extra width of the panels allowed ample material to compensate for the width of the diamond blade, known as the kerf. In many panels, quality manufacturing and careful machining allowed for a 7th coupon.

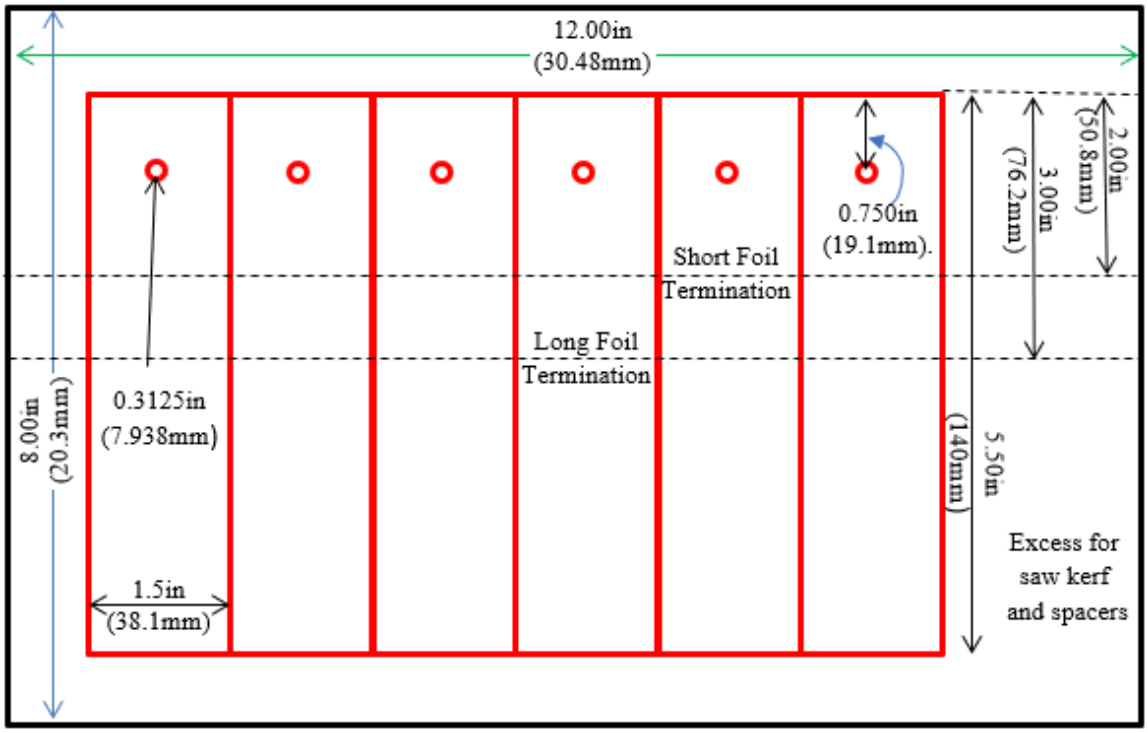

Figure 51: Panel Cut Layout

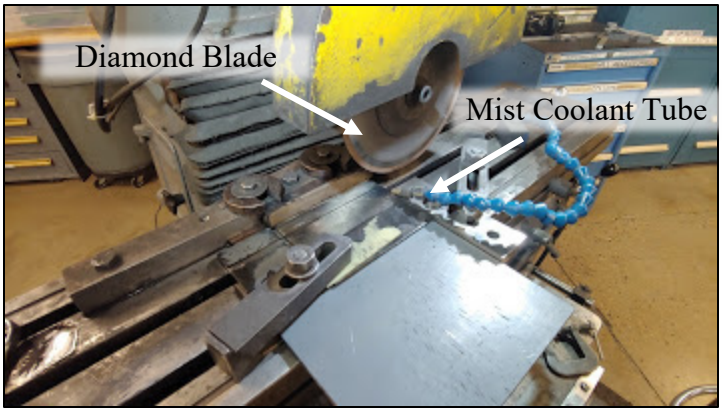

Figure 52: Composite Milling Setup

Hole diameter and concentricity are critical dimensions for bearing samples. Figure 53A depicts the benchtop CNC mill that was used to drill the samples for this study. This machine was used so that a "pecking" method could be programmed. Pecking simply means that the bit contacts and cuts the material in an intermittent pattern. After cutting for a short time, the bit retracts allowing chips to clear and allowing both the bit and part time to cool. Figure 53B depicts the brad point bit that is optimized for cutting composite materials. Shown next to the bit is what engineers have coined as the "hybrid donut." When this bit is employed in a pure composite, it cuts the outside of the hole first then chips out the center of the hole. This ensures a clean bore. However, in this hybrid scenario, the presence of the steel and the complexity of the hybrid results in this donut of material shearing out of the hole and binding the bit with unpredictable timing. Machinists discovered that if the donut were not removed quickly, the bit would attempt to force the donut through the part creating vibration that ruined the bearing surface of the hole and tear-out on the back surface of the coupon.

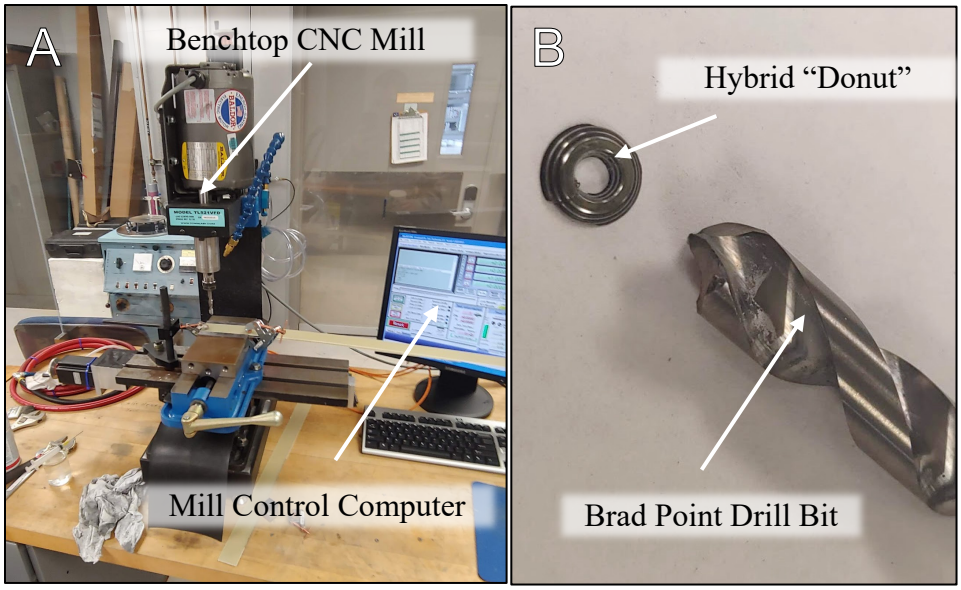

Figure 53: A) Composite Drilling Setup B) Brad Point Bit

3.8 Pre-Test Coupon Characterization and Test Preparation

3.8.1 Measurement

Final coupon dimensions of length, width, and thickness were recorded using calipers with a fine graduation of 0.0005in (.013mm) resulting in a measurement accuracy of 0.00025in (0.0063mm). Width and thickness were recorded at three reference points as depicted in Figure 54. The weight of each sample was recorded using an electronic balance with an accuracy of 0.005grams as a check for any manufacturing errors.

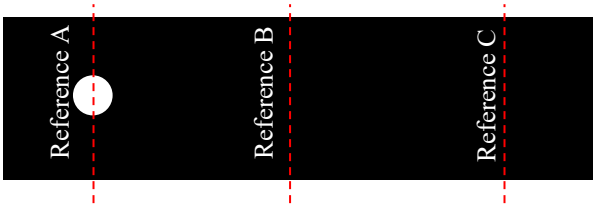

Figure 54: Measurement Reference Points

Final hole dimensions were measured with pin gauges, depicted in Figure 55, which allow for a far more consistent measuring method for holes than calipers. The pin gauges are undersized by 0.00030in (0.0076mm) to allow the gauge to be inserted into a hole of the labeled dimension of the gauge. Since the pin gauges are graduated in 0.0010in (0.025mm) increments, this method has a measurement error of 0.0005in (0.013mm).

Figure 55: Pin Gauges

3.8.2 Nondestructive Inspection (NDI)

Ultrasonic c-scans were performed on each manufactured panel before machining to verify that panels were compacted and cured properly. This system passes ultrasonic energy through a sample which bounces off a sonic mirror and passes back through the part. The amount of energy returned to the receiver is recorded as a percentage of the magnitude of the original signal.

The pre-machining scans were critical in this work. Figure 56A depicts a control panel that was cured in cure cycle A for which the recipe was corrupt. Figure 56B depicts

a similar panel that was cured in cure cycle B which performed properly. The panel from the corrupt cure cycle shows a large variation in sound transmission toward the middle of the panel. In the worst cases, the sound transmission is less than 10%. In contrast, the panel from cure cycle B predominantly shows homogenous sounds throughout the panel.

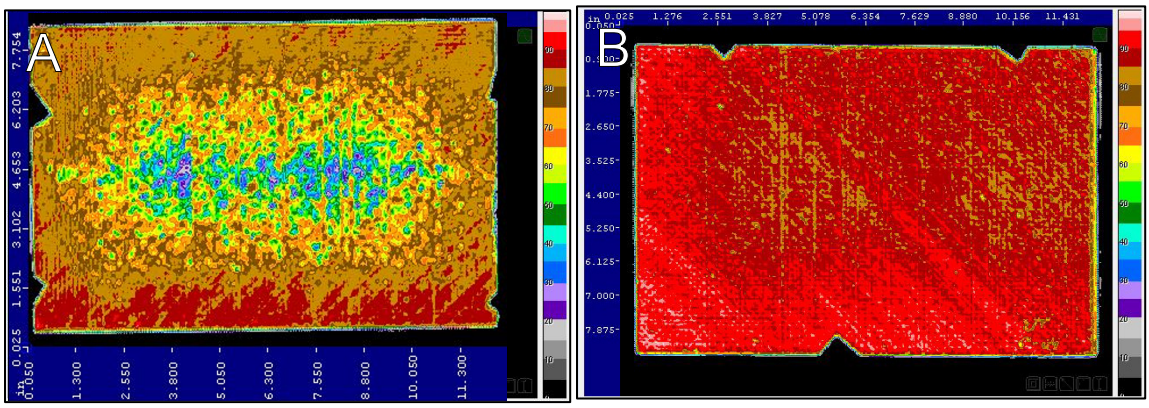

Figure 56: Control Panel Pre-Machining Ultrasonic Scans
A) Corrupt Cure Cycle B) Nominal Cure Cycle

Scans of hybrid panels were less conclusive than those of the control panels. The presence and spacing of the stainless steel proved to be highly attenuative. This attenuation and the stepped transition zone of the hybrid forced NDI personnel to scan each hybrid panel in three separate scans as depicted in Figure 57. In region 1 of the panel depicted in Figure 57A, there is no metal, so the noise in this section is attributed to the 12 plies of adhesive interleaved between 18 composite plies. In region 2 of the panel depicted in Figure 57B, the signal was increased to 40dB to pass the sound through the two stainless foils and 12 layers of adhesive between 16 composite plies. In the bearing section of the panel (region 3) depicted in Figure 57C, the system is transmitting energy through 6 stainless foils, 12 adhesive layers and 12 composite plies. With attenuation from varying materials and the maximum gain setting of 50dB, the noise in these scans is

so high that the scans are not especially useful for flaw detection. X-ray scans were also tested but were only sufficient to show the location of the foils. They did not provide any discernable information on the composite material or compaction of the panel.

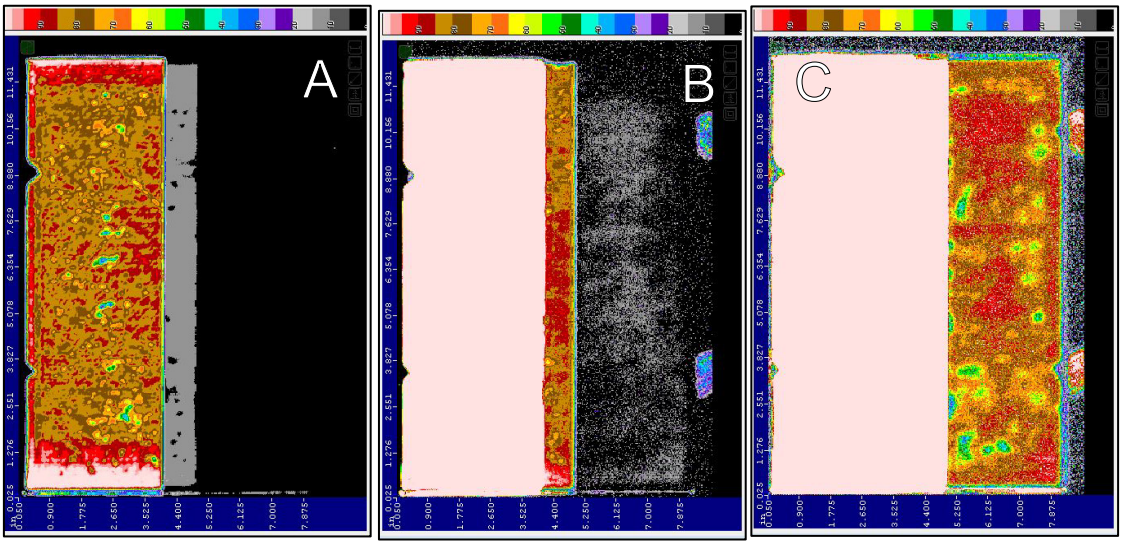

Figure 57: Hybrid Panel Pre-Machining Ultrasonic Scans
A) Region 1-18dB B) Region 2-40dB C) Region 3-50dB

Panels were also scanned after machining to ensure that there were minimal machining induced defects. Examples are depicted in Figure 58. Just as noted in the pre-machining scans, the control results were useful in ensuring that no machining induced defects were present. However, the high energy levels and attenuative nature of the hybrid caused a great deal of noise in the signal, which effectively masked any conclusive evidence that could be drawn from the scans.

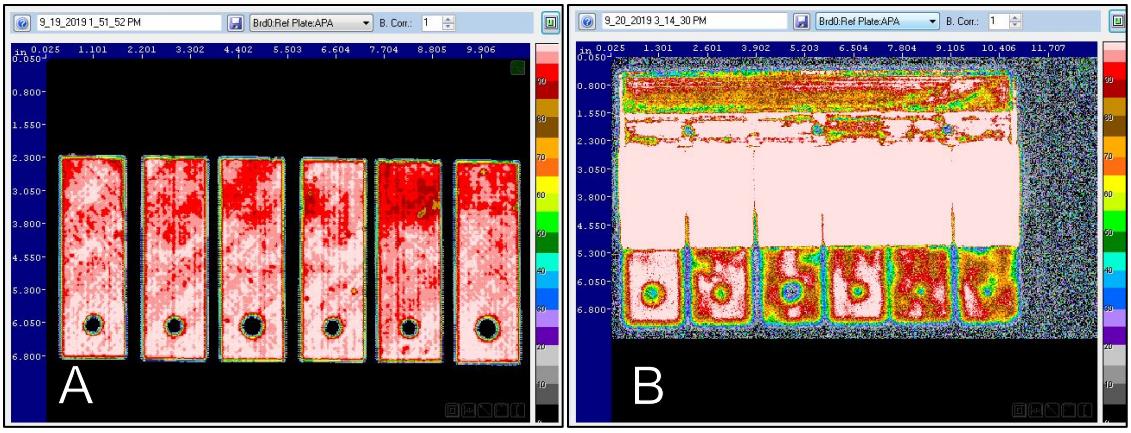

Figure 58: Ultrasonic C-scans A) Control Coupons-7dB B) Hybrid Coupons-50dB

3.8.3 Test Sample Preparation

After machining and NDI, grip tabs and the extension gauge knife edge tabs were bonded to the coupons. The surfaces were first scuffed with 80grit abrasive paper and cleaned with 90% isopropyl alcohol. Jigs were machined to ensure that the knife edge was properly aligned and located the correct distance from the hole. The grip tabs were locally machined from 0.050in (1.30mm) thick fiberglass with a 7° angle to avoid a stress concentration as the grip tab transitions into the surface of the coupon. Drawings of these jigs and grip tabs are included in Appendix L. HySol 9394 epoxy was applied to each mating surface, clamps were applied, and the samples were placed in a 200°F (93°C) oven for 1 hour to cure [91]. The samples were removed from the oven and allowed to cool for a minimum of 12 hours. Engineers learned through the process that the most repeatable method was to bond the grip tabs, oven cure, then bond the knife edge tabs followed by a final oven cure. Figure 59 depicts a sample having the knife edge tab located and bonded.

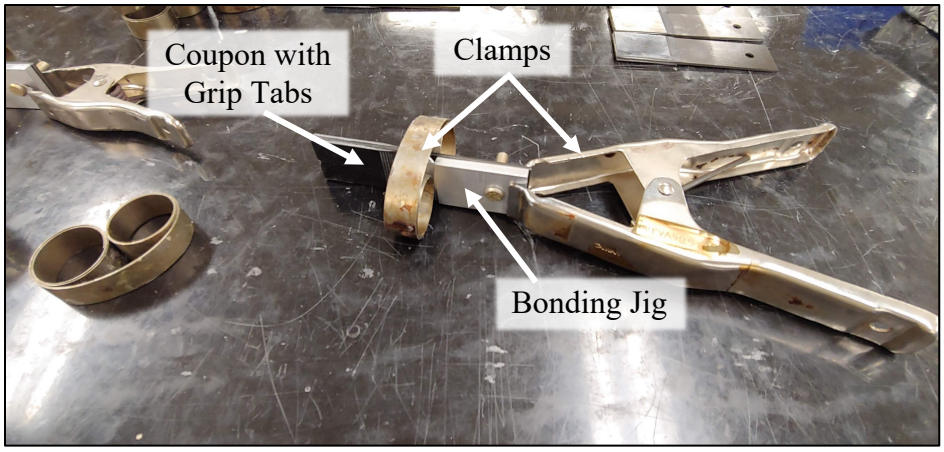

Figure 59: Bonding of Grip Tabs and Knife Edge Tabs

3.9 Quasi-static Experimental Methodology

Since progressive failure characterization was a chief goal of this work, 61 samples were subjected to monotonic quasi-static testing in three bolted bearing configurations.

3.9.1 Double Shear Methodology

Figure 60A shows the double shear experimental setup, and Figure 60B shows a sectioned view of a three-dimensional model. Figure 60B also shows the resultant load path. In this load scenario, a tensile load is applied to the coupon while the fixture is held static. A resultant bearing load is generated between the bolt and the specimen hole. Due to this configuration, much of the loading near the hole is compressive in nature.

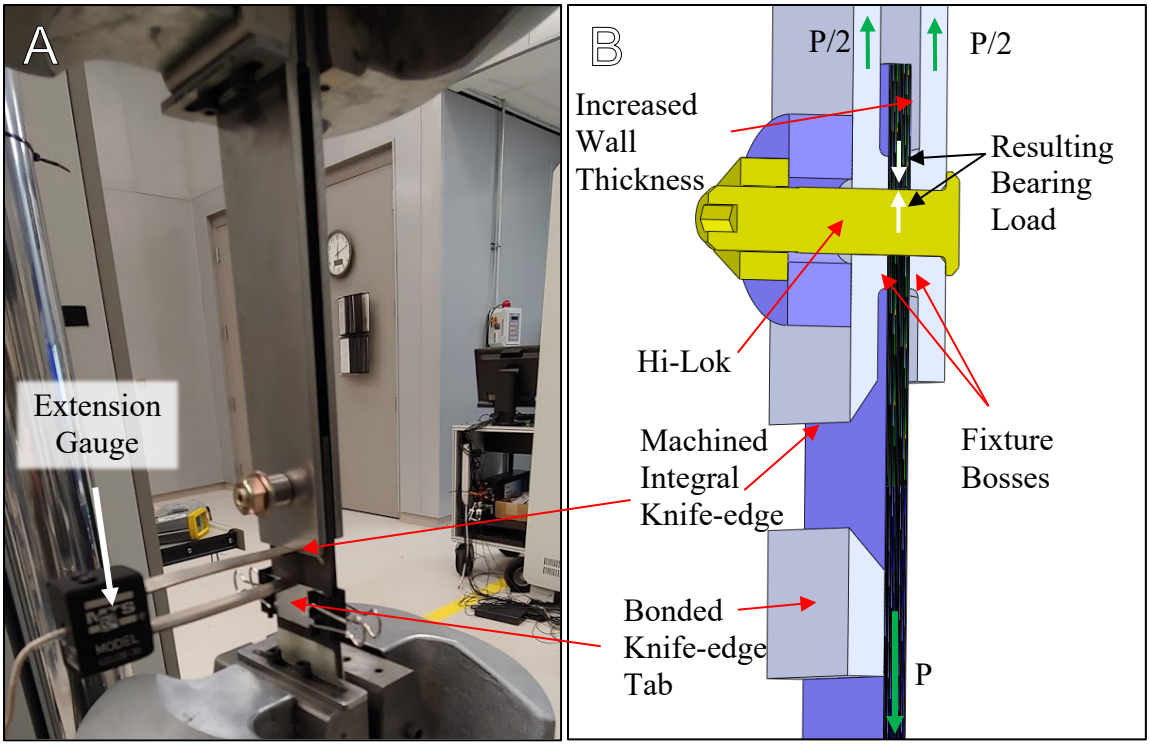

Figure 60: A) Double Shear Experimental Setup B) Sectioned View of 3D Model

Testing was conducted using a 22kip (97.86kN) capacity MTS servo-hydraulic load frame with a FlexTest40 controller. Load was measured with an MTS 661.20F-03 force transducer through a model 494.26 conditioner. Based on an MTS calibration, over the test range, this device has a measured accuracy within ±0.15% which equates to an accuracy of ±12lbf (±53N). Hole elongation was measured with an MTS 632.03E-30 clip-on displacement gauge (as shown in Figure 60A). This displacement gauge was calibrated using a MTS 650.03 extensometer calibrator with an error of ±0.05%. With the displacement gauge calibrated over its range of 0.500in (12.7mm), this results in a hole elongation accuracy of ±0.00025in (±0.0064mm). Head displacement was recorded as a backup for hole elongation using a linear variable displacement transformer (LVDT) through a 494.16 conditioner. Over the range of extension values explored in this study, it

had a maximum error of 0.45% which equates to an accuracy of ±0.00091in (±0.023mm). Time was recorded as a reference.

Procedurally for the double shear case, the fixture and coupon were configured on the bench. A spacer of the same thickness as the coupon was placed between the two sides of the fixture and temporarily secured with tape. With the fixture and coupon aligned against the flat benchtop, the fastener was hand tightened to prevent rotation of the coupon with respect to the fixture. The grip end of the fixture was inserted into the top grip of the test frame, and the grip end of the coupon was inserted into the lower grips. Stops were preset on the grips to ensure that the coupon and fixture remained centered. With grip pressure set to 2000psi (13.79MPa), the top grip was closed on the fixture. Then, the top grip was closed while the load control was activated with a target value of zero. This insured that no load was applied during gripping. After torqueing the fastener to 60 in-lbf (6.8Nm), the extension gauge was clipped onto the knife edges. Coupons were loaded in displacement control at 0.050in/min (1.27mm/min). When the stop criterion based on extension gauge reading was met, the samples were unloaded in load control at 100lbf/s (445N/s). Load, head displacement, gauge displacement, and time were recorded at 10Hz. Stop criteria for the full failure samples evolved throughout the course of testing. It was determined that very little useful information could be gathered past 30% hole elongation or 0.094in (2.38mm). After the test was complete and the sample was unloaded, both grips were released, and the sample was removed from the fixture on the bench.

3.9.2 Single Shear Methodology

Figure 61A shows the single shear experimental setup, and Figure 61B shows a three-dimensional model sectioned through the center of the coupon. This load scenario produces a resultant compressive load between the coupon and the bolt similar to that of the double shear case. However, due to the single shear condition, bending is allowed in both the bolt and fixture. In addition to the load at the bearing surface, this load scenario also places significant compressive loading between the head of the fastener and the surface of the coupon. In effect, the system is attempting to pull the bolt head through the thickness of the coupon.

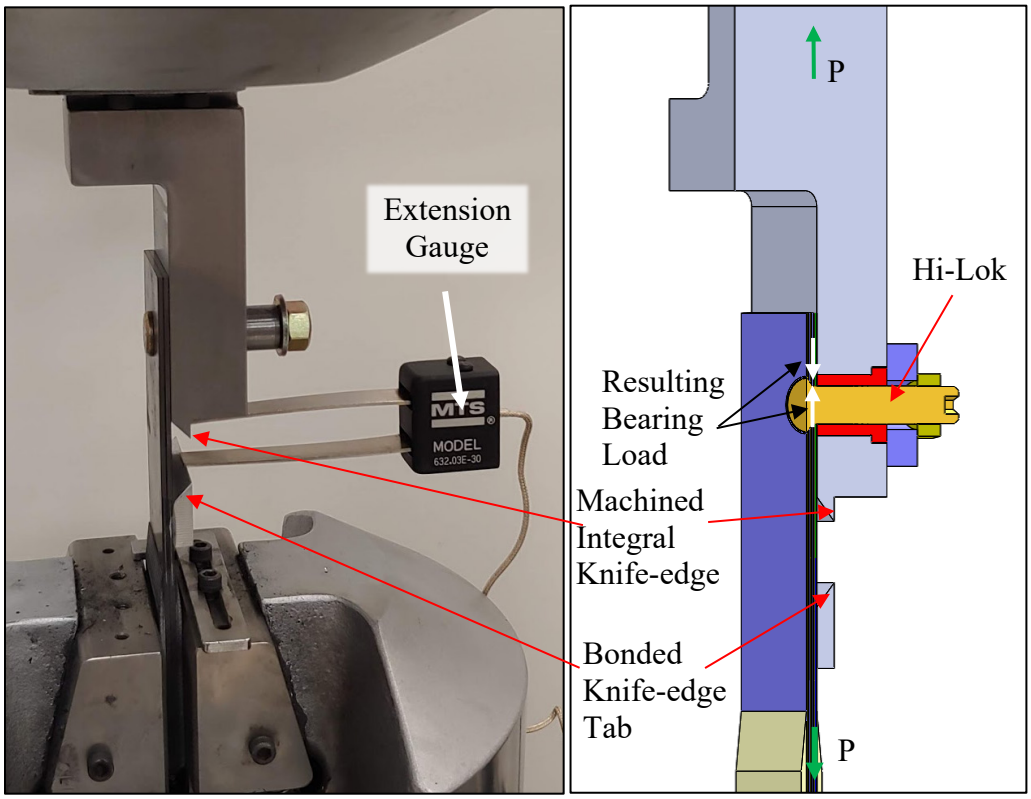

Figure 61: A) Single Shear Experimental Setup B) Sectioned View of 3D Model

In order to conduct the single shear testing, the lower grip was rotated 90° to interface with the fixture. This fixture arrangement allows the tester to ensure that the load is being transmitted through the center of the coupon. This reconfiguration process, which required loading the test frame to near its maximum capacity, was conducted by lab technicians in accordance with MTS instructions. Afterwards, the alignment of the system was verified. Load, hole elongation, head displacement, and time were recorded as described in section 3.9.1.

For the single shear configuration, the fixture was placed in the upper grips based on the thickness of the coupon being considered. A stop was set on the grips to ensure that the coupon was properly aligned with the fixture. The bolt was hand tightened to prevent rotation. After checking alignment with a straight edge, the lower grips were closed using the load control procedure described previously. After torqueing the fastener, the test program was run using the established parameters. With the stop criteria met and the sample unloaded, the coupon was removed from the fixture while the fixture remained configured in the upper grips.

3.9.3 Quasi-Static Mechanical Property Analysis

3.9.3.1 Stress-Strain Calculations

The monotonic quasi-static testing output the following values: head displacement, extension gauge displacement, load, and time. These data were coupled with coupon measurements to process raw data into comparable results.

First raw stress was calculated as

$$\sigma_{br} = \frac{P}{A} = \frac{P}{Dt} \quad (69)$$

Where

σ is stress

P is the applied load measured from the load cell

A is the bearing area

D is the bolt diameter

t is the coupon thickness near the bearing hole

Raw strain, which can be thought of as normalized displacement, was calculated using the following relation:

$$\varepsilon_{raw} = \frac{d}{D} \quad (70)$$

Where

ε_{raw} is the raw strain (before slack correction)

d is hole elongation measured by extension gauge

Diameter and hole elongation references are detailed in Figure 62.

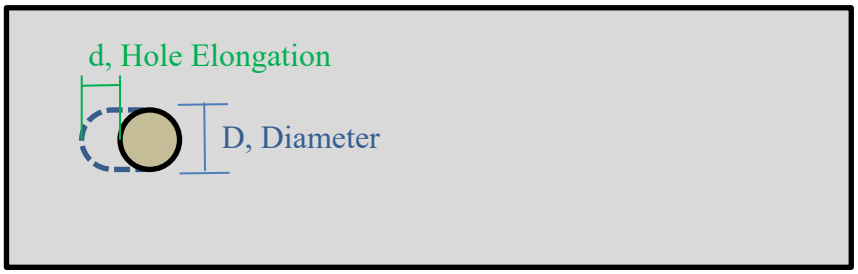

Figure 62: Bearing Strain Calculation References

Bolt diameter was employed in the strain calculation because it was a consistent value between control and hybrid samples, and because the contact area that makes up the stress is defined by the bolt diameter.

3.9.3.2 Data Correction and Comparative Measures

In order to develop the data correction value so that other measures used to compare data could be developed, the procedure below was carried out. In the bolted joints there was some amount of slack between the bolt and the bearing surface of the hole. If the bolt was at its lower tolerance limit (acceptable dimension) and the hole was at its upper tolerance limit, the slack in the hole could be up to 0.002in (0.051mm). The strain correction removed this slack and forced a line through the linear region of a stress-strain curve to pass through the origin. This allowed for an accurate comparison between samples. Per ASTM D5961, the raw data was processed as explained in the following steps and as depicted in Figure 63.

1. Raw stress-strain (dashed red trace in Figure 63) was plotted.

2. Reference points were selected to define the slope of the linear elastic region (green asterisks in Figure 63). Since test articles may vary widely, ASTM leaves the selection of these references points up to the user, as long as they are consistent across samples being compared. For the samples considered here, these reference points were selected as 40ksi and 70ksi (276MPa and 483MPa) in all configurations besides the single shear countersunk configuration, where 50ksi and 80ksi (345MPa and 483MPa) were used. These stress values ensured an appropriate linear approximation throughout all samples.

3. The chord stiffness was calculated, using the reference points described in item 2 as

$$E_{chord} = \frac{\sigma_{ref_{hi}} - \sigma_{ref_{low}}}{\varepsilon_{ref_{hi}} - \varepsilon_{ref_{low}}} \quad (71)$$

Where

E_{chord} is the chord stiffness (elastic modulus)

$\sigma_{ref_{hi}}$ is the stress at the high reference point

$\sigma_{ref_{low}}$ is the stress at the low reference point

$\varepsilon_{ref_{hi}}$ is the strain at the high reference point

$\varepsilon_{ref_{low}}$ is the strain at the low reference point

4. With the chord stiffness determined, it along with the reference points was used to plot a line through the reference points (dashed green in Figure 63).

The basic equation of a line, commonly represented as

$$y = mx + b \quad (72)$$

can be converted into relevant terms as

$$\sigma_{ref_{hi}} = E_{chord}\varepsilon_{ref_{hi}} + b \quad (73)$$

Where b is the y-intercept of the line

5. After solving for the y intercept, the correction factor, ε_{CF}, was determined by setting the right side of Equation 73 to zero to find the x-intercept of the line as

$$\varepsilon_{CF}E_{chord} + b = 0 \quad (74)$$

which simplifies to the x-intercept simplifies to

$$\varepsilon_{CF} = \frac{-b}{E_{chord}} \quad (75)$$

where the value of this x-intercept, ε_{CF}, in strain units is the value of the offset that is subtracted from the raw strain to produce the corrected strain value. In order to plot or perform calculations using corrected strain data, this correction factor must first be applied to each collected data point for the given sample. This corrected strain is easily converted into corrected displacement by multiplying the corrected strain by the bolt diameter. This strain correction is shown in the lower left corner of Figure 63.

6. The "corrected" data were plotted (bold red trace in Figure 63) by applying this correction factor to every point to shift the data such that the linear region passes through the origin. This allows for parallel comparison between samples. A solid green line plotted through the corrected data in Figure 63 confirms that the slope of the corrected linear region passes through the origin.

7. A 0.2% strain offset was used to define yield, as this is the classic method to define a departure from linear behavior. The 0.2% offset is represented as a solid blue line in Figure 63, and yield is represented with a blue asterisk.

8. A 1% strain offset was used for further comparison between samples. This same 1% offset was also used by Iarve et al to compare behavior in composite bearing

samples [87]. This 1% offset is represented by a magenta line and the corresponding 1% strain is represented by a magenta asterisk in Figure 63.

To summarize the example given in Figure 63, the 40ksi and 70ksi (276MPa and 552MPa) reference points are denoted by green asterisks, and the bearing chord stiffness (modulus) is represented by a dashed green line passing through them. The corrected data is represented by the solid red line, with the corrected stiffness represented by the solid green line. Note that the solid green line also passed through the origin as defined by the strain correction. The solid blue line represents the 0.2% offset which passes through the corresponding blue asterisk representing yield. The solid magenta line represents the 1% offset which passes through the corresponding magenta asterisk.

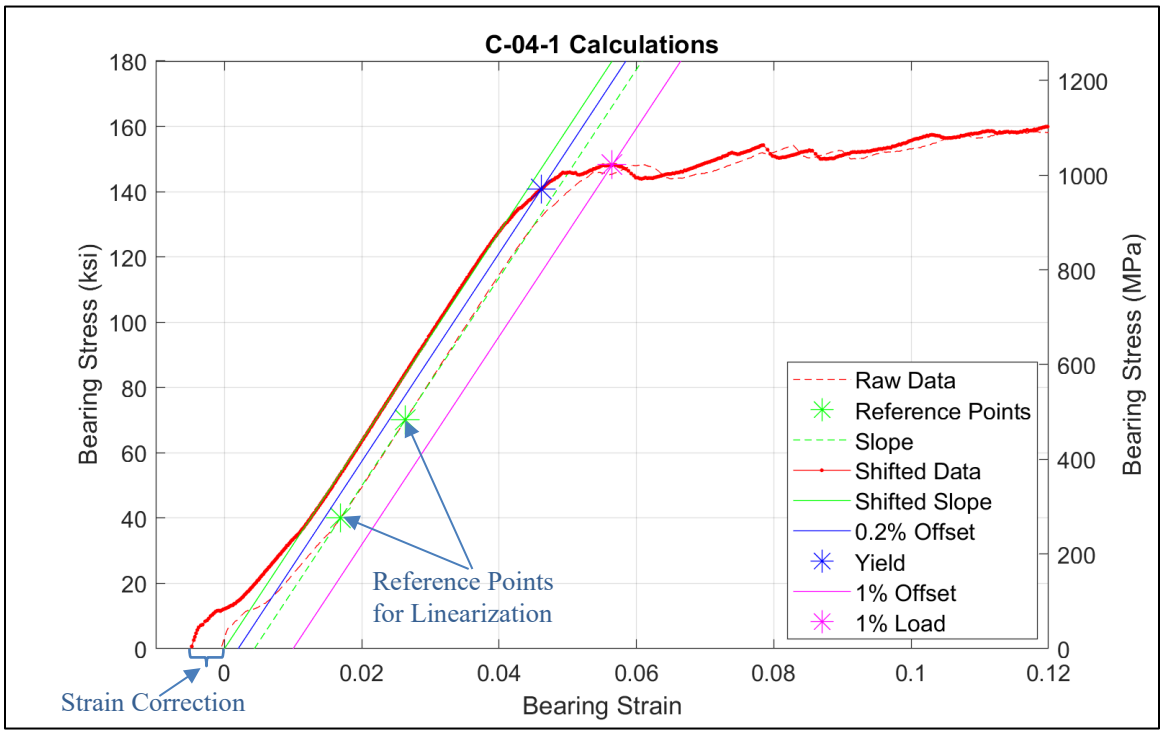

Figure 63: Sample Data Processing Example

Since values such as yield and ultimate stress are point values, another value was desired that could be used to compare samples throughout damage and failure. Strain energy is the most common method for portraying this. Strain energy presented here is defined as the area under the load-displacement curve. Strain energy density is defined as the area under the stress-strain curve. Since each sample has a unique nonlinearity at loading and the samples were not fully fractured, a range over which to integrate had to be established for each configuration. Those bounds were established based on the following strains in each configuration as:

- 9-Ply Double Shear: 1%-30% strain
- 18-Ply Double Shear: 1%-12% strain
- 18-Ply Single Shear Protruding: 1%-30% strain
- 18-Ply Single Shear Countersunk: 1%-25% strain

While lower bounds were established to avoid differences in loading slack, the upper bounds were established to avoid introducing large variation from failure late in the hole elongation of each sample. In other words, after a sample had failed, it still maintained some load carrying capacity, but this behavior was erratic. Including those data would reflect an artificially high strain energy and would complicate comparison between samples. Areas were calculated using the MatLab trapezoidal integral approximation. An example of the strain energy density for the 18-Ply double shear configuration is shown in Figure 64. As defined above, the strain energy in this configuration is calculated between 1% and 12% strain.

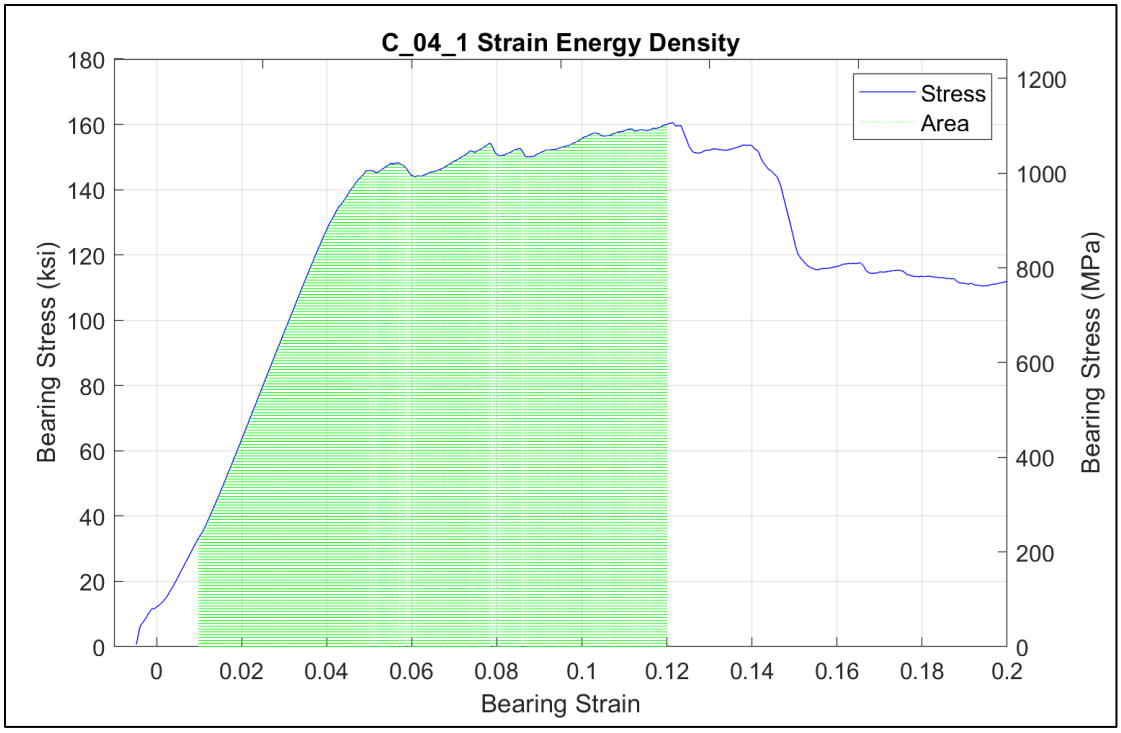

Figure 64: Strain Energy Density Example

3.10 Cyclic Fatigue Experimental Methodology

The fatigue portion of this study employed methods similar to the quasi-static experiments. However, due to material and test equipment limitations, only 18-ply double shear and 18-ply single shear protruding head samples were considered. The Hi-Lok pins were also employed for the fatigue study and were torqued in the same fashion. Load, hole elongation, head displacement, and time were recorded as described in section 3.9.1.

All fatigue samples were loaded in sinusoidal tension-tension loading. This enabled the best comparison between the fatigue samples and the monotonic samples which were only loaded in tension. In effect, only one side of the bearing hole is loaded. Loading in tension versus compression prevents buckling instability in the system. A load

rate of 1Hz was employed. This rate was targeted so the tests would run in an efficient amount of time while also maintaining a relatively slow load rate.

Preliminary samples were loaded sinusoidally at 1Hz by setting the peak tensile load to 85% of the average maximum quasi-static load determined in the full failure monotonically loaded samples for each given configuration. For example, the peak fatigue load for the 18-ply double shear control samples was determined based on the average maximum load of the control monotonic full failure samples. The minimum load was set to 100 lbf. This was a sufficiently low load to consider the joint virtually unloaded. A load near zero was avoided so that slack in the bolted joint was not reintroduced during each cycle. This also prevented compressive loading in the case that the controller overshot the commanded value. An example sinusoidal loading from this research is pictured in Figure 65.

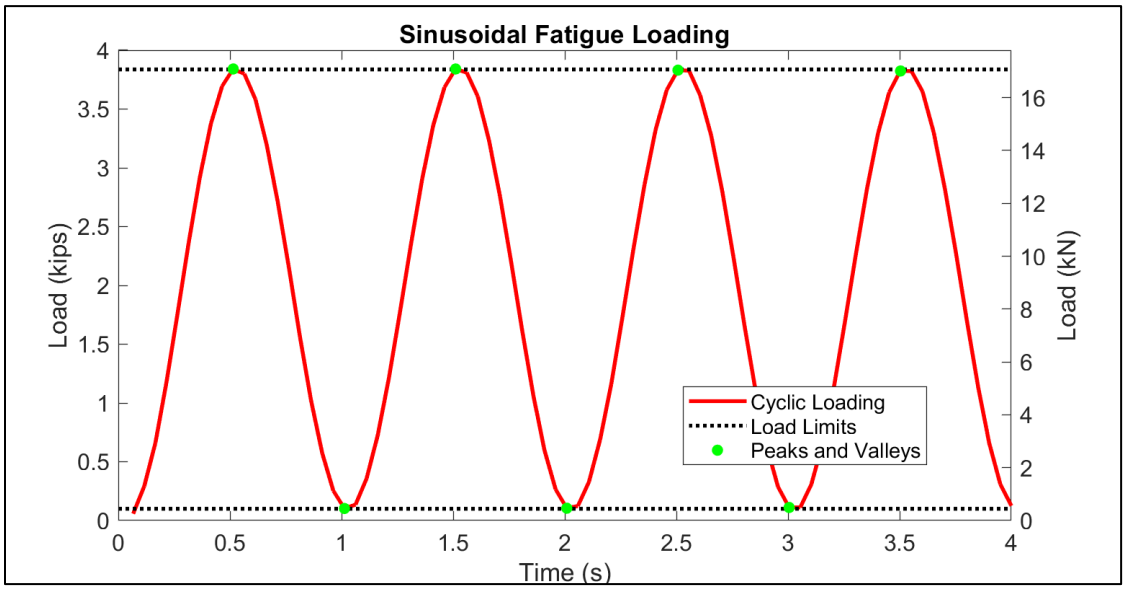

Figure 65: Sinusoidal Fatigue Loading Example

The MTS built-in peak-valley compensation (PVC) was employed to keep the actual peak (load at the crest of the sinusoid) and valley (load at the trough of the

sinusoid) values as close as possible to the commanded values. It was observed that 10 to 20 cycles were usually required for the peak-valley compensation to become effective. Load, displacement, hole elongation (via extension gauge), and cycle count were recorded. In most cases, the values were recorded only at peaks and valleys using MTS built-in peak-valley acquisition to limit the size of the data and post processing time. These peaks and valleys are marked with green circles in Figure 65. A few of the low cycle count samples were recorded at 10 Hz for demonstration purposes. These preliminary samples were allowed to run until a target hole elongation was reached. This target hole elongation was used instead of allowing complete fracture of the hole so that the fiber level failure phenomena could be compared with the failure of the quasi-static samples. After the stop criterion was met, the sample was unloaded at 100lbf (445N) per second.

Due to test time constraints and limited sample quantities, an accelerated step test method based on publications by Maxwell and Nicholas was adopted for the majority of the fatigue samples. In order to use test time most efficiently, a block (step length) of $n = 1000$ cycles was selected. For each configuration, the first step began with the peak load at 85% of average maximum of the full failure quasi-static samples. Then, for each subsequent block, the step was increased by 2.5%. This work verified previous behavior observed in the Composite Airframe Life Extension program that the IM7 showed sensitivity to load rate. Thus, load steps were programmed out to 125% of the average maximum quasi-static load. Figure 66 shows the commanded peak load for this step method graphically. In this load scenario, the load was still applied sinusoidally as pictured in Figure 65.

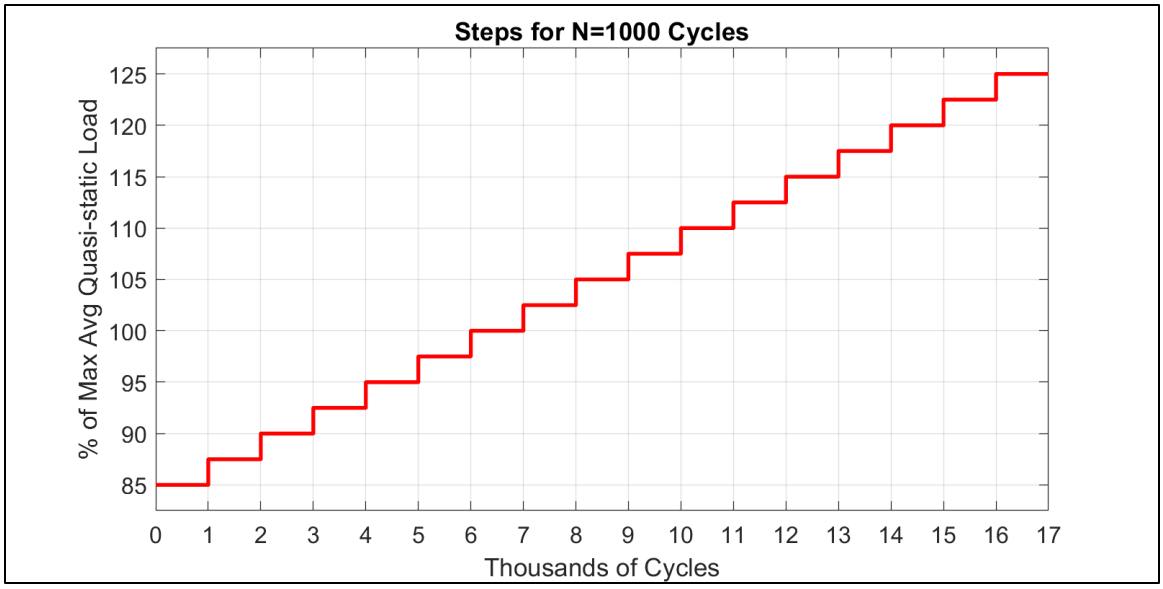

Figure 66: Steps for $n = 1000$ cycles

For this study, a test was considered relevant if it completed at least one full block and 20 cycles of the block in which the stop criterion was met.

3.10.1 Cyclic Property Analysis

After the stop criterion was met in the accelerated step method, an effective stress for $n = 1000$ cycles could be calculated. Loads were converted to stresses using the standard method discussed in section 3.9.3 Quasi-Static Mechanical Property Analysis. The effective fatigue stress or "Fatigue Limit Stress" (FLS) as preferred by Nicholas was calculated using a linear interpolation as defined by Nicholas where [86],

$$\sigma_e = \sigma_0 + \Delta\sigma\left(\frac{N_{fail}}{N_{life}}\right) \quad (76)$$

where

- σ_e is the Fatigue Limit Stress for $n = 1000$
- σ_0 is the stress for the block in which the failure criterion is met

- $\Delta\sigma$ is the increase in stress after each block is complete (2.5% of the average maximum quasi-static load for this study)
- N_{fail} is the number of cycles complete in the block in which the failure criterion was met
- N_{life} is the assigned cycle count being investigated ($n = 1000$ here)

3.11 Statistical Analysis

It was important to demonstrate how conclusive the experimental results were. In order to better understand the results, statistical analysis was performed on both the quasi-static experimentation and the cyclic fatigue experimentation. In order to compare data, for each mean the sample standard deviation, sample size, and a 95% confidence interval are presented. The confidence interval was calculated for each mean using Equation 66. The difference in means is shown in the units of the two means and then is shown as a percentage of the reference mean. The reference means are those of the control samples in all cases except where the shank-only hybrid is compared to the full hybrid. In that case, the shank-only means are the reference.

In order to draw conclusions from data, means were compared to test for statistical significance. One cannot simply calculate two means and begin to draw conclusions. The variance in each sample set influences what conclusions if any can be drawn from given data. If error in either sample set is exceptionally large compared to difference in means, the difference may not be statistically significant. Statistical significance was tested using a two-tailed Student's t-distribution. This assumes that the error values associated with means are different. "Two-tailed" means the test checks for

significance in the case that either of the two means being compared is larger. Thus, the null and alternative hypotheses are

$$H_0: \mu_1 = \mu_2$$
$$H_a: \mu_1 \neq \mu_2 \quad (77)$$

Where μ is the mean of a probability distribution

The test statistic for a difference of means with difference sample size and variance is defined as

$$t_0 = \frac{\bar{x}_1 - \bar{x}_2}{\sqrt{\frac{s_1^2}{n_1} + \frac{s_2^2}{n_2}}} \quad (78)$$

$\bar{x}$ is the sample mean

S is the sample standard deviation

n is the number of samples

Since this value does not exactly follow a t-distribution, a close approximation is found by calculating the degrees of freedom as

$$\mathrm{v} = \frac{\left(\frac{s_1^2}{n_1} + \frac{s_2^2}{n_2}\right)^2}{\frac{\left(\frac{s_1^2}{n_1}\right)^2}{n_1 - 1} + \frac{\left(\frac{s_2^2}{n_2}\right)^2}{n_2 - 1}} \quad (79)$$

t was calculated using Excel as a function of the degrees of freedom and the significance as

$$t = t_{(1-\alpha/2,\mathrm{v})} \quad (80)$$

By comparing the test statistic, t_0, to the value of the t-distribution, one can decide if the two means are significantly different. Here, "significant" means there is statistical evidence to support the conclusion. If $|t_0| < t$, then the null cannot be rejected meaning there is not enough statistical evidence to prove that the means are different. If $|t_0| > t$ then the null hypothesis is rejected, and the data contain enough evidence to conclude that the means are statistically different [106].

In order to test significance of factors, data for the controlled and nuisance factors for each sample were entered in to JMP statistical analysis software [108]. Least squares effects test models were performed. Conclusions drawn here are based on assumptions of normality and constant variance. Normality was verified using the Shapiro-Wilk test. Plots of individual effects versus each response gave no indication that the data departed from the constant variance assumption.

3.12 Post-Test Characterization

After testing was complete, the samples were sectioned in the 0° direction through the hole, so that the damage through the thickness of the material could be investigated to understand the failure mechanisms that occurred during testing. A subset of samples was sectioned through the hole in the 45° direction for additional analysis. For samples analyzed with a scanning electron microscope (SEM), the samples were also sectioned in the 0° direction to allow them to fit in the SEM cell. Figure 67 depicts the sample sectioning used for this work. A detailed drawing is attached in Appendix L.

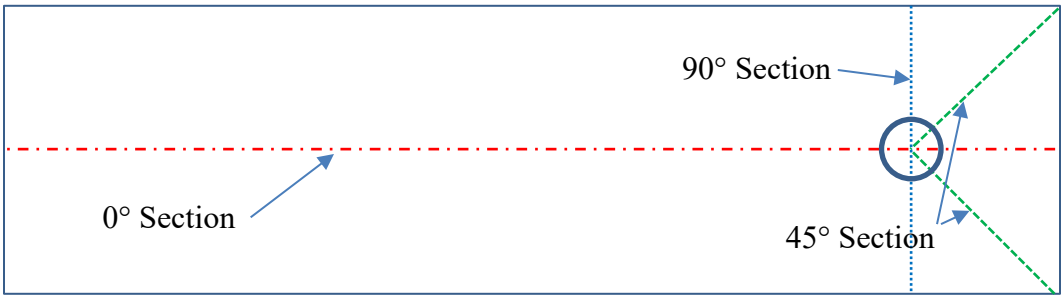

Figure 67: Coupon Sectioning

After sectioning, the samples were investigated using a Zeiss optical microscope using 1x and 0.625x lenses. This allowed for analysis of behavior at the ply and fiber tow level. While optical microscopy provided characterization through the thickness of the layup, the resolution was not sufficient to capture behavior at the individual fiber level. To characterize behavior at the fiber level, a scanning electron microscope (SEM) was employed. The samples were clamped into a dedicated SEM fixture which was lined with conductive tape to prevent charging. The SEM and fixture are shown in Figure 68.

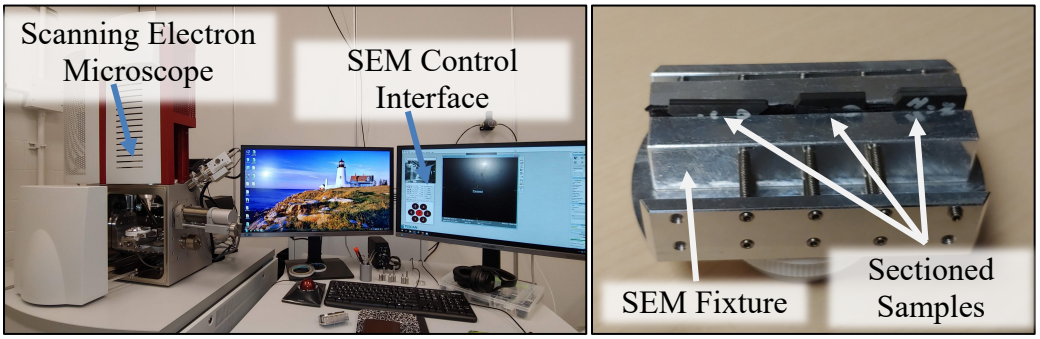

Figure 68: A) Scanning Electron Microscope B) Specimens in SEM Fixture

IV. Computational Methodology

Finite element modeling for this research analyzed control and hybrid layups in 9-ply and 18-ply double shear configurations using Abaqus software by Dassault Systèmes. Work was primarily performed in Abaqus/CAE (Complete Abaqus Environment) [3]. Modeling was performed using U.S. (imperial) units to match the units employed in the experimental study and those commonly employed by AFRL in similar work. Because of the complexities of the progressive failure problem being evaluated, explicit simulation was employed in a stacked, layerwise configuration. The coupons were modeled to a length of 3.5in (8.9cm). This modeled the entire coupon, except the grip section. Similarly, the experimental fixture was modeled except for the grip portion. Modeling the grip portions of the fixture and coupon would unnecessarily increase the number of elements and contact interaction complexity. Since the damage in the experimental samples was focused very near the bearing hole and no damage was noted in the transition region, the transition was not modeled to avoid unnecessary complexity. The configuration of the finite element model is depicted in Figure 69. Details will be explained as the chapter progresses. Figure 70 depicts a close-up section view of the coupon as it interacts with the fixture and bolt. Note that, in keeping with the layerwise modeling technique, each layer of the coupon is modeled as a separate part.

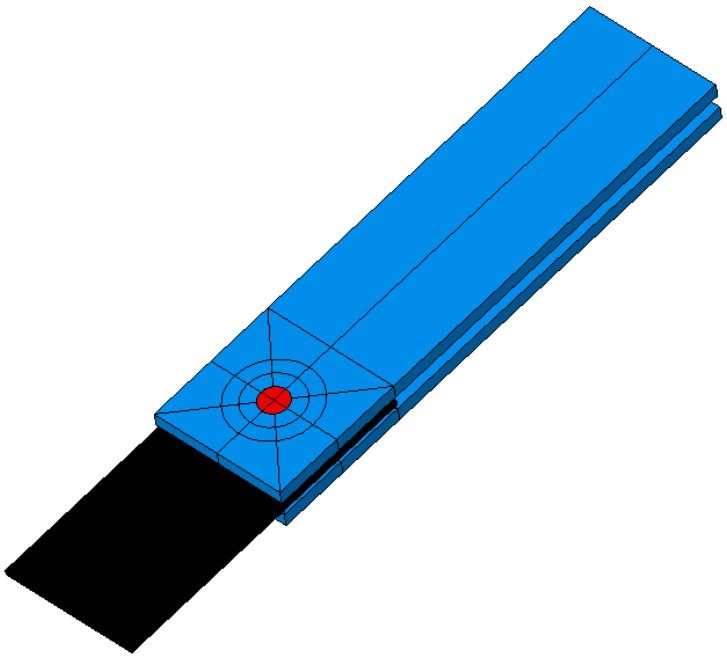

Figure 69: Finite Element Model Configuration

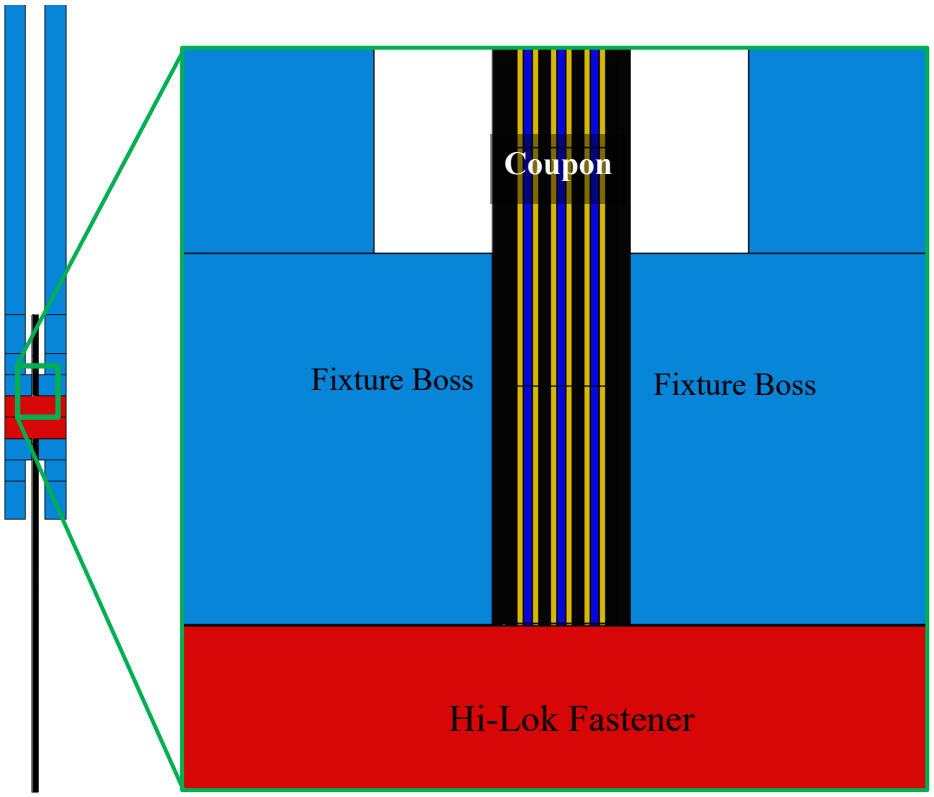

Figure 70: Finite Element Model Configuration-Section View

In order to limit initial overclosures (surface intersections), the bearing hole diameter was modeled at the largest allowable tolerance 0.3135in (7.963mm), and the bolt diameter was modeled at the lowest allowable tolerance 0.3115in (7.912mm). Initial overclosures were also prevented by matching the element size of the bolt and coupon bearing surface as close as allowed by the fiber aligned mesh configuration.

4.1 Bolt and Fixture Representation

4.1.1 Hi-Lok Bolt Representation

When looking to represent the Hi-Lok bolt, the only information provided on the Hi-Lok fasteners by manufacturer Lisi Aerospace are a tensile strength of 160ksi (1100MPa) and a shear strength of 95ksi (660MPa) [109], [110]. This information alone is not sufficient to construct a simple bilinear elastic-plastic model. In many cases, authors simply model the fastener as purely elastic with no failure criteria with the assumption that the Hi-Lok is much stronger than the parts being fastened [111]. However, due to the metal included in the hybrid and the high loads seen in experimentation, it was desirable to be able to detect localized plasticity in the fastener. The Hi-Lok product specifications also show that the material complies with the following standards: AMS6415, AMS6349 or AMS6382, and AMS6322. Here “AMS” refers to Aerospace Material Specifications, which is a set of standards maintained by the Society of Automotive Engineers (SAE). This cross references to the American Iron and Steel Institute (AISI) steel alloy designated AISI-4340. Detailed materials properties that closely match the tensile strength specified by the Hi-Lok specifications are available from MatWeb [112]. A complete list of materials properties is available in Appendix H.

Since tabular stress-strain data are not available, a bilinear model was developed based on the yield stress, elastic modulus, ultimate tensile strength, and elongation at break. Since fracture was not expected in the bolt, damage evolution and element deletion were not considered for this material.

The evolution of the bolt model is shown in Figure 71. The head and threaded portion of the bolt were not modeled to avoid unnecessary complexity. In Figure 71A only the solid portion of the bolt pictured was employed in the model. The bolt was partitioned and then seeded at 0.025in (0.64mm) to closely match the node spacing of the coupon to prevent excess penetration which would complicate the contact calculation. The partitioning is depicted in Figure 71B. The final bolt mesh is shown in Figure 71C. The bolt was modeled using 2940 hexahedral coupled temperature-displacement elements (C3D8T) with a 3D stress behavior and second order accuracy. A schematic of this element is depicted in Figure 72. Each node has three translational degrees of freedom as shown at node 6. The temperature-displacement elements were employed so that a temperature step could be used to apply a tensile load to the bolt (discussed further under Boundary Conditions and Loading-section 4.6).

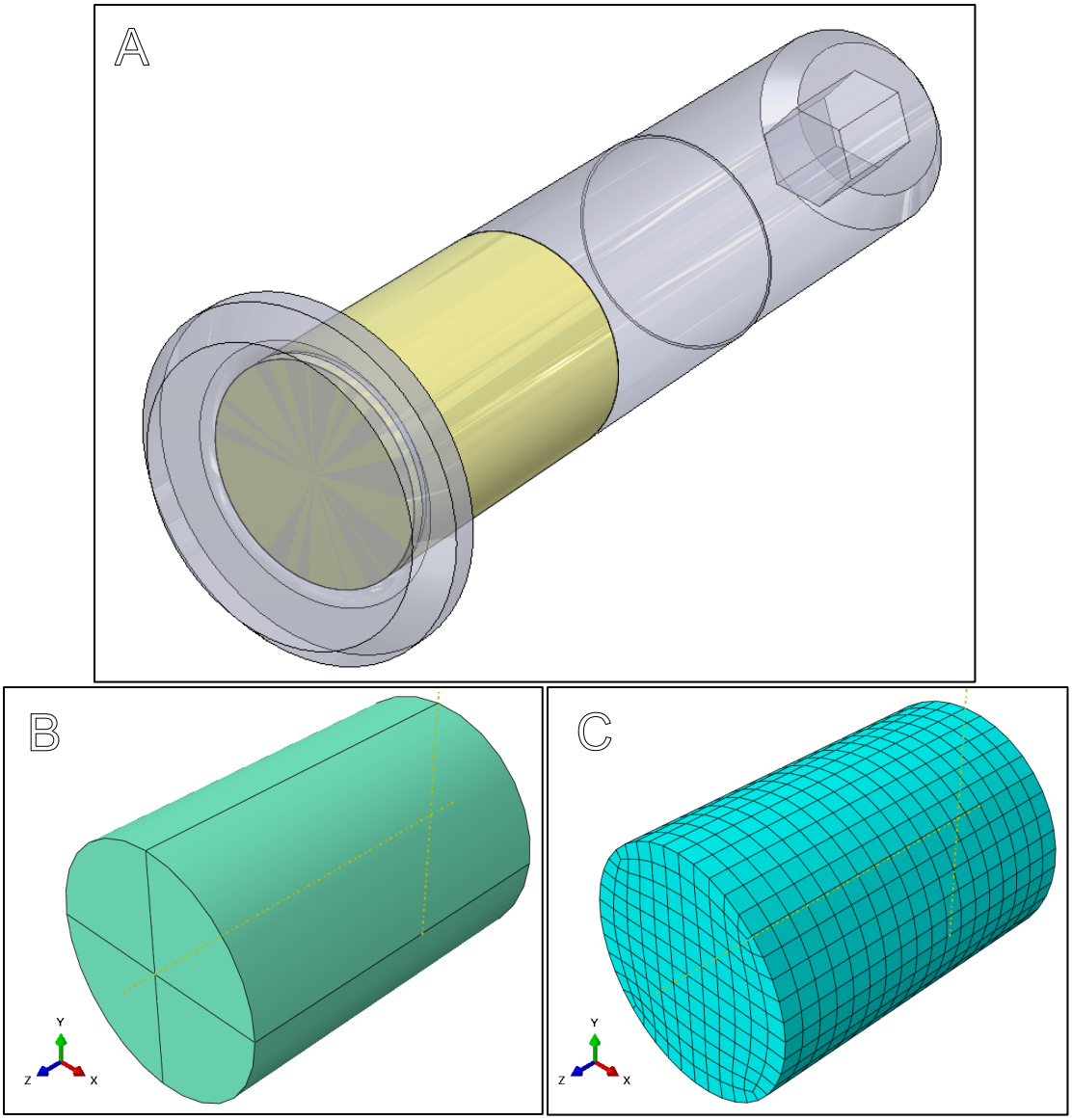

Figure 71: A) Bolt Partition B) Bolt Mesh

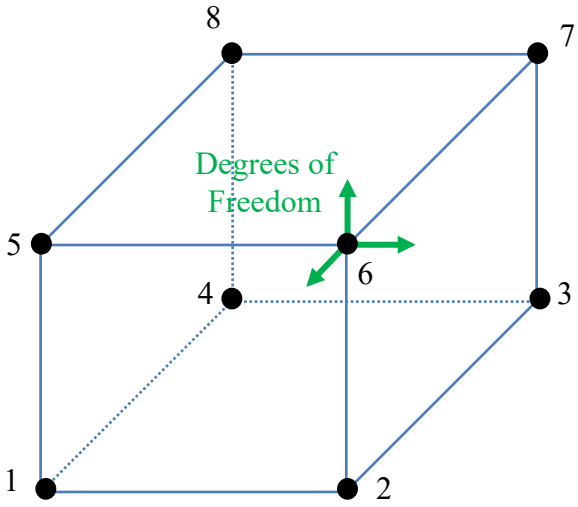

Figure 72: Schematic of 8 Node Temperature-Displacement 3D Stress Element (SC8R) (Adapted from Buentello [47]**)**

Preliminary models did not include the fixture, but rather modeled only the bolt and bosses. This however, proved to be too stiff of a constraint and led to premature failure prediction. Thus, the fixture was added and represented using 682 3D stress elements (see Figure 72)with reduced integration and second order accuracy. The 17-4PH stainless steel was represented using an elastic-plastic bilinear model. Since no plasticity or damage was expected in the fixture, it was modeled using as few elements as possible, and damage evolution and element deletion were not considered. Plasticity in the fixtures was never noted in experimentation or computation. The fixture partition and mesh are shown in Figure 73.

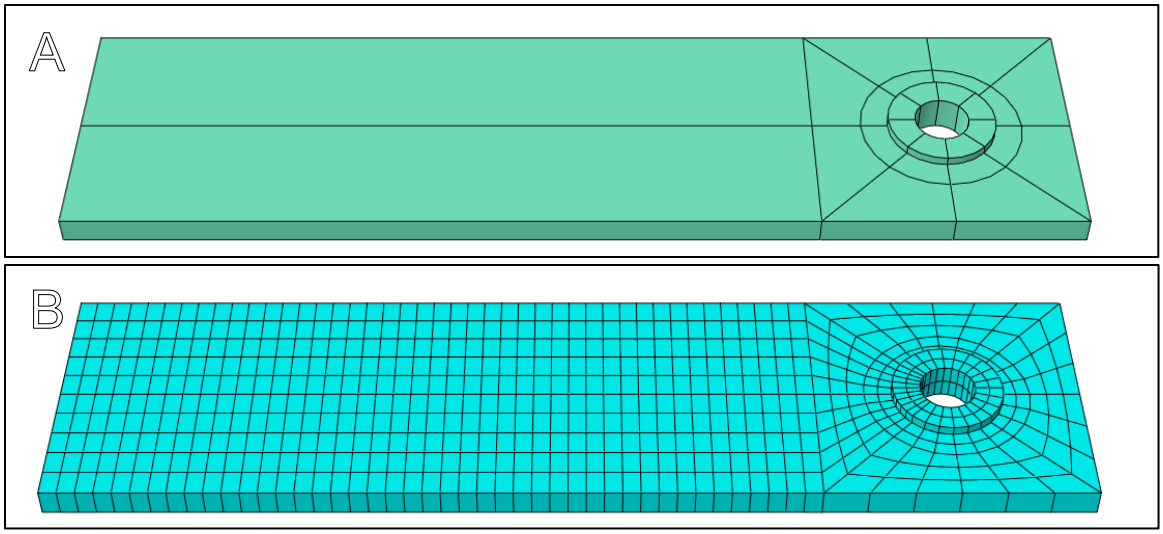

Figure 73: Fixture A) Partition B) Mesh

The interaction between the bolt and the two sides of the fixture was represented by tying the nodes on the circumference of each bolt end to the circumference of the hole on the outside of each of the fixture halves as shown in Figure 74. The bolt nodes were defined as master, and the fixture nodes were defined as slave nodes in the tie relationship.

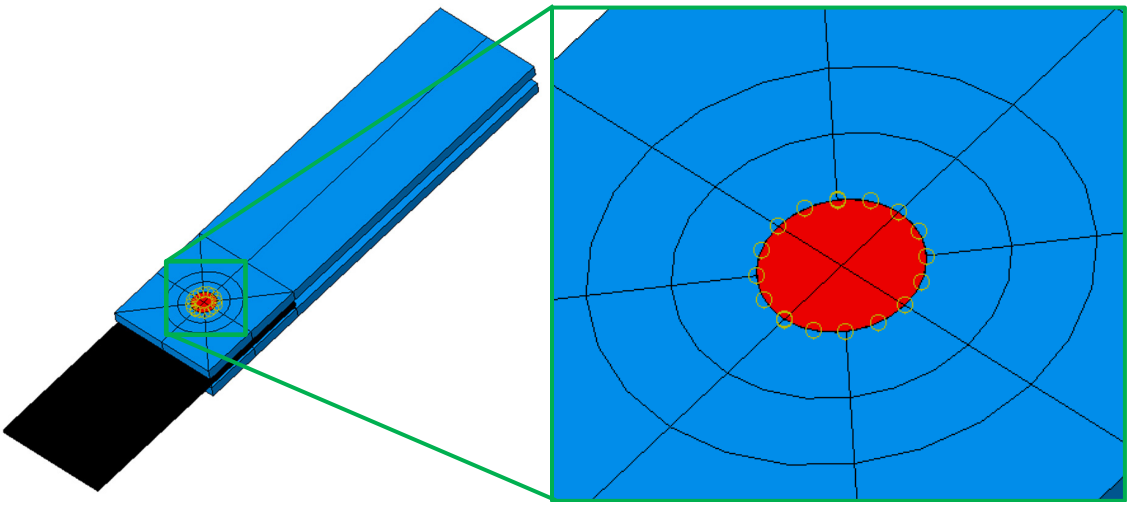

Figure 74: Bolt to Fixture Ties

4.2 Composite Representation

The composite material was represented using a layerwise technique, meaning that each ply is represented as a distinct part modeled using at least one layer of elements through the thickness. In this case, for model efficiency, a single element was used to represent the thickness of a composite ply. Because Hashin failure criteria were to be employed, the use of continuum shell elements was required, since 3D stress elements are not compatible with Hashin Failure in the native Abaqus environment. Figure 75 shows how a continuum shell element compares with a conventional shell element. While a node in a conventional shell element has both translational and rotational degrees of freedom, the thickness of the continuum shell element has a representative finite thickness. This means that it has nodes representing each face of the part. These nodes only have translational degrees of freedom.

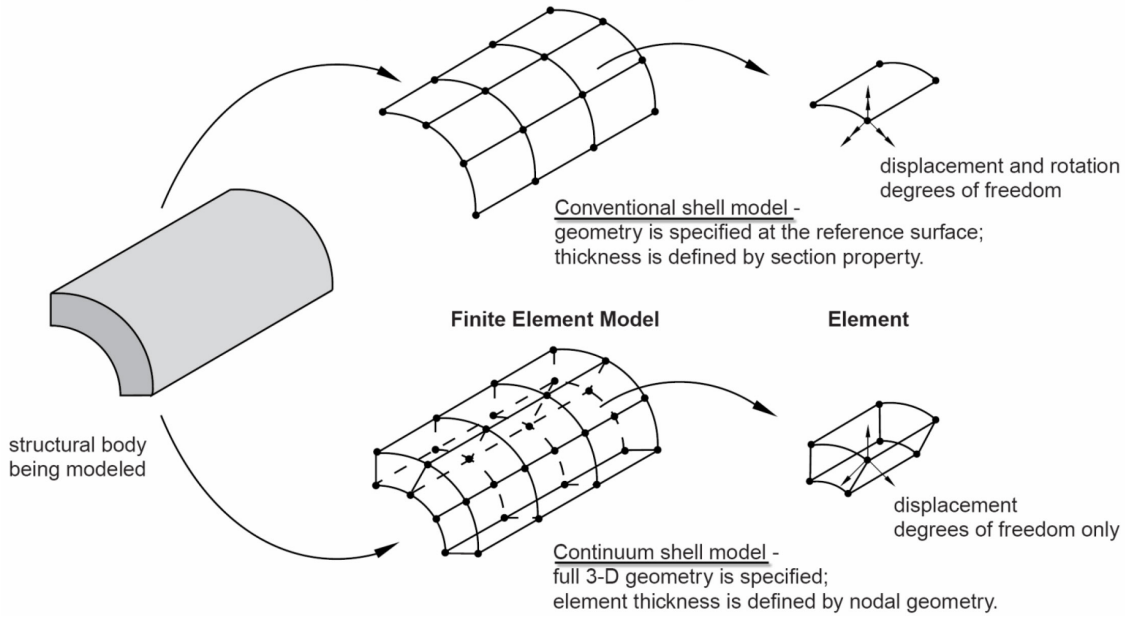

Figure 75: Continuum Shell v. Shell Elements [46]

Continuum shell elements function similarly to 3D stress elements, but they employ First -order Shear Deformation Theory (FSDT) constraints. These constraints are common in composite shell theory and assume that: i) a line normal to the surface drawn through the thickness can rotate but will remain straight and ii) the change in a shell thickness as it undergoes deformation is negligible [113]. A schematic of an 8-node continuum shell element (SC8R) is shown in Figure 76. Each node had three translational (displacement) degrees of freedom as indicated on node 6. The default thickness direction (normal direction) is also identified.

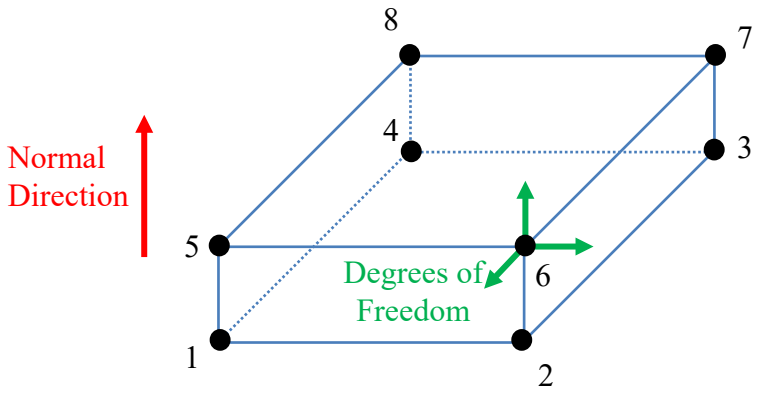

Figure 76: Schematic of 8 Node Continuum Shell Element (SC8R) (Adapted from Dassault Systèmes [114])

Based on experimental results, the thickness of a ply in a layup was modeled at 0.0051in (0.13mm). A fiber aligned mesh was developed to properly model the anisotropy of the unidirectional composite while minimizing the number of elements and nodes.

4.2.1 Composite Mesh Arrangement

In order to investigate the need for a fiber aligned mesh in this study, three models were evaluated in the following configurations: fiber aligned, concentric, and misaligned. The three mesh arrangements considered are shown in Figure 77. While a misaligned configuration would not generally be considered, it is presented here for comparison to demonstrate the utility of a proper fiber aligned mesh and the problems posed by using a concentric mesh to represent a unidirectional composite. Each used a representative element size at the hole of 0.025in (.064mm) and was based on a 45° fiber alignment in a single ply of unidirectional IM7/977-3.

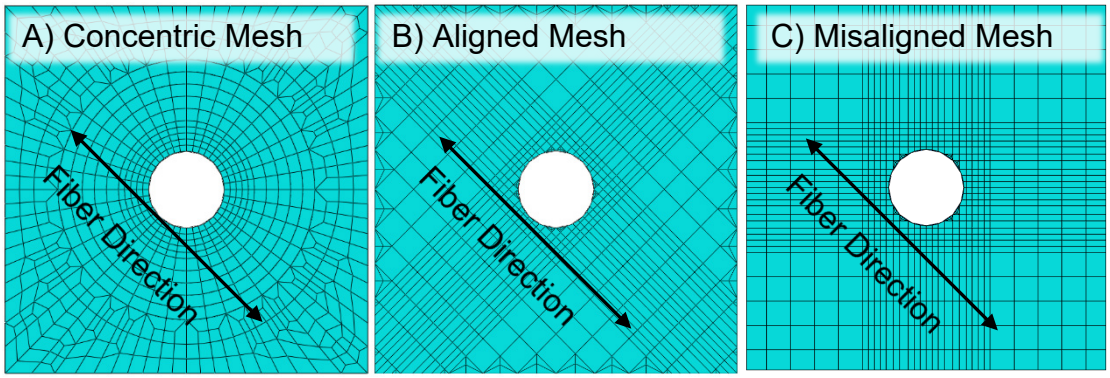

Figure 77: Fiber Aligned Mesh Study A) Concentric B) Fiber Aligned C) Misaligned

The material was represented using Hashin criteria for failure initiation and a linear displacement failure evolution model. In this case, the best mesh would be sensitive to damage near the hole in the correct direction. In order to prevent masking damage initiation, the fiber aligned mesh study was conducted using an open-hole arrangement as seen in Figure 78. With one end constrained using a clamped boundary condition, a tensile displacement of 0.030in (0.76mm) was commanded as a linear ramp

over a unit time step. The displacement symbols appear non-uniform because the fiber aligned mesh makes the node spacing vary. While this research employed plies in ±45°, 90°, and 0° directions, this 45° fiber direction combined with the open hole load scenario was the most effective model to demonstrate a fiber aligned mesh. This is because it not only required the mesh to locate the initial stress concentration at the sides of the hole, it also had to define subsequent failure in the correct direction as the crack progressed away from the hole.

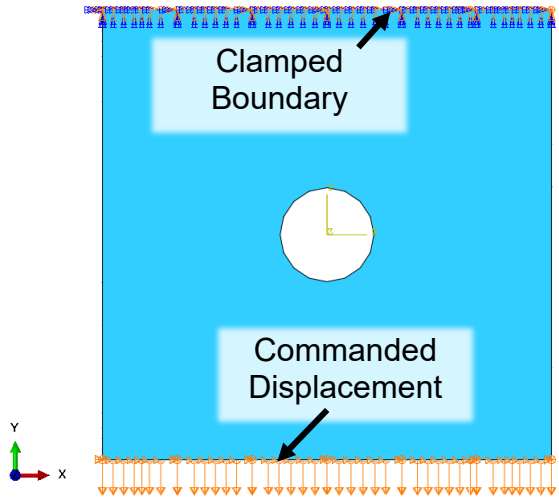

Figure 78: Fiber Aligned Mesh Study Boundary Conditions

Figure 79 depicts an open hole sample comprised of all ±45° plies with a 45° ply on the face. This is a textbook case of what is expected to happen in a 45° ply near a hole. The failure should begin at the stress concentration at the sides of the hole, and then progress away from the hole as matrix cracking.

Figure 80 shows the different models as matrix tension damage begins. When compared with Figure 79, one would expect to see damage in the models begin at the sides of the hole and then progress along the fiber direction. Figure 80A represents the

45° aligned fibers using a conventional concentric mesh that would generally be employed in an isotropic material. Figure 80B represents the material with a mesh that is aligned with the 45° fiber direction. Figure 80C presents the misaligned configuration with a 45° fiber direction and a 0°/90° aligned mesh.

Each model configuration predicts the damage onset at the same simulation time and in the expected location on the side of the hole. In other words, in each case the stress concentration at the sides of the hole is represented well. However, the concentric mesh does not correctly predict the matrix cracking in the correct direction. While damage should propagate in the fiber direction, the concentric mesh shows the damage propagating laterally away from the hole like one would expect in an isotropic material. The fiber aligned mesh accurately represents both the initial stress concentration and also the matrix cracking in the fiber direction. The misaligned mesh generally provides the same result as the concentric mesh.

Figure 79: Expected Failure in 45° Ply

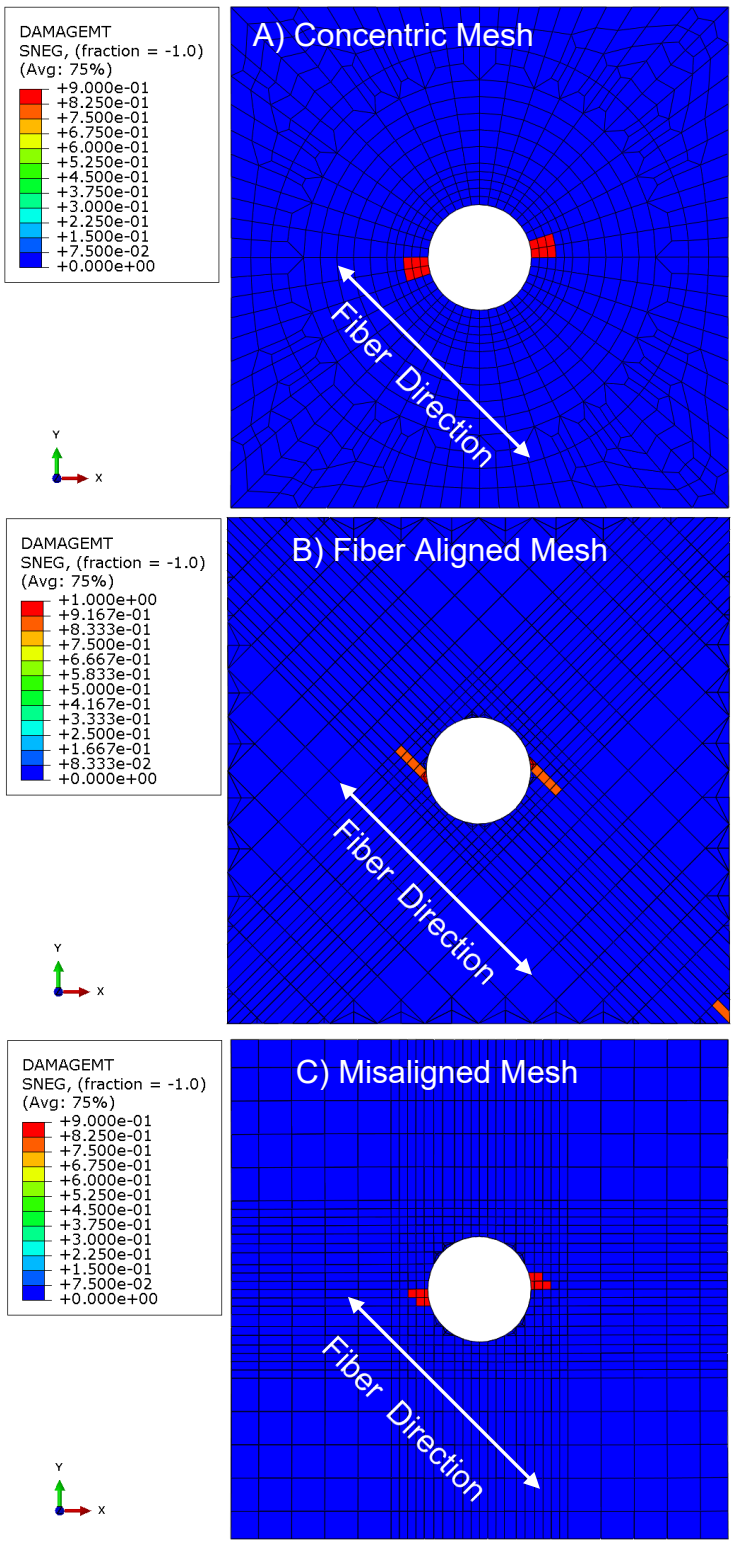

Figure 80: 45° Fiber Direction A) Concentric Mesh B) Fiber Aligned Mesh C) Misaligned Mesh

Based on this investigation, a fiber aligned mesh was employed for this work. In addition to modeling effectiveness, the fiber aligned mesh is also more intuitive for a user to interpret. Since the fiber aligned mesh was developed via face partitions, and continuum shell elements were used, a bottom up mesh was required. This was defined using the partitioned faces projected through the thickness of the material. This mesh type requires that each face of the part be associated with the mesh as a separate step.

4.2.2 Composite Convergence

To determine appropriate element size in the composite, a convergence study was performed using a 0° fiber orientation with a 0°/90° mesh alignment, with four different target dimensions for critical elements at the bearing surface. The goal of convergence was to produce the most effective mesh discretization, based on stress in critical elements, without requiring unnecessary computation time. Since the fiber aligned mesh was employed, similar convergence behavior was expected in the ±45° mesh. Since producing each fiber aligned mesh took a considerable number of man hours, convergence was conducted only on the 0°/90° mesh. The final spacing was then applied to both the 0°/90° mesh and the ±45° mesh. As with the fiber aligned mesh study, Hashin failure initiation and a linear damage evolution model were employed.

Figure 81 depicts the configuration of the convergence model. The models were loaded with a fixture that simulated a bolted configuration that consisted of two bosses with a bolt passing through the bosses and the sample. An encastre (clamped) constraint was applied to the end of the bolt and the bosses to simulate a bolted double shear configuration. Penalty contact was employed between the fixture and the sample. A

displacement was applied at the far end of the sample similar to how the coupon is loaded in the experimental procedure.

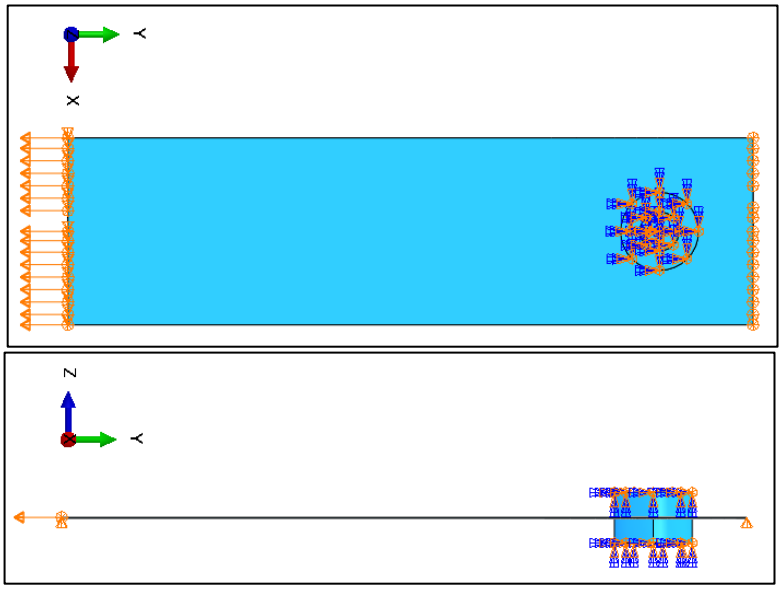

Figure 81: Composite Convergence Model A) X-Y Plane View B) Y-Z Plane

Due to requirements of developing a fiber aligned mesh and the associated geometry, the size of each element cannot be exactly the same. Thus, mesh refinement for convergence cannot be based solely on element size. Also, the size of the elements near the bearing surface is much more critical than the size of the elements far from the hole. This means that convergence should not be based on the number of elements. Thus, the best measure for convergence is the critical element spacing near the hole. In other words, this described how far apart the partition lines are that follow the fiber direction. This spacing was largely driven by how the fiber aligned mesh fit around the hole. The final four values for critical element spacing that were considered were 0.0750in, 0.0500in, 0.0250in, and 0.0125in [1.91mm, 1.27mm, 0.635mm, and 0.318mm] as depicted in Figure 83.

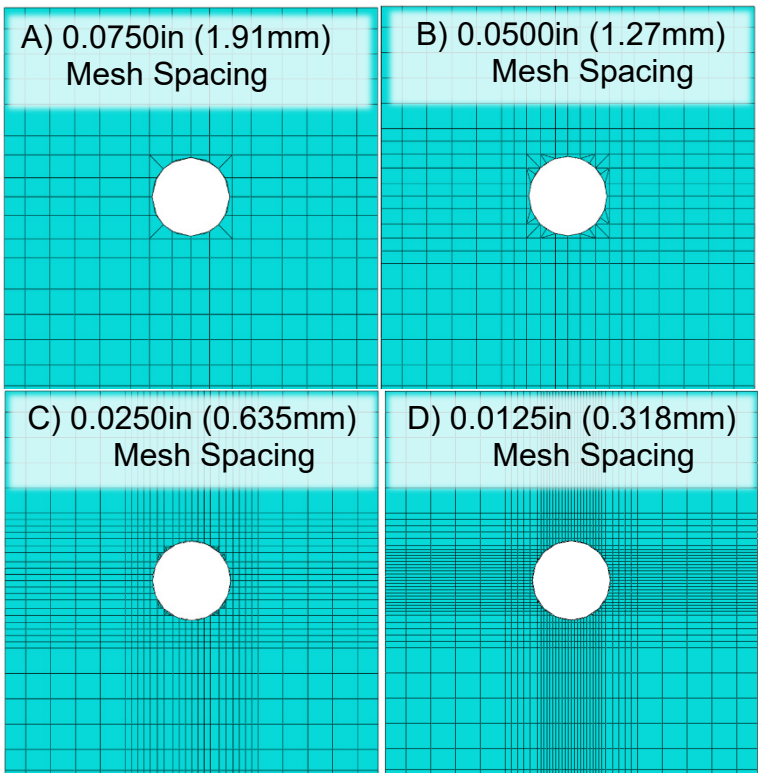

Figure 82: Fiber Aligned Meshes for Convergence
A) 0.0750in (1.91mm) B) 0.0500in (1.27mm)
C) 0.0250in (0.635mm) D) 0.0125in (0.318mm)

The main output used to determine convergence was stress in critical elements at the sides of the holes, as seen in Figure 83. In each case, the stress in these two elements was averaged at a hole elongation of 0.0200in [0.508mm].

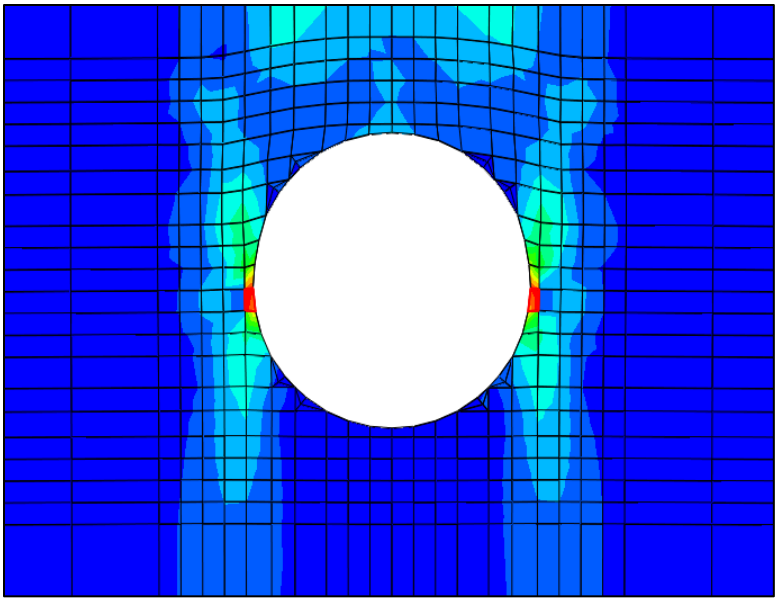

Figure 83: Composite Convergence Critical Elements

Table 7: Composite Convergence

Element Spacing (in) [mm]	Total Elements	Elapsed Time (hr:min)	Average Critical Node Stress (ksi) [MPa]	% Change In Stress
0.01250 [0.3175]	2006	6:49	352.9 [2433]	1.549%
0.02500 [0.6350]	**1286**	**1:24**	**358.4 [2471]**	**61.28%**
0.05000 [1.270]	704	0:48	222.2 [1532]	2.488%
0.07500 [1.905]	496	0:45	216.8 [1495]	

Table 7 shows the results of the convergence study. The initial mesh refinement did not produce a large change in the evaluated stress value (Table 7), but this very coarse mesh was not desirable due to spatial resolution. The final mesh refinement produced a small change in the observed stress value only 1.5%, but the computation time was increased almost five times due to the increase in the element count and the change in element characteristic length, which reduces the stable time step. The computation time was important because if this simple model consumed large amounts of

time, then a more complex laminated model would consume inordinate amounts of time and computational resources. Considering the stress calculation and run time, the optimum element spacing near the bearing hole was set to 0.02500in (0.635mm).

Composite materials properties used throughout this work were referenced from CALE II and Giles and Venkataraman [18], [115].

The interlaminar matrix region was represented using cohesive interactions. These interactions can be compared to a tie over which the user has control. The damage initiation stiffness and nominal stress values were taken from Giles and Venkataraman[115]. Damage evolution used Benzeggagh-Kenane energy criteria with a B-K exponent of 1.45. In order to prevent the interlaminar matrix and composite matrix from failing simultaneously, the interlaminar matrix fracture energy values were set to 90% of the fracture energy values of the composite matrix properties defined in CALE II [18].

4.3 Foil Representation

This section presents how the finite element representation of the foil plies was developed. First, a finite element investigation is presented that proves that the strain rate is consistent in the foil, and strain rate specific materials properties need not be considered. Then convergence of the foil is addressed. Finally, an experimentally determined elastic-plastic curve is derived from testing by Roberts [67]. This testing also proves that the stainless steel behaves similarly at a wide range of strain rates, further suggesting that strain rate dependence need not be considered in quasi-static models.

4.3.1 Foil Strain Rate Dependence

In order to study strain rate dependence in this study, a basic model of a foil was developed as depicted in Figure 84. It was assumed that the quasi-static assumption would hold throughout the simulation, but verification was desired to account for any dynamic effects that took place near the bolt. The foil was modeled with a concentric mesh in a pinned configuration. The edges of the foil were constrained in-plane to confine the damage to the bearing region.

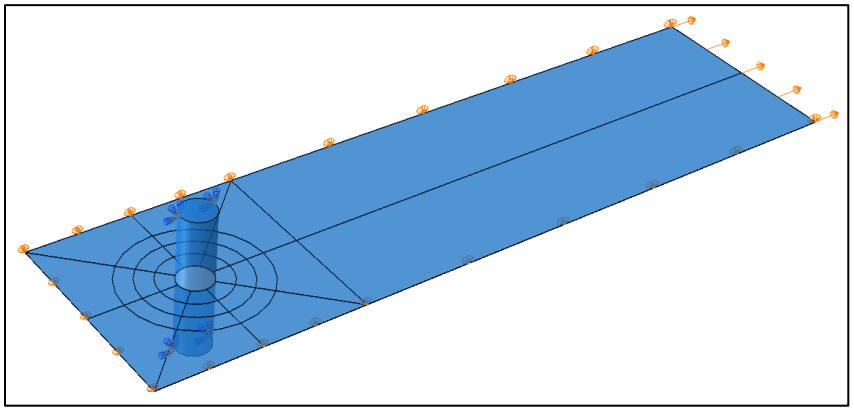

Figure 84: Foil Investigation Model

A bilinear elastic-plastic model was defined for the foil, and a bearing strain of 0.5 (50% hole elongation) was applied over a unit analytical time step. Maximum principal strains were tracked over time at three nodes deemed to have the most critical strain values as depicted in Figure 85A. Von Mises stress and equivalent plastic strain are seen in Figure 85B and Figure 85C. These contour plots correspond well to the behavior of the foil observed in preliminary pinned hybrid samples (Figure 85D). Finally, the maximum principle strain at each of the critical nodes is plotted with respect to time in Figure 86. As time progresses, the strain at the critical elements develops at a rate similar to the commanded rate of bearing strain (hole elongation). The only departure is due to the foil

sliding along the pin in the axial direction. Since the strain at the critical nodes does not vary widely over time as compared to the commanded strain rate, this enabled the decision to exclude strain rate dependence from this study.

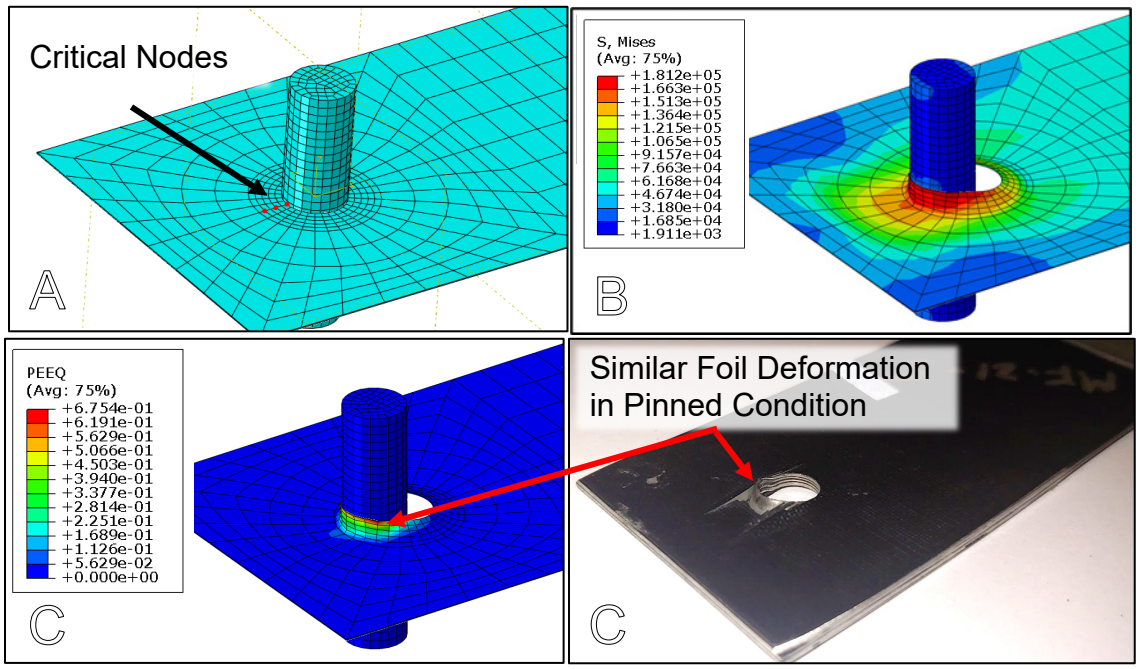

Figure 85: A) Critical Nodes B) Von Mises Stress C) Equivalent Plastic Strain D) Foil Deformation in Preliminary Pinned Sample

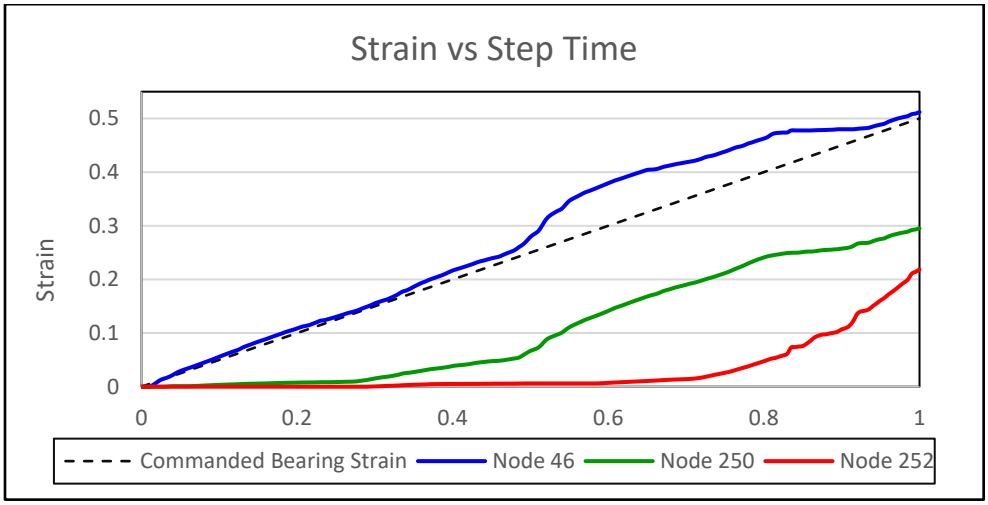

Figure 86: Strain at Critical Nodes

4.3.2 Foil Convergence

The convergence study on the foil was conducted in a similar fashion to the composite, employing the same bearing loading and boundary conditions. However, the foil used a structured mesh arranged concentrically around the hole. Criteria for convergence were peak stress and equivalent plastic strain after a displacement of 0.0200in (0.508mm).

Figure 87 shows the equivalent plastic strain in each of the meshes considered in the foil convergence study, and Table 8 lists all the results. Since refinement in the structured mesh has a more linear effect on element count, and the failure criteria for plasticity are much less intense, simulation times were not affected by mesh refinement. The final refinement to 0.0250in (0.0635mm) was selected because it produced results consistent with the previous step, and closely matched the element size selected for the composite and the bolt to optimize the contact relationships.

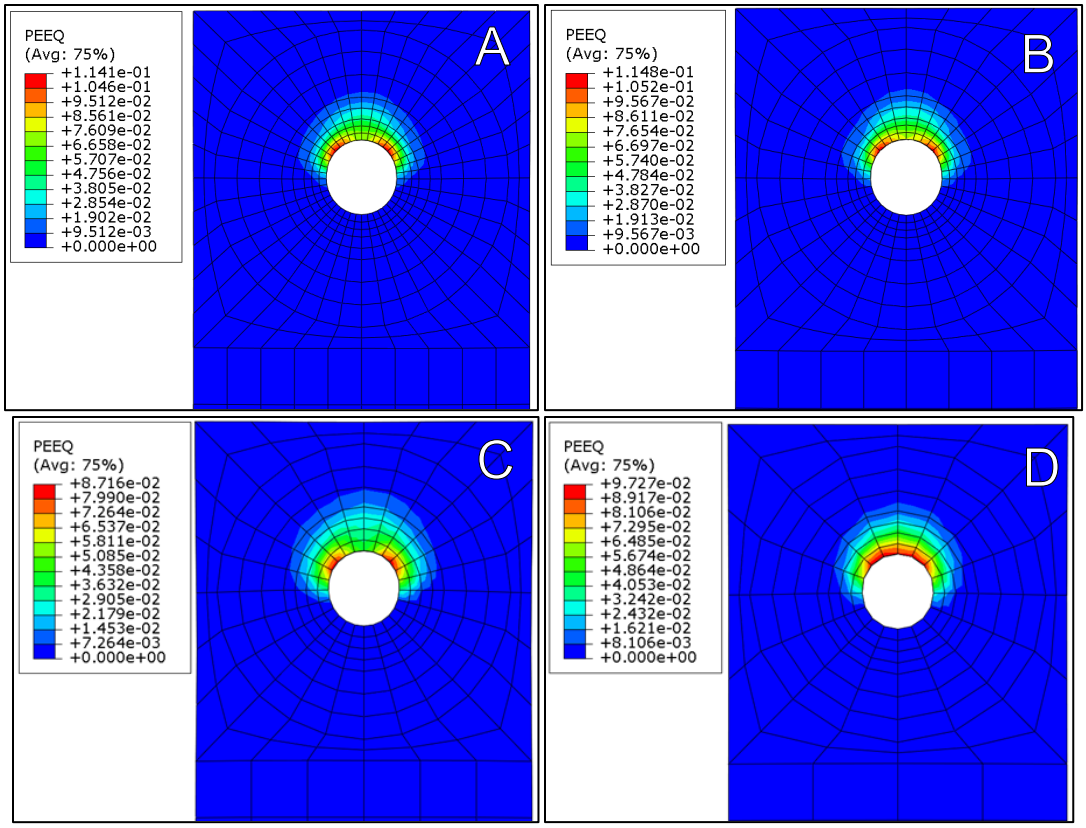

Figure 87: Foil Convergence Equivalent Plastic Stress
A) 0.0250in (0.635mm) B) 0.0310in (0.787mm)
C) 0.0410in (1.04mm) D) 0.060in (1.52mm)

Table 8: Foil Convergence

Element Size (in) [mm]	Total Elements	Elapsed Time (hr:min)	Peak Stress (ksi) [MPa]	% Change	Equivalent Plastic Strain	% Change
0.0250 [0.635]	**560**	**1:03**	**212.7 [1466]**	**0.09394%**	**0.1141**	**0.6098%**
0.0310 [0.787]	448	1:07	212.9 [1468]	5.610%	0.1148	31.71%
0.0410 [1.04]	312	0:59	201.6 [1390]	1.950%	0.08716	10.39%
0.0600 [1.52]	208	1:07	205.6 [1418		0.09727	

4.3.3 Final Foil Representation

The foils were represented using coupled temperature-displacement elements with 3D stress (see Figure 72) behavior, reduced integration, and second order accuracy. The temperature-displacement element type allowed for a temperature step to be assigned to model the cure induced thermal stresses. The employment of the temperature-displacement element to model cure induced thermal stress is discussed in Boundary Conditions and Loading. The part was partitioned concentrically about the hole and then meshed with a structured mesh as see in Figure 88.

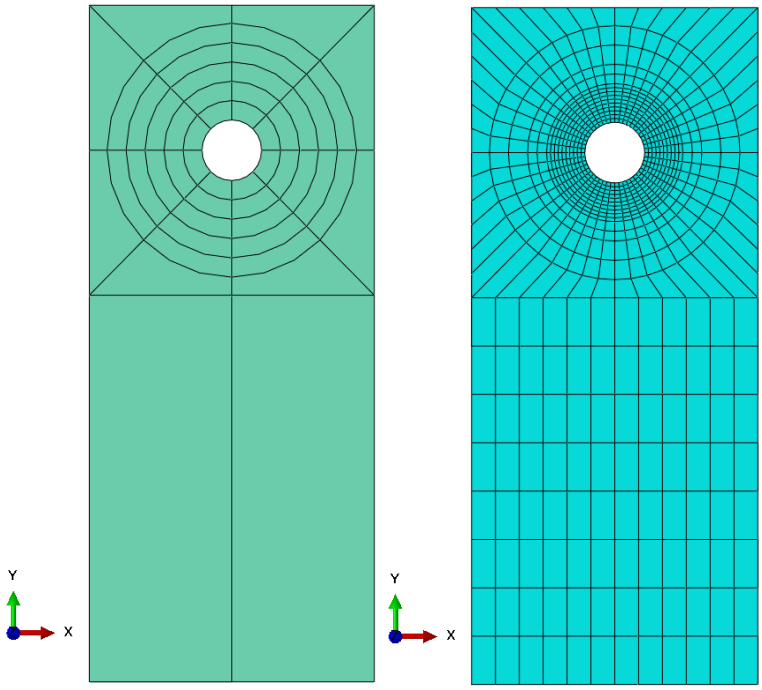

Figure 88: A) Foil Partition B) Foil Mesh

It was hypothesized that published values for 301 stainless steel may not be adequate to describe the foil due to thinness and processing. A more defined elastic-plastic curve was also desired. Thus, computation considered both a bilinear elastic plastic model and an

experimentally determined elastic-plastic curve. Experimentation was performed by Roberts and published by Roberts and Sherburne et al [67], [116], [117].

To get the most representative results and to use available material, tests were performed on foils that had been through the surface preparation process. Tests were performed in accordance with ASTM E345. This test employs a "dog bone" shaped sample with a 0.500in (12.7mm) gauge width which is loaded in tension. These displacement rates listed in Table 9 were selected to study target strain rates expected in bearing experimentation. Table 9 lists the displacement rates at which foil tensile tests were conducted and the estimated strain rate produced by the given displacement rate.

Table 9: Foil Experimental Displacement and Target Strain Rates

Displacement Rate (in/min) [mm/min]	Displacement Rate (in/s) [mm/s]	Estimated Strain Rate ($1/s$)
0.5265 [13.37]	0.008775 [0.2223]	0.0027
0.05265 [1.337]	0.0008775 [.02223]	0.00027
0.02633 [0.6687]	0.00043875 [.01114]	0.000135
0.005265 [0.1337]	0.00008775 [0.002223]	0.000027

The results of the foil testing are listed in Table 10 and the statistical analysis of the data are listed in Table 11. Stress-strain curves are plotted in Figure 89. From Table 10 and Figure 89 it is most noteworthy that across all tested displacement rates, the curves are similar. Statistically, based on a two-tailed T-test, there is no discernable difference in the fracture strain, yield stress and strain, and modulus across the groups. The only statistically significant difference is in the maximum stress when comparing group 1 and group 2 to group 4.

Table 10: Foil Experimental Data

	Group 1: 0.5265 in/min (n=5)		Group 2: 0.05265 in/min (n=5)		Group 3 0.02633 in/min (n=3)		Group 4 0.05265 in/min (n=2)	
	Mean	**stdev**	**Mean**	**stdev**	**Mean**	**stdev**	**Mean**	**stdev**
Fracture Strain	0.1042	0.0227	0.1145	0.0174	0.1372	0.0993	0.2028	0.0294
Max Stress (ksi)	195.1	7.8058	199.7	5.1519	205	2.0158	208.5	2.3282
Yield Strain	0.01345	0.001577	0.01331	0.001415	0.01355	0.001562	0.01312	1.27E-04
Yield Stress (ksi)	153.22	6.662	162.7	16.84	161.47	9.935	154.23	1.6122
Modulus (ksi)	13310	1120	14400	3.892	14070	9966	13880	3010

In order to create stress strain curves for the computation effort, the data for Groups 2 and 3 were averaged and decimated to develop a model composed of 10 segments that could be imported into Abaqus to define the plastic behavior of the material. Since there was a wide range of values for fracture strain, and not a statistically discernable difference between values, the manufacturer published value of 21% elongation at break was used. It is important to note that the material certification provided with the foil does not included an elastic modulus. While a yield stress is provided, a yield strain is not provided so an elastic modulus cannot be directly calculated. Other published values for the modulus of this material were all around 30.7msi (211.7GPa) while the modulus developed from the experimental data curve was a much lower value of 13.3msi (91.7GPa).

Figure 89 depicts this experimentally developed stress strain curve to be used in computation plotted on the experimental values. This shows that the computational curve represents the experimental data well. The tabular form of this curve is outlined in Appendix I.

Table 11: Foil Statistical Analysis

	Group 1 v. Group 2			Group 1 v. Group 3			Group 1 v. Group 4		
	Diff	% Diff	Stat Sig	Diff	% Diff	Stat Sig	Diff	% Diff	Stat Rel
Fracture Strain	0.01030	9.885	No	0.03300	31.67	No	0.09860	94.63	No
Max Stress (kips)	4.600	2.358	No	9.900	5.074	No	13.40	6.868	Yes
Yield Strain	-1.400E-04	-1.041	No	1.000E-04	0.7435	No	-3.300E-04	-2.454	No
Yield Stress (kips)	9.470	6.181	No	8.250	5.384	No	1.010	0.6592	No
Modulus	1090	8.187	No	759.0	5.701	No	562.000	4.221	No
	Group 2 v. Group 3			**Group 2 v. Group 4**			**Group 3 v. Group 4**		
	Diff	% Diff	Stat Rel	Diff	% Diff	Stat Rel	Diff	% Diff	Stat Rel
Fracture Strain	0.02270	19.83	No	0.0883	77.12	No	0.06560	47.81	No
Max Stress (kips)	5.300	2.654	No	8.800	4.407	Yes	3.500	1.707	No
Yield Strain	2.400E-04	1.803	No	-1.90E-04	-1.427	No	-4.30E-04	-3.173	No
Yield Stress (kips)	-1.220	-0.7499	No	-8.460	-5.200	No	-7.240	-4.484	No
Modulus	-331.0	-2.298	No	-528.0	-3.666	No	-197.0	-1.400	No

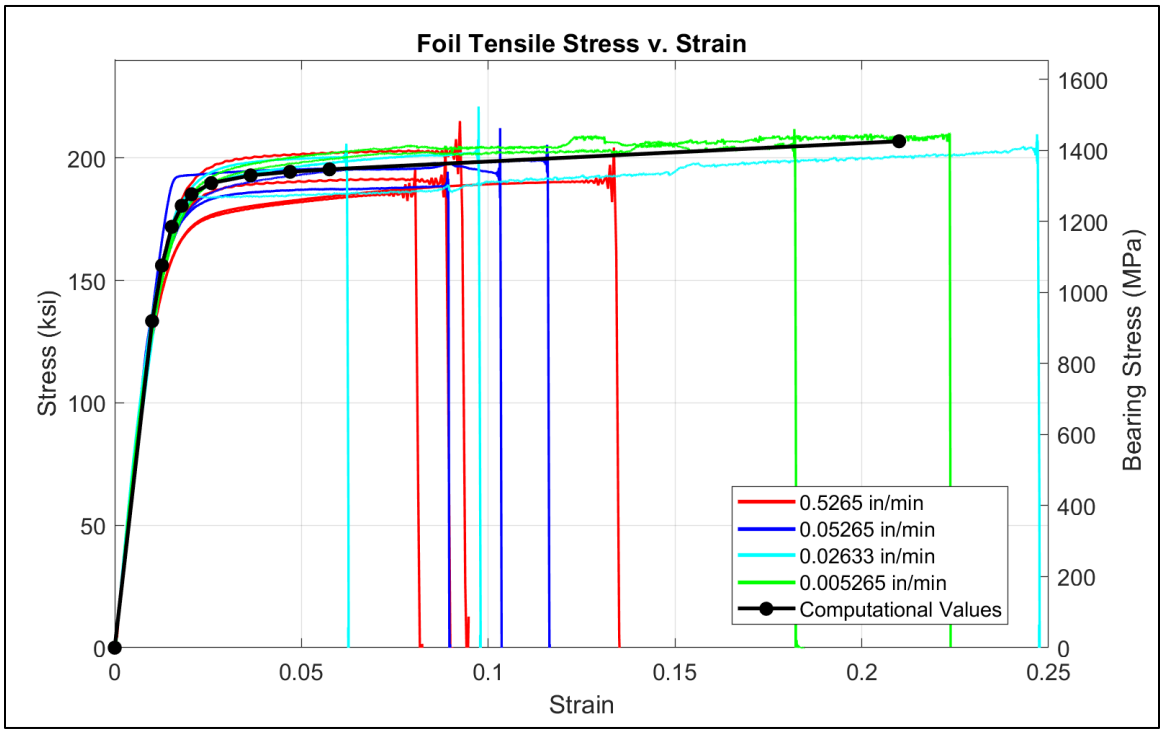

Figure 89: Foil Tensile Stress-Strain Curves and Computational Curve

4.4 AF-191U Adhesive Representation

In initial iterations, the adhesive layers were represented using layers of cohesive elements. However, since the characteristic length of a cohesive element is defined by the thickness, the thinness of the adhesive drove a small stable time step, drastically increasing run time. The cohesive elements also proved to be difficult to employ and troubleshoot. An alternative which was explored was representing the adhesive with cohesive interactions similar to the interlaminar matrix. This however does not represent the relative thickness of the adhesive. Thus, in the most representative models, the adhesive is represented as a continuum using 3D elements described with an elastic modulus and Poisson's Ratio. The adhesive layer is then joined to the composite with the same cohesive interaction properties that represent the interlaminar matrix. The adhesive is joined to the adjacent foil with cohesive interactions defined using published properties of the adhesive. The adhesive employed the same mesh as the foil to reduce complexity in the nodal relationships in the defined interaction properties.

4.5 Assembly definitions

The coupons were laminated in the software much in the same way they were constructed in the laboratory. Each layer was applied to the coupon and located with positional constraints. At the mating surface between two composite layers, a cohesive interaction defined by matrix properties was employed with the 0° ply acting as the master. At the mating surface between the composite and adhesive, the same matrix cohesive interaction was applied with the composite acting as the master. At the mating surface of the foil and adhesive, a cohesive interaction defined by AF191U adhesive

properties was employed with the foil as the master. For each ply, a contact relationship was defined between the bearing surface and the bolt with the bolt acting as the master. A contact relationship was also defined between the plies on either face of the composite and the bosses of the fixture with the fixture assigned as the master.

4.6 Boundary Conditions and Loading

The boundary conditions and loading for the computational models are shown in Figure 90. Since the fixture is composed of two parts, a different constraint was applied to each. The primary side was chosen to be the side that intersected the origin of the model. The end of this primary fixture that would be in the grips was constrained against translation in all three cartesian directions ($u_1 = u_2 = u_3 = 0$) during the initial step and throughout the remainder of the computation. Since 3D stress elements were used for the fixture which do not have rotational degrees of freedom, there was no need to constrain rotation. In order to allow a bolt load to be applied without causing a bending load in the fixture, the secondary fixture was constrained only in the 1 and 2 (x and y) directions, ($u_1 = u_2 = 0$) which allowed the secondary fixture to translate in the 3 (z) direction as the bolt load was applied.

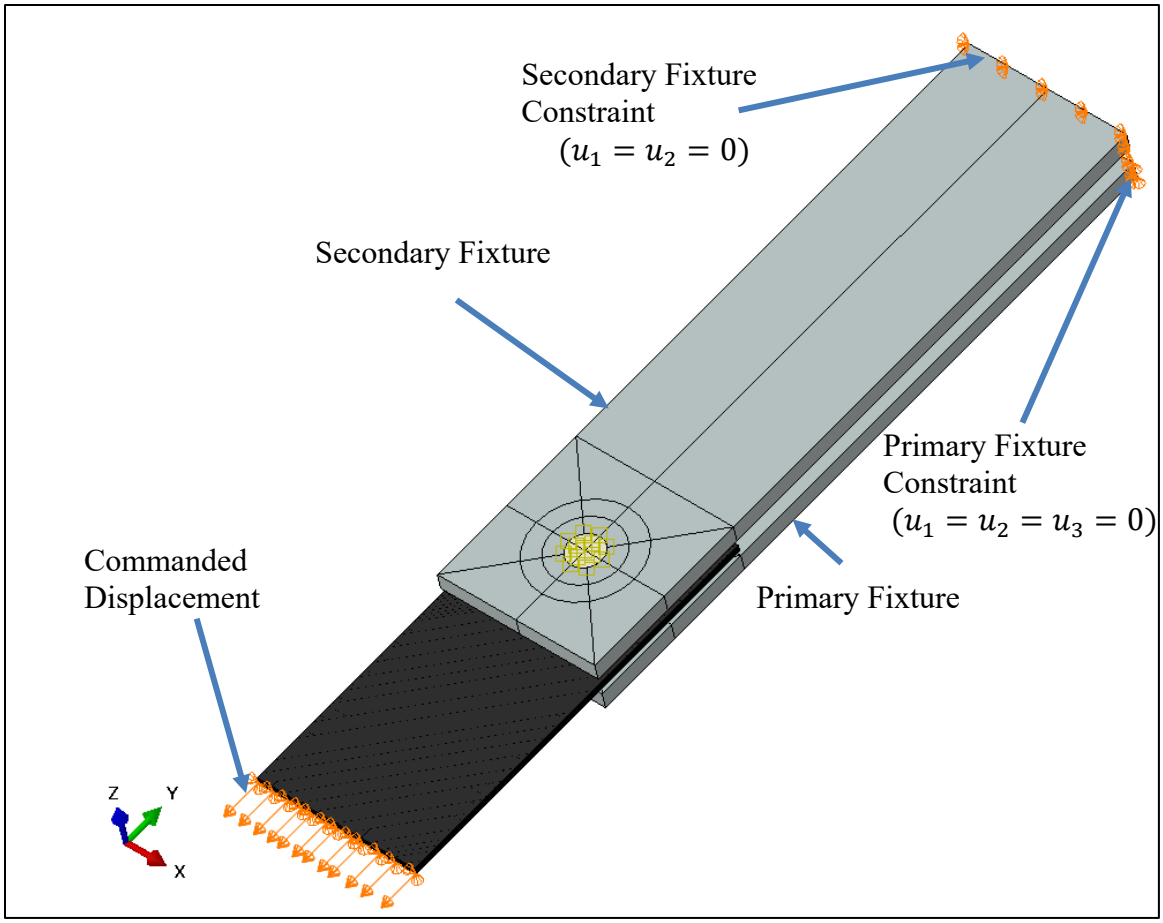

Figure 90: Computational Model and Boundary Conditions

Since Abaqus/Explicit does not offer a bolt tension option, the bolt load was applied using the phenomenon of thermal expansion. In general, for steels, a drop in temperature will cause the material to contract at a measurable ratio directly related to the temperature change. This ratio is known as the coefficient of thermal expansion. This coefficient of thermal expansion can be programmed into Abaqus to simulate the same response to a temperature change. The end goal is not to investigate some thermal response, but to use this physical phenomenon to create stress in the bolt which in turn simulates the clamping force of a fastener. To incorporate this, during the first 10% of the

explicit analysis, a decreasing linear ramp temperature was input into the bolt using an Abaqus amplitude defined with a tabular input. This caused the length of the bolt to attempt to contract. A nonzero coefficient of thermal expansion was defined only along the length of the bolt (in the 3 direction) so that the diameter of the bolt was not affected. In this case, the user was required to set the values of plastic potential to a value of 1. Each end of the bolt was tied to the outside of the hole in the fixture. The resulting reaction was for a clamping force to be applied to the sample between the fixture bosses.

The target temperature was determined by first calculating how much stress was required in the bolt cross section using a target bolt load of 963lbf. This was based on the 60in-lbs (6.78N) torque applied during experimentation. The length of the bolt in these models is defined along the 3 direction.

$$\sigma_{33} = E_{33}\varepsilon_{33} = E_{33}\left(\frac{\Delta L_3}{L_{0_3}}\right) \tag{81}$$

For the tested configurations, the resultant stress in the bolt cross section is 12636psi. The required change in length to produce this stress is given as,

$$\Delta L = \frac{\sigma_{33} L_{0_3}}{E_{33}} \tag{82}$$

The coefficient of thermal expansion, α, is given as

$$\alpha = \frac{\Delta L_3}{\Delta T\left(L_{0_3}\right)} \tag{83}$$

Thus, the target temperature step is given as.

$$\Delta T = \frac{\Delta L_3}{\alpha\left(L_{0_3}\right)} \tag{84}$$

This resulted in an estimated temperature step of -60.3°F (-33.5°C). This however assumes that the ends of the shortening material are perfectly constrained. One could estimate the through-thickness elastic moduli of each material to determine a temperature step that would account for all of the materials' properties. However, this still may not account for all the variables in the models. Since the clamping force operates in the linear elastic region of the materials, the load is applied in a linear fashion. Thus, the temperature step was run with the initial target temperature and then was updated using linear extrapolation and interpolation to converge to within 3.5% of the target stress. The stress in the bolt cross section was measured by averaging the stress (σ_{33}) at the centroid of each element in the cross section of the bolt in the center of the bolt's length. These elements are depicted in Figure 91.

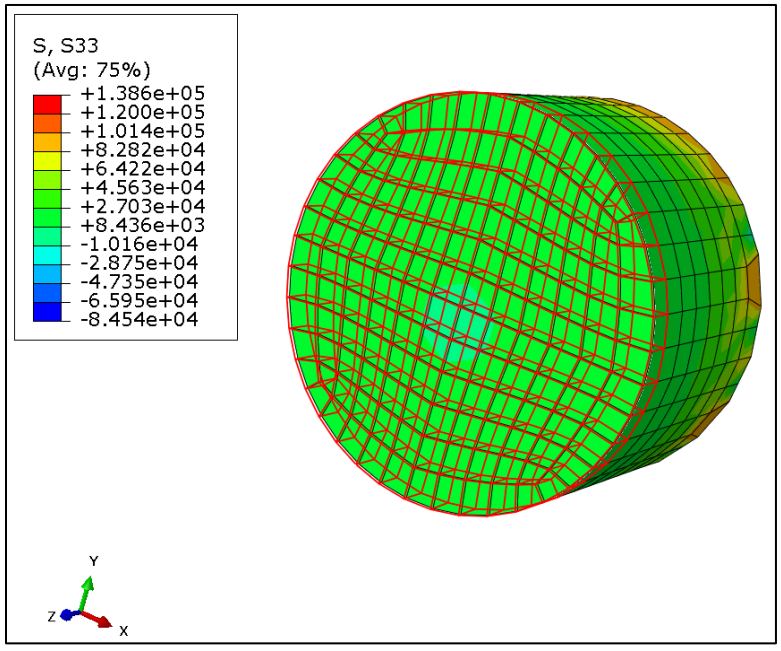

Figure 91: Bolt Cross Sectional Stress Measurement

In the hybrid material, when thermally induced stresses were considered, a temperature step was also assigned to the foil layers resulting in a stress field in each foil. These thermally induced stresses are shown in Figure 92.

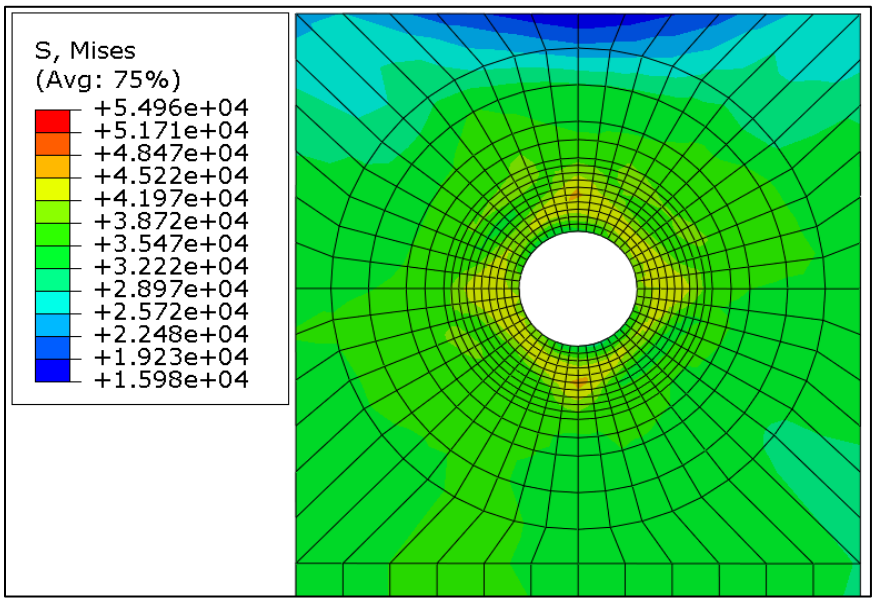

Figure 92: Thermally Induced Stresses in Foil

The temperature ramps defined for the bolt and foil in the 9-ply hybrid case are shown in Figure 93. As defined, each part reached its assigned temperature before the displacement began at $Time\ Step = 0.1$. The relative part temperatures for the same case are displayed in a contour plot in Figure 94. This sectioned image shows that the final temperature in the bolt reached $\Delta T = -350°\text{F}\ (-195°\text{C})$, which placed a compressive stress on the fixture and coupon mimicking the tightening of the bolt. The foils reached $\Delta T = -580°\text{F}\ (-322°\text{C})$ which mimicked the stresses induced during cure. This resulted in a tensile stress in the foils and a compressive stress in the adhesive and composite layers. As stated, the bolt temperature step was determined iteratively to achieve the correct stress in the bolt.

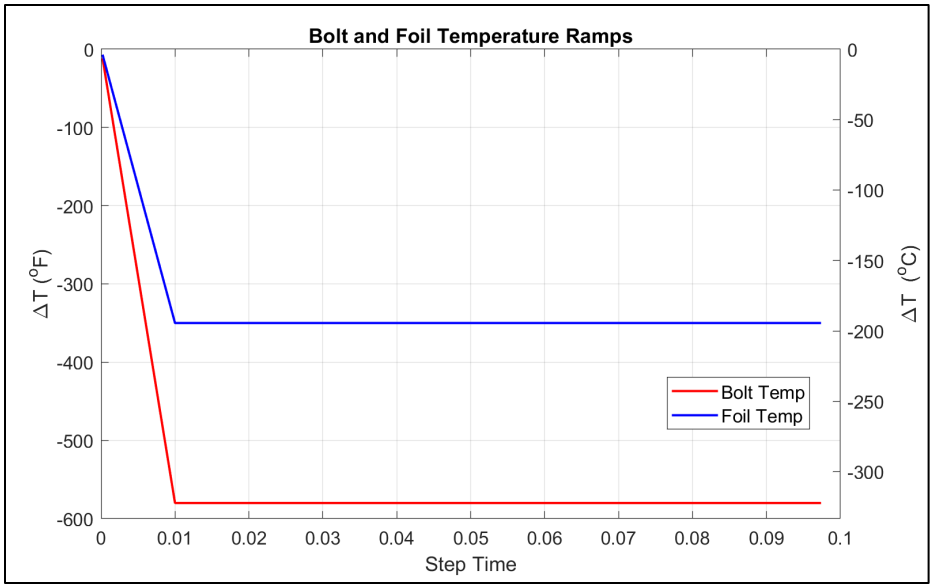

Figure 93: Bolt and Foil Temperature Ramps

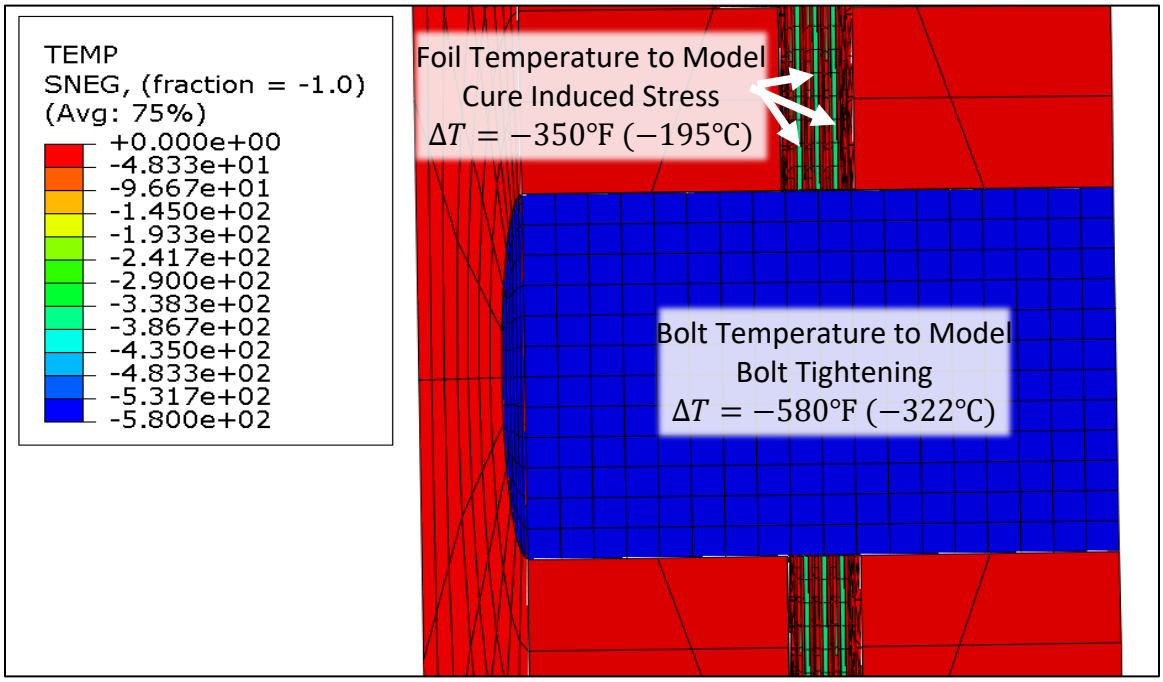

Figure 94: Sectioned Contour Plot of Relative Part Temperatures - 9-Ply Hybrid

The system was loaded by applying a linear displacement boundary condition at the end of the coupon in the 2 (y) direction (down). This was also described using an amplitude with a linear input. Just as in the experimental procedure, a displacement was used instead of a load to allow the system to shed load as displacement occurs. This displacement boundary condition also constrained the displacement of the coupon in the other dimension ($u_1 = u_3 = 0$) in the same way the jaws of the test frame do in the experimental procedure.

Hole elongation was measured at the nodes highlighted in Figure 95, which correspond to the knife edges used to clip on the extension gauge. Load was measured by summing the reaction force in the 2 direction (y direction) of the loads on which the displacement was prescribed. Bearing stress and strain and other values such as yield were determined using the same procedures applied to the experimental data.

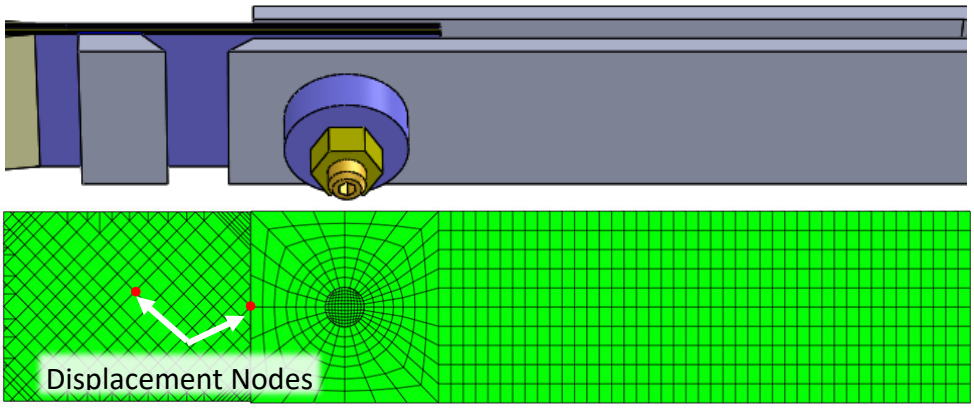

Figure 95: Nodes to Measure Hole Elongation

Load was applied to the system over 10% of a unit step time. If time units were assumed to represent seconds and the model was run over a time which was physically

representative, the models would have likely taken weeks to run. Even running over a unit step, the models took days to run on a 20 core machine. Thus, the time was shortened to 0.1. The utility of this increased loading rate is judged by two considerations. First, none of the materials properties were considered to be time dependent, thus none of the materials behaviors were directly dependent on the overall time step. Second, in order to ensure that the system was modeling quasi-static behavior, the kinetic energy was evaluated and compared to the total energy of the system to ensure that kinetic energy did not exceed 5% of the total energy of the system as is common practice and recommended by Abaqus [118], [119].

V. Double Shear Experimental Results and Discussion

This chapter presents the results of the quasi-static monotonic experimentation in the double shear configuration. The intent of this chapter is to compare and contrast the behavior of control and hybrid bearing samples in 9-ply and 18 ply layups at the macroscopic level, while also investigating the phenomena that occur down to the fiber level which allow progressive bearing failure to take place. First, the results of the coupon dimensionality are presented to discuss the manufacturability of the hybrid material. Next, the results of the double shear testing are presented predominately as load-displacement and stress-strain curves in addition to tabular data. In order to study the failure mechanisms that allow bearing failure to occur, micrographs of progressive failure samples are presented. These have been loaded to target specific features of interest in the full failure data. This chapter also includes a comparison of the 9-ply and 18-ply results in the double shear configuration. The discussion concludes with a statistical analysis. The chapter that follows investigates computational modeling of the double shear scenarios presented here and compares the final finite element model results to experimental results.

5.1 Dimensional Results

Dimensional results reflect the consistency and repeatability of the manufacturing and processing of the hybrid material. This section specifically investigates the thickness of the coupons.

Table 12 lists the average thickness per sample measured using a caliper (detailed in section 3.8.1). Across all the samples used in this research effort, the standard

deviation in thickness is less than 0.002in (0.05mm), which indicates that the layup and cure process is consistent for each sample type. The standard deviation values for the hybrid coupons are actually better than those of the controls, indicating that the hybrids can be manufactured consistently.

It is noteworthy that due to the addition of the adhesive layers, the hybrid materials were thicker than the control layups of the same ply count. In Table 12, the right columns show the thickness increase. While this up to 28% increase in thickness may be substantial in some applications, the magnitude of 0.0250in (.0634mm) is a small magnitude compared to the scale of many aerospace structures. The consistency of the thickness should enable it to be incorporated into designs in a straightforward manner. The implications of this will be discussed throughout this chapter.

Table 12: Coupon Thickness

Layup Type	Average Thickness (in)	Thickness Stdev (in)	Thickness Increase Over Control (in)	Thickness Increase Over Control %
9-Ply Control	0.04733	0.001506	--	--
9-Ply Hybrid	0.06050	5.477E-04	0.01317	27.82
18-Ply Control	0.09264	0.001934	--	--
18-Ply Hybrid	0.1180	0.001262	0.02539	27.41
18-Ply Shank-Only	0.1087	5.164E-04	0.01603	17.30

Note: for clarity, SI equivalent values not included in text are provided in in Appendix M.

One interesting phenomenon is that per ply, for both control and hybrid samples, the 9-ply samples are thicker than the 18-ply. A statistical comparison is made in Table 13. Here the values for the 9-ply samples are doubled for comparison. In addition to the average and standard deviation, the sample size is shown. Finally, a t-test was performed on the difference in means to test for statistical significance (as described in 3.11 Statistical Analysis). While the difference is not statistically significant in the controls

due to the relatively large standard deviation in the 9-ply control, the difference is statistically significant in the hybrid based on the results of the t-test. This suggests that the 18-ply samples are compacted more completely during manufacturing. This comparison is discussed further in the monotonic test results.

Table 13: Thickness Statistical Analysis

	2x 9-Ply Thickness			18-Ply Thickness					
	Average	Stdev	N	Average	Stdev	N	Diff	% Diff	Stat Sig
Control Thickness (in)	0.09467	0.003011	6	0.09264	0.001934	33	-0.002030	-2.145	No
Hybrid Thickness (in)	0.1210	0.001095	6	0.1180	0.001262	33	-0.002970	-2.454	Yes

5.2 Monotonic 9-Ply Double Shear Experimental Results

This section compares the bearing response results of the 9-ply control and hybrid samples. The control samples employed a layup of [45/0/-45/0/90/0/-45/0/45]. To hybridize the samples, as detailed in Chapter 3, the internal non-0° plies were replaced with stainless steel foils resulting in a layup of [45/0/|SS|/0/|SS|/0/|SS|/0/45], where |SS| represents a layer of 301 stainless steel with a layer of AF191U film adhesive on both sides. This case is considered the least complex because it employed the thinnest layup which supported the lowest load. The double shear configuration and thinness of the sample means there was virtually no bending allowed in the bolt. Microscopy of sectioned samples is presented from both control and hybrid progressive failure coupons to explain the internal failure mechanism that corresponds to specific features in the bearing response of each layup.

Figure 96 shows the corrected load-displacement data for all 9-ply samples. "Corrected" means that Equations 71 to 75 in Chapter 3 have been used to calculated the correction factor for each data set. This mathematically removes the slack in the bolted joint from each test to make them comparable.

In Figure 96, control samples are represented in blue, with the full failure controls in blue dashed traces and progressive failure controls in blue dot-dashed traces. The hybrid samples are represented in red with the full failure hybrids in solid red and the progressive failure hybrids in dotted red traces. Table 14 shows summary data and statistical analysis comparing the control and hybrid results pictured in Figure 96. The average and standard deviation are provided for each measure. A 95% confidence interval is given under the average, and N is the number of samples considered in the calculation. Comparison between control and hybrid values was performed using a two-tailed t-test to determine if the difference in the two averages was statistically significant (see section 3.11). The 95% confidence interval is presented because it offers a different way of thinking about the comparison of two means. If two means have confidence intervals that overlap one another, they are not likely to be statistically significant. If the two confidence intervals do not contain any of the same range of values, then the means are statistically different.

In Figure 96, the hybrid samples plotted in red demonstrate a marked increase in bearing load capacity over the control samples represented in blue. As recorded in Table 14, the hybrid material demonstrates a 25% greater yield load, a 35% greater offset load, and a 42% greater ultimate load capacity over the control. The hybrid demonstrates an impressive 51% increase in strain energy capacity over the control. This is not only due

to higher yield and ultimate loads but is also due to the reloading in the hybrid samples which begins near 0.050in (1.3mm) of hole elongation. In contrast, the control samples shed load at a steady rate past 0.050in (1.3mm) of displacement. This reloading effect and other specific phenomena will be discussed further alongside the progressive failure samples.

When looking at the shape of the hybrid curves versus the shape of the control curves, an important phenomenon is observed. The controls display sharp unloading and reloading behavior just after yield, due to load redistribution as individual elements within the laminate failed. These features often approach a 300lbf (1330N) load change. In contrast, the hybrid displays a damping of this behavior creating a more smooth, ductile failure curve, since the load is being redistributed into the homogenous metallic foils. In the hybrid, the magnitude of these redistributions is less than 100 lbf (445N). The specific phenomena that cause these features are discussed in the next sections that cover progressive failure.

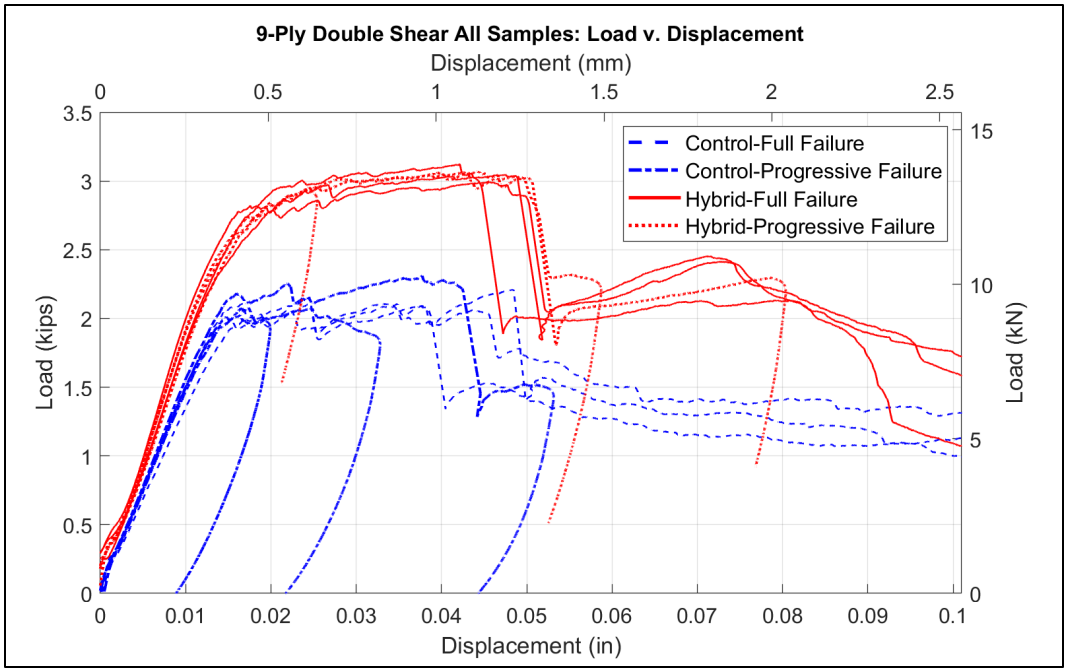

Figure 96: 9-Ply Load v. Displacements

Table 14: 9-Ply Double Shear Load Based Data

	Control			Hybrid					
	Average (95% CI)	**Stdev**	**N**	**Average (95% CI)**	**Stdev**	**N**	**Diff**	**% Diff**	**Stat Sig**
Yield Load (kips)	1.847 (1.744-1.949)	0.09771	6	2.317 (2.215-2.418)	0.09656	6	0.4699	25.44	Yes
Offset Load (kips)	2.038 (1.968-2.107)	0.06604	6	2.750 (2.642-2.858)	0.1029	6	0.7121	34.95	Yes
Ultimate Load (kips)	2.151 (1.999-2.303)	0.06122	3	3.054 (2.891-3.218)	0.06590	3	0.9033	42.00	Yes
Strain Energy (in-lb)	141.0 (120.7-161.3)	8.185	3	213.0 (201.6-224.4)	4.583	3	72.00	51.06	Yes

While the data thus far has been presented in load-displacement terms, it should also be considered in terms of stress and strain. Since the bolt diameter is the same in each case, the stress calculation is essentially normalizing the load by the thickness of the sample (Equation 69). The strain calculation is normalizing displacement (hole

elongation) by the bolt diameter (Equation 70). These calculations are detailed in section 3.9.3.

Figure 97 shows the corrected stress-strain data for all 9-ply monotonic samples. Control samples are represented in blue, with the full failure controls in blue dashed traces and progressive failure controls in blue dot-dashed traces. The hybrid samples are represented in red with the full failure hybrids in solid red and the progressive failure hybrids in dotted red traces. Table 15 shows summary data and statistical analysis of the data pictured in Figure 97. Here, the control and hybrid results are compared in yield stress and strain, 1% offset stress and strain, ultimate stress, modulus (Chord Stiffness)(Equation 71) and the calculated strain energy density (area under the stress-strain curve) as detailed in Section 3.9.3.

A complicating factor arises when one looks at stress-based values. As depicted in Figure 97, the curves appear much closer than those observed in the load-based data (Figure 96). In fact, the gain in ultimate stress due to the hybrid shrinks to 9% and is no longer statistically significant as recorded in Table 15. The offset stress is still statistically significant, but has shrunk to a value just over a 5.5% improvement due to hybridization. Strain energy density (in Table 15) when compared to strain energy (in Table 14) still maintains an increase of 16% due to the reloading effect in the hybrid samples which occurs after 15% bearing strain.

The change in the improvement from hybridization when converting to stress-based values is due to the fact that, despite using the thinnest adhesive available, the adhesive thickens the layup as noted in the dimensional results (Table 12). While the adhesive was employed to toughen the foil-composite bond, this study does not find

delamination to be a critical failure mode near yield, which suggests that other bonding methods could be investigated.

Using the 9-ply configuration, the addition of the adhesive locally thickens the finished part by 0.0132in (0.335mm) on average for the 9-ply samples which equates to a thickness increase of 28% due to hybridization. While this is substantial from a percent increase, the magnitude of the change is fairly small compared to the scale of many aerospace structures and the thickness variation in other joint types. The thickness of the hybrids also has a lower standard deviation than the control which means, despite being thicker, the dimensionality of the hybrid is consistent. Thus, while no change in thickness would be ideal, the small magnitude of the increase and the consistency of the thickness should make designing for this thickening relatively straightforward if the design space allows for it.

If constant thickness at the joint is required, adjustments to the hybrid manufacturing process could be pursued to control the total thickness. The AF-191U Film adhesive employed in this study would have to be removed and replaced with a thinner solution. Spray adhesives that allow for less buildup could be investigated. Also, other fiber metal laminates have shown good performance in bolted joints without employing an adhesive and relying solely on surface preparation [22], [36], [38]. Any of these updates to manufacturing would require new testing and computation to confirm the benefits of hybridization.

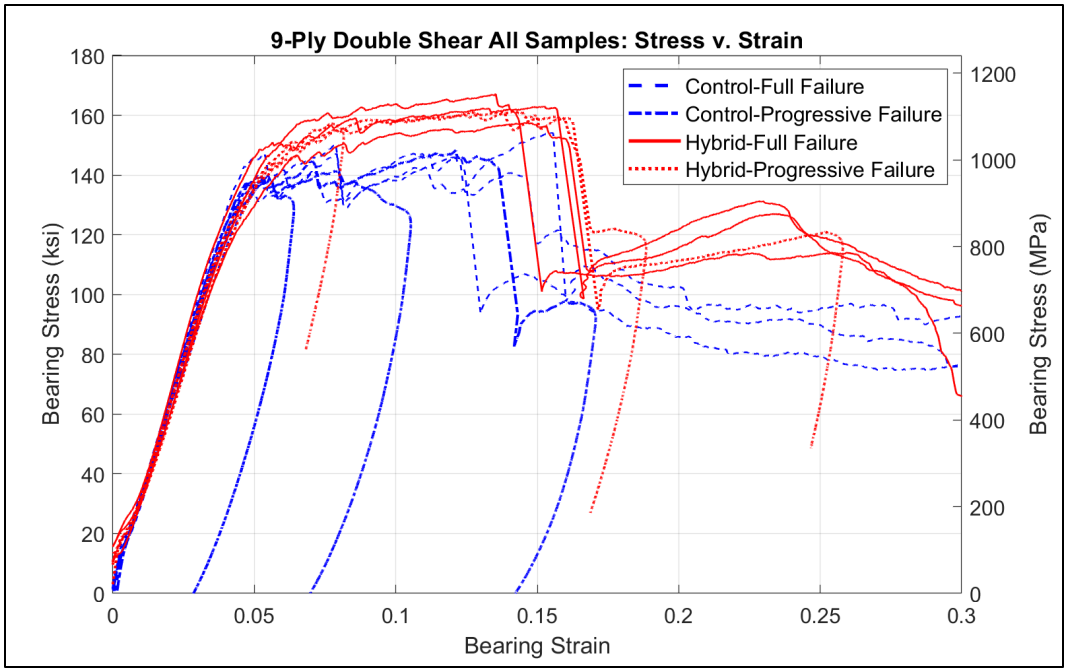

Figure 97: 9-Ply Stress v. Strain

Table 15: 9-Ply Double Shear Stress Based Data

	Control			Hybrid					
	Average (95% CI)	**Stdev**	**N**	**Average (95% CI)**	**Stdev**	**N**	**Diff**	**% Diff**	**Stat Sig**
Yield Stress (ksi)	125.3 (118.0-132.6)	6.971	6	123.0 (116.7-129.3)	5.996	6	-2.353	-1.877	No
Yield Strain	0.04176 (0.03920-0.04432)	0.0024	6	0.04194 (0.03939-0.04449)	0.002431	6	1.817E-4	0.4350	No
Offset Stress (ksi)	138.2 (134.1-142.4)	3.932	6	146.0 (139.0-152.9)	6.636	6	7.715	5.581	Yes
Offset Strain	0.05387 (0.05162-0.05613)	0.002150	6	0.0591 (0.05173-0.06648)	0.007025	6	0.005173	9.714	No
Ultimate Stress (ksi)	149.1 (134.3-163.8)	5.933	3	162.6 (150.6-174.5)	4.826	3	13.48	9.045	No
Modulus (ksi)	3155 (3032-3278)	116.8	6	3092 (2936-3248)	149.0	6	-62.93	-1.995	No
Strain Energy Density (in-lb/in^3)	31340 (27640-35040)	1489	3	36380 (34360-38410)	815.6	3	5039	16.08	Yes

5.2.1 9-Ply Control Progressive Failure

To enable the study of the features that caused bearing failure, three control coupons were sectioned through the thickness along the length, as shown in Figure 98. In the micrographs that follow, the view is in the direction of the blue arrow (into the page) in Figure 98. The area of consideration is that near the bearing surface highlighted in bright green. In each case, the bearing surface of the hole is on the left and the viewer is looking through the thickness of the coupon at the sectioned surface.

Figure 98: Sectioned Sample View

Figure 99 shows the stress-strain curves of the 9-ply control progressive failure samples. Displacement values were selected to target the internal failure mechanism that allowed the features indicated in Figure 99. Here, results from three different progressive failure samples loaded to 6.40%, 10.5%, and 17.1% bearing strain are plotted with one of the full failure samples.

The process of capturing progressive failure was difficult because there is some uncertainty in the initial loading of the joint which complicates selecting a target displacement. Also, it is often difficult to arrest the deformation occurring during a test. If the sample happens to be shedding load at the time, the sample must be unloaded faster than the damage can propagate.

The micrographs in Figure 100 correspond to the curves in Figure 99. The colors and line styles of the traces on the plot in Figure 99 match the color and style identified

beside the title of each image in Figure 100. In each case, the strain listed is the actual maximum strain after the correction factor was applied. The scale in the sectioned images is given as 0.156in (3.96mm) which is one bolt radius. This is intended to provide the viewer a reference to macro-scale hole elongation while viewing microscopic features. In Figure 100, selected failure modes are identified as Fiber Kinking (FK) shown in green, Matrix Cracking (MC) shown in white, and Delamination (DL) shown in orange. This notation is used throughout the rest of the chapter.

Figure 100A shows a sample strained to 6.40% (dotted red trace) which was targeting the load drop just after yield (Feature 1 in Figure 99). The average yield for all samples in this configuration is represented by a horizontal black dotted line in Figure 99. This image, coupled with later 18-ply data, suggests that yield is dominated by in-plane fiber kinking (noted by "FK") in the 0° layers. Some slight out-of-plane fiber kinking in the 0° layers coupled with matrix cracking in the ±45° layers is observable. Some early delamination is also present (noted by "DL").

The sample in Figure 100B (green dashed trace) was targeting the major load drop that occurred in the full-failure samples around 7% to 8% strain (Feature 2 in Figure 99). The in-plane fiber kinking from yield is present, but here the sample is dominated by through thickness cracking and delamination. Delamination exists in both localized regions and large-scale regions. Even at this strain, the majority of the damage has occurred between the bosses on the fixture in the bounds of the sample faces. (Fixture bosses are depicted in Figure 60 in section 3.9.1 and discussed in section 3.3). Most of the through-thickness cracking is constrained inside one bolt radius (represented by the image scale).

Figure 100C shows a 17.1% strained sample (blue dot-dashed trace), which accounts for the major load drop in the full-failure samples around the 15% strain point (Feature 3 in Figure 99). While the fiber kinking, through thickness cracking, and delamination are present, here the failure is dominated by large scale out of plane failure at the edge of the fixture boss. The full failure samples were crushed to such a degree that they could not be reliably sectioned for microscopy and are not pictured.

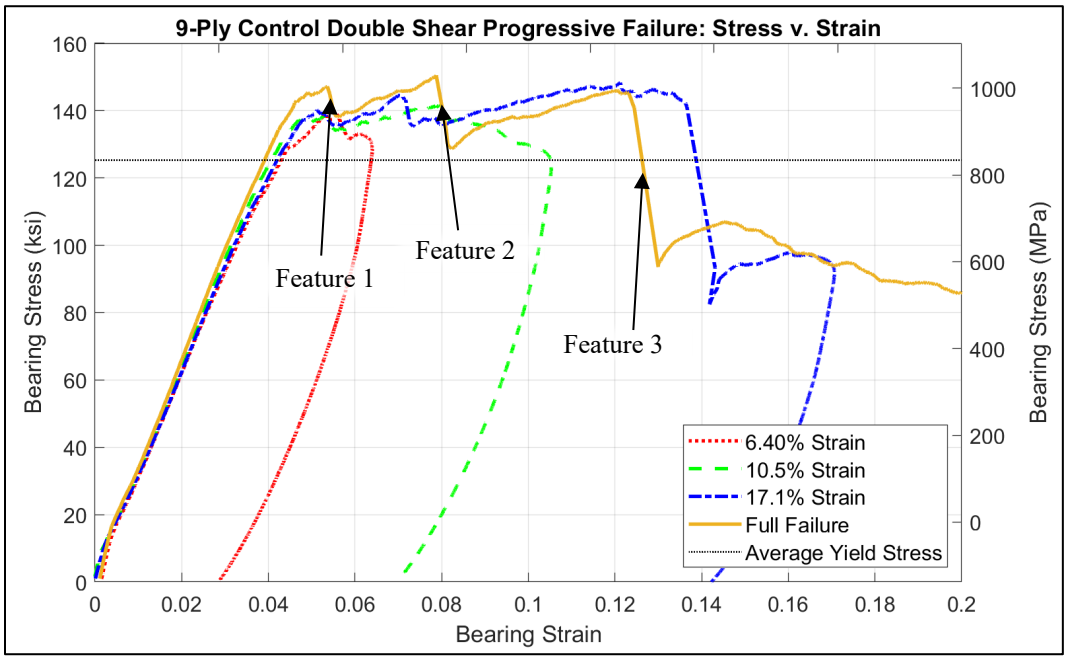

Figure 99: 9-Ply Control Progressive Failure Samples

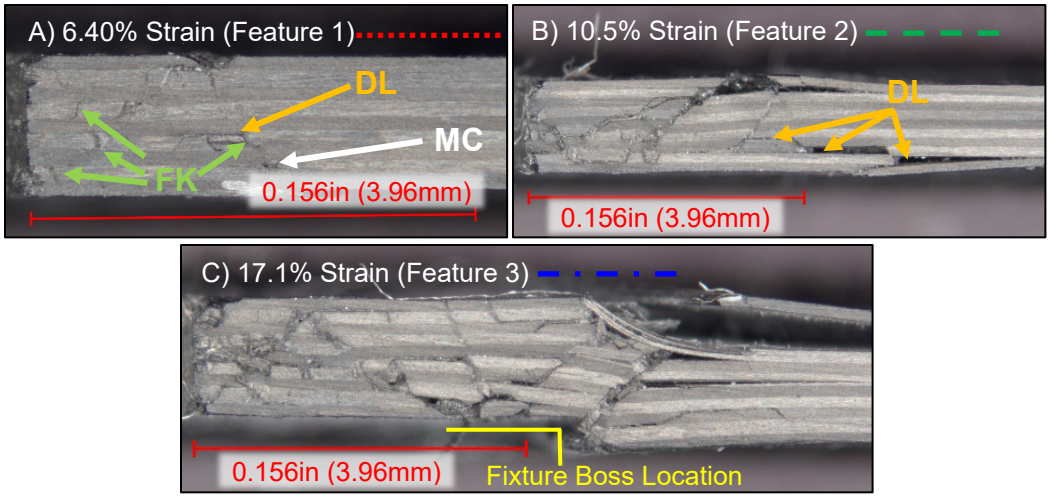

Figure 100: 9-Ply Control Progressive Failure Micrographs

5.2.2 9-Ply Hybrid Progressive Failure

Similar to the control data shown previously, Figure 101 shows the stress-strain curves for the three 9-ply hybrid progressive failure samples strained to 8.38%, 18.8%, and 25.8% bearing strain which targeted the features identified. Corresponding micrographs are shown in Figure 102.

The sample in Figure 102A sought to target the mechanisms causing the knee point after yield (Feature 1 in Figure 101). Similar to the control, in-plane fiber kinking is visible in the 0° layers. It is important to note that, in the area visible in these images, the inner ±45° and 90° layers have been replaced with foils. Only the face lamina oriented at 45° remain. Thus, any internal fiber failure is happening in 0° layers. At this early strain (8.39%), a small amount of instability has been initiated in the foil. This out of plane deflection in the metal foils is commonly known as buckling in structural members. The presence of the ductile foil is halting the matrix cracking that is seen coupled with the fiber kinking in the control micrographs. This is shown by comparing Figure 100A and B

(controls) with Figure 102A (hybrid). The hybrid in Figure 102A shows fiber kinking, but since there are no internal adjacent ±45° or 90° plies, the coupling effect cannot take place.

Figure 102B shows the damage after the major load drop that occurs near the 17% strain mark (Target Feature 2). The early onset fiber kinking in the 0° layers from yield is present as is some slight buckling in the foils within half a bolt radius from the bearing surface (one bolt radius is represented by the image scale). The major feature is the large-scale buckling that occurs at the edge of the fixture boss which caused the sharp unloading in Feature 2. This large-scale buckling is accompanied by intense fiber kinking, fiber breakage, and delamination. Notably, the delamination that occurred internal to the layup near edge of the fixture boss occurred between the composite layer and the adhesive. The adhesive remained bonded to the foil, which indicates that surface preparation of the foil was robust. As one might expect, the foils behaved in a ductile fashion bending around the fixture boss.

The final progressive failure sample targeted a feature that occurred in the hybrid but not the control. After the large-scale deformation that occurred at the edge of the boss, the hybrid demonstrated a reloading noted as Feature 3. Figure 102C shows that after the buckling occurred, the fixture boss then impinged on a relatively undamaged section of the sample causing an increase in load capacity. As depicted in Figure 102D, this load was shed by the continued buckling of the sample against the fixture boss.

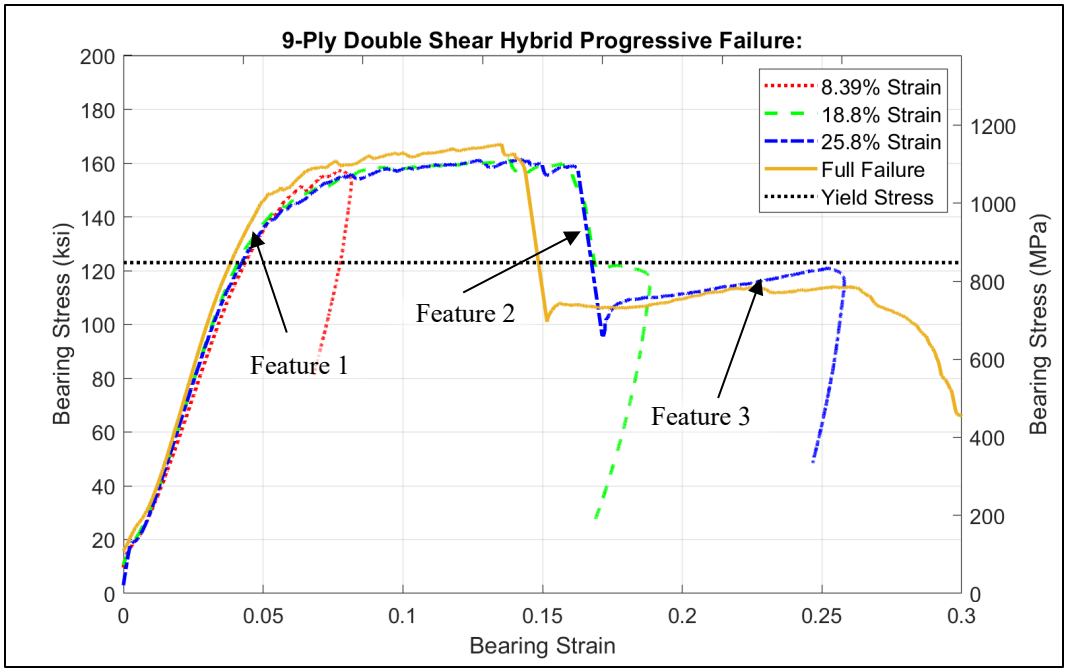

Figure 101: 9-Ply Hybrid Progressive Failure Samples

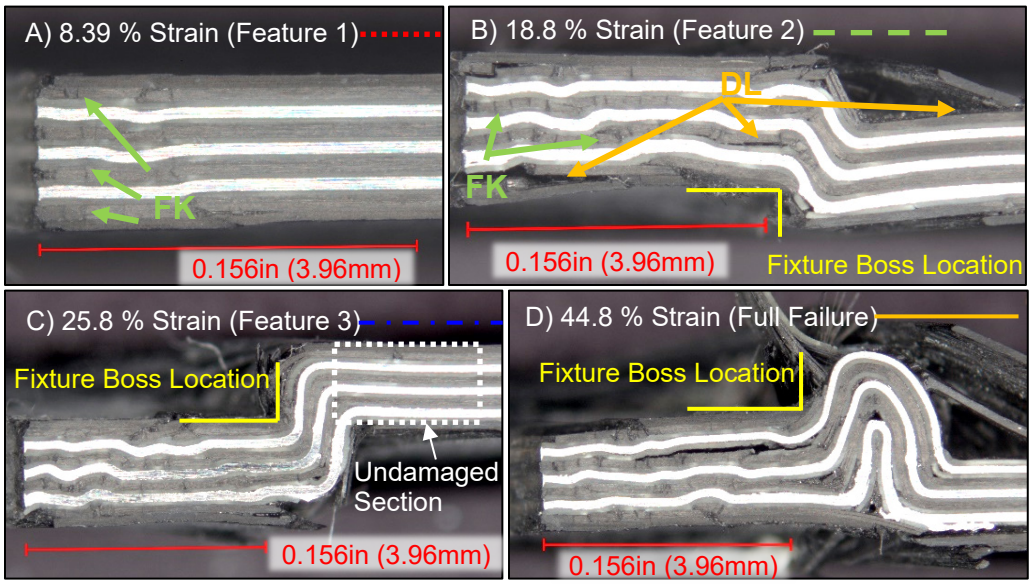

Figure 102:9-Ply Hybrid Progressive Failure Micrographs

5.3 Monotonic Quasi-Static 18-Ply Double Shear Experimental Results

This section presents the next step in complexity by doubling the layup studied in the previous section while maintaining the double shear loading configuration. While the load capacity was expected to be doubled, increasing complexity, the double shear configuration still limited bending in the bolt. The control layup employed was $[45/0/-45/0/90/0/-45/0/45]_2$. To hybridize the sample, as detailed in Chapter 3, the internal non-0° plies were replaced with stainless steel foils resulting in a layup of $[45/0/|SS|/0/|SS|/0/|SS|/0/45]_2$.

Load-displacement curves for the 18-ply double shear samples are shown in Figure 103. Control samples are represented in blue, with the full failure controls in blue dashed traces and progressive failure controls in blue dot-dashed traces. The hybrid samples are represented in red with the full failure hybrids in solid red and the progressive failure hybrids in dotted red traces. Table 16 contains detailed comparative data and statistical analysis for yield, offset, and ultimate loads as well as strain energy. Strain energy is presented because it measures performance throughout deformation while the other values are taken from single points. In Table 16, statistical significance in the far right column compares the means using a t-test as described in section 3.11 to decide if the two means are statistically discernible.

For both the hybrid and control, a progressive failure sample was excessively strained due to the inability to unload the sample quickly enough to arrest the deformation. These are visible in Figure 103 as the long, linear unloading lines that depart from the rest of the data. An additional hybrid progressive failure sample

displayed anomalous bearing failure upon unloading as well. These data were kept, enabling larger samples sizes for other calculations such as yield and modulus.

In Figure 103 it is clear that the hybrid curves (red traces) reach a much higher load capacity than the controls. The hybrid curves also appear much smoother due to the ductile nature of the foils which are integral to the layup. A feature here that was not observed in the 9-ply case is the sharp unloading that occurred between 0.040in and 0.060in (1.0mm and 1.5mm) in the hybrid full failure samples (solid red traces). This unloading was caused by a catastrophic crack through the thickness of the material that developed at the hole and propagated to the edge of the sample which effectively shed all the load capacity of the joint. In contrast, the control displayed a gradual bearing failure as previously observed in the 9-ply data. Figure 104 compares macroscopic images of control and hybrid samples loaded to similar hole elongations. The control displays textbook bearing failure while the hybrid displays the large through thickness crack. This crack always occurred on the same side of the hole since the internal -45° plies were replaced with foils which caused asymmetric loading around the circumference of the hole. The specific phenomena that cause other features are discussed in the next sections that cover progressive failure.

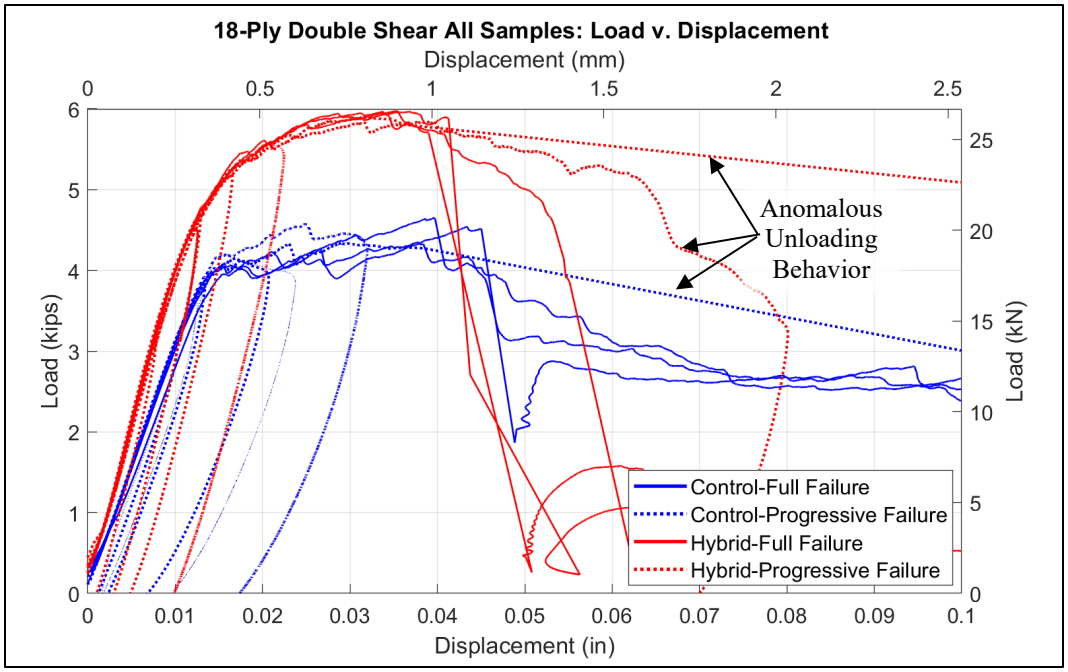

Figure 103: 9-Ply Double Shear Load Based Data

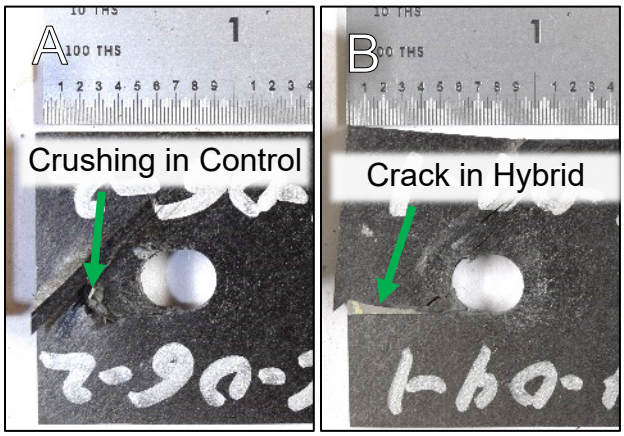

Figure 104: 18-Ply Full Failure Comparison A) Control B) Hybrid

Table 16: 18-Ply Double Shear Load Based Data

	Control 18-Ply			Hybrid 18-Ply					
	Average	Stdev	N	Average	Stdev	N	Diff	% Diff	Stat Sig
Yield Load (kips)	3.670 (3.547-3.793)	0.1329	7	4.125 (4.029-4.221)	0.1247	9	0.4552	12.40	Yes
Offset Load (kips)	4.053 (3.976-4.129)	0.07285	6	5.110 (5.037-5.183)	0.07886	7	1.057	26.08	Yes
Ultimate Load (kips)	4.514 (4.138-4.890)	0.1514	3	5.940 (5.844-6.035)	0.05972	4	1.425	31.57	Yes
Strain Energy (in-lb)	124.2 (115.6-132.9)	3.483	3	169.0 (167.1-170.9)	1.176	4	44.74	36.01	Yes

In the 18-ply case, hybridization produced results similar to those noted in the 9-ply case but did not produce the same percentage increases. As listed in Table 16, the 18-ply hybrid produced a yield load 12% greater and an ultimate load 32% greater when compared to the control, while absorbing 36% more strain energy. A detailed comparison between the 9-ply and 18-ply double shear cases is presented in section 5.4.

After investigating the 18-ply case in terms of load and displacement, it should be considered in terms of bearing stress and strain. Figure 105 depicts plots of the 18-ply double shear control and hybrid samples in terms of bearing stress and strain. Control samples are represented in blue, with the full failure controls in blue dashed traces and progressive failure controls in blue dot-dashed traces. The hybrid samples are represented in red with the full failure hybrids in solid red and the progressive failure hybrids in dotted red traces. Table 17 shows summary data and statistical analysis of the data pictured in Figure 105 comparing the control and hybrid results in yield stress and strain, 1% offset stress and strain, ultimate stress, modulus, (Chord Stiffness)(Equation 71) and the calculated strain energy density (area under the stress-strain curve) as detailed in Section 3.9.3.

As noted in the 9-ply configuration, when converting 18-ply data to stress-strain based values (Figure 105 and Table 17), the thickness increase of the hybrid masks the gains observed in the load data. Due to the smooth, ductile shape of the hybrid curves, the yield stress of the hybrid is actually calculated to be almost 13% lower than that of the control, and the offset stress is almost 3% lower than the control. The difference in the ultimate stress and modulus is no longer statistically significant. Even with the thickness masking some of the differences, it is noteworthy that the modulus (chord stiffness) of the hybrid is significantly stiffer than that of the control. This is because the internal -45° and 90° layers in the control were providing relatively low stiffness in the loading direction and were replaced with the stiffer metal foils in the hybrid.

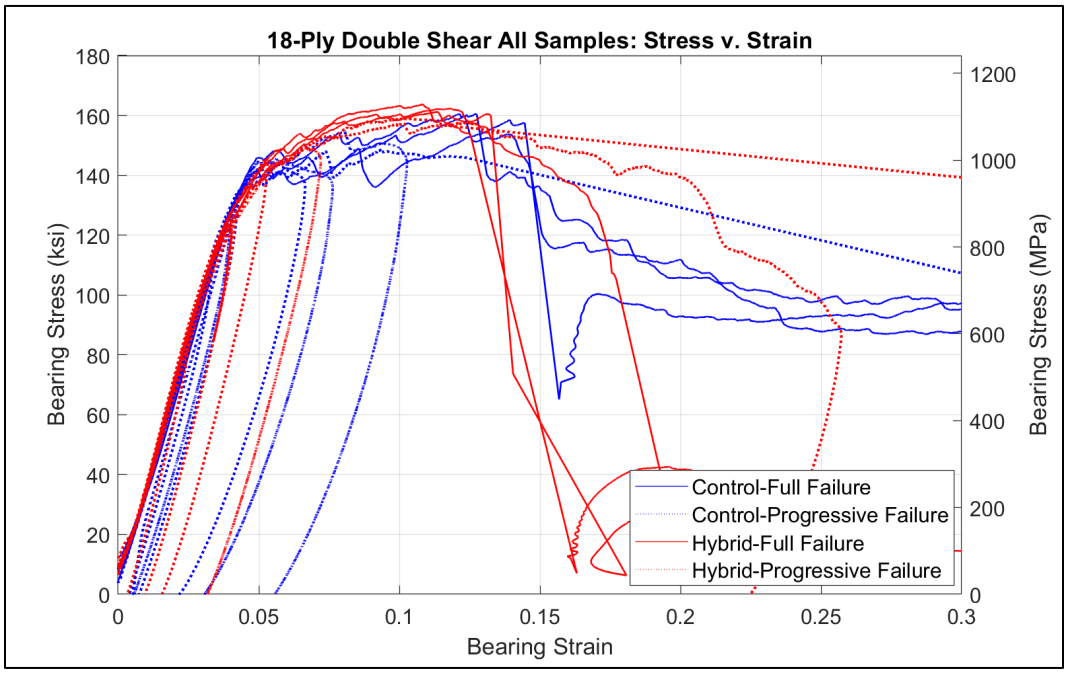

Figure 105: 18-Ply Double Shear All Samples: Stress v. Strain

Table 17: 18-Ply Double Shear Stress-Strain Data

	Control 18-Ply			Hybrid 18-Ply					
	Average (95% CI)	Stdev	N	Average (95% CI)	Stdev	N	Diff	% Diff	Stat Sig
Yield Stress (ksi)	128.2 (122.5-133.8)	6.098	7	111.8 (108.9-114.7)	3.773	9	-16.33	-12.74	Yes
Yield Strain	0.04027 (0.03754-0.04300)	0.002956	7	0.03379 (0.03242- 0.03515)	0.001775	9	-0.006481	-16.09	Yes
Offset Stress (ksi)	141.3 (137.1-145.4)	3.982	6	138.694 (136.4-140.9)	2.436	7	-2.556	-1.810	Yes
Offset Strain	0.05254 (0.05047-0.05461)	0.001976	6	0.04937 (0.04797- 0.05077)	0.001512	7	-0.003169	-6.031	No
Ultimate Stress (ksi)	159.8 (156.9-162.8)	1.184	3	161.3 (157.2-165.3)	2.532	4	1.413	0.8842	No
Modulus (ksi)	3361 (3289-3433)	93.36	9	3518 (3446-3590)	100.5	10	156.7	4.661	Yes
Strain Energy Density (in-lb/in^3)	14130 (13340-14920)	317.6	3	14729 (14440-15020)	182.2	4	601.5	4.258	No

5.3.1 18-Ply Double Shear Control Progressive Failure

In order to understand the features that occur in the sample to allow bearing failure, six of the 18-ply control double shear samples were sectioned and evaluated through microscopy. Figure 106 shows the stress-strain curves for these samples and indicates the features that were targeted by the progressive failure samples. Corresponding sectioned images of these samples are shown in Figure 107.

Due to the availability of more samples, several samples were run to lesser strain values with the goal of characterizing yield more completely. Figure 107A depicts a sample loaded to only a 3.39% strain (Feature 1 in Figure 106). While the damage is difficult to detect, a small amount of permanent deformation is observed in the stress-strain curve. Similar to that observed by Yamada et al in a carbon-titanium hybrid, this deformation is attributed to fiber kinking at the bearing surface in the 0° plies [36]. This

phenomenon is detailed in Figure 108. This behavior is not attributable to machining as it is not present in the non-loaded sided of the holes.

Figure 107B depicts the behavior in a sample loaded to 4.30% strain to target yield (Feature 2 in Figure 106). This matches the yield failure noted in the 9-ply controls. It is dominated by fiber kinking in the 0° plies that begins near the bearing surface. Figure 107C and D were loaded to target Feature 3. While the early onset fiber kinking is present, through-thickness cracking has come about rapidly and delamination has initiated away from the bearing surface.

The sample in Figure 107E targeted the load drop in feature 4. This shows that this feature was caused by a wedge failure forming through the thickness of the layup between the fixture bosses. Finally, Figure 107F shows full failure that has occurred as large-scale crushing outside the radius of the fixture boss.

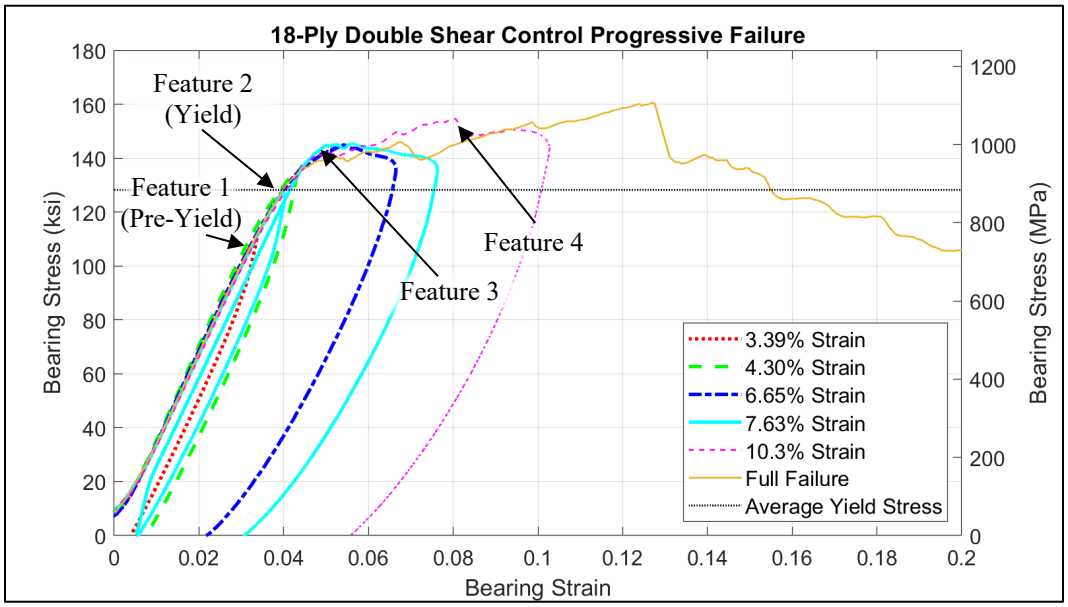

Figure 106: 18-Ply Control Progressive Failure

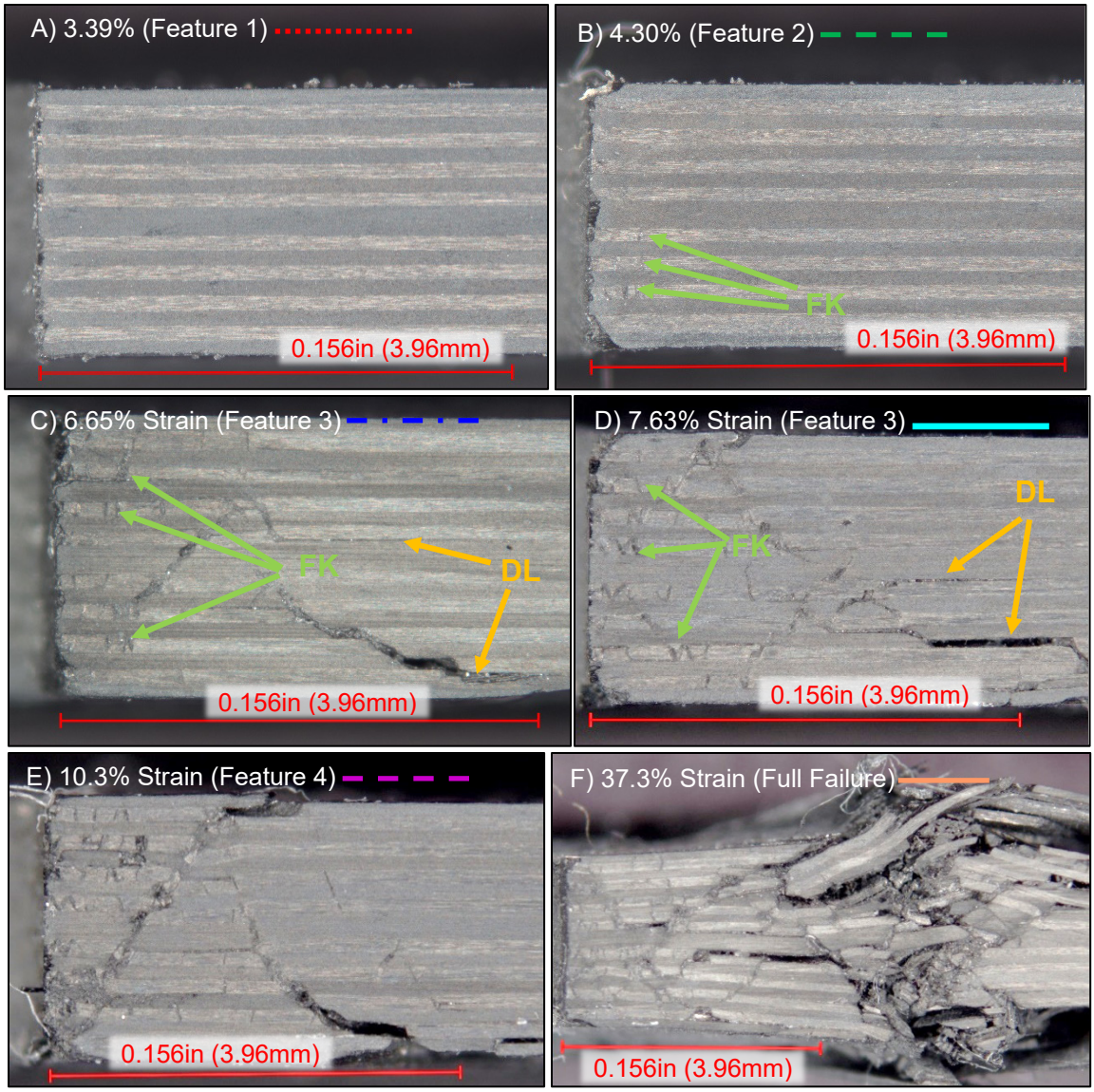

Figure 107: 18-Ply Control Progressive Failure Micrographs

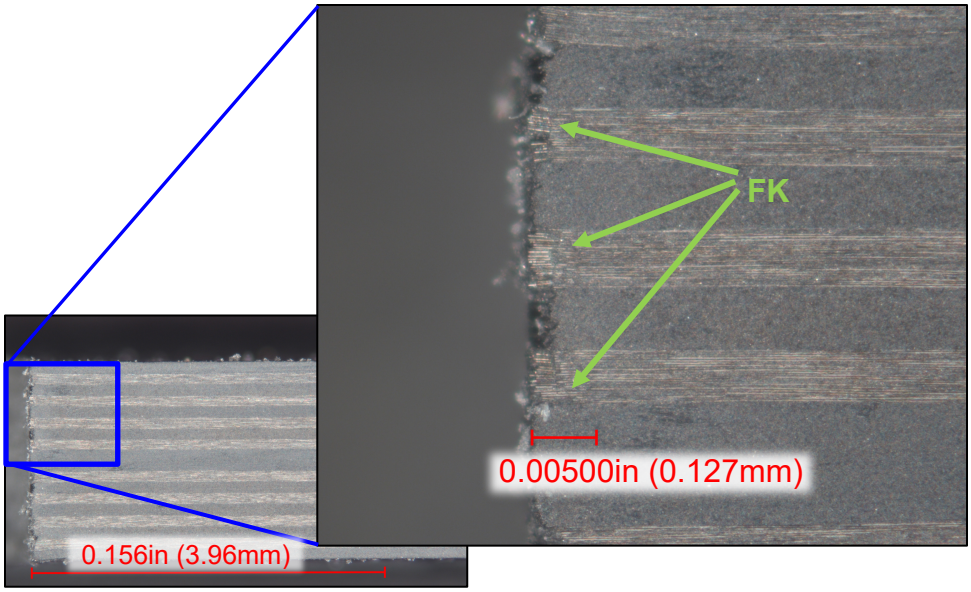

Figure 108: 3.39% Strain Fiber Kinking Detail

5.3.2 18-Ply Double Shear Hybrid Progressive Failure

In order to study the damage that occurred in the 18-ply double shear hybrid samples, six coupons were studied through microscopy. Stress-strain curves of the progressive failure samples are presented in Figure 109 where the features targeted by these samples are labeled. Corresponding images of the sectioned samples are presented in Figure 110.

As in the control, one sample, pictured in Figure 110A, was strained to target the behavior just prior to the calculated yield (Feature 1). This is represented by a dotted red trace in Figure 109. As in the control, permanent deformation is still attributable to fiber kinking in the 0° plies at the bearing surface.

The next two samples (pictured in Figure 110B and C), were deformed just past yield (Feature 2), as noted in the dashed green and dot-dashed blue traces representing

4.04% and 4.14% strain. These two samples both demonstrate that yield is caused by in-plane fiber kinking in the 0° plies near the bearing surface.

Since the hybrid produced a smoother curve, there were no obvious load drops to characterize after yield. Thus, progressive displacements were selected inside 10% strain. As strain progressed to 5.32% (Feature 3- heavy cyan trace), the in-plane fiber kinking progresses further into the material and mild instability set into the metal foils as shown in Figure 110D. As the strain progressed past 7% (Feature 4- dotted magenta trace), the damage was defined by increased fiber kinking and foil buckling. Also, some areas of coupled fiber kinking and matrix cracking have come about at the internal 45° layers. Localized delamination is also present. In contrast to the 9-ply hybrid, due to increased stiffness, the 18-ply hybrid does not demonstrate the full thickness buckling at the edge of the fixture boss.

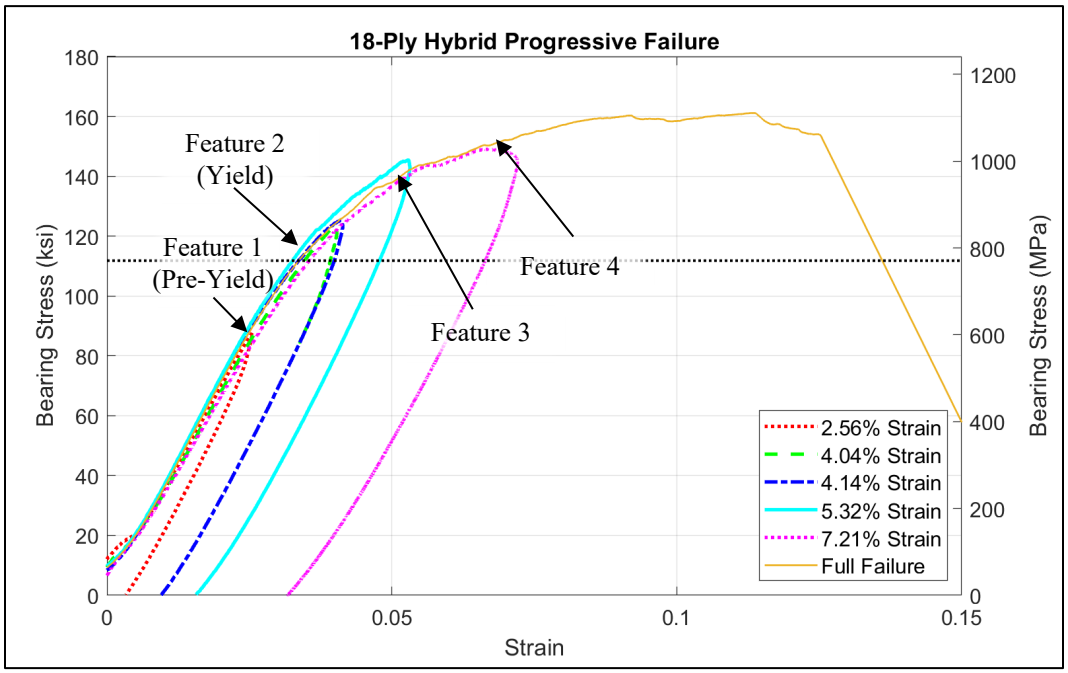

Figure 109: 18-Ply Hybrid Progressive Failure

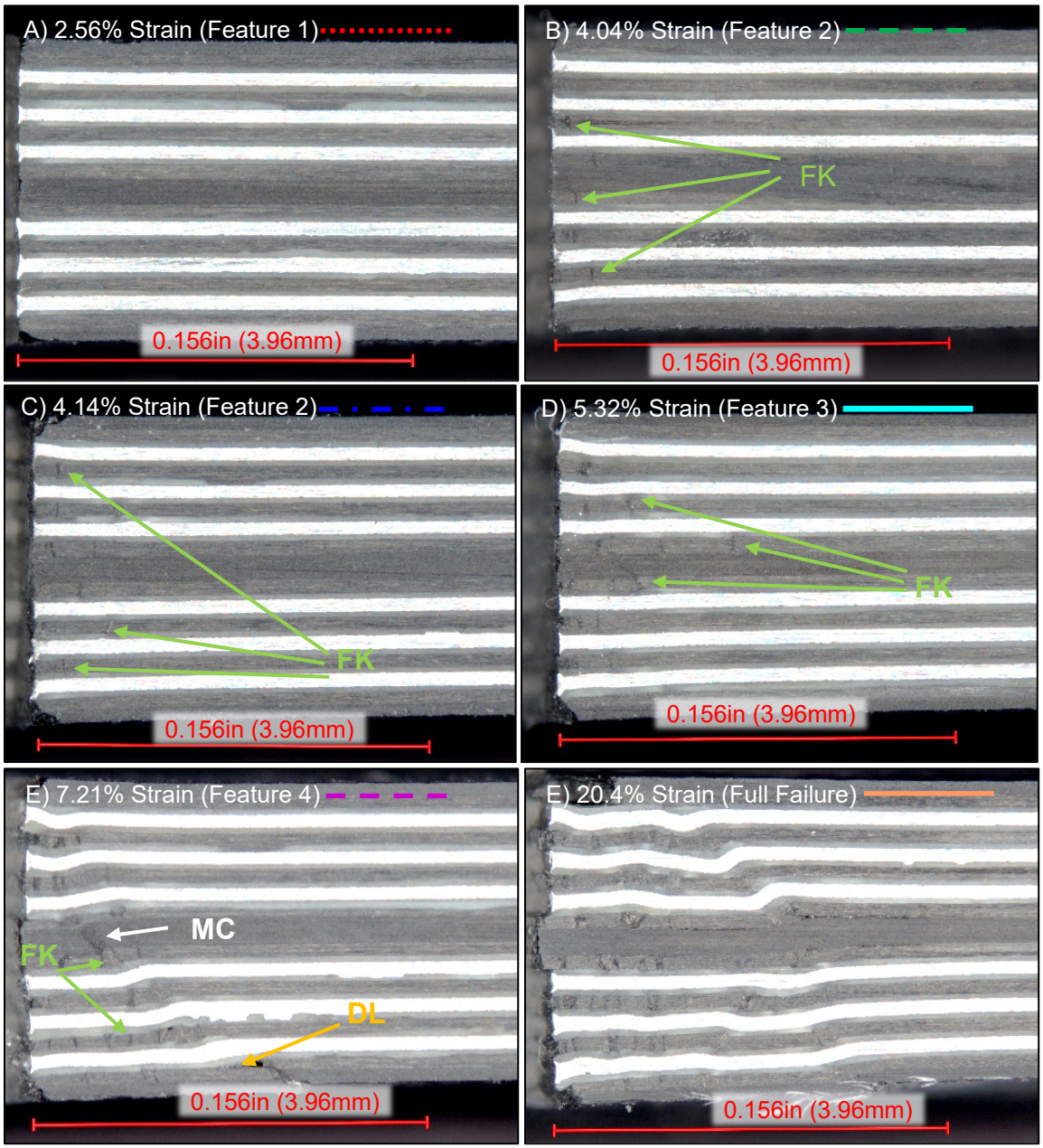

Figure 110:18-Ply Double Shear Hybrid Progressive Failure Micrographs

5.4 Comparison of 9-Ply and 18-Ply Double Shear Results

Since the 18-ply layup was formed by repeating the 9-ply layup, a comparison was made between the performance of the two in both the control and hybrid cases. The practical question being, how well does the 9-ply predict the behavior of the 18-ply? Figure 111 compares the average load-displacement curves for the 9-ply and 18-ply double shear specimens by doubling the load from the 9-ply samples.

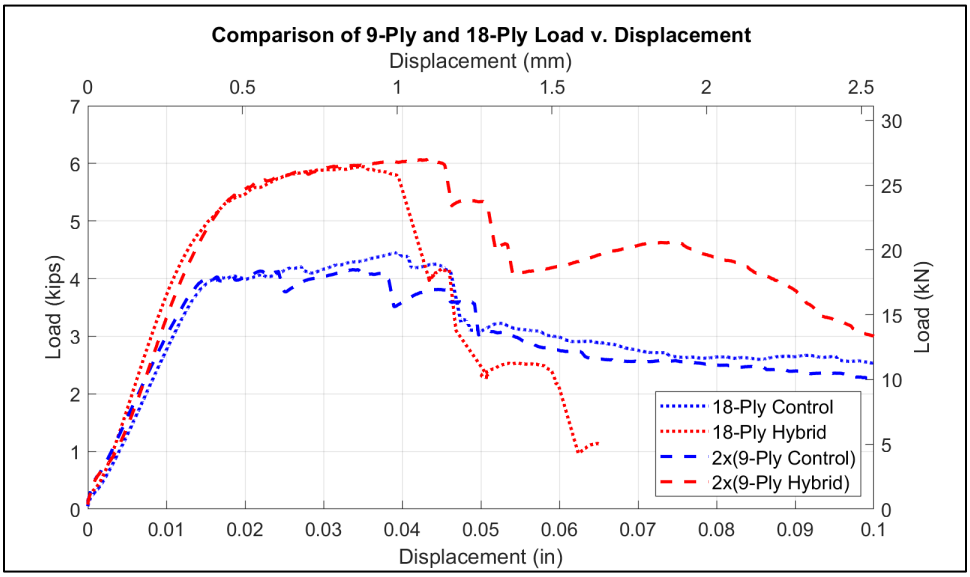

Figure 111: Comparison of 9-Ply and 18-ply Average Load-Displacement

Graphically, the control curves display similarity across the entire displacement. In the hybrid, the curves display similarity until they depart around the 0.040in (1.0mm) point. It was at this point that the 9-ply hybrid samples displayed buckling around the fixture boss while the stiffer 18-ply material displayed a more brittle failure which was characterized by a crack through the thickness of the layup propagating away from the hole (Figure 104). Table 18 shows the load data for the 9-ply layup as a predictor of the 18-ply layup. Here again, the experimental values for the 9-ply layup have been doubled

for comparison. For the control, the 9-ply is an excellent predictor of the 18-ply behavior. The fact that none of the differences are statistically different means that there is not statistical evidence to prove that the two means are different. This is further evidenced by the fact that the 95% confidence intervals largely overlap. For the yield load and offset load, the difference is less than 1%.

Table 18: Control 9-Ply and 18-Ply Load Data

	2x Control 9-Ply			Control 18-Ply					
	Average (95% CI)	Stdev	N	Average (95% CI)	Stdev	N	Diff	% Diff	Stat Sig
Yield Load (kips)	3.693 (3.488-3.899)	0.1954	6	3.670 (3.547-3.793)	0.1329	7	-0.02338	-0.6331	No
Offset Load (kips)	4.075 (3.936-4.214)	0.1321	6	4.053 (3.976-4.129)	0.07285	6	-0.02218	-0.5443	No
Ultimate Load (kips)	4.302 (3.998-4.606)	0.1224	3	4.514 (4.138-4.890)	0.1514	3	0.2123	4.936	No

Table 19 shows a similar comparison for the hybrid layups. In this case, the 9-ply case is not as close of a predictor. It overestimates in yield and offset load almost 11% and 7%, respectively. There is not statistical evidence to prove that the ultimate loads are different.

Table 19: Hybrid 9-Ply and 18-Ply Load Data

	2x Hybrid 9-Ply			Hybrid 18-Ply					
	Average (95% CI)	Stdev	N	Average (95% CI)	Stdev	N	Diff	% Diff	Stat Sig
Yield Load (kips)	4.633 (4.431-4.836)	0.1931	6	4.125 (4.029-4.221)	0.1247	9	-0.5080	-10.96	Yes
Offset Load (kips)	5.499 (5.283-5.715)	0.2058	6	5.110 (5.037-5.183)	0.07886	7	-0.3895	-7.083	Yes
Ultimate Load (kips)	6.109 (5.781-6.436)	0.1318	3	5.940 (5.844-6.035)	0.05972	4	-0.1692	-2.769	No

Further testing and modeling would be required to use a 9-ply layup to predict thicker layups comprised of the same constituents for specific design purposes. However, if considering similar testing or estimates for initial design parameters, using 9-ply testing to predict 18-ply behavior could be useful. 9-ply samples require half the material and layup time. Since foil prep consumed the largest amount of time, reducing the number of foils by half could save days of preparation. Testing 9-ply samples requires less load overall, so preliminary 9-ply samples could be run on a smaller capacity load frame with less stored strain energy in order to predict parameters for a larger scale test.

A feature that is evident in both the control and hybrid cases is that the modulus of each is significantly higher in the 18-ply layups. This is attributed to more complete compaction in the 18-ply layups as discussed in the dimensional results. This difference not only effects the bearing stress calculation and thus the modulus calculation, but it effects the overall properties of the composite, resulting in a stiffer material in the more compacted cases. Similar work has shown that compaction has a direct effect on composite properties similar to that observed here [120], [121].

VI. Computational Results for Double Shear

This chapter presents the results of the computational portion of this research as compared to the double shear experimental results presented in Chapter V. Models were prepared using Abaqus finite element software. This chapter begins with an overview of how the models were represented. Then, the computational results are compared to experimental results separately in 9-ply and 18-ply layups in both control and hybrid configurations. Computational load-displacement curves are compared to those determined experimentally and the ply-level computational behavior is compared with experimental progressive failure microscopy. While over 100 models were developed throughout the course of this research, this chapter focuses on the four models that were the most accurate. Other models are presented only to state why certain methods were included or avoided.

6.1 Model Overview

As detailed in Chapter 3, the finite element models developed in this research employed layerwise modeling where each ply in the layup was modeled as a different part. To ensure that the models performed accurately and efficiently, convergence was performed on the individual components prior to assembling the coupon to optimize mesh arrangements. The mesh arrangements for the components of the coupons are shown in Figure 112. The composite layers were modeled using a fiber aligned mesh arrangement with one continuum shell element through the thickness. The parts representing the ±45°plies (Figure 112A) used 1051 elements per ply and the parts representing the 0°/90° plies (Figure 112B) used 1060 elements. Both had a target

element size at the bearing surface of 0.0250in (.135mm). Hashin criteria were used to describe damage initiation and Benzeggagh-Kenane energy criteria defined damage evolution in the composite layers. Unabridged modeling parameters are provided in Appendix I. The foil and adhesive were modeled using the same structured, concentric mesh arrangement (Figure 112B) using 860 reduced integration 3D stress elements with elements seeded at 0.0250in (.135mm) at the bearing surface. One element was used through the thickness. The final foil model used an elastic-plastic curve derived from experimentation by Roberts [67] with linear damage evolution. Coupled temperature-displacement elements with 3D stress behavior were used for the foil so that physically representative cure induced stresses could be investigated. The bulk of the adhesive was represented as a purely elastic model based on bulk properties of the adhesive.

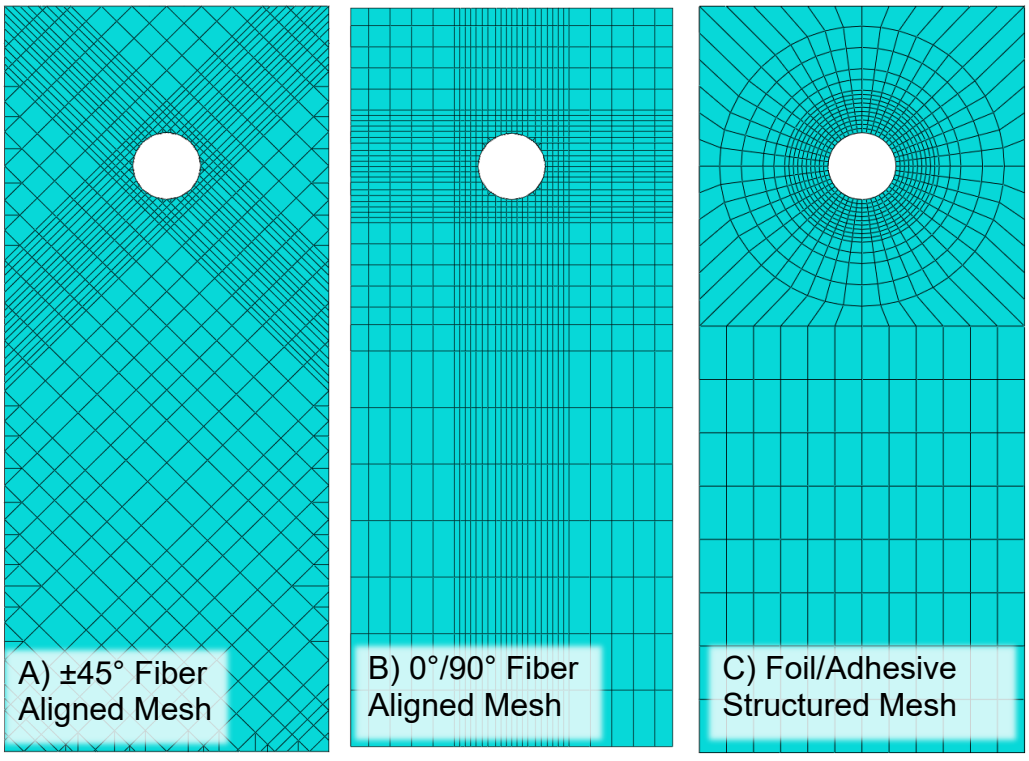

Figure 112: Mesh Arrangements

The final representation for the models considered in this research is depicted in Figure 90. The coupon was assembled with positional constraints and the layers were joined with cohesive interactions. Where two composite layers met or where a composite layer met adhesive, layers were joined with cohesive interactions based on the properties of the composite matrix using traction-separation laws with Benzeggagh-Kenane energy criteria. The joint between the adhesive and foil was defined using published properties of AF191U adhesive defined with traction-separation laws and linear displacement damage evolution. Contact relationships were defined between the individual components of the coupon and the bolt with the bolt as the master part. The fixture bosses were defined as master in contact relationships with the face plies of the coupon. General contact with self-contact was defined for the rest of the model. The bolt was constrained to the fixture using ties and the two parts of the fixture were constrained so that the secondary fixture could move along the bolt axis, which allowed the bolt tightening step to occur. Since the bolt was meshed using coupled temperature-displacement elements with 3D stress behavior, a temperature step could be applied to the bolt to take advantage of thermal expansion (or contraction) to cause a preloading effect on the coupon. The system was loaded by commanding a displacement at the bottom edge of the coupon as depicted in Figure 90.

After the simulation was run, load was taken as the sum of the reaction forces in the y-direction of the nodes to which the displacement was applied. Displacement was recorded as the difference in displacement in two nodes representing the fixture and bonded knife edges as discussed in section 4.6 and shown in Figure 95. Critical values

such as correction factor, yield, offset, and modulus were calculated using the same process applied to the experimental data (section 3.9.3).

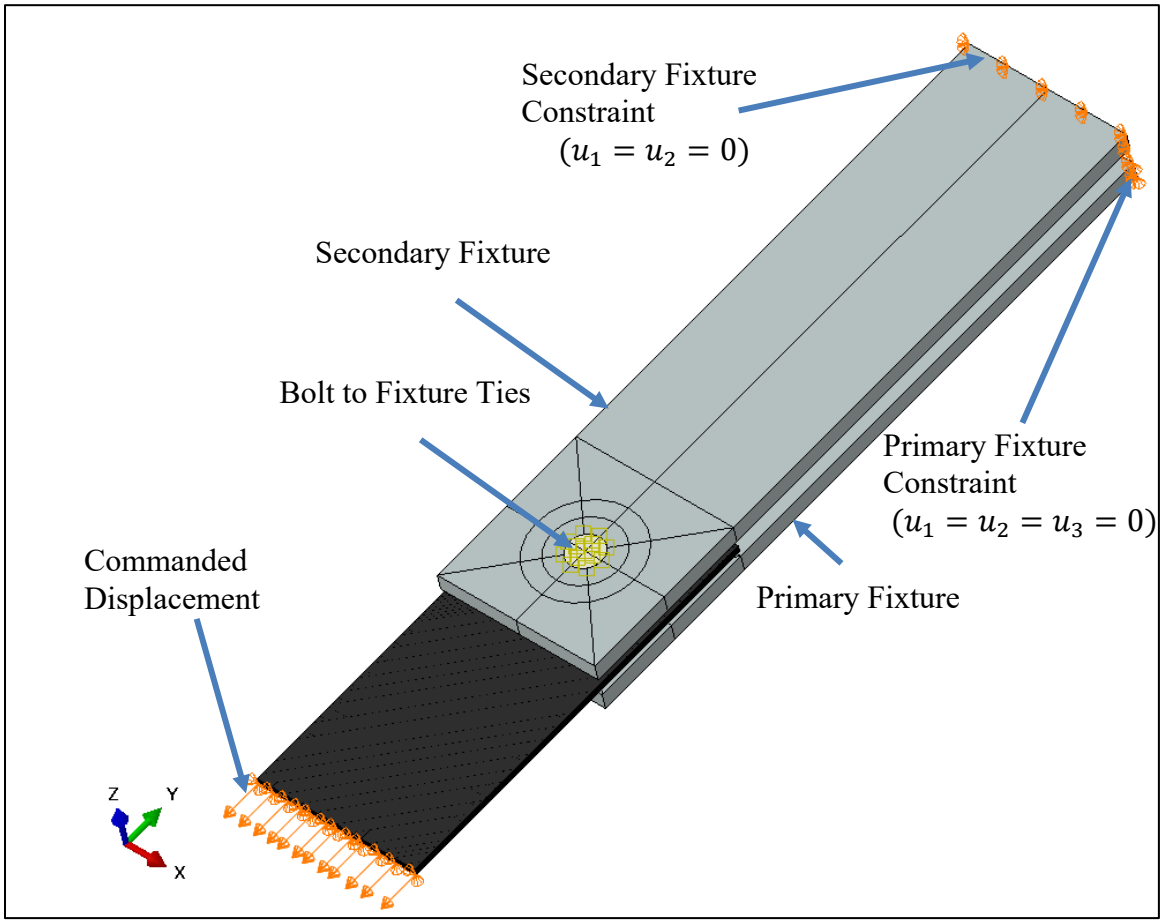

Figure 113: Computational Model and Boundary Conditions

The remainder of this chapter presents the results of each case considered. The materials properties and model parameters were kept constant across all configurations. The only variations between models were those that represent physical variations between the models such as the presence of the adhesive and foil and number of plies. A less obvious example is that the length of the bolt varied in order to accommodate different material thicknesses. This drove slight variations in the number of elements used to model the bolt. Since these physical differences in the real-world configurations

existed and were modeled, a summary table is provided with the discussion of each modeled configuration on the type and number of elements that were used.

6.2 9-Ply Control Computational Results

In order to establish a baseline for the composite behavior, the modeling effort and analysis began with the simplest case of the 9-ply control with a layup sequence of [45/0/-45/0/90/0/-45/0/45]. The summary of the elements employed is listed in Table 20.

Table 20: 9-Ply Control Finite Element Model Summary

Component	Mesh	Element Description	Element Type	# of Elements
Composite	Fiber Aligned	Continuum Shell	SC8R	9504
Bolt	Structured	Coupled Temp-Disp with 3D Stress Behavior	C3D8T	2520
Fixture	Structured	3D Stress Element-Reduced Integration	C3D8R	1364
			Total Elements	13388

As the least complex, this model ran in just over 3 hours using 20 cores. Cores are essentially independent processors that can be tasked to work in parallel. The default Abaqus method is to divide the model into regions or “domains” and assign the calculation for each domain to a single processor which reduces the overall run time of the given simulation [46].

Before analyzing the output of a model to predict quasi-static behavior, the quasi-static assumption must be verified with an energy comparison. The most common practice states that if the kinetic energy remains below 5% of the internal energy, the system is quasi-static [118], [119]. In an explicit analysis, Abaqus records these energy values by default as a history output. Kinetic energy is calculable since nodal velocities

are tracked in the explicit step, and element masses are known. Strain energy (internal energy) is processed in the software from nodal loads and displacements. Figure 114 shows the kinetic energy compared to the internal energy for this case. Since the load rate was increased to facilitate more efficient testing, the energy comparison was employed to ensure that the model was still behaving quasi-statically. The red dashed trace and blue dot-dashed trace in the upper subplot show the internal (strain) energy and kinetic energy respectively, while the green dotted trace in the lower subplot shows the kinetic energy as a percentage of the internal energy. In this case, throughout the computational step time, the kinetic energy is far below 1% of the internal energy. The initial spike is neglected since there is initially no load in the system and no resultant strain energy, but there is motion as the load is applied. Once the application of the bolt load begins, the kinetic energy to internal energy percentage shrinks rapidly and remains low throughout the simulation. Theoretically, the model could be executed with the simulation time set equal to the clock time required to run the experiment. However, in that case, the computation time would likely extend to days or weeks, on the desired computer systems. Based on this energy comparison, the quasi-static assumption holds for this simulation.

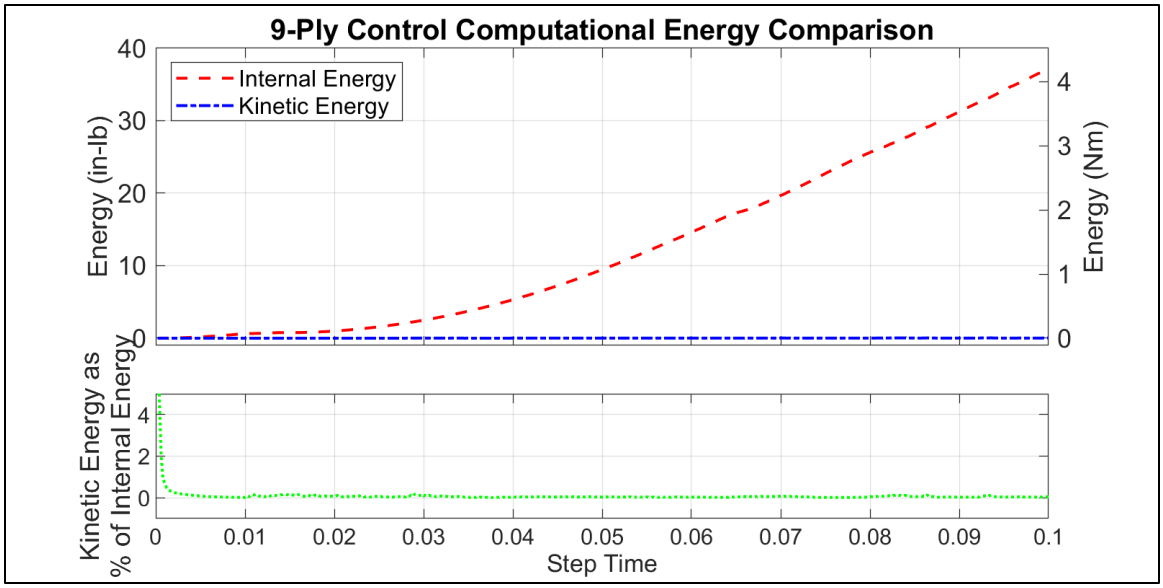

Figure 114: 9-Ply Control Energy Comparison

With the quasi-static assumption verified, the 9-ply control finite element model should be compared to the experimental results. Figure 115 shows the model output compared to the experimental data, and critical values are listed in Table 21 and Table 22. In Figure 115, the load-displacement curve of the 9-ply control model (bold black trace) is plotted over the average of the 9-ply control experimental data (blue trace). The shaded areas represent one and two standard deviations away from the experimental average. The computational curve predicts the experimental behavior well, with the model lying within two standard deviations for the majority of the simulation. The first instance of each failure initiation as well as damage evolution are marked on the computational curve. Due to the compressive nature of the load scenario, matrix compression initiation and cohesive damage initiation arise early in the simulation on the surface that contacts the bolt. Next, matrix tension arises as a result of the Poisson effect caused by loading fiber compression. Thus, fiber compression damage is initiated next.

Since the fiber compression mode has the highest stress capacity by far, it dominates the failure and is equated to the fiber kinking seen in the experimentation. From the model, yield will occur only after fiber compression damage is well into the evolution stage. Just after yield, full damage exists in every mode. In looking at the initial loading, it is important to note that the slack in the bolted joint near 250lbf (1110N) happens at a similar load in both the experimental and computational curves. This indicates that the bolt tension application and frictional contact parameters functioned well.

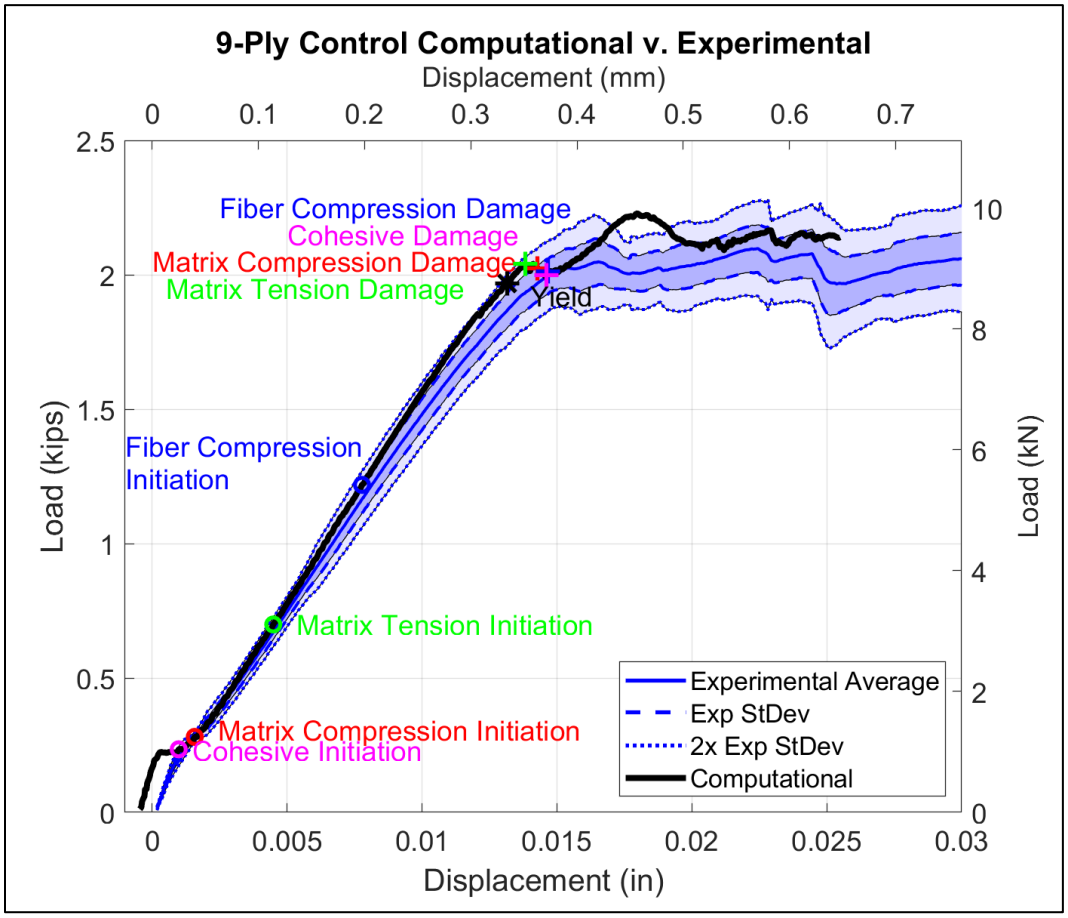

Figure 115: 9-Ply Computational v. Experimental Results

Table 21 and Table 22 list critical load-based values and stress-based values respectively as produced by the finite element model compared to averaged experimental data. Across all values, the finite element model predicts the experimental average within 10%, with some values near 1% error. From a load perspective, the model over-predicts the yield load by only 6.5%. Since hole failure in aerospace applications is typically measured in elongation, the yield displacement prediction with less than 1% error is quite remarkable. This, in addition to the offset displacement and ultimate load, fall within the 95% confidence interval of the experimental average values. In Table 22, the stress values deviate from the experimental values slightly more than the load based values. This is because the final modeled thickness of the IM7/977-3 plies was based on the thickness of the 18-ply samples. However, from the dimensional statistics, the 18-ply layups achieved more complete compaction which resulted in an individual ply which was about 2% thinner. Thus, the modeled thickness of the individual plies in the 9-ply layup is slightly thicker than the condition as modeled. This resulted in a slight inflation of stress-based values shown in Table 22. Despite this, the stress values still lie within 10% error. The yield strain, offset strain, and ultimate stress all lie within the 95% confidence interval of the experimental value.

Table 21: 9-Ply Control Computational v. Experimental Load Data

	9-Ply Control Load-Based				
	Computational	**Experimental Avg (95% CI)**	**Diff**	**% Diff**	**Comp Falls in 95% CI**
Yield Load (kips)	1.966	1.847 (1.744-1.949)	-0.1193	-6.458	No
Yield Disp (in)	0.01315	0.01301 (0.01221-0.01380)	-1.423E-04	-1.094	Yes
Offset Load (kips)	2.137	2.038 (1.968-2.107)	-0.09945	-4.881	No
Offset Disp (in)	0.01673	0.01678 (0.01608-0.01748)	5.102E-05	0.3041	Yes
Ultimate Load (kips)	2.228	2.151 (1.999-2.303)	-0.0770	-3.580	Yes

Table 22: 9-Ply Control Computational v. Experimental Stress Data

	9-Ply Control Stress-Based				
	Computational	**Experimental Avg (95% CI)**	**Diff**	**% Diff**	**Comp Falls in 95% CI**
Yield Stress (ksi)	137.5	125.3 (118.0-132.6)	-12.183	-9.722	No
Yield Strain	0.04221	0.04176 (0.03920-0.04432)	-4.517E-04	-1.082	Yes
Offset Stress (ksi)	149.5	138.2 (134.1-142.4)	-11.265	-8.149	No
Offset Strain	0.05372	0.05387 (0.05162-0.05613)	1.517E-04	0.2815	Yes
Ultimate Stress (ksi)	155.8	149.1 (134.3-163.8)	-6.730	-4.515	Yes
Modulus (ksi)	3419	3155 (3032-3278)	-264.1	-8.370	No

This model proved the efficacy of this modeling method and set a robust baseline from which the more complex models could be developed. The most important factor was the employment of cohesive layers. In early models considered in this research, the stacked plies were joined using ties. Ties essentially lock the spacing between tied nodes. A load-displacement curve for the 9-ply control model using ties between composite plies is pictured in Figure 116. This shows that behavior of the model using ties is far too stiff to represent the actual system. From here, cohesive elements were employed but

drastically increased computation times due to the thinness of the layers required to represent the interlaminar matrix region. The cohesive elements also proved to be very sensitive boundary conditions, loading, and contact relationships. The employment of cohesive interactions proved to be accurate as well as more computationally efficient while also being more intuitive for the user.

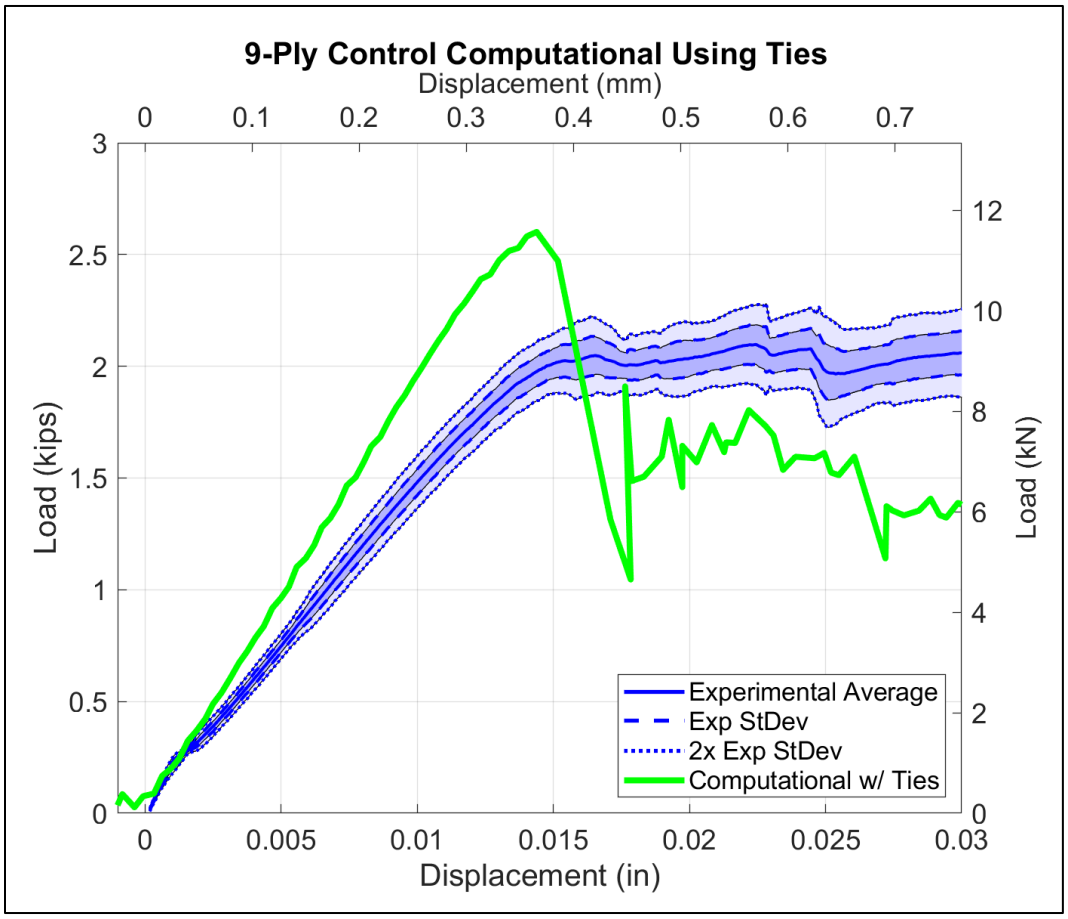

Figure 116: Computational Model Using Ties

Finite element models provide the capability to not only see through-thickness sections of a sample as with experimental coupons, but they also provide the capability to study criteria over the entire area of a given ply.

Table 23 shows the functionality of the Hashin damage initiation criteria at the computationally determined yield. A contour plot of each ply orientation is presented depicting Hashin Fiber Compression and Hashin Matrix Compression. The fiber direction is marked on each image. The bottom row displays quadratic stress damage initiation criteria for the cohesive interaction used to model the interlaminar relationship. As expected in the composite layers, the fiber compression damage is initiated near the bearing surface in the fiber direction while matrix compression damage is initiated near the bearing surface 90° to the fiber direction. In row 2 of Table 23, fiber compression is shown as being the most developed in the most central 0° plies. Cohesive damage (last row of Table 23) is initiated at the nodes near the bearing surface.

Table 23: Damage Initiation Criteria at Yield

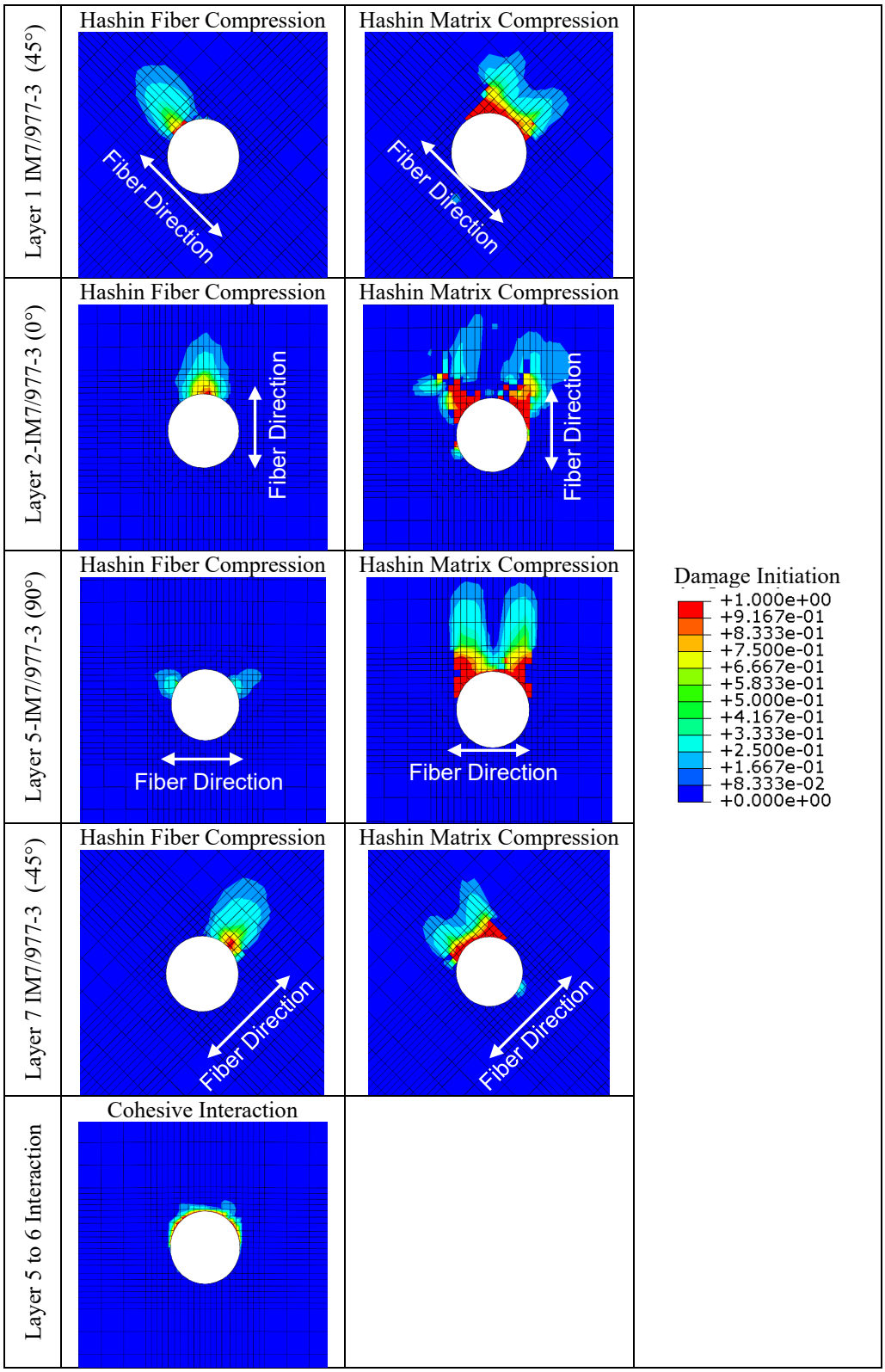

Figure 117 shows 3D sectioned views of damage evolution criteria as compared to an experimental sample tested to 6.40% strain (Figure 117B), which lies just beyond yield. Most evident is the fiber compression damage in the 0° plies which dominates the failure. This damage correlates well to the fiber kinking that arose in the experimental sample in the 0° plies (Figure 117A compared to Figure 117B). Figure 117C displays matrix compression failure in the ±45° and 90° plies. While this is more widespread and developed in the computational model, it is indicative of the matrix cracking that has developed in the experimental sample. Figure 117D plots the damage evolution criteria for the cohesive interactions. At this point, the damage has not fully evolved (value is less than 1). While this appears artificially elevated at the nodes on the bearing surface due to the complexities of contact at those nodes, away from the bearing surface, this is a good predictor of delamination and crushing behavior as strain progresses.

Behavior closest to yield here was selected because it should be the most important point to understand from a design perspective. While the behavior at any of the features is academically interesting, and important to characterize for survivability, engineers typically design based on factors of safety of yield. Additionally, the models were displaced to 0.030in (0.76mm) for modeling efficiency. Since the models were constructed completely in the native Abaqus environment, they simulate bearing behavior accurately to about 8% bearing strain. Accurate modeling beyond that point would require the use of user defined subroutines which would increase complexity and computation time. Because of software requirements, the employment of user subroutines is nearly logistically impossible on government computer systems.

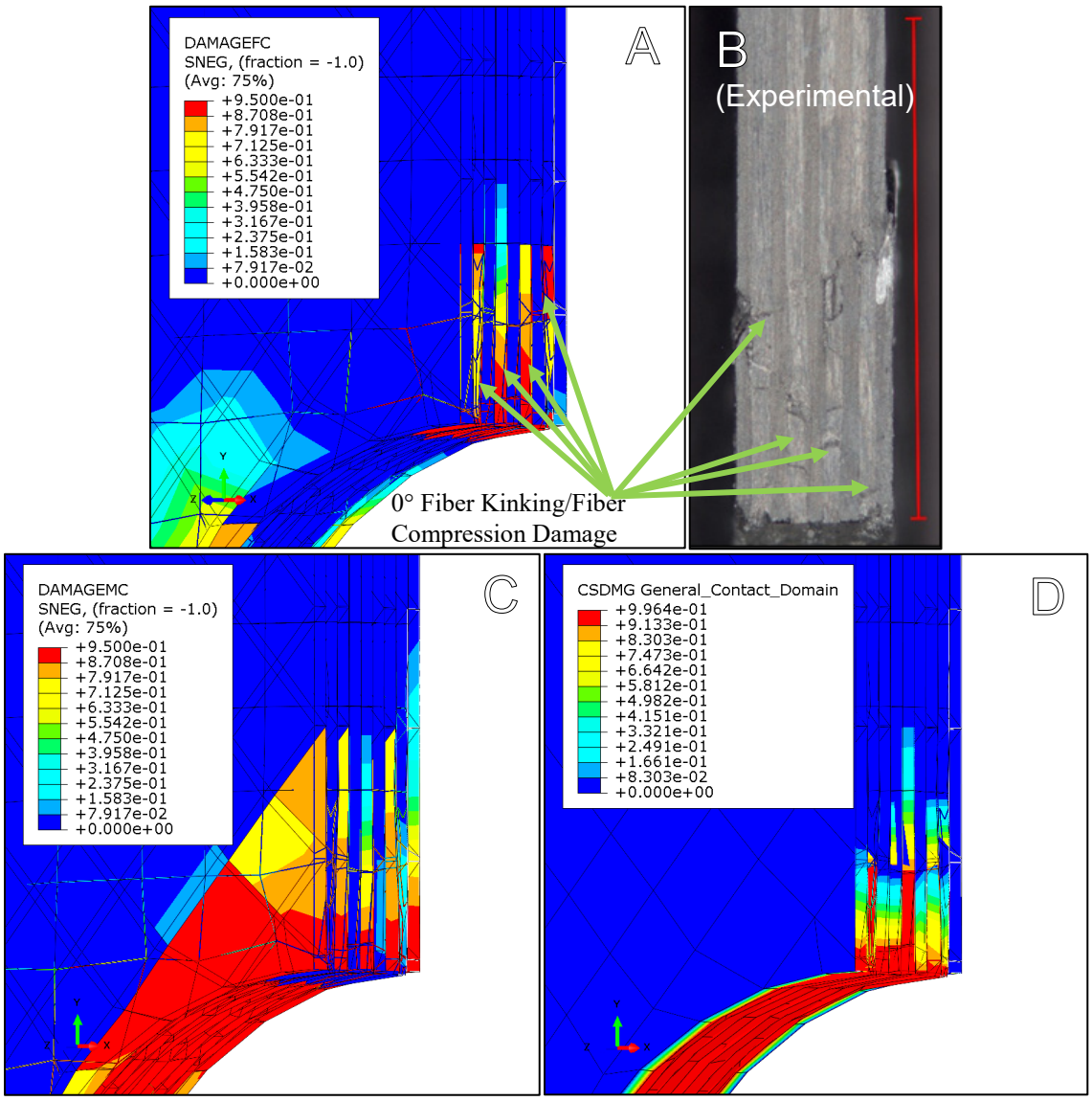

Figure 117: 9-Ply Computational v. Experimental Sectioned at 6.4% Strain
A) Fiber Compression Damage B) Experimental Sample
C) Matrix Compression Damage D) Cohesive Damage

6.3 18-Ply Control Computational Results

With the baseline established in the 9-ply control, the 18-ply control case was modeled using the exact same properties and criteria which resulted in a layup of $[45/0/-45/0/90/0/-45/0/45]_{2.}$ Increasing ply count not only increased the number of elements by 75%, it also increased the number of nodes involved in complex contact interaction which are computationally expensive. Due to the complexity of doubling the number of plies, the computation time grew to just over 5 hours on 20 cores. A summary of the mesh and element arrangement is provided in Table 24. A 10% increase in the number of elements used to define the bolt was caused by the increase in coupon thickness.

Table 24: 9-Ply Control Finite Element Model Summary

Component	Mesh	Element Description	Element Type	# of Elements
Composite	Fiber Aligned	Continuum Shell	SC8R	19008
Bolt	Structured	Coupled Temp-Disp with 3D Stress Behavior	C3D8T	2800
Fixture	Structured	3D Stress Element-Reduced Integration	C3D8R	1364
			Total Elements	23172

As with the previous case, the energy comparison in Figure 118 demonstrates that the kinetic energy is less than 1% of the internal energy throughout the simulation, proving that the analysis is indeed a good quasi-static approximation.

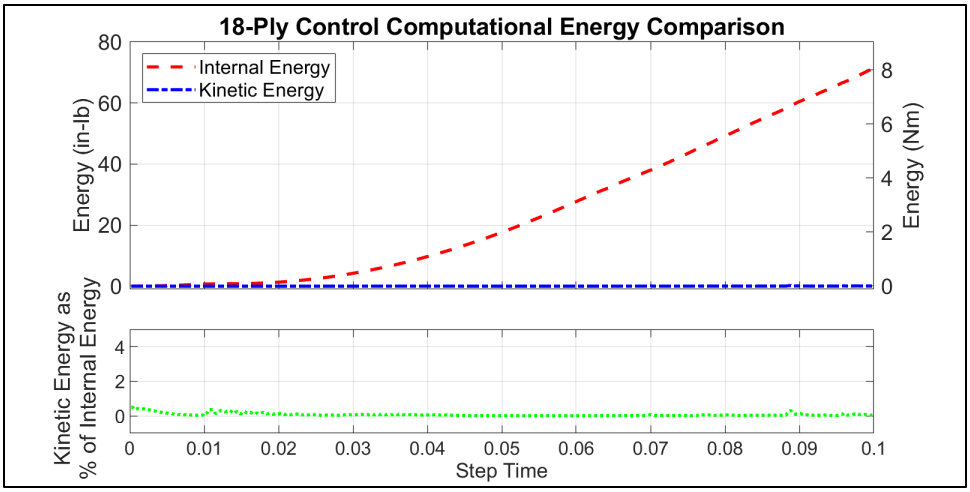

Figure 118: 18-Ply Control Computational Energy Comparison

Figure 119 depicts the 18-ply control finite element load-displacement curve (bold black trace) plotted over averaged experimental data (blue trace). The shaded areas mark one and two standard deviations away from the experimental mean. Here, throughout the entire curve, the model lies within two standard deviations of the experimental average and lies with one standard deviation for much of the curve. Despite increased complexity, the 18-ply case actually follows the experimental average more closely than the 9-ply. This is attributed to the fact that the 18-ply experimental results demonstrate a stiffer modulus, which more closely matches the modulus of the simulation. As in the previous case, the damage initiation and evolution points of each criterion are marked. As noted in the 9-ply case, yield cannot occur until fiber compression damage has been initiated. In contrast to the 9-ply simulation, matrix compression damage here evolves just before the calculated yield value.

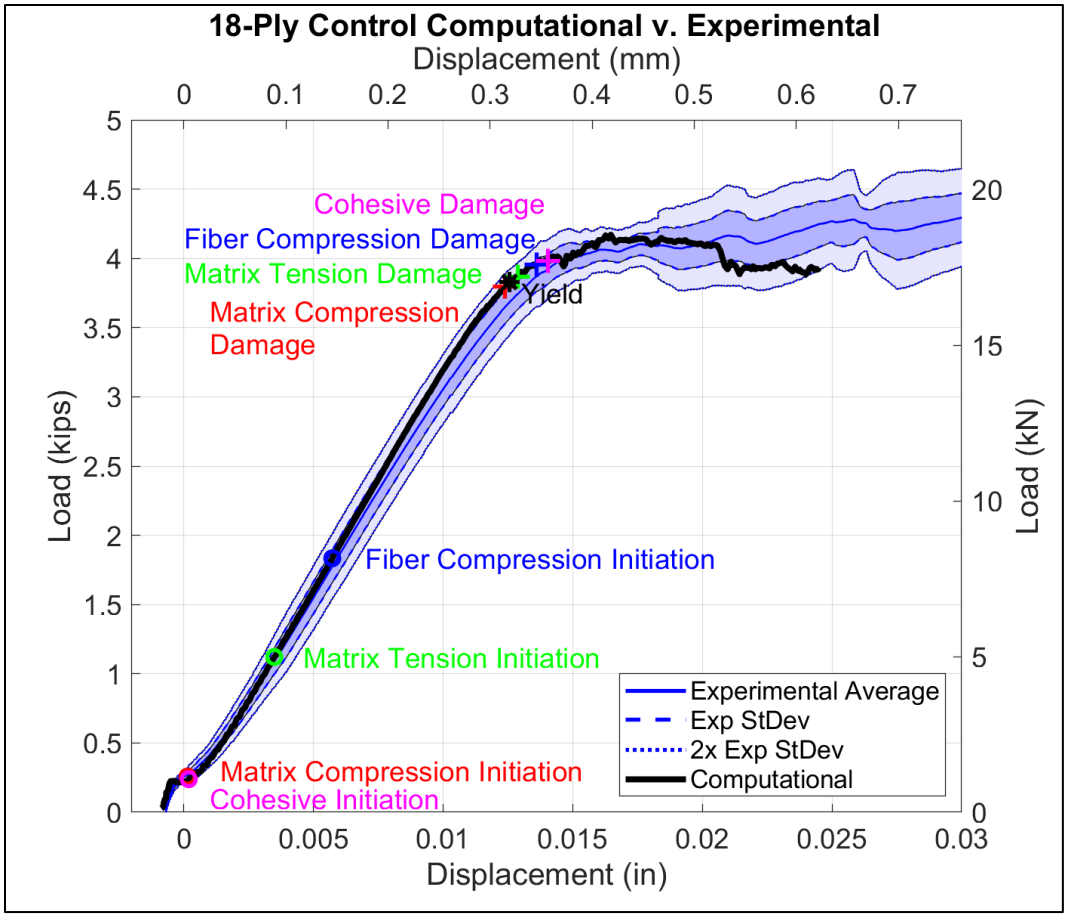

Figure 119: 18-Ply Control Computational v. Experimental Results

Table 25 and Table 26 compare the computational load-based and stress-based data to the experimental average values. Here, the error in the yield load prediction is reduced to nearly 4%, while the yield displacement, which is used to measure hole failure in aerospace applications, displays an error of only 0.11%. The predictions for the 1% offset are also remarkably close, both lying within the 95% confidence intervals for their respective values. Because the modeled ply thickness was based off the 18-ply experimental data, the stress-based values generally display less error than observed in the 9-ply case. Here all the stress based values in Table 26 lie within the 95% confidence interval of their respective experimental values.

Table 25: 18-Ply Control Computational v. Experimental Load Data

	18-Ply Control Load Based Data				
	Computational	**Experimental Avg (95% CI)**	**Diff**	**% Diff**	**Comp Falls in 95% CI**
Yield Load (kips)	3.827	3.670 (3.547-3.793)	-0.1569	-4.275	No
Yield Disp (in)	0.01257	0.01258 (0.01173-0.01344)	1.438E-05	0.1142	Yes
Offset Load (kips)	4.084	4.053 (3.976-4.129)	-0.03108	-0.7670	Yes
Offset Disp (in)	0.01586	0.01637 (0.01572-0.01701)	5.062E-04	3.093	Yes
Ultimate Load (kips)	4.171	4.514 (4.138-4.890)	0.3433	7.605	Yes

Table 26: 18-Ply Control Computational v. Experimental Stress Data

	18-Ply Control Stress Based Data				
	Computational	**Experimental Avg (95% CI)**	**Diff**	**% Diff**	**Comp Falls in 95% CI**
Yield Stress (ksi)	133.8	128.2 (122.5-133.8)	-5.643	-4.403	Yes
Yield Strain	0.04036	0.04027 (0.03754-0.04300)	-9.000E-05	-0.2235	Yes
Offset Stress (ksi)	142.8	141.3 (137.1-145.4)	-1.550	-1.097	Yes
Offset Strain	0.05092	0.05254 (0.05047-0.0546)	0.001620	3.083	Yes
Ultimate Stress (ksi)	145.9	159.8 (156.9-162.8)	13.95	8.725	Yes
Modulus (ksi)	3489	3361 (3289-3433)	-128.0	-3.809	Yes

Table 27 shows the Hashin damage initiation at the computationally determined yield for each ply orientation. An example of the damage in the cohesive interaction is also provided. As expected, fiber compression damage is initiated near the bearing surface in the fiber direction while matrix compression is initiated at 90° to the fiber direction. Damage in the cohesive interactions is isolated to the elements at the bearing surface. Figure 120 depicts select damage evolution criteria as compared to an experimental sample stressed to 4.30% strain (Figure 120B), which lies just beyond the experimental and computational yield. Fiber compression in the model slightly lags but correctly predicts the location of fiber kinking in the experimental samples (Figure 120A and B). The damage criteria in matrix compression manifests as matrix cracking in subsequent experimental samples (see Figure 107). Matrix compression (Figure 120C) accurately predicts that matrix compression damage has not yet fully evolved in the sectioned plane being observed in the experimental sample. If that were the case, matrix cracking would be expected in the experimental sample, but it is not present here. The interaction damage (Figure 120A) appears to overpredict delamination right at the bearing surface which is not evident in the experimental sample. This is attributed to the contact relationship in the model. When examining one node away from the bearing surface, the cohesive damage displays a much more accurate representation which has not yet predicted delamination.

Table 27: 18-Ply Control Damage Initiation Criteria at Yield

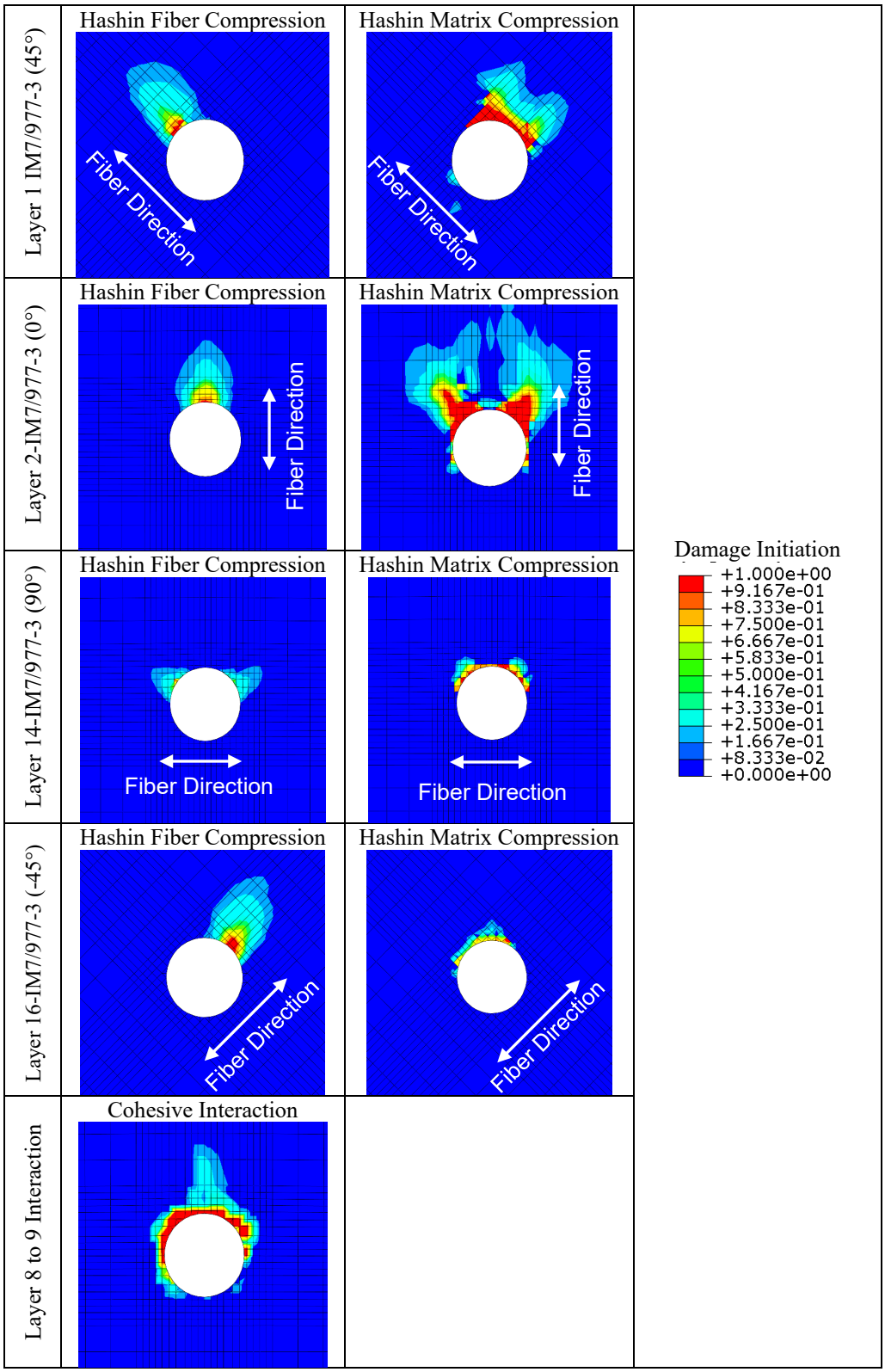

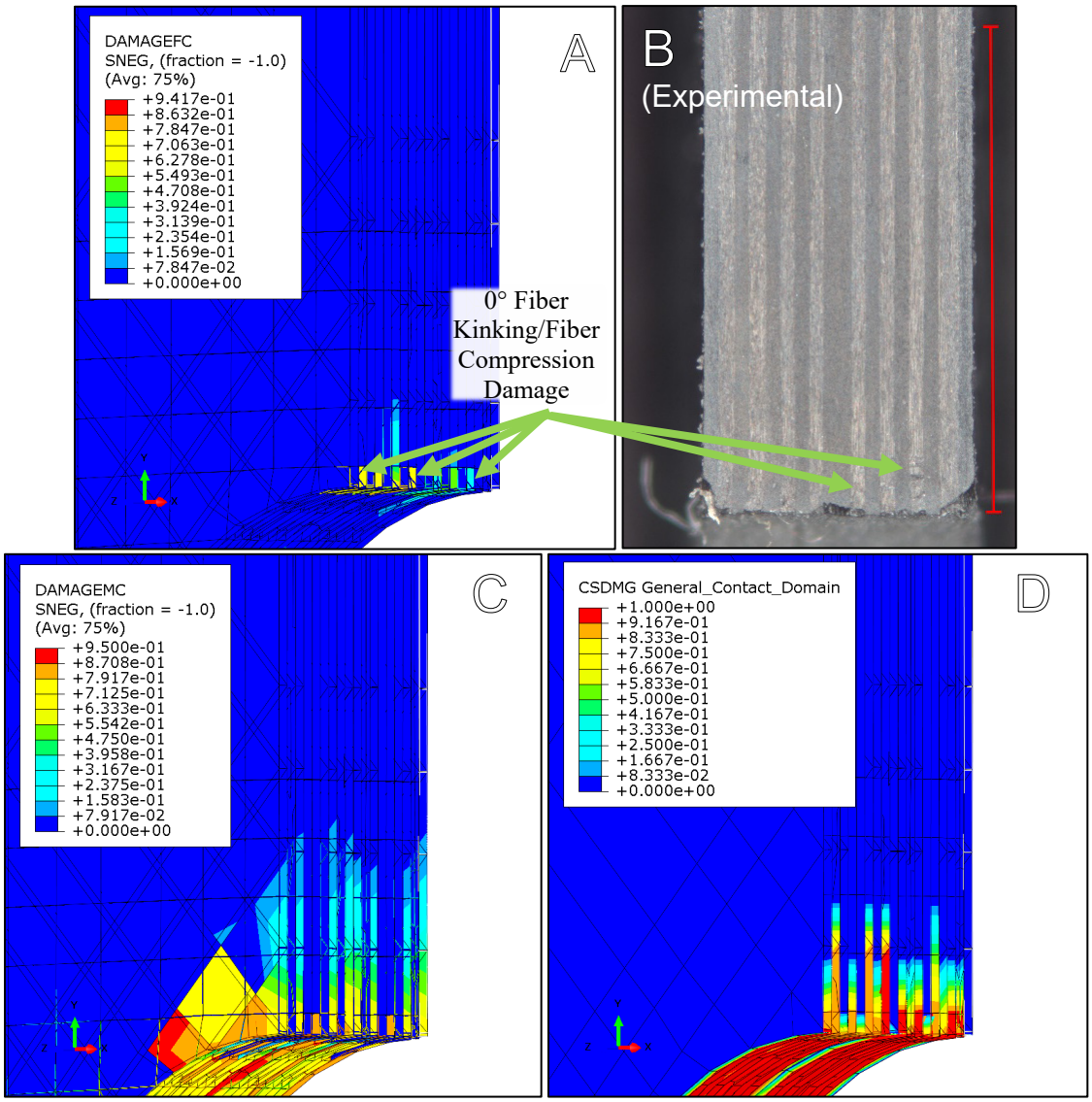

Figure 120: 18-Ply Control Computational v. Experimental Sectioned at 4.30% Strain
A) Fiber Compression Damage B) Experimental Sample
C) Matrix Compression Damage D) Cohesive Damage

6.4 9-Ply Hybrid Computational Results

The 9-ply hybrid was modeled using the same criteria as the control cases with the addition of the properties and damage and failure criteria describing the adhesive and foil to simulate the [45/0/|SS|/0/|SS|/0/|SS|/0/45] layup. The boundary conditions and loading were identical to the control cases except for the temperature step initially applied to the foils to simulate the stresses imparted into the foils during cure, known as cure induced stress. This occurred during the same computational time that the bolt load was being applied using a similar thermal process. During this time, a slight displacement was commanded in the coupon to prevent premature loading of the bearing surface during the temperature step. This kept the bolt centered in the hole until the bolt and foils reached stabilized temperatures after which the physically representative displacement step was applied. Section 6.6 compares the methods used here, to include consideration of thermally induced stresses, with other models that consider less complex model considerations.

Table 28 lists the summary of mesh and element arrangements of each component. This model required a 31% increase in the number of elements as compared to the 9-ply control which allowed the simulation to run in just over 3 hours on 20 cores.

Table 28: 9-Ply Hybrid Model Summary

Component	Mesh	Element Description	Element Type	# of Elements
Composite	Fiber Aligned	Continuum Shell	SC8R	6342
Adhesive	Structured	3D Stress Element-Reduced Integration	C3D8R	4896
Foil	Structured	Coupled Temp-Disp with 3D Stress Behavior and Reduced Integration	C3D8RT	2448
Bolt	Structured	Coupled Temp-Disp with 3D Stress Behavior	C3D8T	2520
Fixture	Structured	3D Stress Element-Reduced Integration	C3D8R	1364
			Total Elements	17570

Before the results can be evaluated, the assumption of quasi-static behavior must be verified. Figure 121 depicts the energy comparison to show that the model is a good quasi-static approximation since the kinetic energy remains below 3% of the internal energy throughout the commanded displacement.

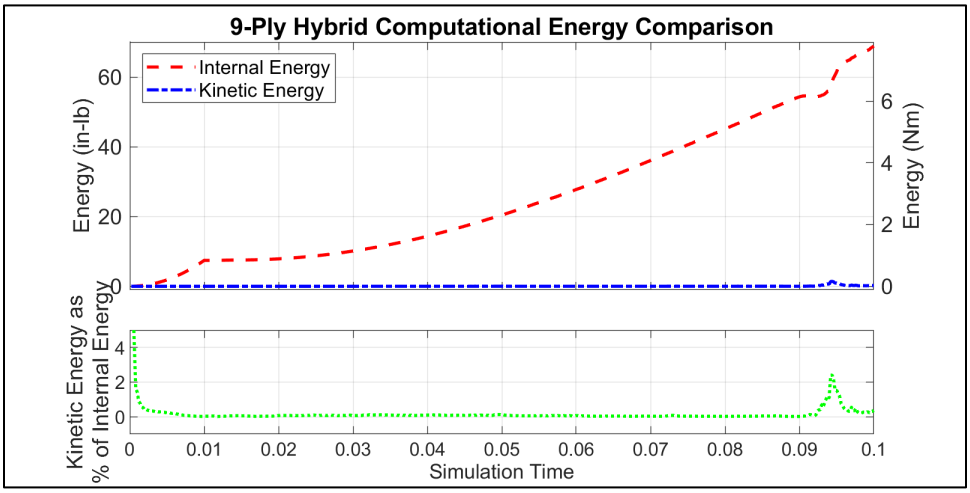

Figure 121: 9-Ply Hybrid Computational Energy Comparison

Figure 122 depicts the 9-ply hybrid computational load-displacement curve (bold black trace) compared to averaged experimental data (red trace). The shaded areas represent one and two standard deviations from the experimental average. For the majority of the simulation, the computational curve lies within one standard deviation of

the experimental data. As in previous cases, the damage initiation and evolution in each mode are marked as they appeared in the simulation. Plasticity arises in the foils earlier than expected, but this plasticity lies only in the elements at the contact surface and is not widespread. In the control cases, damage in the composite fully evolves before or just after yield. In this case, there is substantial displacement after yield until fiber compression and the accompanying matrix tension damage fully evolve. This follows the experimental conclusion that the metal intrinsically changed the failure nature of the hybrid.

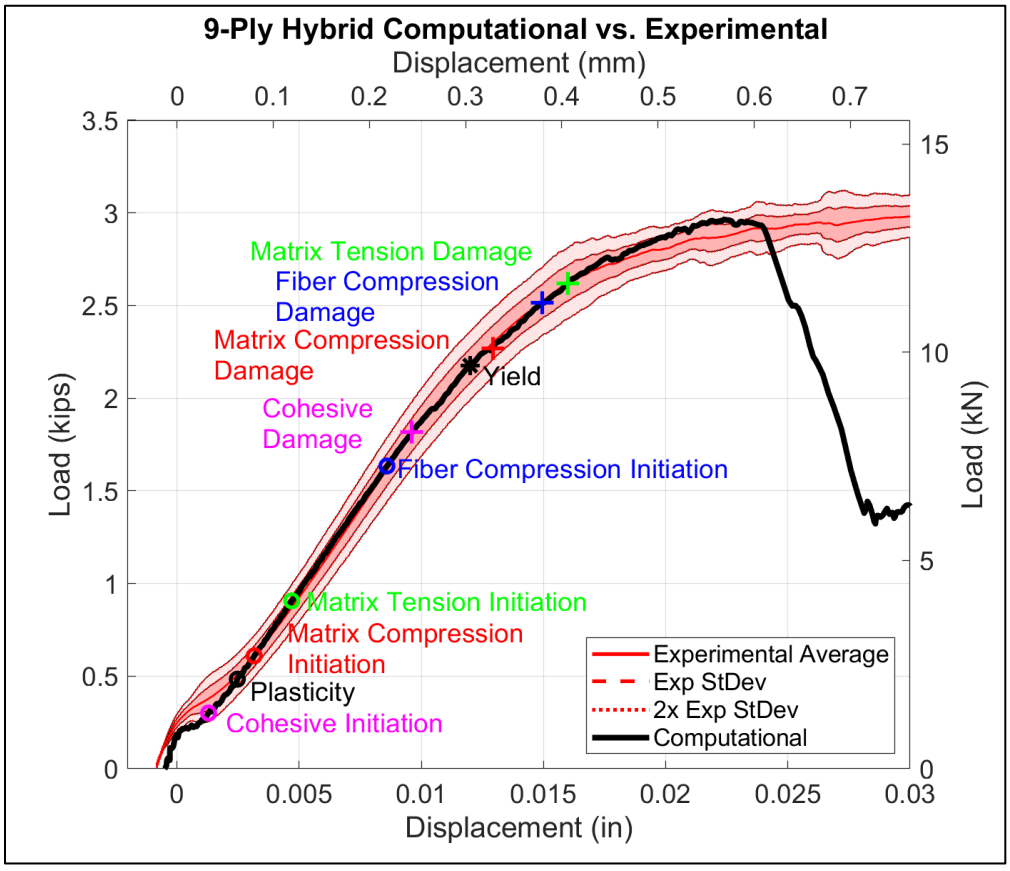

Figure 122: 9-Ply Hybrid Computational v. Experimental Results

Table 29 and Table 30 list the load based and stress based data respectively as compared to the experimental average. In all cases except the yield displacement and yield strain, the simulation differs from the experimental average by less than 6%. The error in the yield and offset values is attributed to the error in the modulus. Since the model begins stiffer than the experimental results, the yield and offset values are predicted slightly early. The magnitude of the relative differences is small, with the magnitude of the error in yield displacement being 0.0015in (0.038mm). The yield load and stress, offset load, displacement, and strain, as well as the ultimate load and stress all lie within the 95% confidence intervals of the respective experimental values meaning these values could statistically be the same as the experimental mean.

Table 29: 9-Ply Hybrid Computational v. Experimental Load Data

	9-Ply Hybrid Load Based Data				
	Computational	**Experimental Avg (95% CI)**	**Diff**	**% Diff**	**Comp Falls in 95% CI**
Yield Load (kips)	2.176	2.317 (2.215-2.418)	0.1406	6.071	Yes
Yield Disp (in)	0.01199	0.01306 (0.01227-0.01386)	0.001074	8.223	No
Offset Load (kips)	2.751	2.750 (2.642-2.858)	-0.001322	-0.04808	Yes
Offset Disp (in)	0.01748	0.01841 (0.01611-0.02071)	9.312E-04	5.058	Yes
Ultimate Load (kips)	2.965	3.054 (2.891-3.218)	0.08933	2.925	Yes

Table 30: 9-Ply Hybrid Computational v. Experimental Stress Data

	9-Ply Hybrid Stress Based Data				
	Computational	**Experimental Avg (95% CI)**	**Diff**	**% Diff**	**Comp Falls in 95% CI**
Yield Stress (ksi)	121.3	123.0 (116.7-129.3)	1.664	1.353	Yes
Yield Strain	0.03849	0.04194 (0.03939-0.04449)	0.003450	8.226	No
Offset Stress (ksi)	153.3	146.0 (139.0-152.9)	-7.350	-5.036	No
Offset Strain	0.05612	0.0591 (0.05173-0.06648)	0.002985	5.050	Yes
Ultimate Stress (ksi)	165.3	162.6 (150.6-174.5)	-2.747	-1.690	Yes
Modulus (ksi)	3324	3092 (2936-3248)	-232.0	-7.503	No

Table 31 depicts the damage initiation criteria at yield in select representative plies in the 9-ply hybrid composite. As in other cases, fiber compression is evident near the bearing surface in the fiber direction with matrix compression observed 90° to the fiber direction. The plastic strain in the foil (row 3 in Table 31) is present mostly in the oblique (±45°) directions and not in the center of the bearing surface. This is because the load in the center of the bearing surface is supported largely by the stiffer 0° carbon fiber tows in that location. Plasticity is asymmetrical because the layup contains +45° plies but the -45° composite plies have been replaced with foils. The matrix damage is initiated close to the bearing surface while the adhesive damage radiates much farther from the hole due to much softer materials properties.

Table 31: 9-Ply Hybrid Damage Initiation Criteria at Yield

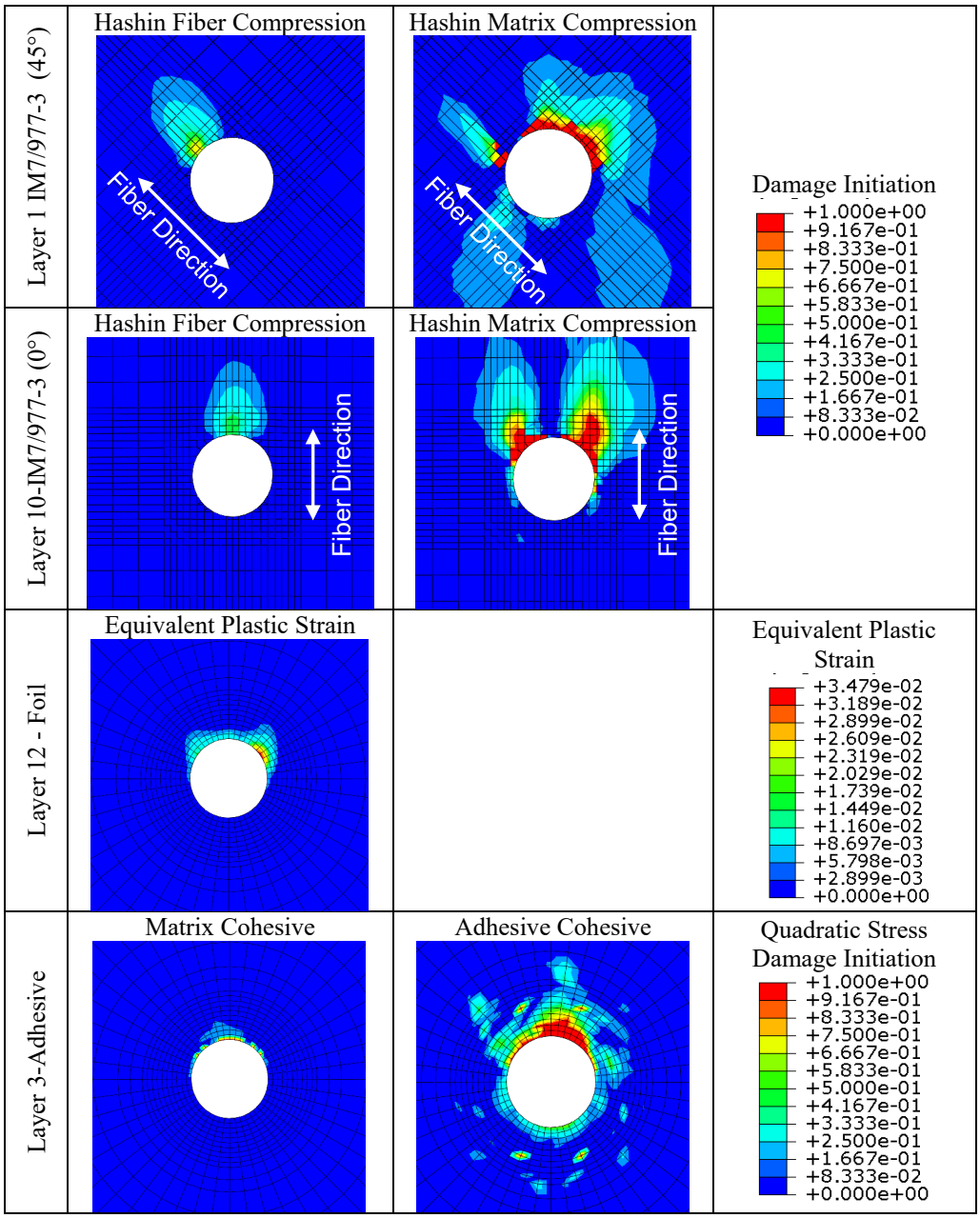

Figure 123 depicts select damage evolution criteria as compared to an experimental sample stressed to 8.39% strain. Due to other progressive failure targets, this is the lowest strain sample available in this configuration. The model predicts the 0° fiber kinking well as compared in Figure 123A and B. The model even predicts the

through thickness cracking as matrix compression (Figure 123C). The model predicts the buckling in the foils well, but it occurs to a greater magnitude earlier than noted in the experimental samples. Figure 123E depicts the out of plane deformation (3 or z direction) in the foils at the corresponding 8.39% strain point. It shows deformation of almost 0.018in (0.46mm), while the deformation noted in the experimental sample foils is less than the thickness of the foils at 0.004in (0.010mm). This is attributed to the shortcomings of the continuum shell elements with respect to predicting through-thickness stresses and the complex contact relationships occurring at the bearing surface. It is also suspected that the bond between the foil and adhesive may be stronger than the available published properties. If experimentation determined a higher failure stress for the bond, then the curve would retain more stiffness near yield and would also delay buckling in the foils. This is further proved by examining Figure 123C which depicts a large area of fully developed delamination at this strain which is not observed in the experimental sample.

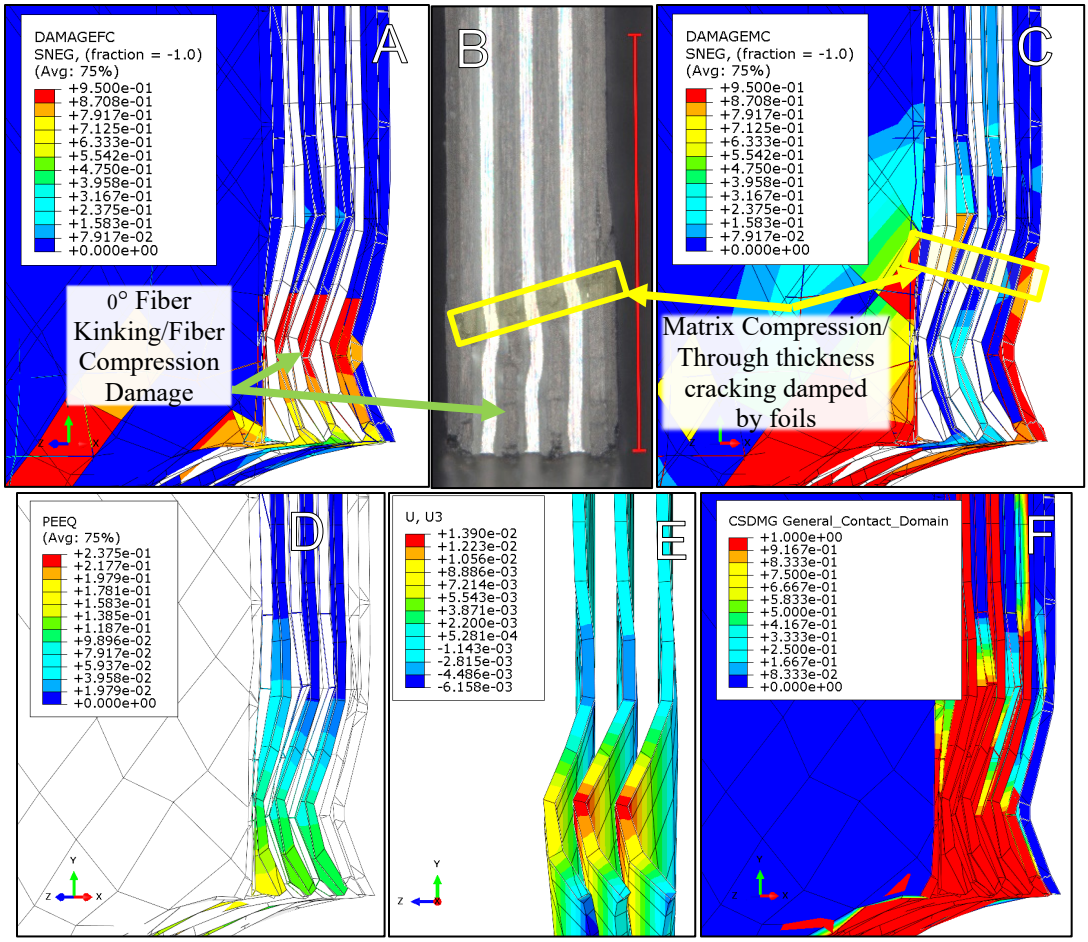

Figure 123: 9-Ply Hybrid Computational v. Experimental Sectioned at 8.39% Strain
A) Fiber Compression Damage B) Experimental Sample
C) Matrix Compression Damage D) Equivalent Plastic Strain
E) Foil Displacement F) Cohesive Damage

6.5 18-Ply Hybrid Computational Results

The 18-ply hybrid model used the exact same materials properties and modeling parameters as the 9-ply hybrid. Doubling the layup $[45/0/|SS|/0/|SS|/0/|SS|/0/45]_2$ required an 80% increase in the total number of elements required. This also increased the number of nodes involved in contact relationships. Representing the most complex case, the 18-ply hybrid simulation ran in 11.5 hours. The run time was lengthened by large deformations reducing the stable time step near the end of the simulation. A summary of the mesh and element arrangement is listed in Table 32. Due to the increased thickness of the coupon, the bolt required a 17% increase in the number of nodes. The 18-ply hybrid used the same procedure used in the 9-ply hybrid to simulate the stresses induced during cure.

Table 32: 18-Ply Hybrid Model Summary

Component	Mesh	Element Description	Element Type	# of Elements
Composite	Fiber Aligned	Continuum Shell	SC8R	12684
Adhesive	Structured	3D Stress Element-Reduced Integration	C3D8R	9792
Foil	Structured	Coupled Temp-Disp with 3D Stress Behavior and Reduced Integration	C3D8RT	4896
Bolt	Structured	Coupled Temp-Disp with 3D Stress Behavior	C3D8T	2940
Fixture	Structured	3D Stress Element-Reduced Integration	C3D8R	1364
			Total Elements	31676

Before the results can be analyzed conclusively, the quasi-static assumption must be verified. The energy comparison in Figure 124 shows that the simulation simulates quasi-static behavior well as the kinetic energy remains below 2% of the strain energy throughout the commanded displacement.

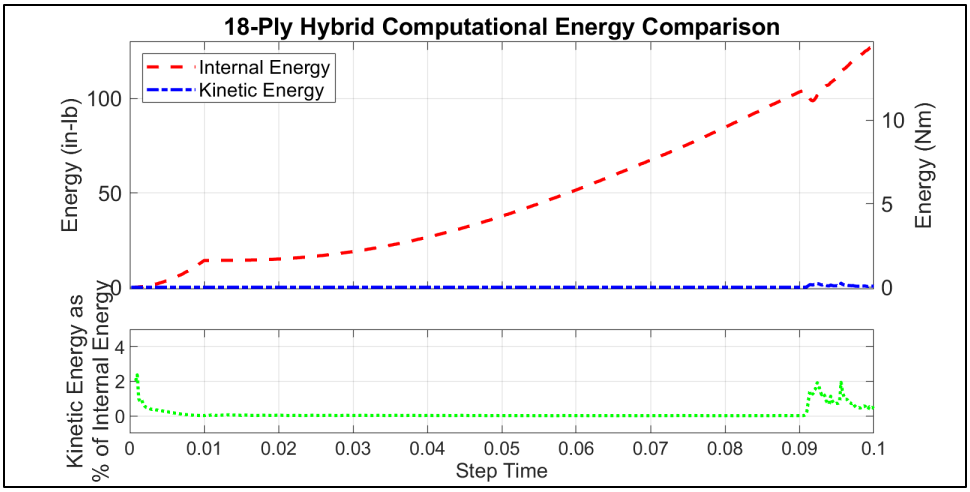

Figure 124: 18-Ply Hybrid Computational Energy Comparison

Figure 125 depicts the 18-ply computational load-displacement curve (bold trace) plotted over the experimental average. The shaded areas represent one and two standard deviations away from the experimental average. The damage initiation and evolution criteria demonstrate some uniqueness here. In this case, fiber compression evolution occurs well after yield. This demonstrates that the yield behavior is much more dependent on the foils. This is also supported by the more ductile shape of the curve as compared to the controls. The model displays less stiffness compared to the experimental curve which is also indicative of an adhesive damage initiation stress that is lower than what occurred in the actual samples. This model proved the requirement to represent the foil using experimental data instead of published data, and proved the necessity of considering thermally induced stress in the foil. This is expounded upon in Section 6.6

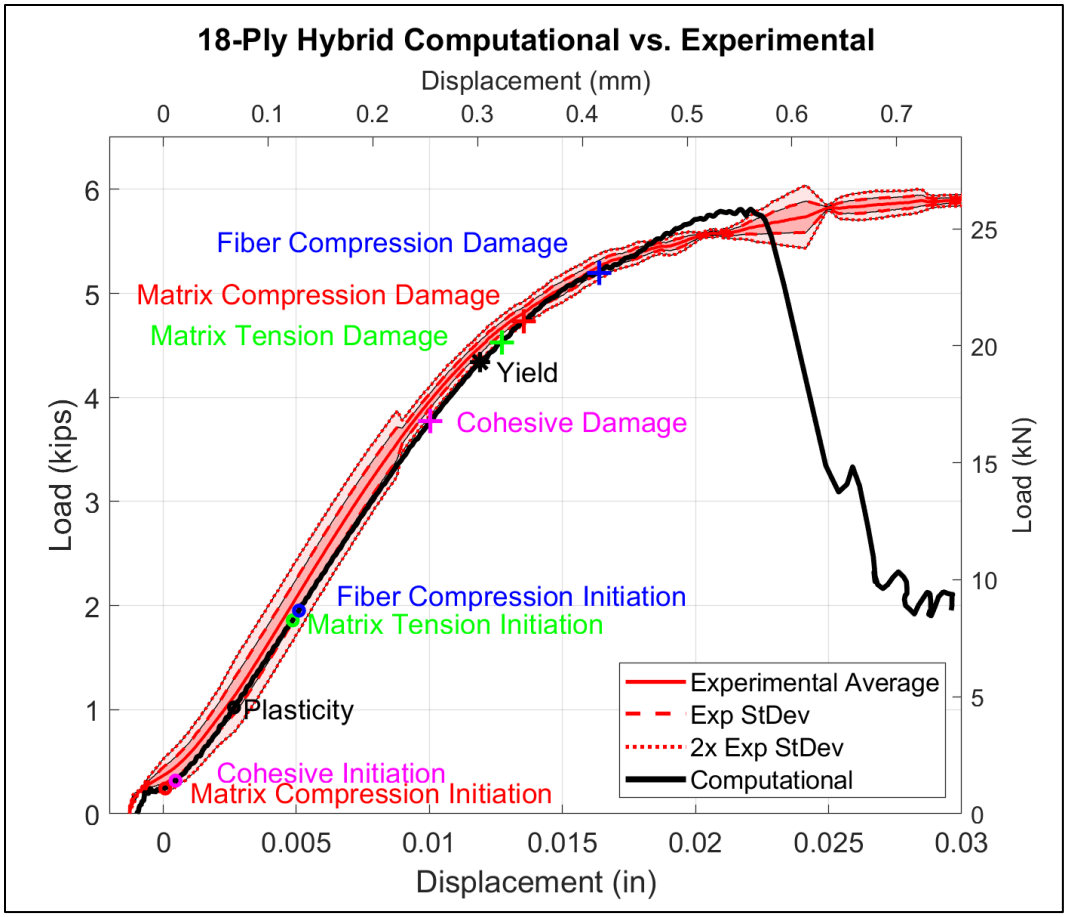

Figure 125: 18-Ply Hybrid Computational v. Experimental Results

Table 33 and Table 34 show the hybrid computational load-based data and stress-based data respectively, as compared to experimental averaged data. Considering that this is the most complex simulation, it has modeled the yield, offset and ultimate loads remarkably well with all lying inside 5% error. Here, the simulation has slightly under-predicted the chord stiffness (modulus) as noted in Table 34, which has, in-turn, induced errors in where the yield and offset lines pass through the modeled curve. Though the error by percentage in strain and displacement might seem large, the magnitude of the error in yield strain is less than 0.5% strain.

Table 33: 18-Ply Hybrid Computational v. Experimental Load Data

	18-Ply Hybrid Load Based Data				
	Computational	**Experimental Avg (95% CI)**	**Diff**	**% Diff**	**Comp Falls in 95% CI**
Yield Load (kips)	4.341	4.125 (4.029-4.221)	-0.2157	-5.230	No
Yield Disp (in)	0.01189	0.01056 (0.01013-0.01099)	-0.001334	-12.63	No
Offset Load (kips)	5.250	5.110 (5.037-5.183)	-0.1401	-2.742	No
Offset Disp (in)	0.01647	0.01538 (0.01494-0.01581)	-0.001091	-7.093	No
Ultimate Load (kips)	5.810	5.940 (5.844-6.035)	0.1295	2.180	No

Table 34: 18-Ply Hybrid Computational v. Experimental Load Data

	18-Ply Hybrid Stress Based Data				
	Computational	**Experimental Avg (95% CI)**	**Diff**	**% Diff**	**Comp Falls in 95% CI**
Yield Stress (ksi)	121.0	111.8 (108.9-114.7)	-9.173	-8.203	No
Yield Strain	0.03818	0.03379 (0.03242- 0.03515)	-0.004391	-13.00	No
Offset Stress (ksi)	146.3	138.694 (136.4-140.9)	-7.606	-5.484	No
Offset Strain	0.05374	0.04937 (0.04797- 0.05077)	-0.004369	-8.848	No
Ultimate Stress (ksi)	161.9	161.3 (157.2-165.3)	-0.6400	-0.3969	Yes
Modulus (ksi)	3344	3518 (3446-3590)	173.7	4.937	No

Table 35 depicts the failure initiation criteria in select layers for the 18-ply hybrid model. The fiber compression and matrix compression behave as expected with fiber compression being initiated in the fiber direction and matrix compression being initiated 90° to the fiber direction. Again, the plasticity in the foil (Table 35 row 3) exists away from the center of the bearing surface since the load in that region is largely supported by

the stiffer 0° fibers. As also noted in the thinner hybrid, there is a slight asymmetry in the plasticity due to the existence of +45° plies and the lack of -45° plies. The cohesive damage on the matrix side of the adhesive is localized near the hole, while the more compliant adhesive side expands farther away from the hole. The cohesive damage initiation is very localized in the strong and stiff interlaminar matrix while it is more widespread in the more compliant adhesive representation (Table 35 row 4).

Table 35: 18-Ply Hybrid Damage Initiation Criteria at Yield

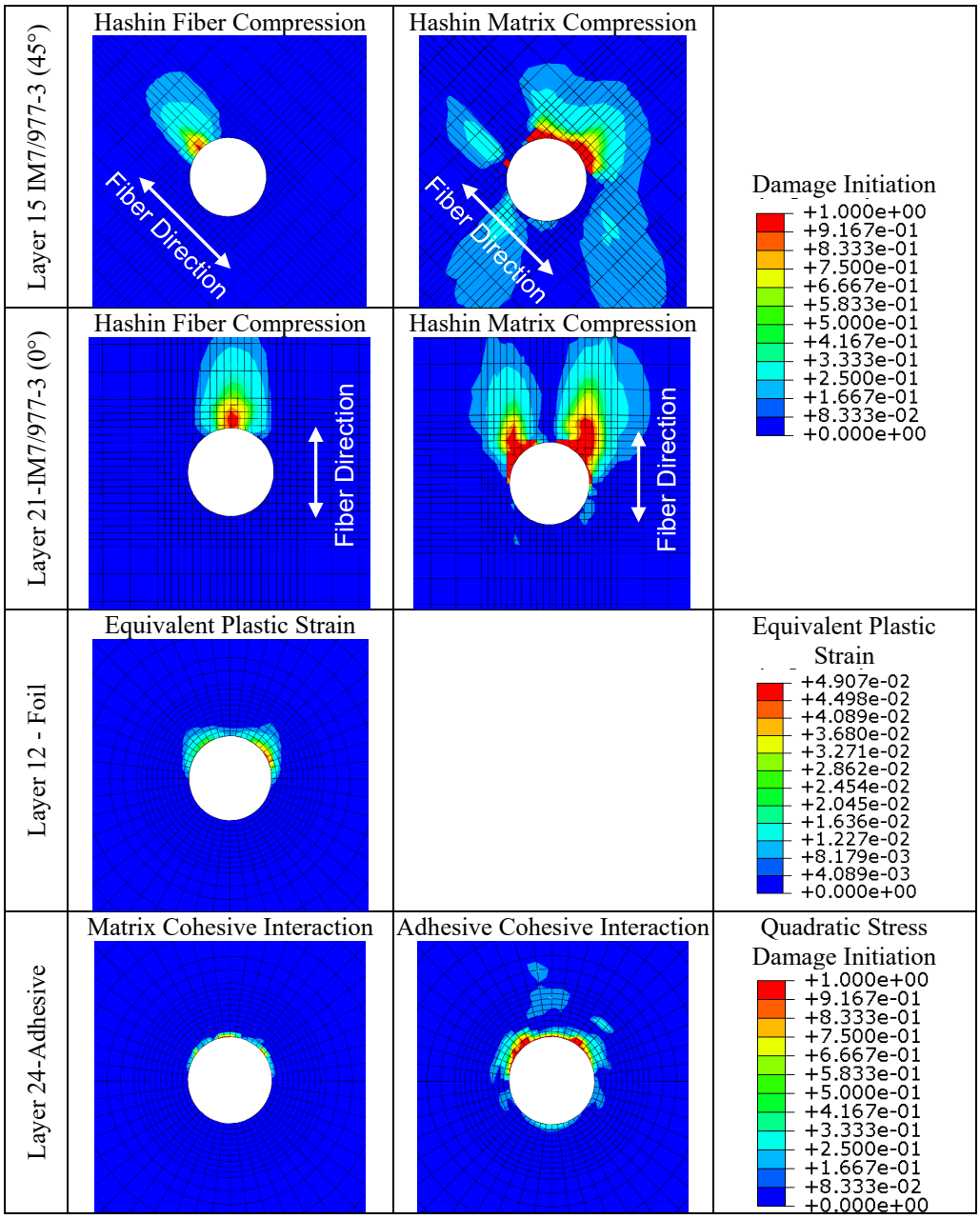

Figure 126 depicts sectioned contour plots from the 18-ply hybrid model as compared to an experimental coupon loaded to 5.32% strain, which lies just beyond yield. As in other cases, the fiber compression damage manifests as fiber kinking in the 0° plies (compare Figure 126A and B). Matrix compression damage is manifest as matrix

cracking in the 45° plies. At this fairly low strain, mild buckling is visible in the model (Figure 126D) which matches the coupon. The cohesive damage indicates delamination between the foil and adhesive that is not present in the foil. This supports the assertion that an experimental value of the bond between the adhesive and foil should be determined. This would increase the stiffness in the curve in Figure 125 which would more accurately predict critical values at yield, offset, and ultimate points.

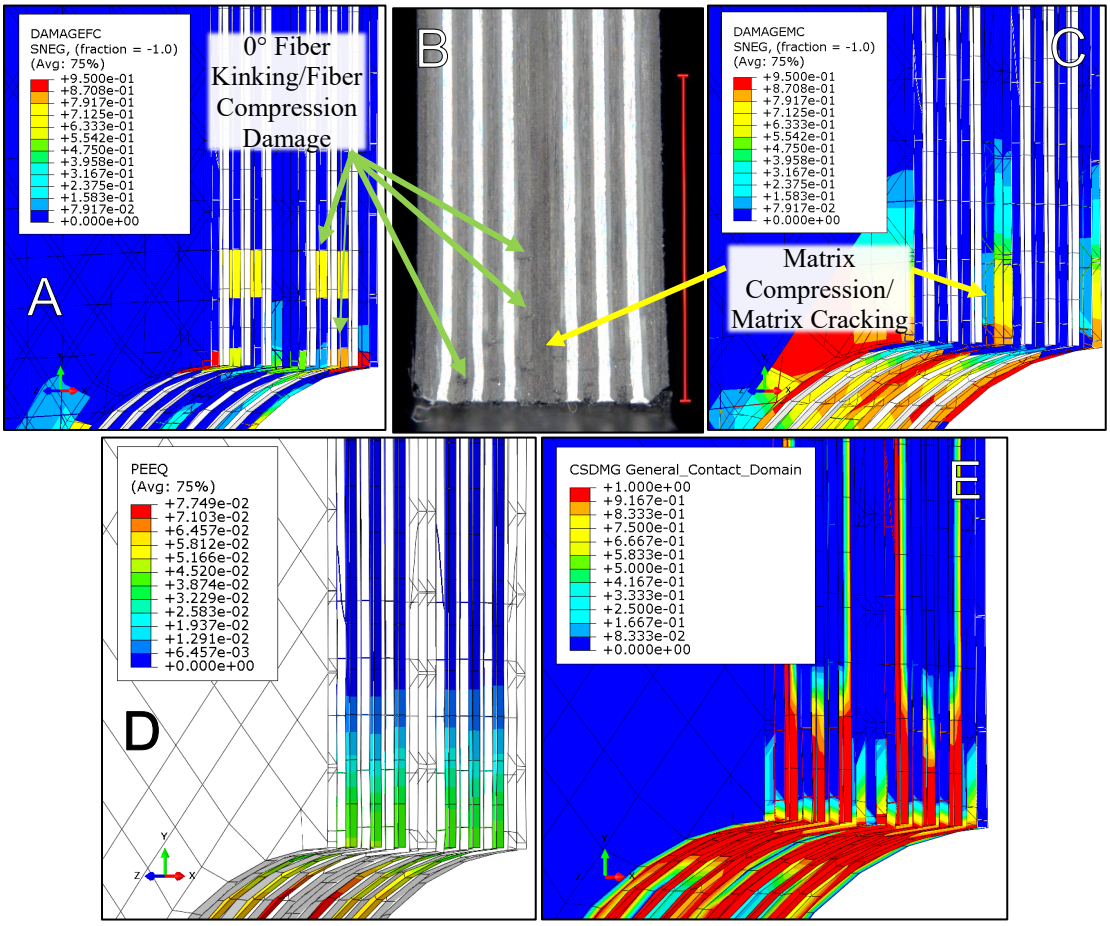

Figure 126: 18-Ply Hybrid Computational v. Experimental Sectioned at 5.32% Strain
A) Fiber Compression Damage B) Experimental Sample
C) Matrix Compression Damage D) Equivalent Plastic Strain
E) Cohesive Damage

6.6 Modeling Technique Comparison

Figure 127 shows the final 18-ply hybrid model compared to other simulations that considered different modeling techniques for the metal foils. These models represent the four possible combinations of the following conditions:

- Foil elastic-plastic model based on
    - Published values of elastic modulus, yield, and fracture
    - Experimentally determined elastic-plastic curve
- Cure induced thermal stresses
    - Considered
    - Not Considered

The models shown in the dashed green and dotted magenta traces both employed the published values for the properties of stainless steel. Regardless of the consideration of the thermal stress, both of these are far stiffer than the experimental samples. The blue trace employs the experimentally determined properties for the foils. This is much more compliant than the experimental results. Finally, the black trace plots the simulation that considered both the experimentally determined foil elastic-plastic curve and the cure induced stresses. These considerations produce the most accurate results as listed in Table 33 and Table 34.

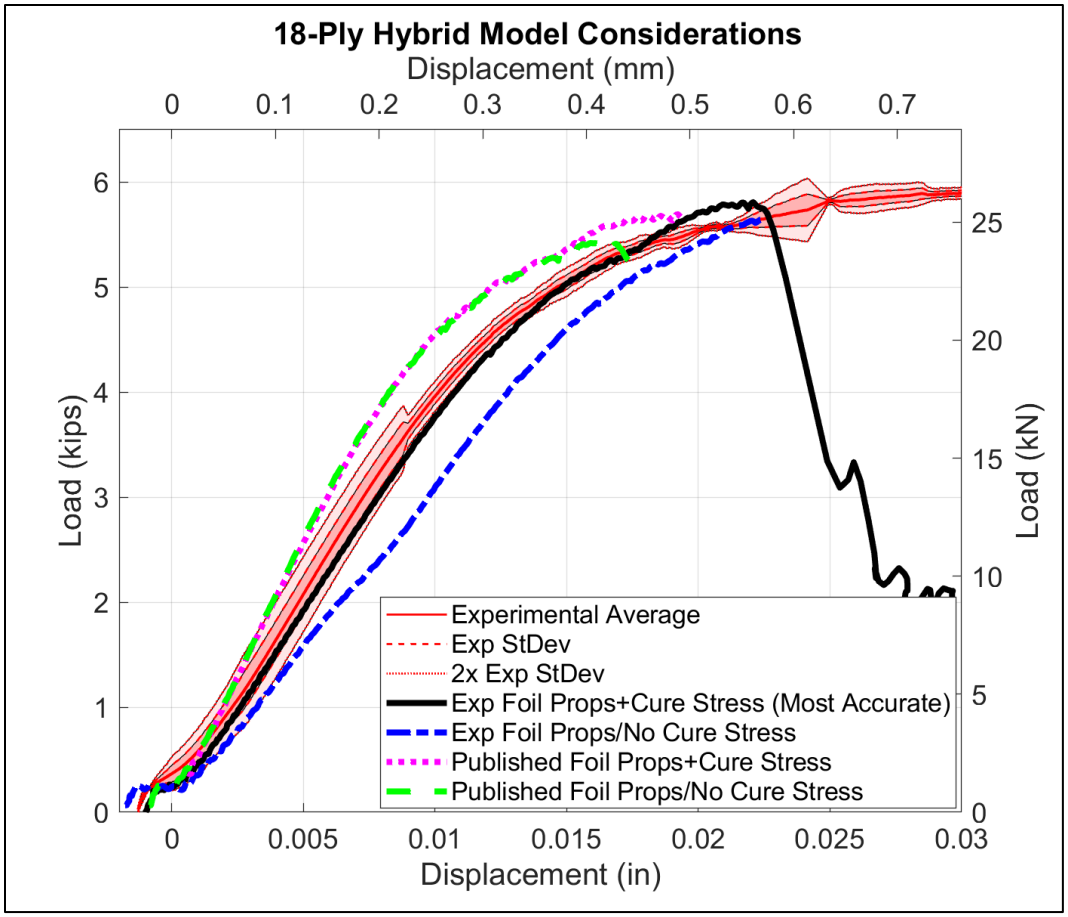

Figure 127: 9-Ply Hybrid Model Considerations

6.7 Failure Criteria Behavior

This section examines specific elements and nodes to demonstrate how the critical damage and failure criteria function as the simulations are carried out.

6.7.1 Composite Failure Behavior

Since fiber compression is the dominant failure mode in the composite, the failure in a critical 0° ply element near the bearing surface was studied to demonstrate the functionality of Hashin failure criteria. The particular element that was studied is Element 1026 from Layer 4 (0° IM7/977-3 ply) near the center of the layup in the 9-ply control.

Figure 128 shows composite fiber compression damage evolution criteria that was based on Hashin damage initiation for this ply. The location of element 1026 is highlighted. Based on the experimental data and finite element analysis, since this is a 0° ply, this element close to the bearing surface is expected to experience fiber kinking which manifests as fiber compression damage in the finite element representation.

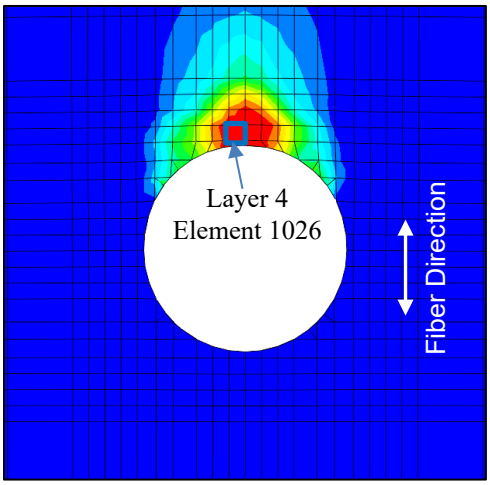

Figure 128: Fiber Compression Single Element Study Location

Figure 129 follows the damage initiation and evolution criteria for this element as the simulation occurs. The top plot shows the Von Mises stress in the element which is dominated by stress in the fiber direction. The middle plot shows the Hashin damage initiation variable for each of the four modes. The last plot depicts the damage evolution variable for each mode which equates to stiffness or load capacity degradation for the given mode. This element experiences almost pure compression in the fiber direction. Thus, as the bearing load is applied at $t = 0.01$ (unit time step), fiber compression damage initiation rises first. Due to the Poisson effect, compression in the fiber direction produces a resultant stress in the matrix direction which results in matrix tension. Then,

around $t = 0.067$, the Hashin matrix tension damage initiation variable reaches a value of one, which triggers a matrix tension damage evolution variable. This begins to degrade the stress capacity of the element in matrix tension which manifests as a drop in the element stress. During this time, the element is loaded further in fiber compression which results in Hashin fiber compression initiation near $t = 0.078$. At this point, the fiber compression damage variable reaches a maximum default value of $D = 0.95$ meaning that the stress capacity in fiber compression is reduced by 95%. During this time, the matrix tension damage variable remains between 0.35 and 0.50 until the near the end of the simulation where it approaches a value of 0.90. If element deletion were used, based on user input, this element would have been deleted as soon as the fiber compression damage variable reached 0.95. Without using element deletion, the element retains some stress capacity. Since there was no expectation of material erosion and the critical elements are in compression throughout this work, element deletion in preliminary models tended to cause non-physical, nearly instantaneous load drops as elements were deleted. This did not model the experimental results well and complicated the analysis due to the rapid change. For these reasons, in the final models presented in this work, element deletion was not employed.

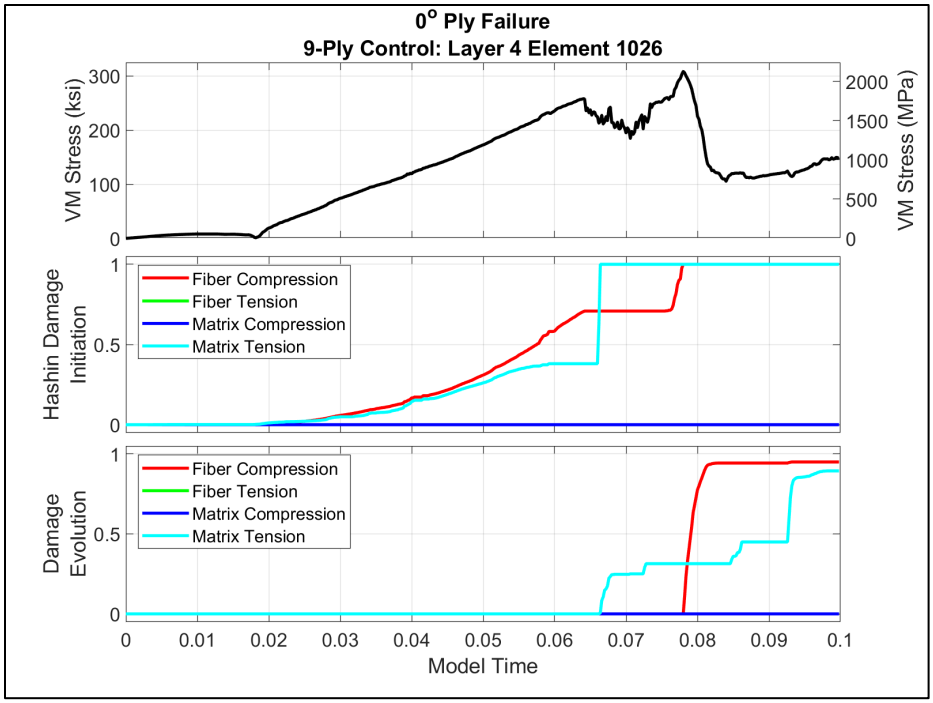

Figure 129: Fiber Compression Damage Initiation and Evolution

6.7.2 Foil Ductile Behavior

Figure 130 depicts the single element selected from the 9-ply hybrid simulation from the center foil. Figure 131 depicts the Von Mises Stress versus Von Mises Strain for this element as compared to the user input equivalent stress-strain curve. Even in this complex failure scenario, the model behaves as predicted and defined. The oscillations in the simulation data are attributable to the wave propagation technique used in explicit finite element modeling and the complex contact interactions at the bearing surface which must account for penetration and slip. Since the element never reaches the failure, stress damage is never initiated so no damage evolution appears in the computational stress-strain curve from element 576.

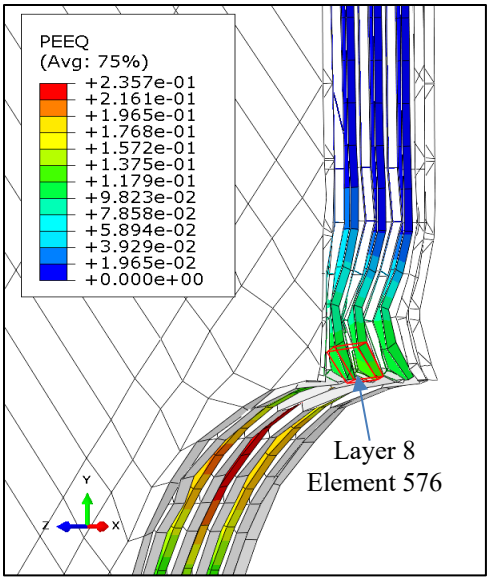

Figure 130: Elastic-Plastic Single Element Study Location

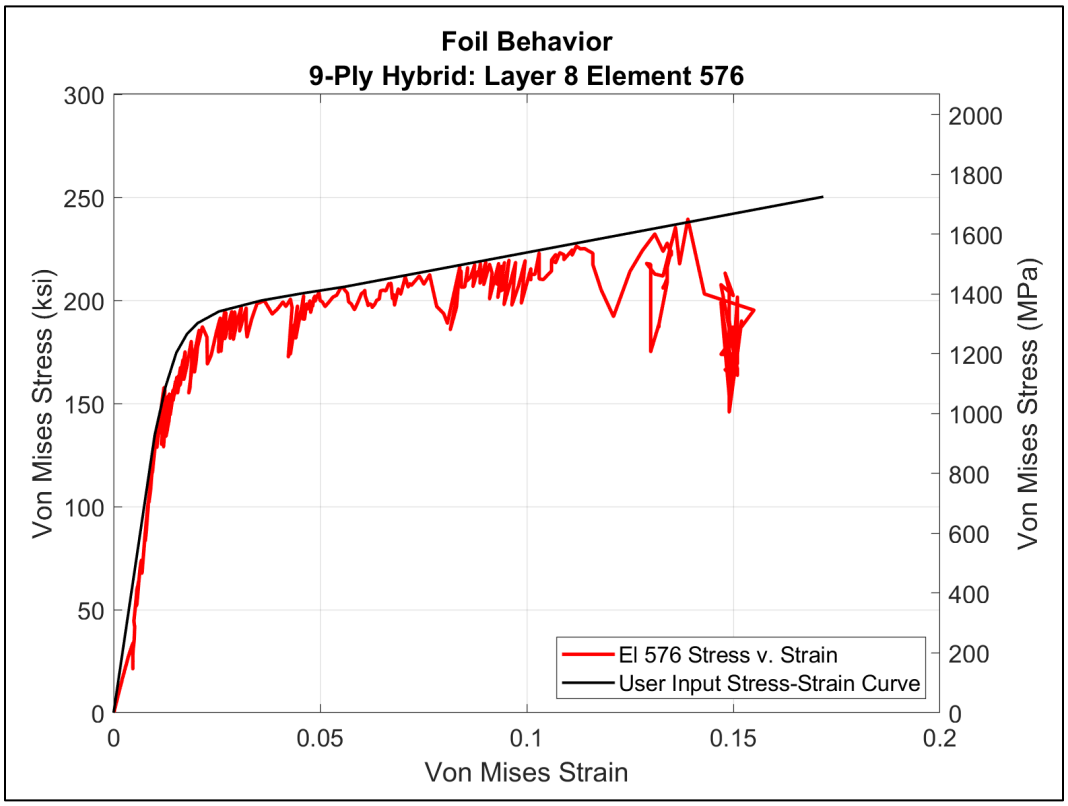

Figure 131: Foil Elastic-Plastic Curve v. User Input

VII. Single Shear Experimental Results

This chapter presents the results of the quasi-static monotonic experimentation in the single shear configuration. With a basis established from the double shear results, the intent of this chapter is to compare and contrast the behavior of control and hybrid bearing samples in the more complex single shear cases. 18-ply hybrid and control samples are compared in protruding head and countersunk head configurations at the macroscopic level while also investigating the phenomena that occur down to the fiber level, which allow progressive bearing failure to take place. The results of the single shear testing are presented predominately as load-displacement and stress-strain curves in addition to tabular data. In order to study the failure mechanisms that allow bearing failure to occur, micrographs of progressive failure samples are presented. These have been loaded to target specific features of interest in the full failure data. This chapter concludes with a statistical analysis of all the quasi-static results.

7.1 Monotonic Single Shear Protruding Head Experimental Results

With the background gained from exploring the less complex double shear cases, the more complex single shear results can be explored. This load condition is more complex because the single shear nature allows bending in both the fixture and the bolt. The layups here are the same 18-ply layups employed in the 18-ply double shear testing.

Figure 132 depicts load-displacement data for the single shear protruding head samples. Control samples are represented in blue, with the full failure controls in blue dashed traces and progressive failure controls in blue dot-dashed traces. The hybrid samples are represented in red with the full failure hybrids in solid red and the

progressive failure hybrids in dotted red traces. Table 36 lists averaged critical data and statistical analysis corresponding to the sample results plotted in Figure 132.

When studying Figure 132 overall, the curves appear quite different than those observed in the double shear configurations. Both the hybrid and control curves pass two knee points before reaching an initial peak. Then near 0.040in (1.02mm) of displacement (15% bearing strain) as the control is gradually failing in bearing, the hybrid samples display a remarkable reloading phenomenon (labeled in Figure 132), that returns to a load near the original peak. This is explored further alongside the progressive failure micrographs.

In referencing Table 36, the hybrids demonstrate an increase over the control of 31% in yield load, 25% in offset load, and 37% in ultimate load. However, the most remarkable improvement is the over 60% increase in strain energy. This is attributed to the reloading phenomenon observed in the hybrid. In the tested cases, the material reloaded to a value near that of the previous peak. This will be discussed further in the hybrid progressive failure section. Since the single shear configuration allows bending in both the fixture and fastener, reduced maximum loads and chord stiffnesses (moduli) are observed compared to the double shear configuration.

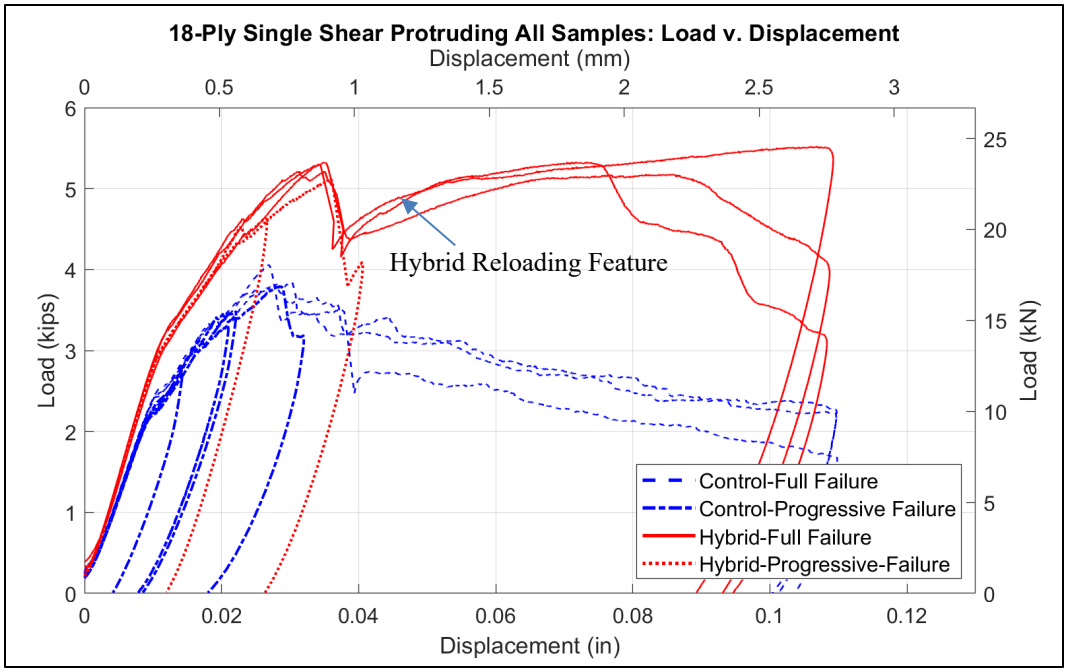

Figure 132: 18-Ply Single Shear Protruding All Samples: Load v. Displacement

Table 36: 18-Ply Single Shear Protruding Load Displacement Data

	Control			Hybrid					
	Average (95% CI)	**Stdev**	**N**	**Average (95% CI)**	**Stdev**	**N**	**Diff**	**% Diff**	**Stat Sig**
Yield Load (kips)	2.356 (2.245-2.467)	0.1201	7	3.093 (2.978-3.208)	0.09281	5	0.7368	31.27	Yes
Offset Load (kips)	2.916 (2.857-2.975)	0.05627	6	3.650 (3.539-3.761)	0.08948	5	0.7338	25.16	Yes
Ultimate Load (kips)	3.909 (3.590-4.228)	0.1284	3	5.354 (4.969-5.740)	0.1552	3	1.445	36.96	Yes
Strain Energy (in-lb)	252.3 (217.0-287.7)	14.22	3	412.7 (391.2-434.1)	8.622	3	160.3	63.54	Yes

With the data analyzed in terms of load and displacement, it should also be considered in terms of bearing stress and strain. Figure 133 displays plots for both the control and hybrid 18-ply single shear protruding head samples in terms of stress and strain. Control samples are represented in blue, with the full failure controls in blue

dashed traces and progressive failure controls in blue dot-dashed traces. The hybrid samples are represented in red with the full failure hybrids in solid red and the progressive failure hybrids in dotted red traces. Table 37 contains the corresponding stress-based data for the configuration. As in other cases, the adhesive thickness masks the gains made by hybridization. The differences in yield and offset stress are no longer statistically discernible. However, the hybrid demonstrates a statistically significant increase of over 6% in ultimate stress and a remarkable increase of nearly 27% in strain energy density, due to the reloading phenomenon that occurs near 12% strain. It is noteworthy that the hybrid yield and offset occur at strains 10% and 5% greater respectively than the controls.

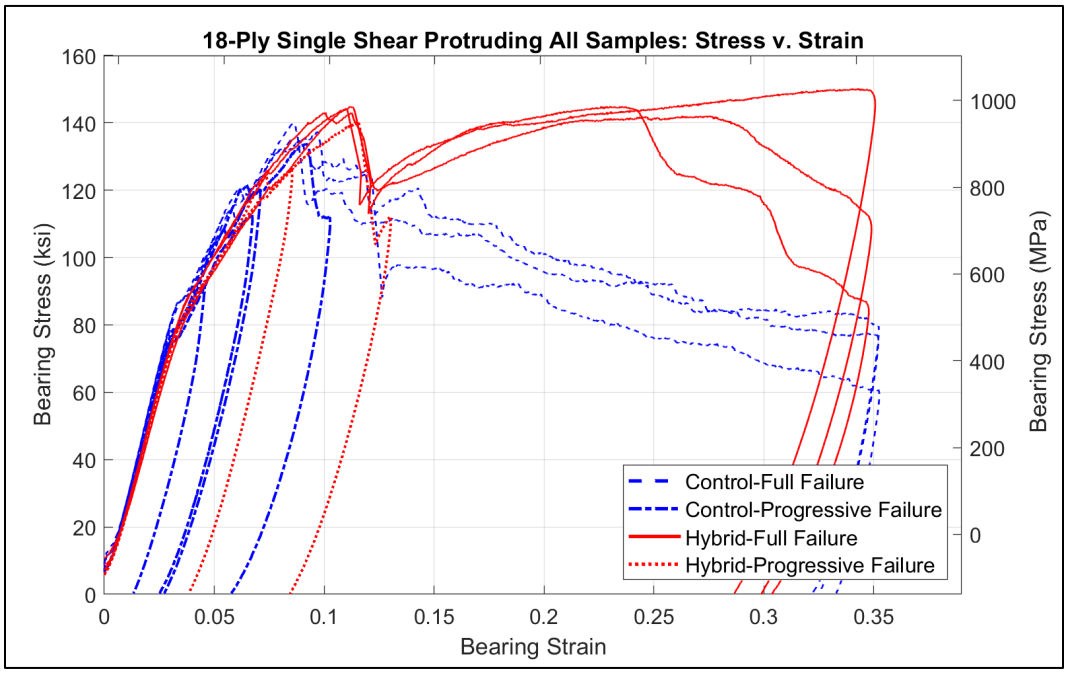

Figure 133: 18-Ply Single Shear Protruding All Samples: Stress v. Strain

Table 37: 18-Ply Single Shear Stress-Strain Data

	Control			Hybrid					
	Average (95% CI)	**Stdev**	**N**	**Average (95% CI)**	**Stdev**	**N**	**Diff**	**% Diff**	**Stat**
Yield Stress (ksi)	81.99 (77.61-86.38)	4.741	7	84.43 (81.23-87.63)	2.580	5	2.44	2.971	No
Yield Strain	0.03342 (0.03247-0.03436)	0.001024	7	0.03691 (0.03572-0.03810)	9.574E-04	5	0.003496	10.46	Yes
Offset Stress (ksi)	101.8 (98.87-104.7)	2.785	6	99.64 (96.70-102.58)	2.366	5	-2.151	-2.113	No
Offset Strain	0.04876 (0.04788-0.04965)	0.0008	6	0.05124 (0.04988-0.05260)	0.001098	5	0.002478	5.083	Yes
Ultimate Stress (ksi)	137.4 (131.0-143.8)	2.580	3	146.1 (136.9-155.2)	3.689	3	8.668	6.308	Yes
Modulus (ksi)	2609 (2517-2701)	99.19	7	2417 (2334-2500)	66.66	5	-192.1	-7.364	Yes
Strain Energy Density (in-lb/in^3)	28480 (25200-31760)	1320	3	36130 (34280-37990)	746.3	3	7649	26.86	Yes

7.1.1 18-Ply Single Shear Protruding Control Progressive Failure

In order to study the features that brought about bearing failure, four control samples were run to specific displacements to target features in the data. These curves are plotted Figure 134 where the targeted features are labeled. Figure 135 depicts the focus area in the sectioned samples pictured in Figure 136. Figure 136 shows micrographs of the sectioned samples that correspond to the curves and features in Figure 134.

Due to bending and bolt tension, in this configuration the system can be thought of as attempting to pull the bolt through the hole as well as into the bearing surface. The loading at the bearing surface is present just as in the double shear case. However, in the single shear configuration, a significant component load is pulling the bolt into and through the sample due to bolt tension and bending in the bolt.

As seen in Figure 136A, this results in yield behavior that includes coupled fiber kinking and matrix cracking along planes that are at an angle to the bearing surface. This behavior corresponds to the first knee point (Feature 1) that occurs around 3% strain (dotted red trace). A detailed view of this image is presented in Figure 137 which clearly shows this coupled fiber kinking and matrix cracking behavior.

The samples pictured in Figure 137 B and C and plotted in dashed green and solid blue traces in Figure 134 targeted the second knee point that occurs in the 6% to 7% strain range (Feature 2). This knee point is due to the through thickness wedge cracking displayed in these two micrographs in Figure 137 B and C. This cracking is coupled with delamination initiating in the bottom plies of the layup.

Figure 137D shows a sample that was stressed just past the ultimate stress (Feature 3). This is represented by the bold cyan trace in Figure 134. This sample is dominated by through thickness cracking and delamination that caused the load drop after reaching ultimate stress. A sectioned full failure sample is displayed in Figure 137D. This sample displays large scale crushing that occurred at the edge of the bolt head.

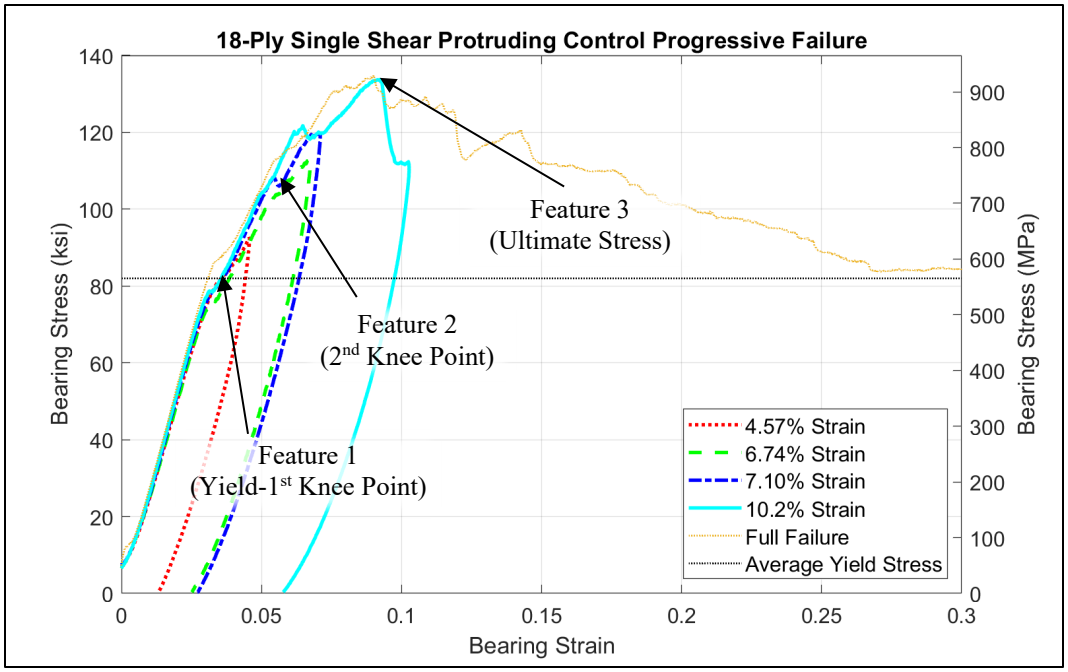

Figure 134: 18-Ply Single Shear Protruding Control Progressive Failure

Figure 135: Single Shear Protruding Sectioned View and Observed Area

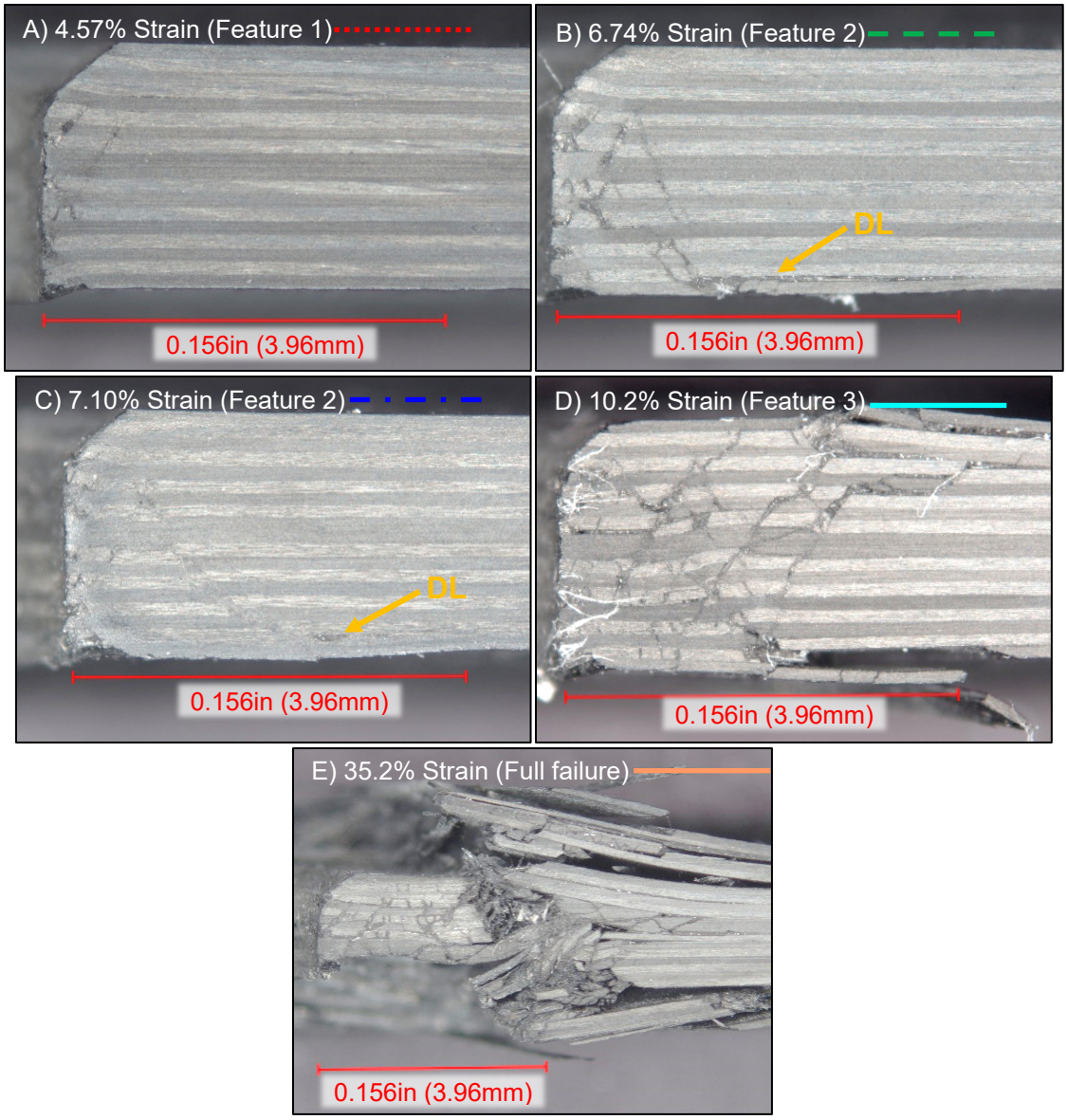

Figure 136: 18-Ply Single Shear Protruding Control Progressive Failure Micrographs

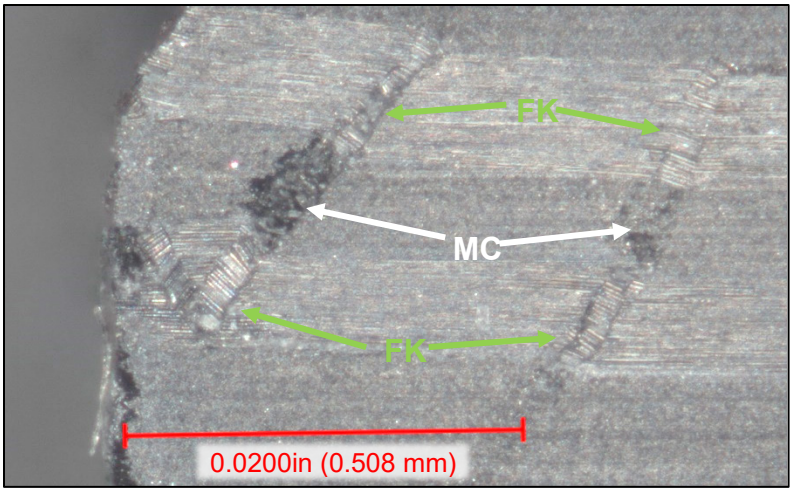

Figure 137: Coupled Fiber Kinking and Matrix Cracking at 4.57% Strain

7.1.2 18-Ply Single Shear Protruding Hybrid Progressive Failure

Two progressive failure samples were loaded to target specific features of interest in the hybrid single shear protruding head curves. Figure 138 shows stress-strain data for these samples and one full failure sample. Figure 139 shows micrographs of the sectioned samples which correspond to the curves in Figure 138. Due to other requirements, only two progressive failure samples were available. However, these two samples are very telling.

Figure 139A shows behavior just after yield at the second knee point (Feature 1 in Figure 138). While the two knee points due to load redistribution near 3% and 6% strain in the controls still exist, they are delayed and attenuated by the presence of the stainless steel. Figure 139A shows that the presence of the steel is preventing through-thickness cracks from forming as noted in the control samples (Figure 137B and C).

Figure 139B and C show how the reload phenomenon comes about as plotted in the green dashed and orange dot-dashed traces in Figure 138. As buckling in individual

foils becomes through-thickness buckling coupled with delamination, a new pristine bearing surface is effectively presented to the system allowing the system to be reloaded to a value near the original maximum stress. This is similar to the reloading that occurred in the 9-ply double shear samples but is more effective here due to the stiffness of the 18-ply layup. The large-scale delamination that occurs as a result of the load drop in Feature 2 occurs just outside of the bolt head. It is noteworthy that 34% hole elongation in the hybrid is more conservative than a 35% hole elongation in the control (Figure 139C vs Figure 139E).

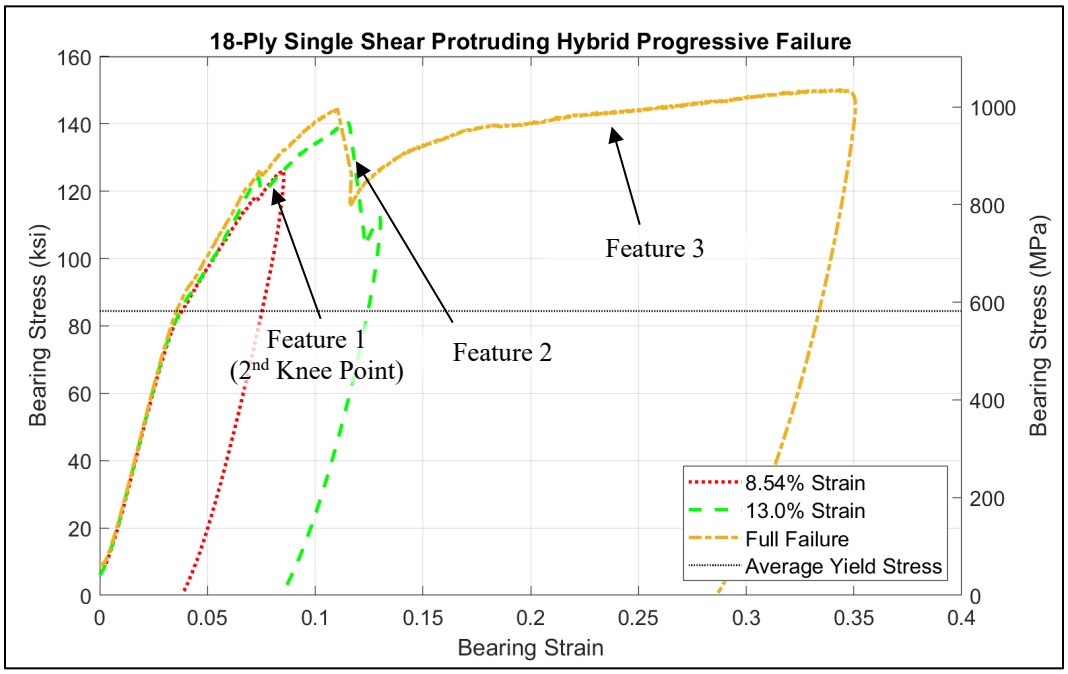

Figure 138: 18-Ply Single Shear Protruding Hybrid Progressive Failure

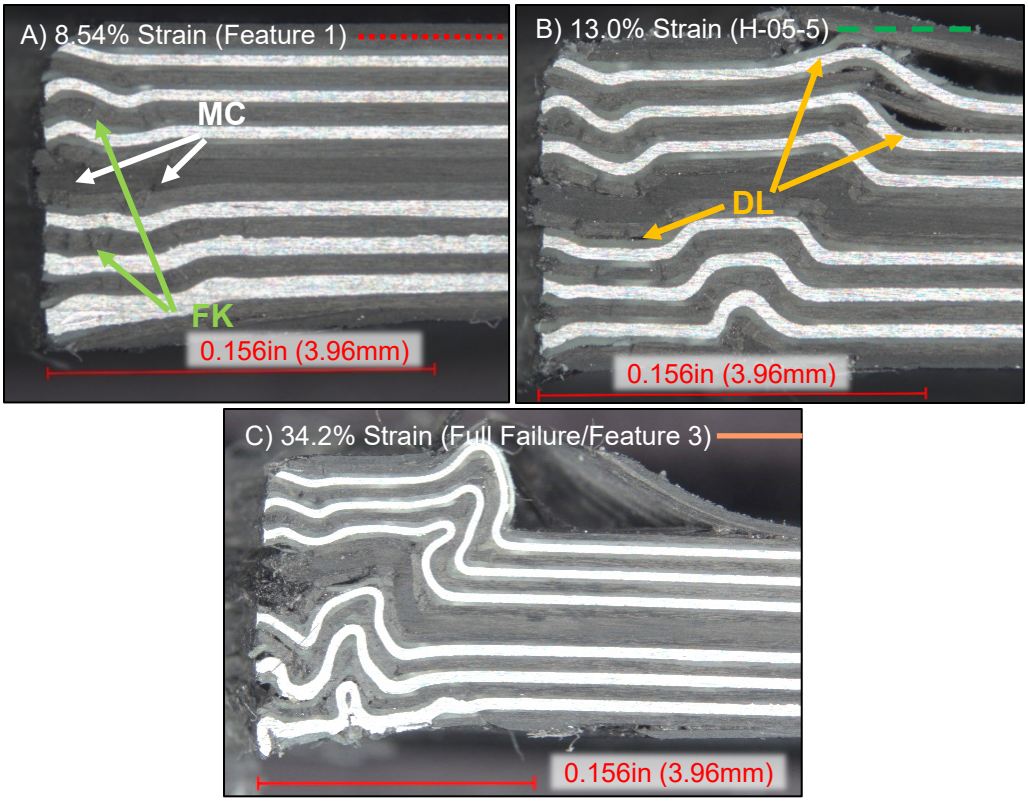

Figure 139: 18-Ply Single Shear Protruding Hybrid

7.2 Monotonic Single Shear Countersunk Head Experimental Results

With a basis established in double shear and protruding head configurations, the most complex of the cases, single shear countersunk, can be investigated. This case is the most complex because it not only allows bending in the fixture and bolt like in the protruding head case, but it also does not constrain both faces of the coupon as in the other configurations.

Figure 140 shows all the load-displacement data collected in the single shear countersunk configuration. This includes control and hybrid as in previous configurations, while also including the shank only hybrid which only includes foils in contact with the shank region of the bolt (see discussion in Section 3.4.5). In Figure 140, control samples are represented by blue dashed lines, while control progressive failure

samples are represented by blue dotted lines. Hybrid full failure samples are represented by solid red lines while hybrid progressive failure samples are represented by dotted red lines. Shank-only full failure samples are in dashed green lines and shank-only progressive failure samples are in dot-dashed green. Table 38 and Table 39 show the calculated data and statistical significance which correspond to the data in Figure 140. These two tables compare the shank-only to the control, and the full hybrid to the control respectively. A table comparing the full hybrid and shank-only data is found in Appendix J.

In Figure 140, it is clear that the shank-only hybrid (green traces) has outperformed the control (blue traces) and that the full hybrid (red traces) has outperformed both the other layup configurations with respect to the ultimate load achieved. The shank-only and full hybrid also carry more load capacity in the later phases of bearing failure. The shank-only experiences a load drop around 0.060in (1.5mm) of displacement (19% strain) which does not exist in the other samples. This will be discussed further in the examination of the progressive failure samples.

In reference to Table 38, the shank-only hybrid produced a nearly 10% gain in yield load and over a 20% gain in offset load, ultimate load, and strain energy. However, from this work, the shank only scenario is not advised.

Since the shank-only layup was asymmetric through the thickness, a significant bending moment was imparted to the laminate by cure induced stresses. Thus at rest, the 12.0in (30.4 cm) wide panel had a 0.500in (12.7mm) curvature as depicted in Figure 141. This could potentially produce parts that are unusable due to incorrect geometry. The curvature and internal stresses also complicated machining. Aside from manufacturability

limitations, the full hybrid is superior in that it produced a larger improvement over the control in all measured criteria. The shank-only effect is less evident here because the procedure-C joint is stiffer than a standard lap joint studied by Egan [43], [44]. While the shank-only provides a 9.5% increase in yield load (Table 38), the full hybrid provides a yield load improvement of 15.5% over the control (Table 39). The full hybrid displays over a 30% improvement over the control in offset load, ultimate load, and strain energy.

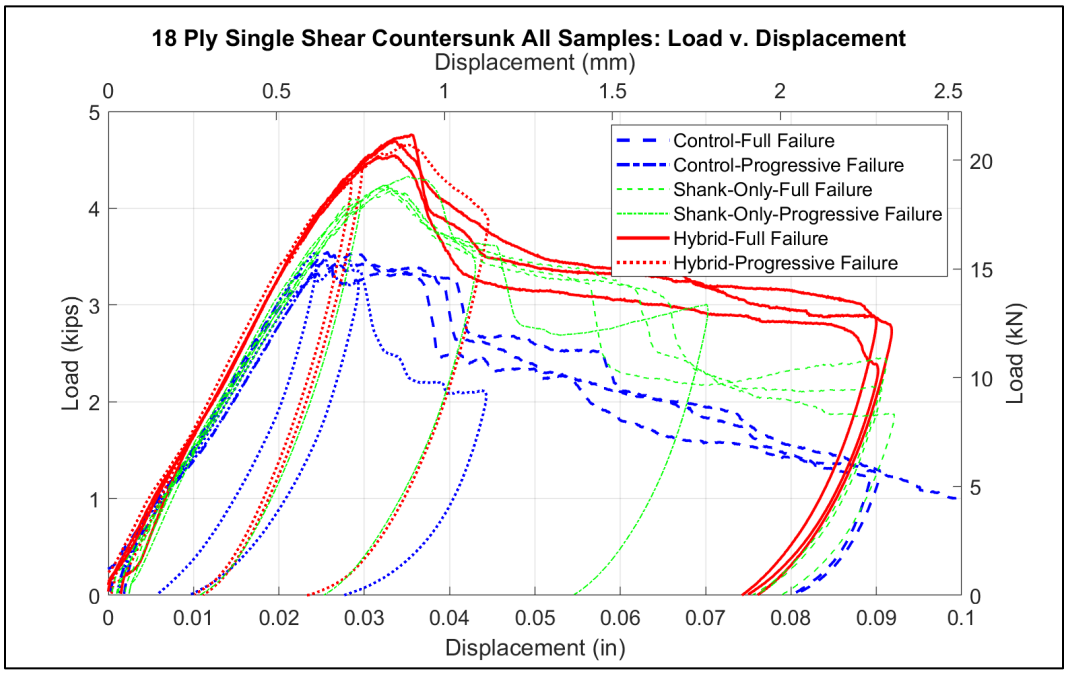

Figure 140: 18-Ply Single Shear Protruding All Samples: Load v. Displacement

Table 38: 18-Ply Single Shear Countersunk Load-Displacement Data: Control v. Shank-Only

	Control			Shank-Only Hybrid					
	Average (95% CI)	Stdev	N	Average (95% CI)	Stdev	N	Diff	% Diff	Stat Sig
Yield Load (kips)	3.344 (3.175-3.514)	0.1617	6	3.662 (3.523-3.801)	0.1325	6	0.3177	9.500	Yes
Offset Load (kips)	3.393 (3.307-3.480)	0.06969	5	4.113 (4.045-4.181)	0.05481	5	0.7195	21.2	Yes
Ultimate Load (kips)	3.519 (3.454-3.583)	0.04048	4	4.234 (4.162-4.306)	0.05778	5	0.7155	20.3	Yes
Strain Energy (in-lb)	175.3 (157.7-193.0)	7.095	3	215.7 (205.6-225.7)	4.041	3	40.33	23.0	Yes

Table 39: 18-Ply Single Shear Countersunk Load-Displacement Data: Control v. Hybrid

	Control			Hybrid					
	Average (95% CI)	Stdev	N	Average (95% CI)	Stdev	N	Diff	% Diff	Stat Sig
Yield Load (kips)	3.344 (3.175-3.514)	0.1617	6	3.862 (3.740-3.985)	0.1533	6	0.5178	15.48	Yes
Offset Load (kips)	3.393 (3.307-3.480)	0.06969	5	4.459 (4.383-4.535)	0.08678	5	1.065	31.39	Yes
Ultimate Load (kips)	3.519 (3.454-3.583)	0.04048	4	4.667 (4.542-4.791)	0.1099	3	1.148	32.62	Yes
Strain Energy (in-lb)	175.3 (157.7-193.0)	7.095	3	239.0 (230.0-248.0)	7.937	3	63.67	36.31	Yes

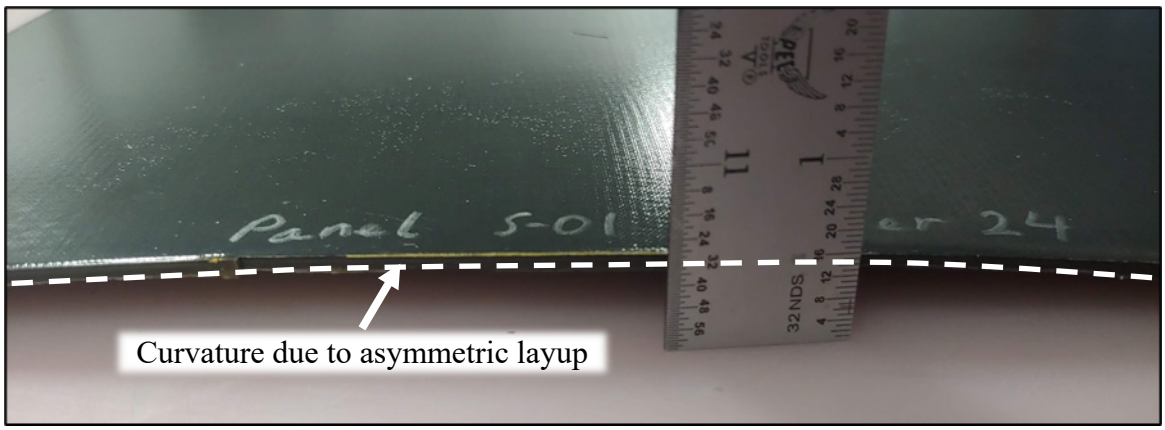

Figure 141: Shank-Only Panel Curvature

Having explored the single shear countersunk data in terms of load and displacement, it should be investigated in terms of bearing stress and strain. Figure 142 depicts the stress-strain data for all the 18-ply countersunk samples. Control full failure samples are represented by blue dashed lines, while control progressive failure samples are represented by blue dotted lines. Hybrid full failure samples are represented by solid red lines while hybrid progressive failure samples are represented by dotted red lines. Shank-only full failure samples are in dashed green lines and shank-only progressive failure samples are in dot-dashed green. Corresponding key data are compared in Table 40 and Table 41.

In Figure 142, in terms of bearing stress and strain, the gains noted in the load-based data are again being masked by adhesive thickness. All the configurations appear to reach a similar ultimate stress peak. However, both the shank-only and full hybrid demonstrate a higher stress capacity than the control as extended bearing failure comes about past 15% bearing strain. Here the modulus of the controls appears to be stiffer than those of both hybrids.

In reference to Table 40, the shank-only hybrid has a yield stress 6.5% lower than that of the control. Differences in the yield strain, ultimate stress, and strain energy density are not statistically different. The modulus of the shank-only is almost 12% lower than that of the control, while the offset strain is over 4% greater than that of the control.

In Table 41 the hybrid demonstrates a yield stress 9.5% lower than that of the control. The modulus is almost 11% lower while the offset strain is over 12% greater in the hybrid. The remaining values are not statistically conclusive.

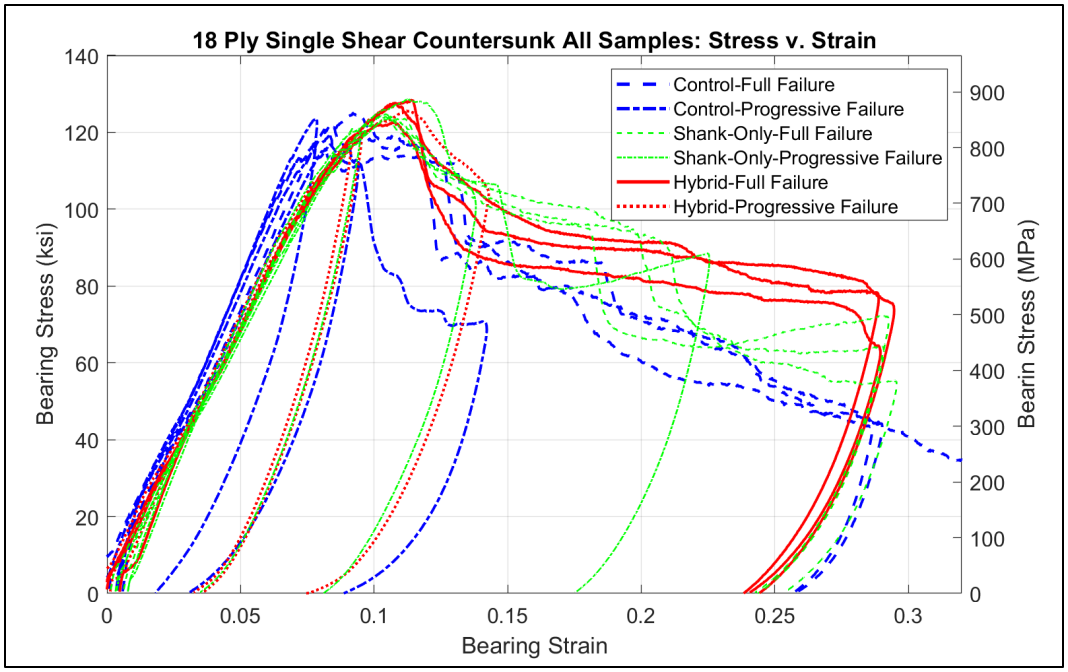

Figure 142: 18-Ply Single Shear Protruding All Samples: Stress v. Strain

Table 40: 18-Ply Single Shear Countersunk Stress-Strain Data: Control v. Shank-Only Hybrid

	Control			Shank-Only Hybrid					
	Average (95% CI)	**Stdev**	**N**	**Average (95% CI)**	**Stdev**	**N**	Diff	% Diff	Stat Sig
Yield Stress (ksi)	115.7 (110.1-121.2)	5.263	6	108.2 (104.5-111.9)	3.526	6	-7.480	-6.467	Yes
Yield Strain	0.07609 (0.07012-0.08206)	0.005687	6	0.08050 (0.07666-0.08434)	0.003658	6	0.004408	5.794	No
Offset Stress (ksi)	117.2 (114.9-119.4)	1.842	5	121.6 (120.0-123.2)	1.275	5	4.426	3.778	Yes
Offset Strain	0.08564 (0.08168-0.08961)	0.003195	5	0.09798 (0.09377-0.1022)	0.003390	5	0.01234	14.41	Yes
Ultimate Stress (ksi)	120.9 (114.7-127.0)	3.866	4	125.2 (122.7-127.7)	2.002	5	4.290	3.549	No
Modulus (ksi)	1566 (1478-1653.9)	84.04	6	1379 (1339-1419)	37.98	6	-186.9	-11.94	Yes
Strain Energy Density (in-lb/in^3)	19501 (17784-21218)	691.0	3	20447 (19294-21599)	463.9	3	945.7	4.849	No

Table 41: 18-Ply Single Shear Countersunk Stress-Strain Data: Control v. Hybrid

	Control			Hybrid					
	Average (95% CI)	**Stdev**	**N**	**Average (95% CI)**	**Stdev**	**N**	Diff	% Diff	Stat Sig
Yield Stress (ksi)	115.7 (110.1-121.2)	5.263	6	104.6 (101.3-108.0)	4.168	6	-11.02	-9.532	Yes
Yield Strain	0.07609 (0.07012-0.08206)	0.005687	6	0.07686 (0.07365-0.08008)	0.0040	6	7.733E-04	1.016	No
Offset Stress (ksi)	117.2 (114.9-119.4)	1.842	5	120.5 (118.2-122.7)	2.574	5	3.338	2.849	No
Offset Strain	0.08564 (0.08168-0.08961)	0.003195	5	0.09631 (0.09338-0.09925)	0.0033	5	0.0107	12.46	Yes
Ultimate Stress (ksi)	120.9 (114.7-127.0)	3.866	4	126.2 (122.7-129.8)	3.156	3	5.372	4.444	No
Modulus (ksi)	1566 (1478-1653.9)	84.04	6	1399 (1377-1420)	27.00	6	-167.0	-10.67	Yes
Strain Energy Density (in-lb/in^3)	19501 (17784-21218)	691.0	3	20767 (19911-21623)	756.8	3	1266	6.492	No

7.2.1 18-Ply Single Shear Countersunk Progressive Failure

In order to understand the features that allowed bearing failure in the control single shear countersunk bolted joints, three progressive failure samples and one full failure sample were sectioned for microscopy. Progressive failure stress-strain curves for the single shear countersunk configurations are shown in Figure 143 where specific features of interest are labeled. The area subjected to microscopy for the countersunk samples is depicted in Figure 144 and micrographs of sectioned samples are shown in Figure 145 which correspond to the stress-strain curves in Figure 143.

As in previous configurations, yield (Feature 1), represented by the red trace at 7.86% strain, is dominated by fiber kinking in the 0° plies (Figure 145A). This early damage is localized in the plies in contact with the shank of the bolt due to the bolt bending allowed by the countersunk configuration and the smaller diameter of the shank

which concentrates stress. Delamination has already occurred in the lower plies of the layup.

The sample Figure 145B, represented by the dashed green line in Figure 143 targeted the load drop just after the ultimate stress was reached (Feature 2). This sample shows coupled fiber kinking and matrix cracking progressing away from the bearing surface. The delamination noted after yield has progressed further.

Feature 3, the large load drop was targeted by the sample pictured in Figure 145C (blue dot-dashed trace in Figure 143). Here, since the countersunk head does not constrain the top surface of the laminate, out of plane buckling has occurred at the edge of the countersink which is allowed by large scale coupled fiber kinking and matrix cracking. The angle of the load path between the bolt and bearing surface caused this failure to come about in a wedge shape.

As bearing failure continues toward 30% bearing strain, as plotted in the orange trace in Figure 143 and as pictured in Figure 145D, failure is dominated by crushing and delamination. This is allowed to come about and progress rapidly since the top face of the laminate is not constrained.

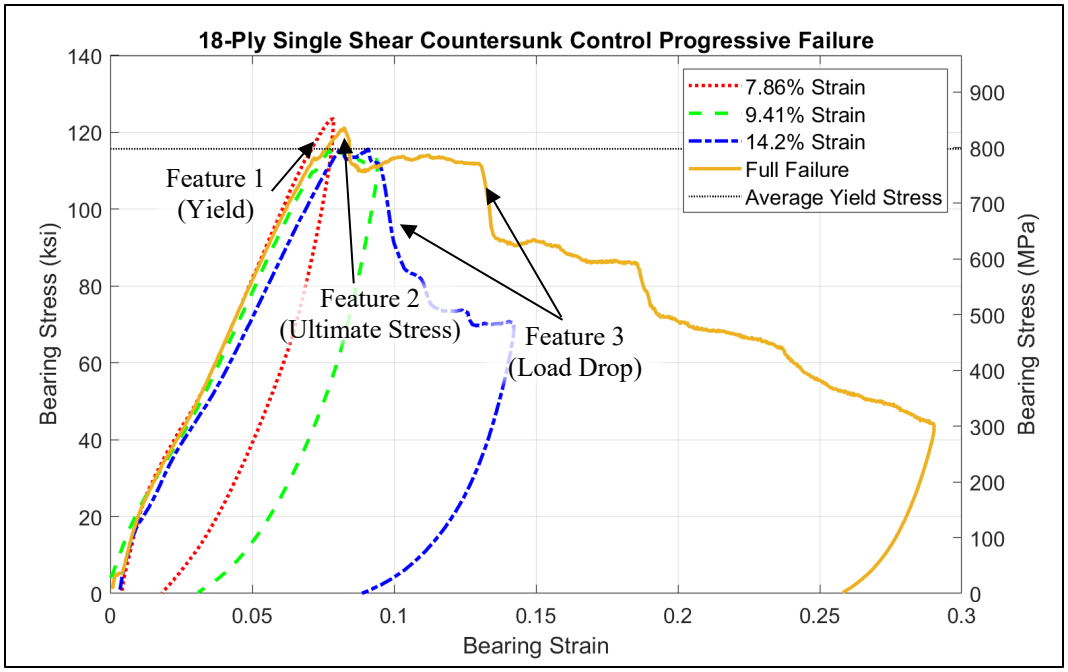

Figure 143: 18-Ply Single Shear Countersunk Control Progressive Failure

Figure 144: Single Shear Countersunk Focus Area

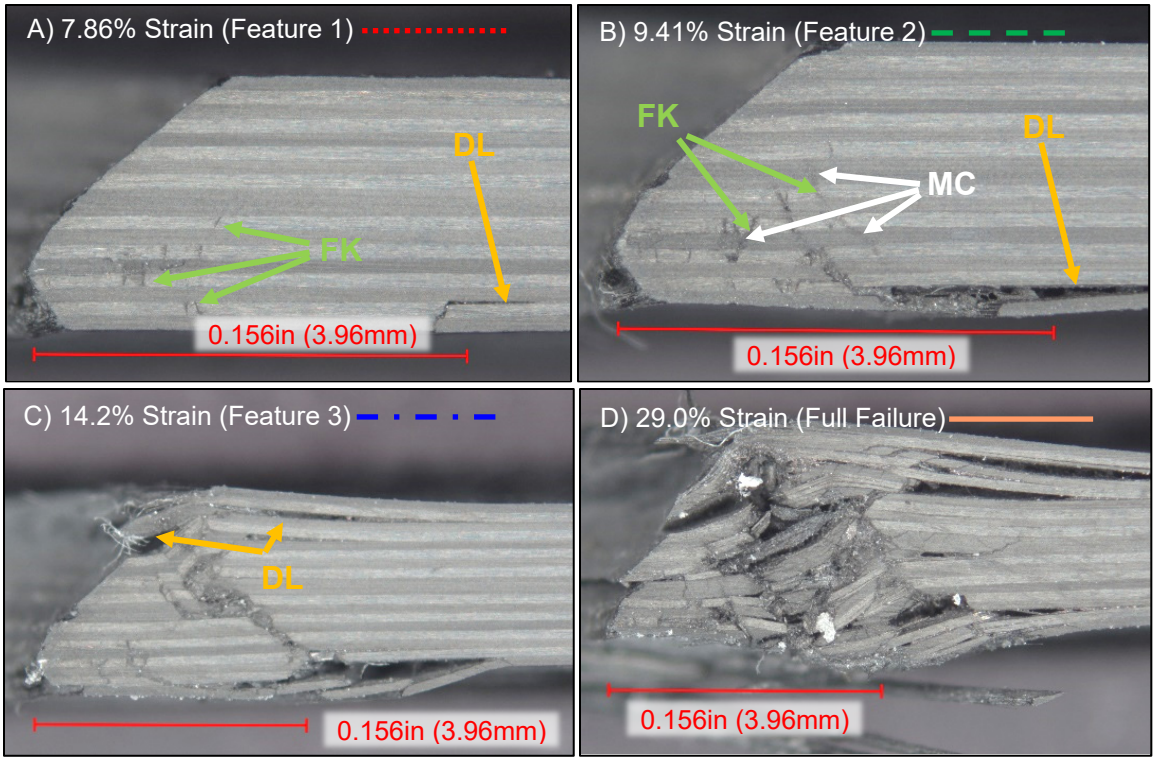

Figure 145: 18-Ply Single Shear Countersunk Control Micrographs

7.2.2 18-Ply Single Shear Countersunk Hybrid Progressive Failure

In order to compare the failure mechanism in the countersunk joint in the hybrid material to the control, three progressive failure samples and one full failure sample were sectioned for microscopy. Figure 146 shows curves for the single shear countersunk hybrid progressive failure samples. Figure 147 shows micrographs of the sectioned samples which correspond to the curves plotted in Figure 146.

The sample in Figure 147A corresponds to the red dotted trace in Figure 146 which targeted behavior that allowed yield (Feature 1). As noted in the control, the damage at this early strain exists in the layers in contact with the shank of the bolt, while those layers in contact with the head of the bolt are still intact. Fiber kinking is present in the lower 0° layers which is coupled with buckling in the foils. Delamination has just set

in in the bottom of the laminate similar to that seen in the control. As strain progresses slightly as pictured in Figure 147B and plotted in the dashed green trace in Figure 146, fiber kinking coupled with buckling and delamination has developed further.

The sectioned sample in Figure 147C targeted the behavior just after the ultimate stress was reached (Feature 2). This shows that the load after ultimate stress was due to large scale buckling in the lower foils accompanied by widespread delamination. This buckling corresponds to the through thickness cracking in the control samples at the same strain (Figure 147C vs. Figure 145C). Since the stress is more focused at the shank, the bottom foils have buckled further. Unique delamination behavior is seen between the two top plies (countersink side) because the head of the fastener does not come into direct contact with these layers. Thus, as the stress is concentrated in the third layer, delamination sets in between the second and third plies.

The sectioned sample in Figure 147D demonstrates that as the sample approached full bearing failure, it shed load through complete buckling of the foils which led to extreme delamination since the top face of the coupon is not constrained.

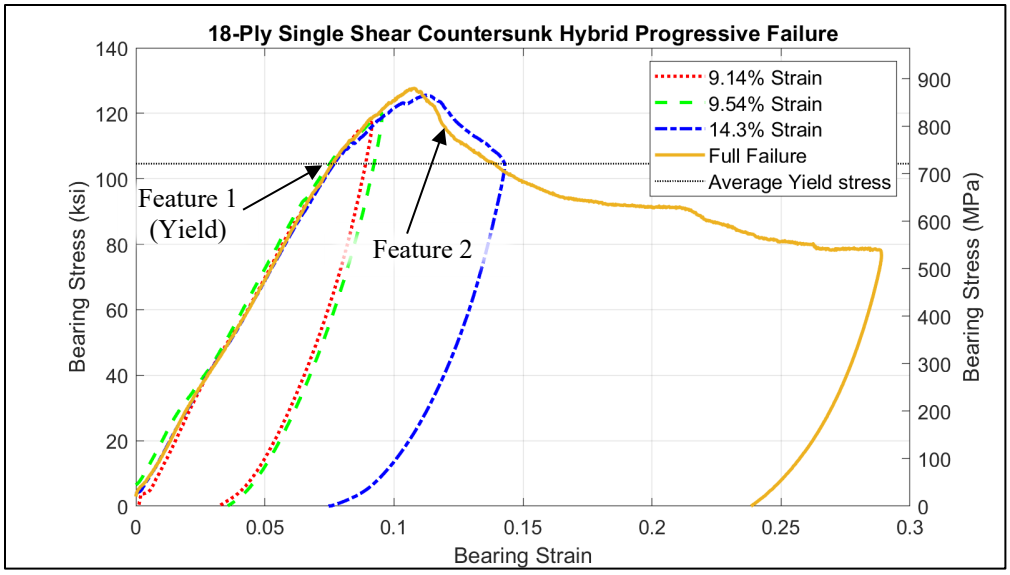

Figure 146: 18-Ply Single Shear Countersunk Hybrid Progressive Failure

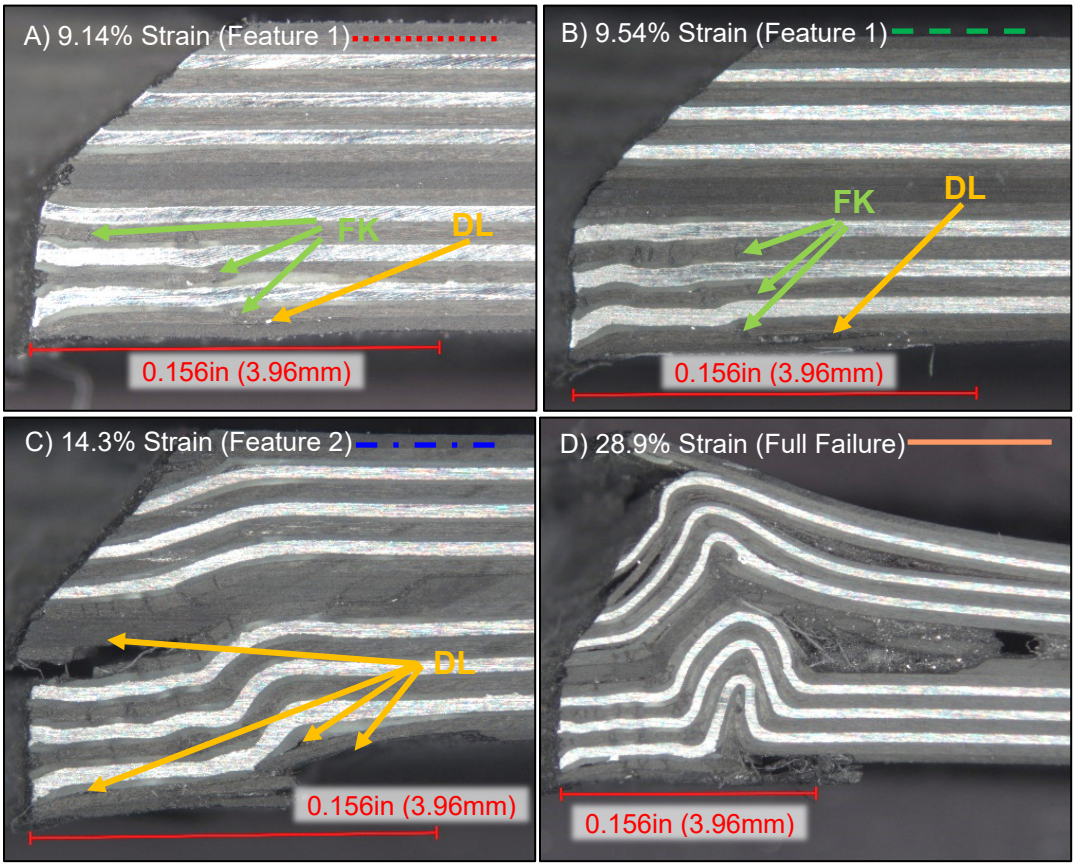

Figure 147: 18-Ply Single Shear Countersunk Hybrid Micrographs

7.2.3 18-Ply Single Shear Countersunk Shank-only Hybrid Progressive Failure

In order to compare the features allowing bearing failure in the shank-only samples to the control and full hybrid samples, three progressive failure samples were sectioned for microscopy. Figure 148 shows the stress-strain curves for the single shear shank-only countersunk progressive failure samples. Figure 149 shows micrographs of the sectioned samples corresponding to the curves in Figure 148.

The sectioned sampled in Figure 149A (red dotted trace in Figure 148) targeted the behavior just after yield (Feature 1). As noted in the other countersunk samples, the damage at yield exists near the shank of the bolt where the stress is more concentrated. Fiber kinking is again present in the 0° plies and early delamination has begun in the lower composite plies.

The sectioned sampled in Figure 149B targeted the load drop just after ultimate stress (Feature 2). Fiber kinking is widespread and is coupled with localized buckling in the foils. The load drop is due to the through thickness buckling in the lower, hybridized layers. This corresponds to the through thickness cracking near the same strain noted in the control (Figure 145C).

The damage pictured in Figure 149C demonstrates that the final large load drop (Feature 3 in Figure 148) is due to complete buckling in the foil layers and crushing in the upper, non-hybrid layers. Here the foils have effectively delayed the load drop seen in the control (Feature 3 in Figure 143).

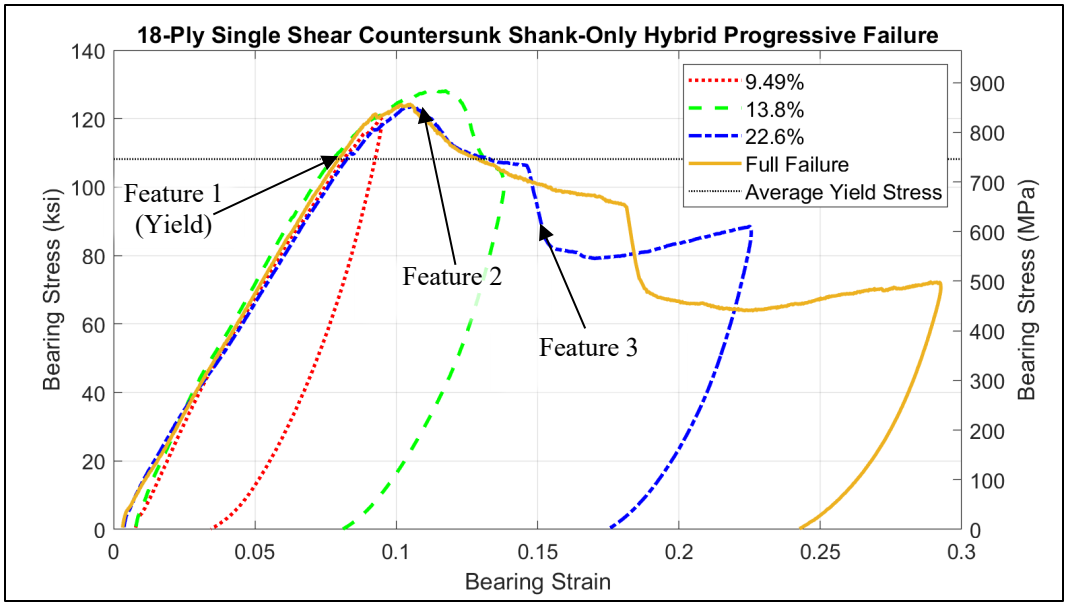

Figure 148: 18-Ply Single Shear Countersunk Shank-only Progressive Failure

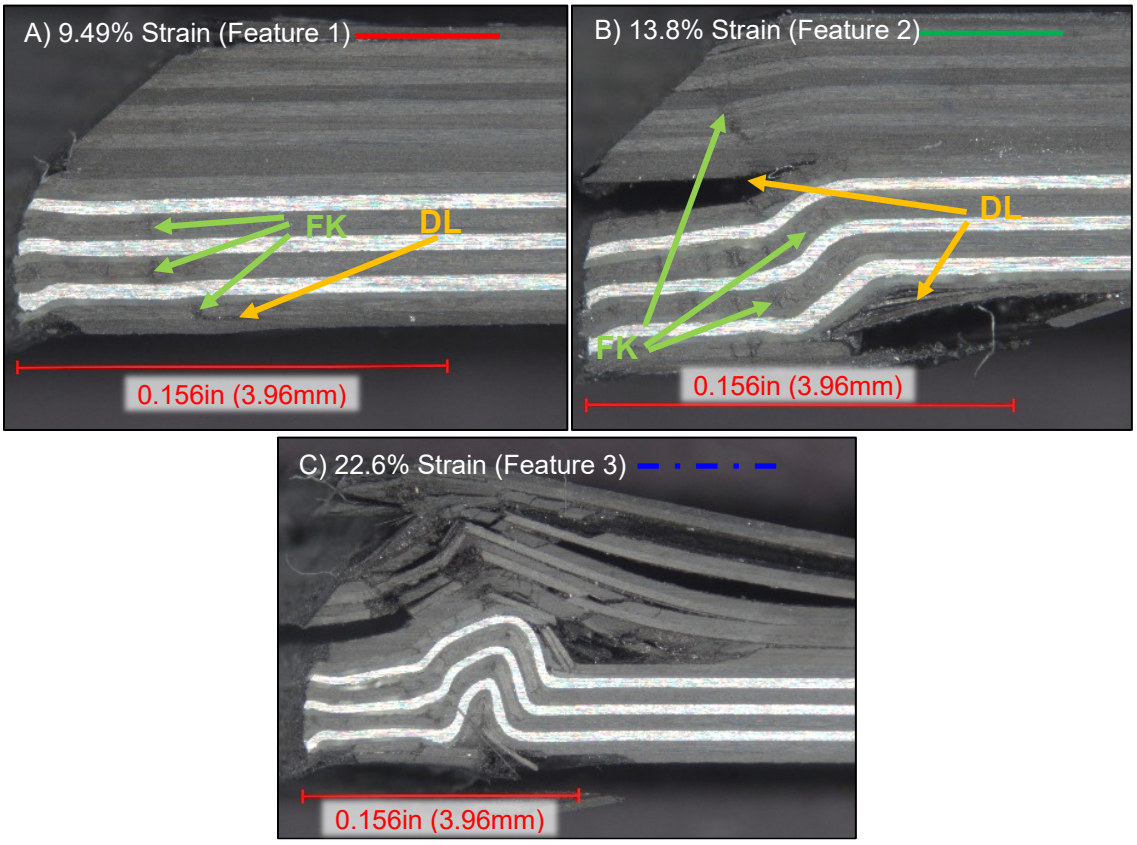

Figure 149: 18-Ply Single Shear Countersunk Shank-only Micrographs

7.3 Statistical Analysis of Quasi-Static Results

In order to verify that the results of the quasi-static analysis were conclusive, linear effects test statistical models were constructed using JMP software [108]. This step is critical because it provides indication of which variables, controlled or uncontrolled, significantly influence the results. In some cases, the influence of a nuisance variable may render the results inconclusive. As a simple example, if one were experimenting with two different heat treatments of steel, if all of the samples with treatment A were tested on a hot day with no climate control and all with treatment B were tested on a cold day with no heat, the near 100°F (56°C) temperature swing could drastically affect the results. For this research, ideally only the controlled variables of configuration, ply count, and hybridization would be statistically significant. Table 42 shows the results of linear effects models which included all controlled and nuisance variables. The RSquare Adjusted values measure how much of the variation in the system is explained by the model considered. In all cases, these models are conclusive. As expected, configuration, ply count and hybridization are all statistically significant when yield load and ultimate load were considered as responses. When transitioning to stress based data (yield stress and ultimate stress as response variables), ply count becomes insignificant since bearing stress is essentially normalizing load by thickness. In all cases, the nuisance variables proved to be statistically insignificant. Thus, the manufacturing method was stable enough that the panel position, cure cycle, and hole diameter did not introduce measurably significant variance into the coupons. As expected, the relatively stable test temperature did not affect the sample strength. Because only the controlled variables are

statistically significant, any comparative assessment made between samples can be conclusively attributed to configuration, ply count, and hybridization of the samples.

Table 42: Quasi-Static Statistical Significance

Response:	Yield Load		Ultimate Load		Yield Stress		Ultimate Stress	
Effects	**P-Value**	**Stat Sig**	**P-Value**	**Stat Sig**	**P-Value**	**Stat Sig**	**P-Value**	**Stat Sig**
Configuration	**<.0001**	**Yes**	**<.0001**	**Yes**	**<.0001**	**Yes**	**<.0001**	**Yes**
Ply Count	**<.0001**	**Yes**	**<.0001**	**Yes**	0.1540	No	0.2189	No
Hybrid	**<.0001**	**Yes**	**<.0001**	**Yes**	**0.0020**	**Yes**	**0.0020**	**Yes**
Panel Position	0.7406	No	0.7739	No	0.7802	No	0.6514	No
Cure Cycle	0.9439	No	0.9625	No	0.8934	No	0.6245	No
Temperature	0.1707	No	0.5358	No	0.5979	No	0.3783	No
Hole Diameter	0.2867	No	0.7662	No	.4553	No	0.7401	No
RSquare Adj	0.9754		0.9807		0.8254		0.9303	

VIII. Cyclic Fatigue Results

This chapter presents the results of the cyclic fatigue experimentation which was considered in double shear and in the single shear protruding head configuration with 18-ply control and hybrid samples. This chapter begins with a discussion on how the fatigue study developed as initial results were collected. Then, results obtained using the accelerated step test method are presented. Microscopy of sectioned fatigue samples is presented and compared with the failure mechanisms of the quasi-static testing. The fatigue results are presented using load and displacement with respect to cycle count. Summary fatigue data are presented in tabular form and statistical analysis is presented.

8.1 Fatigue Development

The original intent for the fatigue study was to run samples to fairly low cycle counts of 10, 100, and 500 cycles at a peak load equal to 85% of the maximum quasi-static load. However, as tests were observed in real time, little permanent deformation was noted based on the data from the extension gauge. The displacement at the peak and minimum loads are plotted with respect to cycle count for three control samples and three hybrid samples loaded in double shear in Figure 150. Since these displacements were small and the goal was to section fatigue samples to compare internal failure mechanisms to those presented in the quasi-static experimentation, more permanent deformation was desired.

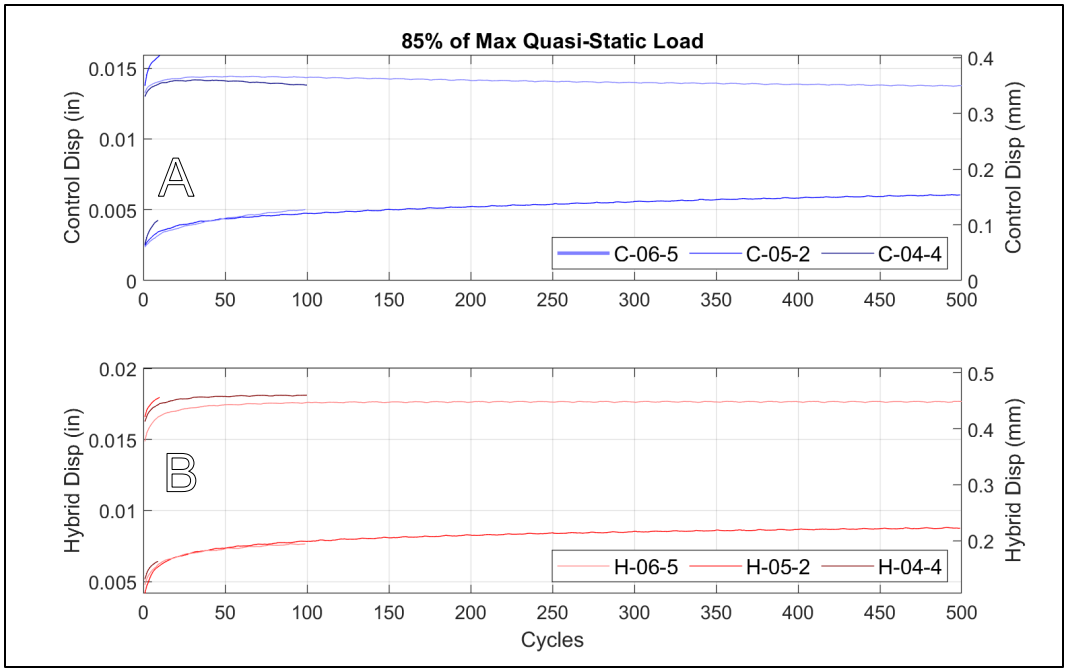

Figure 150: Low Cycle Count Fatigue Displacement

In order to obtain more deformation, the load and cycle count could be manipulated. The most conservative step was to first increase the cycle count to determine the number of cycles required to produce at least 4% hole elongation, which is commonly used to define hole failure in operational applications [18]. Using the same 85% load, a sample was run to 250K cycles but still very little permanent deformation was noted as depicted in Figure 115. After all the testing was completed and the samples were able to be sectioned, despite no obvious features in the displacement curve, the sample shown in Figure 152 displayed fiber kinking in the 0° plies, as was consistent with early damage in the quasi-static testing. This method was undesirable since, due to the high cycle count, the test ran over four days and laboratory availability was limited.

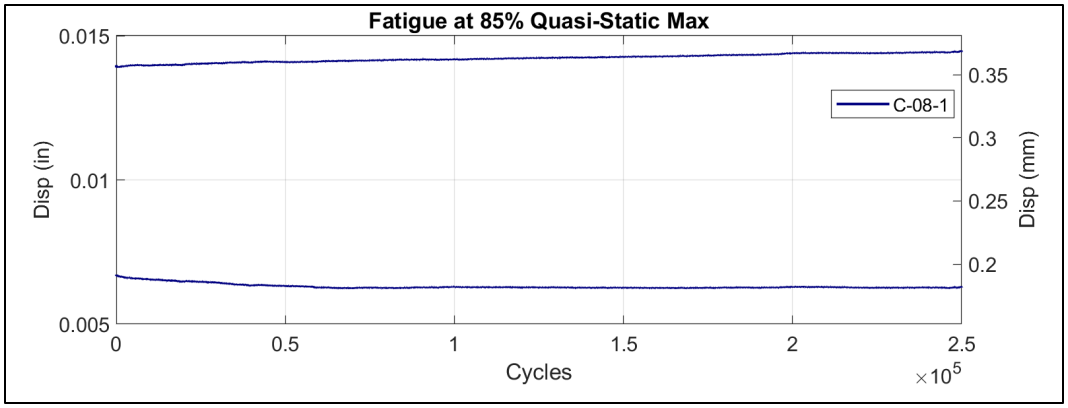

Figure 151: Control Sample at 250K cycles at 85% of Quasi-Static Maximum Load

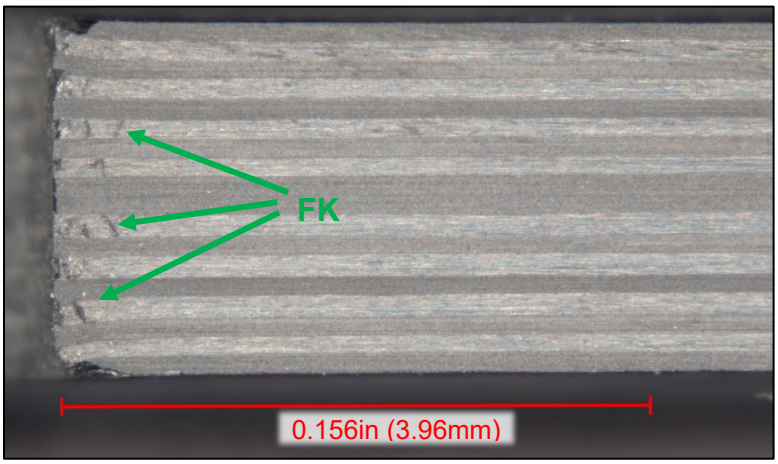

Figure 152: Damage after 250K cycles at 85% of Quasi-Static Maximum Load

Next, the decision was made to increase the load to 90% of the average maximum quasi-static load in an effort to shorten test run times. Again, in real-time, permanent deformation (Figure 153) was not seen to be developing in the sample and the test was halted near 22K cycles. After all testing was complete and the samples were sectioned, despite the small deformation, this sample displays fiber kinking and through thickness cracking as shown in Figure 154. While faster, this test still took over 6 hours to run.

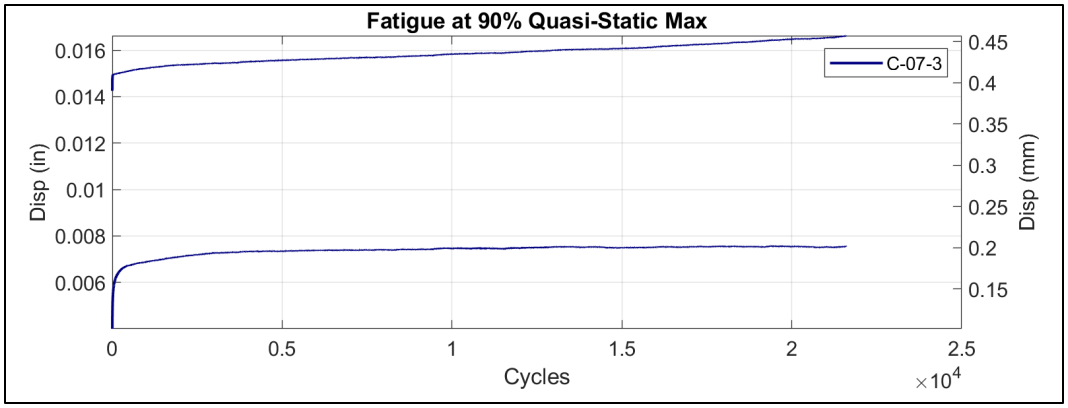

Figure 153: Control Sample at 22K cycles at 90% of Quasi-Static Maximum Load

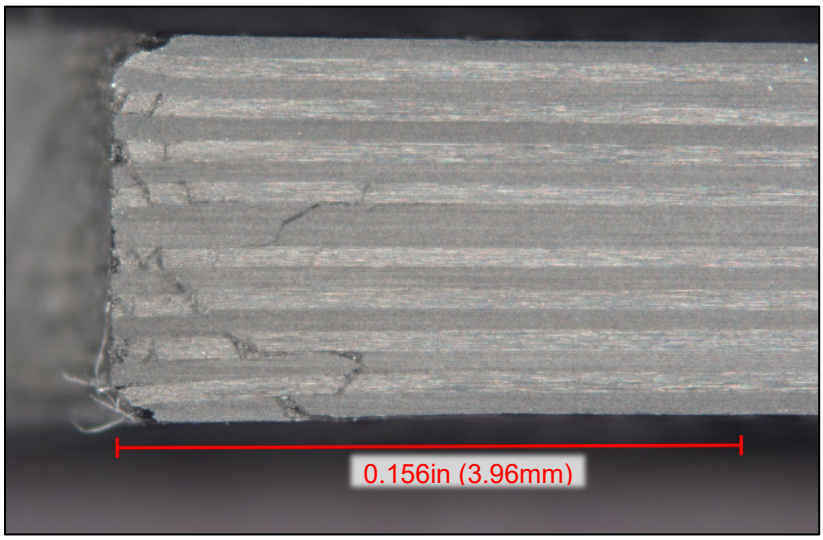

Figure 154: Damage after 22K cycles at 90% of Quasi-Static Maximum Load

Due to limited test time, a test method was desired that produced a more predictable test run time with more measurable permanent deformation. The accelerated fatigue step test method documented by Nicholas was adopted [85], [86]. This method produced consistent results and each test ran in about 3.5 hours, allowing two tests to be conducted each day. In the following sections, results from 18-ply control and hybrid samples are presented in both double shear and single shear protruding head

configurations. Micrographs of sectioned samples are presented. After both control and hybrid are presented, a comparison of the two is discussed. Finally, a statistical analysis is discussed on all the fatigue step method data.

8.2 Double Shear Cyclic Fatigue Results

The load-displacement data for the control double shear fatigue step test samples are plotted in Figure 155. Critical values are presented in terms of stress and strain later in this section. Figure 155A (top subplot) displays the bearing load at each step in the procedure. The stress began at 85% of the average peak load from the quasi-static samples in the same configuration and then increased by 2.5%. The low end of the load was maintained at 100lbf (445N) throughout. The resultant fatigue limit load for each sample is represented by a horizontal line in Figure 155A (top subplot). The stop criterion was standardized for the control and hybrid based on the results of the quasi-static testing at a displacement of 0.0250in (0.635mm) which equates to 8.03% strain. The results are consistent with the samples having an average fatigue limit load of 4.87kips (21.7kN) with a standard deviation of 165 lbf (734N). Figure 155 (bottom subplot) depicts the resultant hole elongation throughout the test. A dotted line denotes the hole elongation stop criterion.

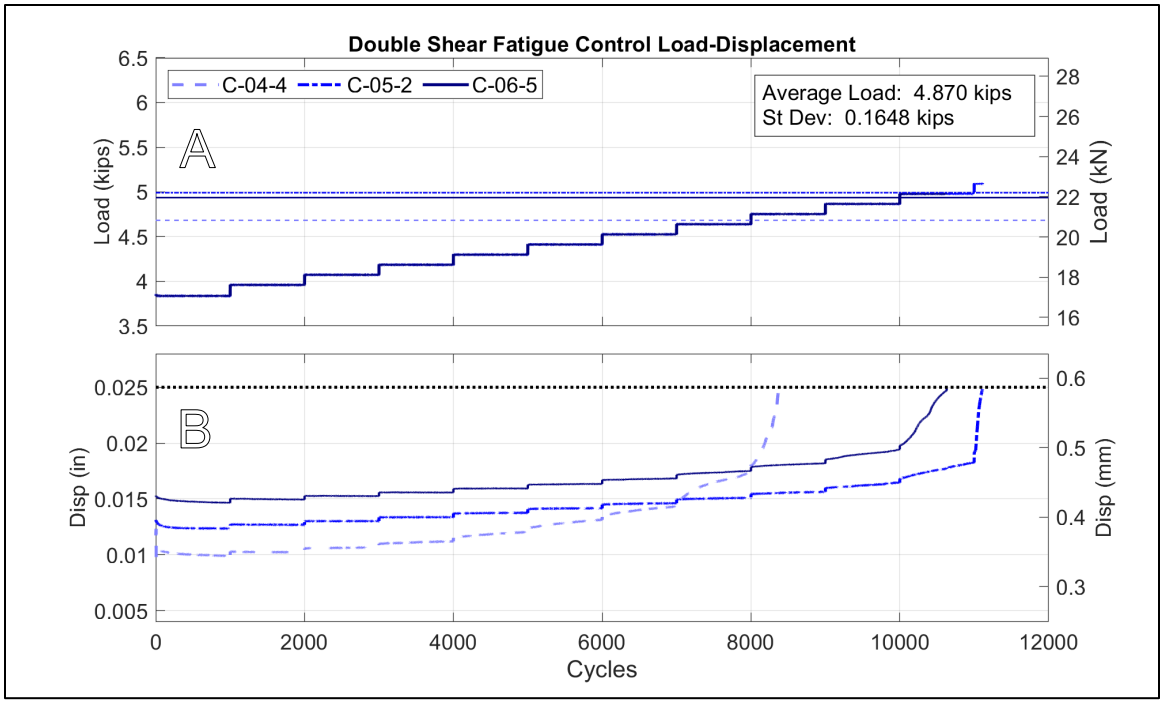

Figure 155: Control Double Shear Fatigue Step Test Results

Figure 156 shows microscopy of the sectioned control double shear fatigue samples. Since the fatigue stop criterion was 8% strain, these samples are compared to a quasi-static sample strained to 7.63%. All the samples display through thickness cracking composed of coupled fiber kinking and matrix cracking. This behavior matches that seen in the quasi-static sample. However, the fatigue samples have progressed further into this behavior. The two samples in Figure 15A and B, which exceeded 10K cycles both display delamination near the center of the layup. While similar delamination exists near the center plies in the quasi-static sample, it is more evolved in the two fatigue samples. The third fatigue sample which ran to just past 8000 cycles did not demonstrate this delamination behavior.

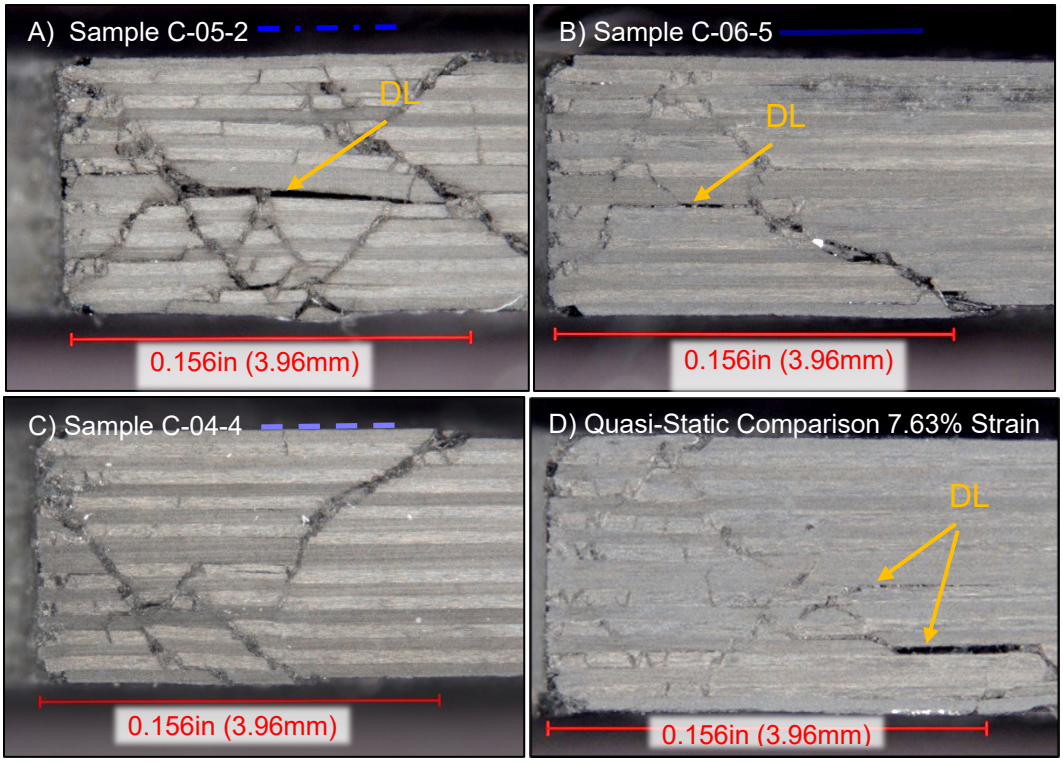

Figure 156: Control Double Shear Fatigue Step Test Sectioned Samples

Figure 157 plots the double shear fatigue step data for three hybrid samples. For comparison to the control samples, the same 0.0250in (0.635mm) stop criteria was used. These results are extremely consistent with a standard deviation in fatigue limit load of less than 93lbf (414N). The one feature here that is most undesirable is that one of the samples (H-06-5) failed catastrophically as it approached the stop criterion as denoted by the dotted line in Figure 157B (lower subplot). While no obvious defects in this sample were noted, this combined with later samples in single shear show that samples loaded cyclically are much more sensitive to machining defects.

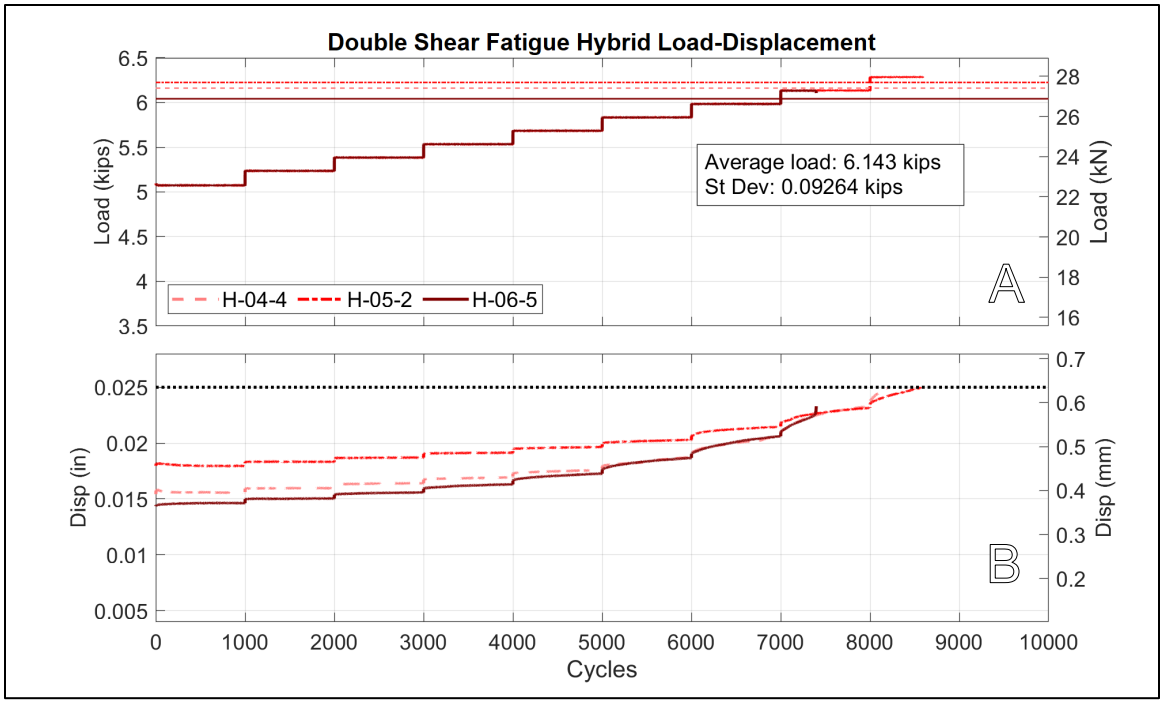

Figure 157: Hybrid Double Shear Fatigue Step Test Results

Fig. 14 shows micrographs of the double shear fatigue hybrid step test samples as compared to a quasi-static sample loaded to 7.21% bearing strain. In Fig. 14A and B, the failure is dominated by fiber kinking in the 0° plies and foil buckling, which is damping the through thickness cracking. The behavior of these samples is quite similar to that of the quasi-static behavior. However, the delamination detected and matrix cracking ("MC") in the quasi-static sample has not set into the fatigue samples.

Fig. 14C shows the sample (H-06-5) that failed catastrophically. This failure is similar to that seen in the quasi-static samples past 0.040in (1.0mm) hole elongation in Brewer et al [90]. Since a low cycle count of $n = 1000$ was selected for this fatigue study with a load rate that is relatively fast when compared to quasi-static, the fatigue limit stress here is critically high. Thus, the probability of a sample failing

catastrophically is increased. If a larger cycle count were selected, the failure would come about more gradually, and a lower load would be required which would reduce the probability of a catastrophic failure. In this case, the fatigue limit stress is just over the average maximum stress found in the quasi-static study. In reality, engineers would not design a cyclically loaded part to operate near the maximum quasi-static stress. Rather, a design would be based on a factor of safety from the quasi-static yield and a number of fatigue lifetimes.

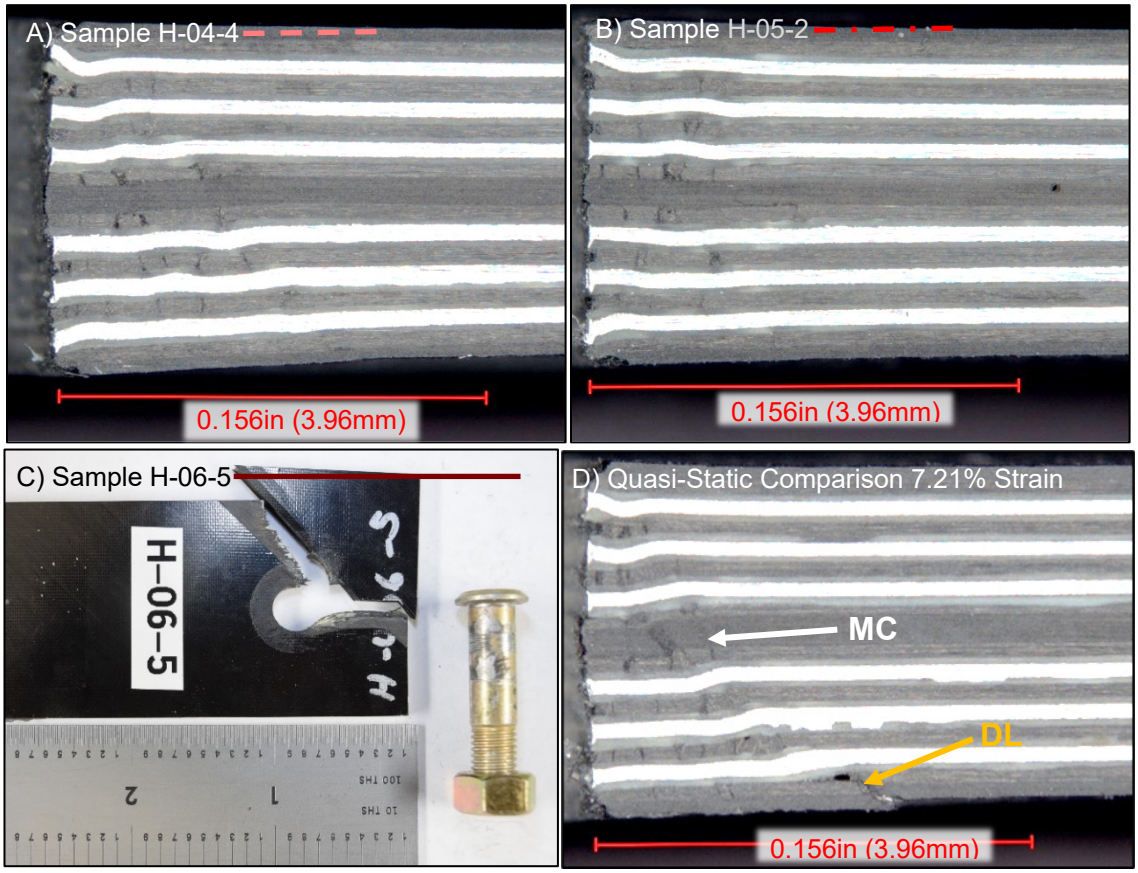

Fig. 158: Control Double Shear Fatigue Step Test Sectioned Samples

Table 43 compares the outcomes of the control and hybrid samples in the double shear step test cyclic fatigue load scenario. From a load perspective, the fatigue limit load

for 1000 cycles is 26% higher in the hybrid material. As noted in the quasi-static samples, in a stress calculation, the gains made by hybridization are masked by the thickness increase and the difference in the two means becomes statistically insignificant.

Table 43: Double Shear Fatigue Step Test Method Data

	Control			Hybrid					
	Average (95%CI)	Stdev	N	Average (95%CI)	Stdev	N	Diff	% Diff	Stat Sig
Fatigue Load (kips)	4.870 (4.461-5.280)	0.1648	3	5.913 (5.913-6.373)	0.09264	3	1.273	26.13	Yes
Fatigue Stress (ksi)	167.5 (165.2-169.9)	0.9466	3	165.7 (157.6-173.9)	3.268	3	-1.782	-1.064	No

8.3 Single Shear Cyclic Fatigue Results

The results of the control single shear fatigue step tests are plotted in Figure 159. As shown in Figure 159A (upper subplot), the steps were applied in 2.5% load steps beginning at 85% of the average maximum load of the quasi-static singe shear control samples. The resultant fatigue limit load for each sample is represented by a horizontal line in Figure 159A (top subplot). As noted in the quasi-static experimentation, the single shear condition allows for bending in the sample, fixture, and fastener which results in a lower fatigue limit stress as compared to the double shear samples. Since this load condition is more flexible, a stop criterion of 0.0400in (1.02mm) which equates to 12.8% strain was selected based on results of the quasi-static tests. Figure 159B (lower subplot) depicts the hole elongation with respect to the cycle count for each of the three samples. It is important that all three samples cross the failure criterion as they failed catastrophically as depicted in Figure 160. In contrast, under quasi-static loading the samples were consistently able to be strained to 30% hole elongation without catastrophic

failure. This early failure is attributed to the combination of a high cyclic (1hz) rate compared to quasi-static and a low cycle count which drove the fatigue stresses critically high. Due to the catastrophic failure, the bearing region of the samples was completely crushed, rendering the sample unusable for microscopy.

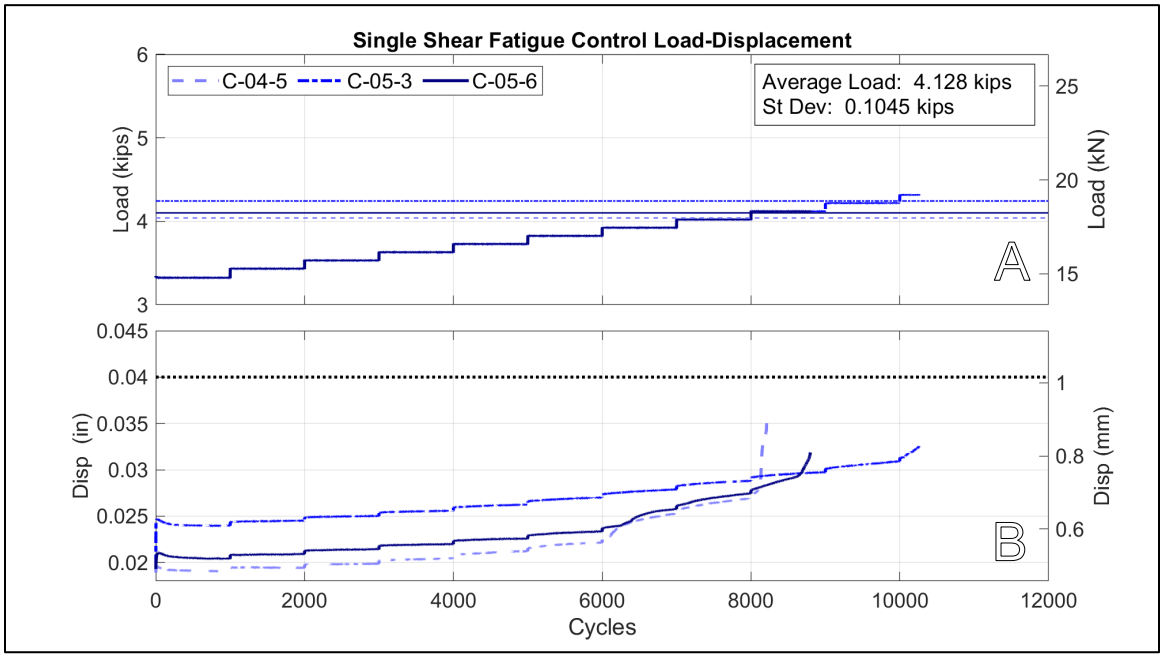

Figure 159: Control Single Shear Fatigue Step Test Results

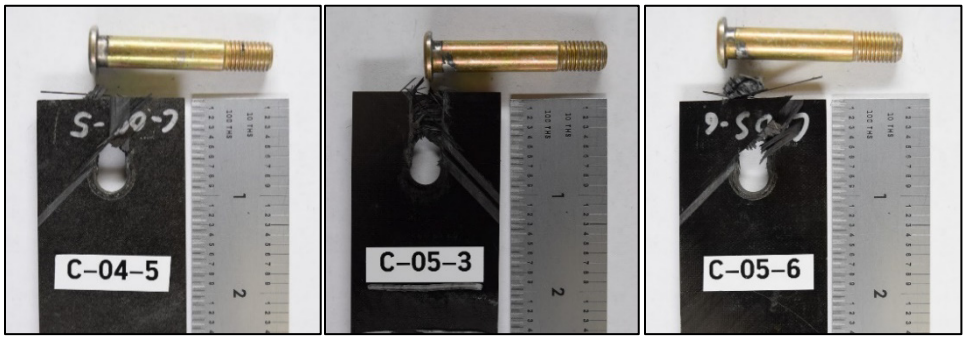

Figure 160: Control Single Shear Protruding Fatigue Samples

Figure 161 depicts the experimental results for the hybrid single shear fatigue step test samples. Figure 161A (top subplot) displays the load beginning at 85% of the average maximum quasi-static load with each step increasing by 2.5%. The bottom subplot displays the hole elongation over the cycle count.

One feature that stands out in the data are the three samples (in green traces) with cycle counts and fatigue limit stresses far lower than other samples. These three samples all had defects produced during the hole drilling process and were run to understand the effects. Samples H-04-5 and H-05-3, shown in Figure 162A and B, both suffered from delamination of the lower plies during drilling causing them to fail extremely early. H-04-5 (Figure 162A) also suffered from internal tearing. This sample was damaged to such an extent that it did not complete and entire block and does not meet Nicholas' criteria for calculation of a fatigue limit. Sample H-06-7 displayed a different machining phenomenon commonly known as "chatter." Here, when the chamfering bit was employed, vibration was introduced. This caused the bit to skip around the edge of the hole cutting out scalloped sections of material instead of cutting evenly around the diameter. This scalloped appearance on a macroscopic scale is shown in Figure 162D and the resulting damage is visible in Figure 162E. These three samples show that careful machining is critical to the strength and fatigue life of this hybrid material, and that specific nondestructive inspection methods of the holes must be developed and employed before parts enter service life. Since these samples had known defects, they were not included in the statistical analysis.

The remaining samples which were considered in the statistical analysis produced consistent results with all reaching the stop criterion on the same step and achieving a

standard deviation in load of 25lbf (110N). In contrast to the control samples, each single shear hybrid, including the damaged samples reached the hole elongation stop criteria without catastrophic failure.

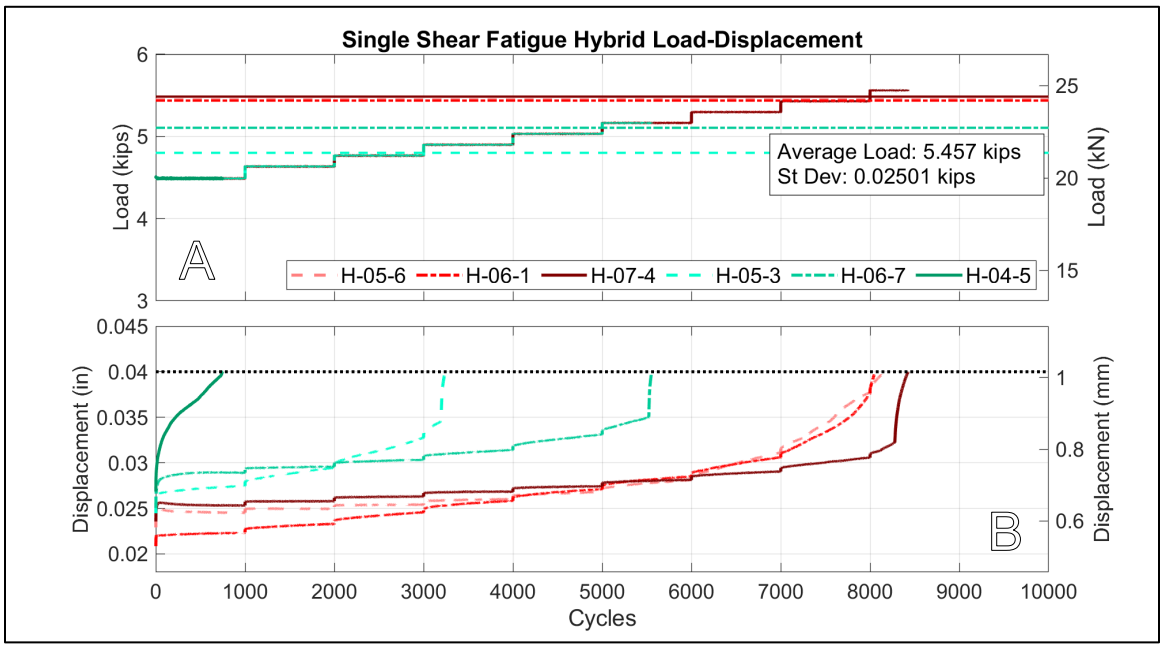

Figure 161: Hybrid Single Shear Fatigue Step Test Results

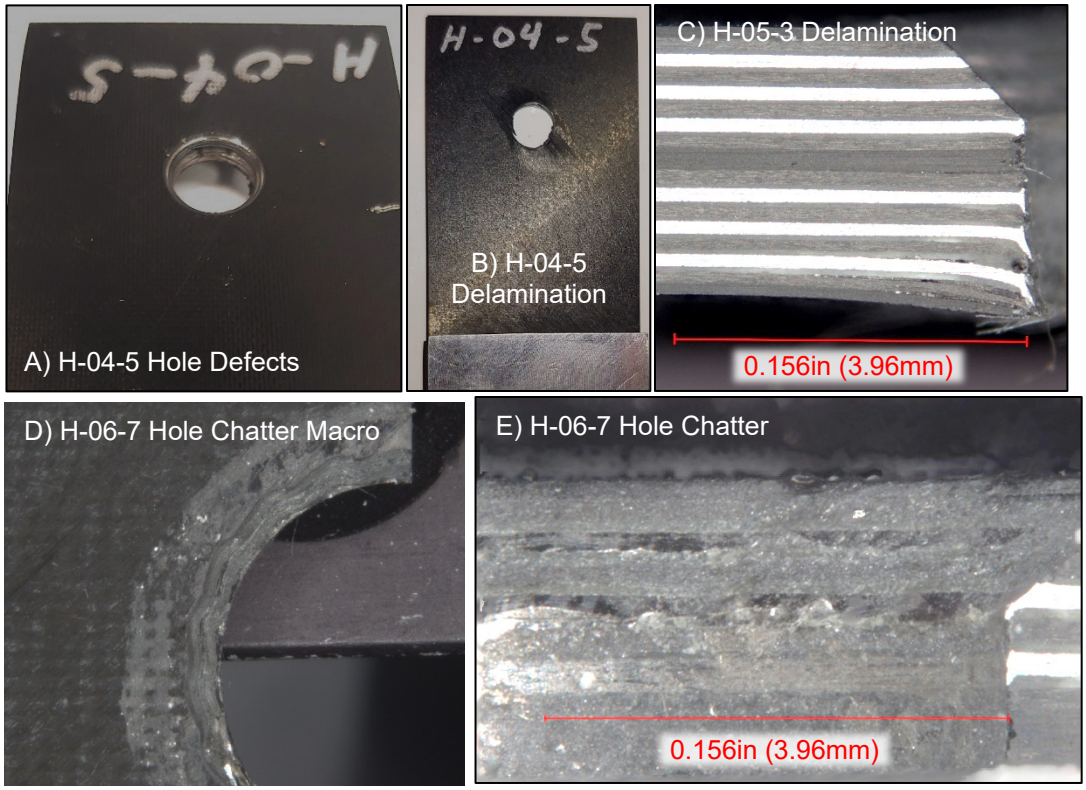

Figure 162: Machining Damage in Hybrid Singe Shear Protruding Fatigue Samples

Figure 163 shows microscopy of sectioned hybrid single shear protruding head fatigue samples that were pristine prior to testing. Figure 163A shows a unique failure pattern that was not displayed in the quasi-static samples. Here the damage is closer to the bearing surface and actually displays a fracture in the uppermost foil. This corresponds to a curve that shows a sharp change (in Figure 126) as it approaches the stop criterion. The other two samples in Figure 163B and C behaved similarly to the quasi-static condition that was loaded to 13.0% strain which is close to the 12.8% strain used as the stop criterion here. They show developed wedge buckling through the thickness of the coupons with delamination occurring near the surface plies and midplane plies.

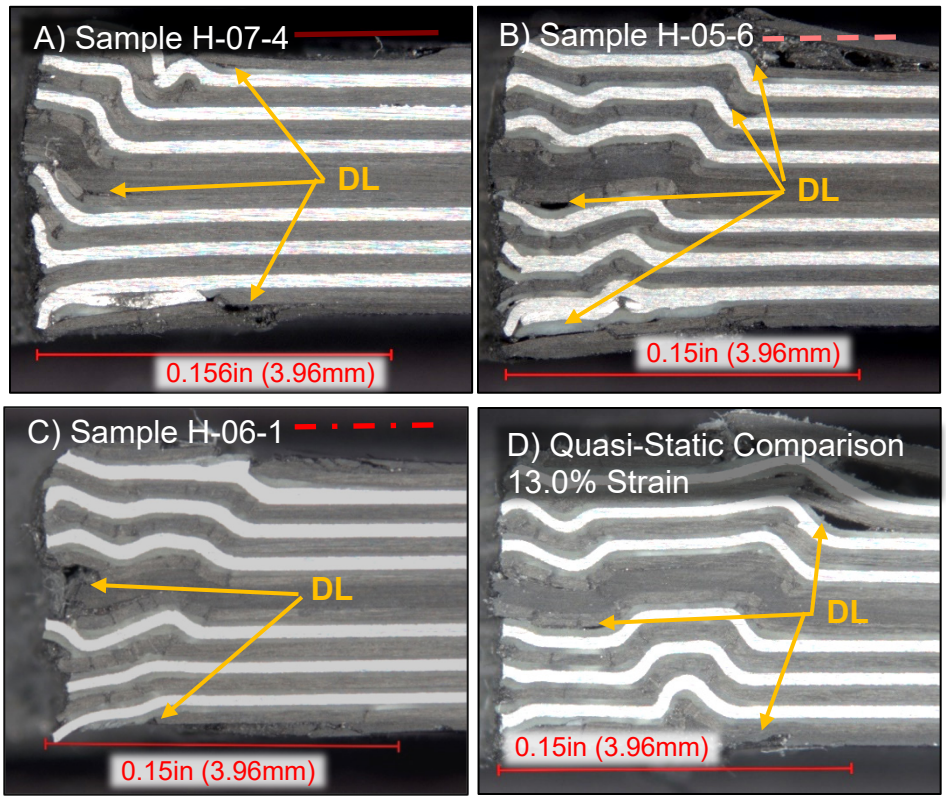

Figure 163: Representative Hybrid Singe Shear Protruding Fatigue Samples

The critical data for the single shear protruding head samples are compared in Table 44. The hybrid displays a fatigue limit load that is 32% greater than that of the control. Furthermore, the hybrid displays standard deviations that are far less than those of the control samples. When stress is calculated, the hybrid appears to be significantly greater, but the standard deviation in the control samples is large enough that the 95% confidence intervals overlap, and difference is not statistically discernable.

Table 44: Single Shear Fatigue Step Test Method Data

	Control			Hybrid					
	Average (95%CI)	Stdev	N	Average (95%CI)	Stdev	N	Diff	% Diff	Stat Sig
Fatigue Load (kips)	4.128 (3.869-4.388)	0.1045	3	5.457 (5.395-5.519)	0.02501	3	1.329	32.19	Yes
Fatigue Stress (ksi)	143.6 (129.0-158.2)	5.8790	3	151.0 (149.4-152.7)	0.6589	3	7.436	5.178	No

8.4 Fatigue Statistical Effects Analysis

In order to verify that the results of the fatigue analysis were conclusive, JMP statistical analysis software was used to construct linear effects tests models on the fatigue step test data [108]. Ideally, only the controlled variables of configuration (single shear or double shear) and hybridization (control or hybrid) would significantly affect the bolted joint. Nuisance variables were test ambient temperature, hole diameter, cure cycle and panel position. The limited number of samples caused aliasing between the variables which prevented the inclusion of all of the nuisance variables into the final models. Temperature and hole diameter were not significant in the quasi-static statistical analysis and were not significant in preliminary models. Specifically, in linear effects models considering temperature and hole diameter as effects, neither was significant and the RSquare Adjusted value was negative, meaning these nuisance variables explained virtually none of the variation. Thus, the final models presented here include the variables related to layup which was of greatest concern.

First, the fatigue limit load was considered as the response. Here, configuration and hybridization were both statistically significant while panel position and cure cycle were not significant. With an RSquare Adjusted value of .9825, variation from configuration (single shear v. double shear) and hybridization explain 98% of the

variation in the model. When the response was changed to fatigue limit stress, configuration remained significant, but hybridization was no longer significant. This is due to the thickening caused by the adhesive. Overall, this statistical analysis proves that the largest sources of variation in the data are the configuration and hybridization, which was desired and expected. Additionally, this supports the conclusion that the panel position and cure cycle are not significant. This means that the manufacturing process is sufficiently consistent across the area of each panel and between cure cycles. Because only the controlled variables are statistically significant, any comparative assessment made between samples can be conclusively attributed to configuration and hybridization of the samples.

Table 45: Fatigue Step Statistical Analysis

Response:	Fatigue Limit Load		Fatigue Limit Stress	
Effects	**P-Value**	**Stat Sig**	**P-Value**	**Stat Sig**
Configuration	**<.0001**	**Yes**	**0.0018**	**Yes**
Hybrid	**<.0001**	**Yes**	.3558	No
Panel Position	0.8816	No	0.8855	No
Cure Cycle	.1450	No	0.2803	No
RSquare Adj	0.9825		0.7992	

IX. Contributions, Conclusions, Recommendations, and Summary

This research focused on characterizing the loading and failure of a novel hybrid material composed of a unidirectional carbon fiber co-cured with stainless steel foils in place of composite plies at a bolted joint as compared to a control material. A parallel objective was to trace the failure computationally by producing representative finite element models to predict the behavior of this hybrid material in a bolted joint. Quasi-static bolted bearing experimentation was performed per ASTM D5961 on hybrid and control samples in 9-ply and 18-ply layups in double shear. 18-ply single shear samples were considered with protruding head and countersunk head bolts. Double shear and single shear protruding head samples were compared in cyclic fatigue using the step test method as described by Nicholas [86]. Finally, finite element models of 9-ply and 18-ply, control and hybrid models were developed using Abaqus finite element software and compared to experimental data.

9.1 Contributions

This work added many novel contributions to the research area. This was the first effort to explore this layup employing the AF191U film adhesive in bearing samples. This was the first effort to consider a hybrid composed of IM7/977-3 carbon fiber and stainless steel across multiple configurations, which allowed enough testing to produce statistical evaluation.

To aid the experimentation, updated fixtures were designed and machined that are more consistent than those commonly purchased. Engineers who had worked on bearing samples previously, cited issues with other fixtures and extension measurement

techniques. Specifically, the integral knife edges and bonded knife edge tabs were 100% effective. Slipping of the extension measurement apparatus was never noted. Because of its effectiveness, this design was incorporated into a 0.250in (6.35mm) hole diameter fixture for AFRL/RQ to replace the fixtures sourced from a prominent manufacturer. These updated fixtures have already been used by engineers and technicians from AFRL/RQ and San Diego State University. Drawings have been distributed to contractors of AFRL and the fixture system has been recommended for use in their work.

This was the first cyclic fatigue testing performed on this hybrid material and the first accelerated step method performed on composite bearing samples.

From a modeling perspective, this was the first modeling effort to focus on producing accurate and efficient models in different layups while working inside the native Abaqus environment. This was also the first effort to employ parallel computational failure criteria to explain failure in this novel hybrid across multiple configurations.

From a manufacturing perspective, this research proved that the hybrid material can be manufactured consistently at the coupon level. The completed coupons were as dimensionally stable as the controls and the standard deviations of the strength of the coupons were similar to those of the controls.

9.2 Conclusions

The quasi-static testing proved that hybridization increased the load capacity of the layup in every tested configuration. In double shear, hybridization increased the yield load by 25.4% in the 9-ply case and by 12.4% in the 18-ply case. In single shear,

hybridization increased the yield load by 31.3% with a protruding head, and by 15.5% with a countersunk head. While the adhesive did thicken the layup by about 27%, the magnitude of this thickening is only 0.025in (0.64mm) in the 18-ply. In many design cases this thickness may be a reasonable trade for the benefits of hybridization. Future efforts should investigate thinner adhesive solutions and the removal of adhesive altogether. The quasi-static data also demonstrated that the addition of the ductile stainless steel damped sharp reloading behavior bringing about a smoother stress-strain curve.

This research demonstrated that in both the control and hybrid in double shear, the 9-ply layup was a good predictor of the 18-ply behavior up to about 10% strain. In the control, doubling the 9-ply load capacity predicted the load capacity of the 18-ply so closely that the values are not statistically discernible. In the hybrid, doubling the 9-ply loads overestimated yield by about 10% making it a usefully conservative estimate. Since foil preparation was one of the most time-consuming aspects of the manufacturing for this work, employment of 9-ply samples for early development and investigation would be resource and time efficient.

One of the most remarkable results of this work is the reloading effect noted in the single shear hybrid protruding head case. The unique buckling condition caused by the foils near 12% strain allows the material to reach a second peak load near the magnitude of the first peak load. This phenomenon could help reshape the way engineers design composite structures for survivability.

While the scope of the fatigue effort was limited, it proved that for a low cycle count, the hybrid supported a higher fatigue load than the control in both double and

single shear. While adhesive thickening was still a factor, the improvements would be worth the slight thickening in applications where the design space allows for local thickening. The fatigue data suggests that the hybrid has less probability of failing catastrophically due to cyclic fatigue loading.

The goals of providing accurate and efficient finite element models while working inside the native Abaqus environment were met. Across all four modeled configurations (9-ply and 18-ply, control and hybrid), the models predicted the yield load within 6.5% and the offset load within 4.5%. This demonstrates that the modeling methods scaled well from 9-plies to 18-plies and simulated the complexities of the hybrid and bearing condition well. Not only did the models function well on a macroscopic scale for load prediction, they also functioned well at the ply level. The models corroborated the experimental evidence that bearing failure is dominated by fiber compression and predicted the location and onset strain of the failure modes in a representative fashion. Even with adding the complexities of hybridization, Hashin failure criteria performed well in predicting the location and modes of failure in the composite layers.

In addition to performing accurately, the models were also efficient. Even the most complex, the 18-ply hybrid, ran in 12.5 hours using 20 cores (parallel processors). This is efficient enough that an engineer could develop a coupon level model in one day and return to a representative solution output the following day. This also means that as the models are scaled to include multiple holes or included in subcomponent simulations, they should not become overly computationally burdensome.

9.3 Recommendations for Future Work

Future work should examine optimization of the adhesive to control thickening. Then, an optimization effort could be explored to optimize the size and shape of the foils near stress concentrations. Based on hole diameter measurements and observed hole defects, an optimization effort should be pursued to discern the best tooling and parameters for hole drilling in the hybrid composite. A detailed study should be pursued exploring the time dependence of this hybrid material. This should explore how the thermally induced stresses may relax in the material and investigate creep effects during extended periods of loading. Since preload relaxation is a known phenomenon in composite materials, the time dependent preload relaxation response of the hybrid material should be characterized [70], [104]. A detailed fatigue study should be explored to characterize fatigue limits of the hybrid as stress and cyclic rate are varied. As the system is understood better, an environmental study should be conducted to characterize how the material will behave in operational conditions with exposure to moisture and thermal cycles. Hybridization should then be tested at the subcomponent and component level before inclusion in flight test articles and eventual operational structures.

9.4 Summary

In summary, if an engineer needs to increase the load capacity, strain energy capacity, and fatigue load of a composite joint, he/she should investigate local hybridization with stainless steel foil as a solution. If local thickening of the layup is not viable in the design space, this work should be used as a baseline for the further investigation of other adhesive methods such as spray adhesives as a replacement for the

AF-191U employed here. A solution without adhesive should also be studied. The finite element models developed in the research should aid in the development of coupon and subcomponent level test article to feed a design.

Appendix A Materials Requirements

In order to prepare materials or layup, an organized list of required materials was assembled. Table 46 lists the materials to make a single panel per each configuration.

Table 47 shows the materials required for the sum of each panel type. The total column in Table 47 is effectively a material cut list. Lastly, Table 48shows the area required for each type of material. It is important to note that the width of the foils here is different than the final target transition lengths of 2.00in and 3.00in (5.08cm and 7.62cm). This excess material is included in the "trim" material and allowed the machinists to ensure that the transitions occurred at the correct location in the coupons.

Table 46: Materials Required Per Panel

				1x 9-Ply Control Panel	1x 9-Ply Hybrid Panel	1x 18-Ply Control Panel	1x 18-Ply Hybrid Panel	1x 18-Ply Shank-Only Panel
Material	Fiber Direction	Length 1 (in) [mm]	Length 2 (in) [mm]	Number Required	Number Required	Number Required	Number Required	Number Required
IM7	0	8.00 [203]	12.0 [305]	4	4	8	8	8
IM7	45	8.00 [203]	12.0 [305]	4	2	8	4	6
IM7	45	4.75 [121]	12.0 [305]	0	2	0	4	2
IM7	90	8.00 [203]	12.0 [305]	1	0	2	0	1
IM7	90	3.75 [95.3]	12.0 [305]	0	1	0	2	1
SS	-	3.25 [82.6]	12.0 [305]	0	2	0	4	2
SS	-	4.25 [108]	12.0 [305]	0	1	0	2	1
AF 191	-	8.00 [203]	12.0 [305]	0	6	0	12	6

Table 47: Materials Required For all Panels

				1x 9-Ply Control Panel	1x 9-Ply Hybrid Panel	5x 18-Ply Control Panel	5x 18-Ply Hybrid Panel	1x 18-Ply Shank-Only Panel	Total
Material	Fiber Direction	Length 1 (in)	Length 2 (in) [mm]	Number Required	Number Required	Number Required	Number Required	Number Required	Number
IM7	0	8.00 [203]	12.0 [305]	4	4	40	40	8	96
IM7	45	8.00 [203]	12.0 [305]	4	2	40	20	6	72
IM7	45	4.75 [121]	12.0 [305]	0	2	0	20	2	24
IM7	90	8.00 [203]	12.0 [305]	1	0	10	0	1	12
IM7	90	3.75 [95.3]	12.0 [305]	0	1	0	10	1	12
SS	-	3.25 [82.6]	12.0 [305]	0	2	0	20	2	24
SS	-	4.25 [108]	12.0 [305]	0	1	0	10	1	12
AF 191	-	8.00 [203]	12.0 [305]	0	6	0	60	6	72

Table 48: Total Raw Materials Required

	Total (ft^2)[m^2]
IM7	133.3 [12.38]
SS	10.75 [0.9987]
AF 191	48.00 [4.459]

Appendix B Vacuum Bagging and Cure

Vacuum Bagging

After enough layups were complete and ready to cure, the panels were vacuum bagged as diagramed in Figure 164. During this work, engineers developed an autoclave cure checklist on which each step was initialed to ensure that all steps were completed properly (checklist included in Appendix C). Vacuum bagging began by coating steel platen (base plate) and aluminum caul plate (top plate) with Frekote mold release agent. The protective backing was removed from the uncured panel and the panel was debulked for three minutes between two sheets of non-porous Armalon. Because, the prepreg is manufactured with a precise resin ratio from the factory, the manufacturer recommends fully encasing the composite layup to prevent resin from escaping from the part into other portions of the bag. In this case, the composite panel is encased in non-porous Armalon and surrounded on all sides with rubber dam material. A5000 release film was applied and then an aluminum caul plate was placed over each panel to keep the two faces of the panel parallel. Breather cloth distributed the vacuum evenly throughout the part. Two K-type thermocouples were installed for redundancy to track the part temperature through the cure cycle. The system was sealed using nylon bagging film and vacuum tape. After two vacuum ports were attached, vacuum was drawn on the system to perform a leak test. The leak test was passed of the system lost less than 2.00in-hg (inches of mercury) (6.77kPa) in 10 minutes. Figure 165 shows a complete vacuum bag setup containing six panels.

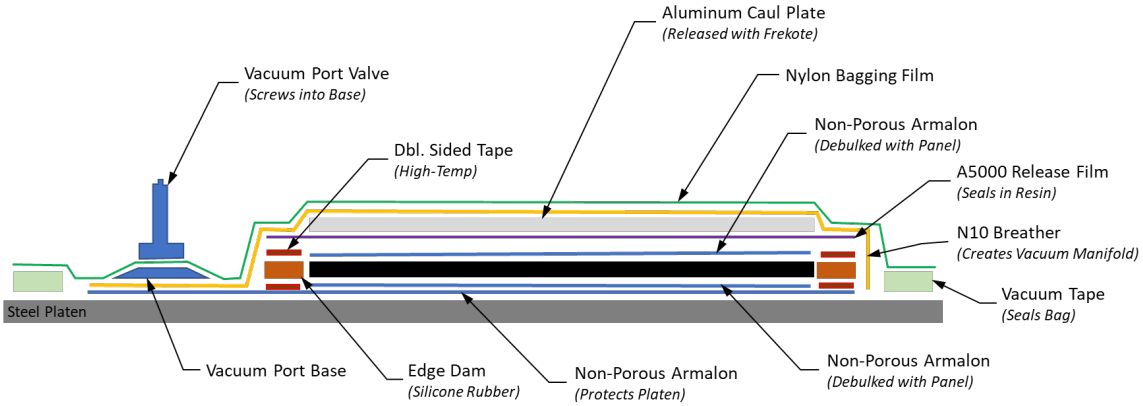

Figure 164: Vacuum Bag Diagram
(Courtesy of Jason Miller, AFRL/RQVS)

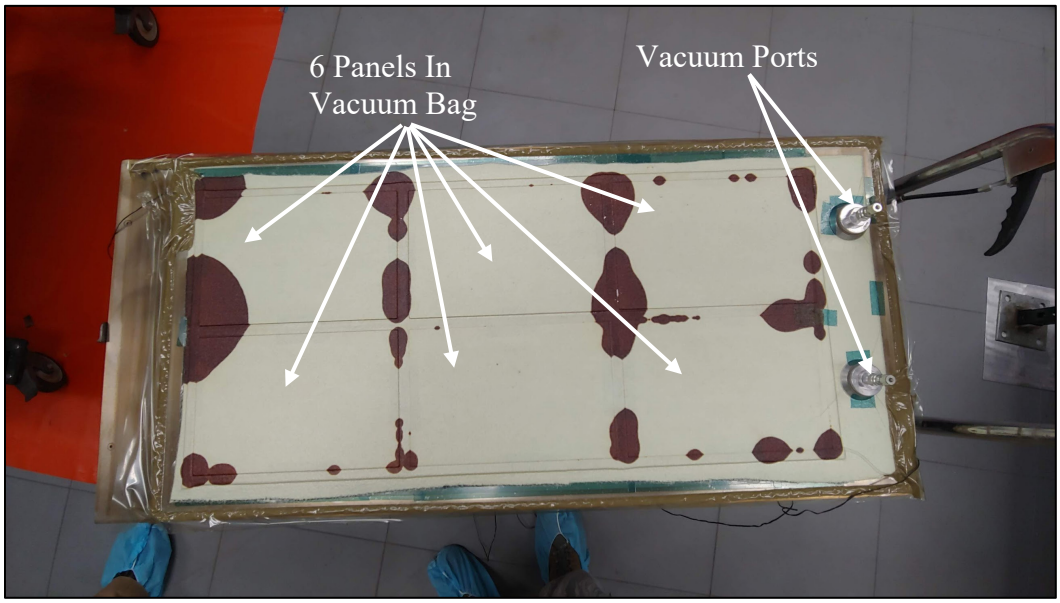

Figure 165: Complete Vacuum Bag

Curing

Before final cure, the bagging and cure checklist was reviewed to ensure the parts were ready to be cured. The parts were cured using the ASC Econoclave EC2X4 autoclave [122]. Figure 166 depicts the autoclave system used for this study.

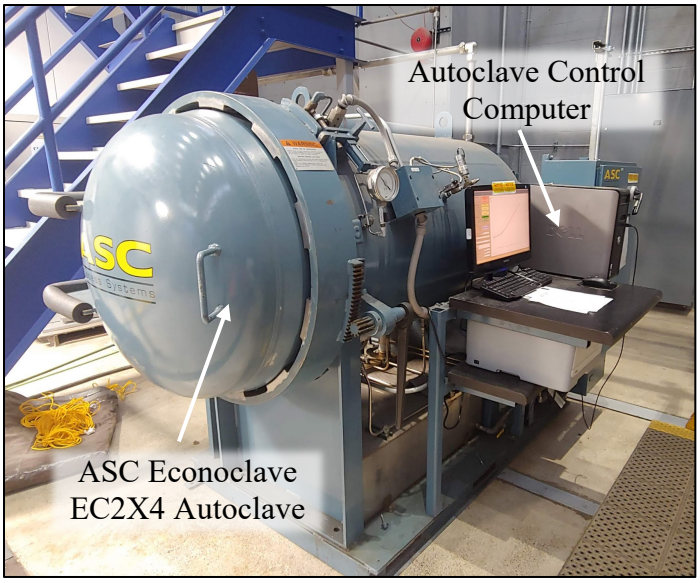

Figure 166: ASC Autoclave System

With the platen in the autoclave and vacuum lines and thermocouples connected to their respective ports, the door was sealed. From there, the computer controlled a cure "recipe" that ramped to 100psi (689kPa) and 350°F (177°C) and held those conditions for six hours as specified by Hexcel Composites provided in Appendix D.

Appendix C Pre-Cure Checklist

_____Wax backing paper has been removed

_____Orange poly has been removed

_____Release has been applied to platen/autoclave cart

_____Release has been applied to caul plates

_____J-Type thermal couples have been verified with meter

_____Minimum 2 J-Type thermocouples installed

_____All materials inclusive of vacuum bag are rated for run temperature

_____Minimum 2 vacuum ports installed

_____Vacuum ports have been checked for flow

_____Vacuum ports have been tightened with adjustable wrench

_____All paper has been removed from autoclave interior

_____Part vacuum leak check (Max leak rate 2 in-Hg/10 mins)

Date:_____

Part / Bagging certified by:_____

Part point of contact:_____ Phone

Number:_____

Material in run:_____

Cure Temperature (°F)_____ Dwell Time (mins)_____

Pressure (PSI)_____

Appendix D Hexcel Recommended Cure Cycle

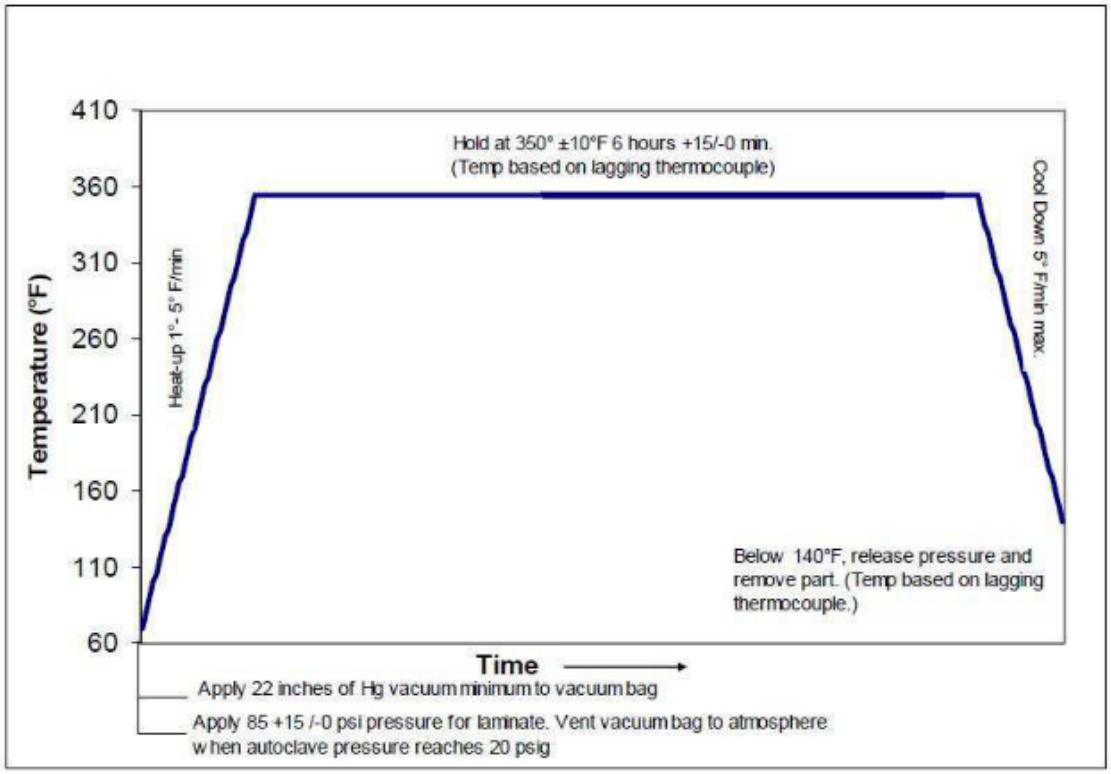

Figure 167: 977-3 Cure Cycle [93]

Appendix E Foil Preparation Procedure

Degreasing

All adherend surfaces of the adherends were wiped with clean, acetone-moistened, lint-free wipes (Chicopee® Duralace® 9404). Wiping continued until the surface of a new, clean wipe did not present discoloration from contamination.

Grit-Blast Process

The bonding surface of each adherend was grit-blasted with 50 μm diameter (nominal) [240 grit #] aluminum oxide grit using a 0.22-inch blast nozzle and 70 psig of clean, dry nitrogen propellant. The surface was grit-blasted using a 90 ± 15-degree angle of incidence, and a stand-off distance of 6 to 9 inches was maintained throughout the process. Grit-blasting continued until a uniform finish was achieved on the treated surface. Residual grit was removed from the treated surface using ~35 psig of clean, dry nitrogen.

Sol-Gel Application

Sol-gel application was initiated within 60 minutes after completion of the grit-blast process. AC-130-2 sol-gel was mixed per the manufacturer's recommendations and used within 8 hours after the initial mixing of the solution. The mixed solution was applied to the bonding surface of each adherend using a clean acid brush, and the surface remained wetted for 3-4 minutes before being oriented vertically to allow excess solution to drain. The surface was dried at ambient conditions (75 ± 5 °F and 40 ± 5% relative humidity (RH)) for 60 minutes in a clean laboratory environment.

Primer Application

Cytec Solvay BR 6747-1 primer was sprayed on using a horizontal and vertical box pattern to achieve a thickness of 0.0002in. The adhesive thickness was measured using a “traveler panel” that was prepped and sprayed alongside the main panel. This prevents contamination of the main panel from over handling.

Appendix F Panel Cut Layout

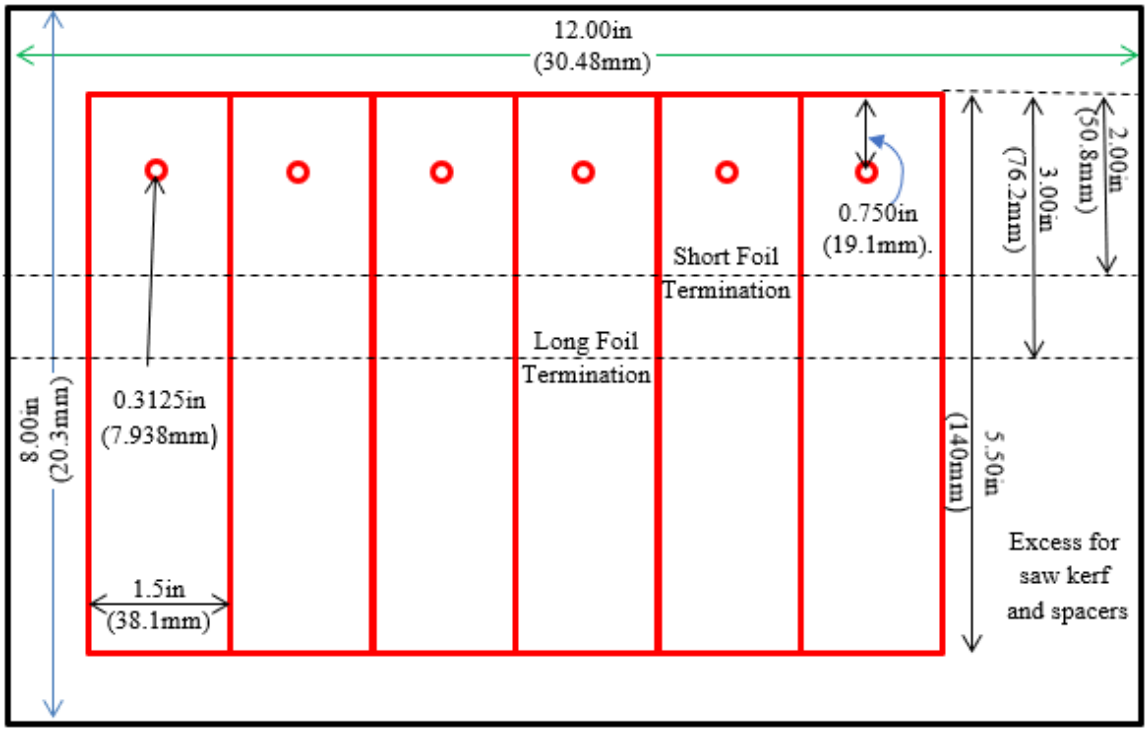

Figure 168: Panel Cut Layout

Notes:

- Control coupons should be centered in the panel such that defects in the manufactured edge are avoided.
- Hybrid coupons should be machined such that the outermost stainless steel foil extends 2” into the finished coupon. The cut sheet assumes 0.75 inches of excess foil and composite, to allow for the precision cutting step.
- Coupons should be labeled with the coupon closest to the edge denoted with “1” appended to the panel name. For example, the 3rd coupon in panel C-01 would be inscribed with C-01-3.

Appendix G Test Procedure

Testing Procedure

Bearing Testing – ASTM D5961 Standards

Bearing Test Equipment

- Bearing Test Fixture A and C (ASTM D5961)
- Clip-on extension gauge
- Ultrasonic Scanner (C-scan)
- 6inCalipers (all other measurements)
- Pin Gauges
- Load Cell (Test Frame)

Pre-test Measurements

- w – specimen width (near hole)
- h – specimen thickness (near hole)
- D – hole diameter
- f – distance to closest specimen side
- g – distance to specimen end
- d – bolt diameter

Sample Installation

- Double Shear
    - With fixture on bench, install coupon and bolt and finger tighten nut.
    - Grip Fixture in upper grip. (Grip Pressure 2000psi)
    - With controller in load control set to hold zero load, grip sample in lower grip. (Grip Pressure 2000psi)
    - Torque bolt to 60in-lbf
- Single Shear
    - Grip Fixture in upper grip. (Grip Pressure 2000psi)
    - With lower grips open, install coupon and bold and finger tighten nut.
    - With controller in load control set to hold zero load, grip sample in lower grip. (Grip Pressure 2000psi)
    - Torque bolt to 60in-lbf

Loading procedure

- Load in displacement control at 0.050in/min
- Data recording – 10Hz
    - head displacement
    - Bearing load
    - Extensometer displacement
    - Time
    - Command (was not recorded for this work but it recommended)
- Set stop criterion to 30% hole elongation or prescribed progressive failure point
- Unload in load control at 500lbf/mil

Post-Processing

- Section samples though center of hole along 0° direction to enable microscopy
- Ensure that all sectioned parts are labeled with original specimen number

Appendix H Materials Properties

Table 49: IM7/977-3 Properties [18]

Lamina Properties		Strength Properties		Toughness Properties	
E11 [msi]{GPa}	18.91 {130.4}	F11tu [ksi]	392.45 {2705.8}	G_FT (psi-in) {kPa-m}	600 {105}
E22 (E33) [msi] {GPa}	1.26 {8.69}	F11cu [ksi]	256.06 {1765.5}	G_FC (psi-in)	85.65 15.00
nu12 (nu13)	0.32	F22tu [ksi]	13.88 {95.70}	GIC_MT (psi-in)	1.69 {0.296}
nu23	0.461	F22cu [ksi]	34.33 {236.7}	GIIC_MC (psi-in)	3.538 {0.620}
G12(G13) [msi] {GPa}	0.824 {5.68}	F33tu [ksi]	13.88 {95.70}		
G23 [msi] {GPa}	0.432 {2.98}	F12su [ksi]	17.11 {110.0}		
CTE [µin/in-°F] {µm/m-°C}	-0.36 {-0.20}	F23tu [ksi]	17.11 {110.0}		
Thickness (in) (experimental)	0.00515	F13su [ksi]	17.11 {110.0}		

Table 50: 301 Stainless Steel Full Hard Properties

Mechanical Properties		Thermal Properties	
[1]Density (lb/in^3) {g/cc}	0.289 {8.03}	CTE[1] (68-572 °F) (µin/in-°F) {µm/m-°C}	9.78 {17.6}
[2]Ultimate Tensile Strength (ksi){MPa}	200.2 {1380}	[1]Specific Heat Capacity (BTU/lb-°F) {J/g-°C}	0.120 {0.500}
[2]Yield Strength (ksi)	167.8 {1157}	[1]Thermal Conductivity (BTU-in/hr-ft^2-°F) {W/m-K}	113 {16.3}
[1]Modulus of Elasticity (msi){GPa}	30.7 {211.7}	Chemical Makup[2] (%)	
[1]Poissons Ratio	0.29	Carbon-C	0.110
[2]Elongation at break (strain)	0.21	Chromium-Cr	17.270
[2]Thickness (in){mm}	0.004 {0.1016}	Copper-Cu	.290
[2]Thickness Tolerance (in){mm}	±0.0002 {5.08E-3}	Manganese-Mn	1.170
[2]Hardness (Rockwell C)	43	Molybdenum-Mo	0.180
		Nickel-Ni	6.700
		Nitrogen-N	0.054
		Phosphorus-P	0.033
		Silicon-Si	0.520
		Sulfur-S	0.001
		Iron	balance

[1]Reference [123]; [2]Reference [94]

Table 51: AF-191U Properties

Mechanical Properties		Thermal Properties	
[1]Modulus of Elasticity (msi) {GPa}	0.415 {2.86}	[1]CTE (µin/in-°F) {µm/m-°C}[124][124][122][122][122][122][122][122]	45.0 {81.0}
[1]Poissons Ratio [124][124][122][122][122][122][122][122]	0.414		
[2]Thickness (in){mm}	0.00250 {0.635}		

[1]Reference [124]; [2]Reference [101]

Table 52: Hi-Lok Alloy Steel Properties (AISI 4340)

Mechanical Properties	
[1]Yield Stress (ksi) {MPa}	103 {710}
[2]Ultimate Tensile Strength(ksi) {MPa}	160 {1100}
[1]Elastic Modulus (msi) {GPa}	29.7 {205}
Elongation at Break	13.2%
[1]Poisson's Ratio	0.29
[1]Density (lbf/in^3) {g/cc}	0.284

[1]Reference [112]; [2]Reference [94]

Appendix I Computational Properties

Model Units
- Pounds
- Inches
- °F

Prepreg-Composite (Using Hashin Failure Criteria)
- E11 = 18,910,000psi
- E22 = 1,260,000psi
- V12 = 0.32
- G12 = 760,000psi
- G13 = 760,000psi
- G23 = 460,000psi
- Density = 0.0643lb/in^3
- Damage Initiation
    - Longitudinal Tensile stress = 421,00psi
    - Longitudinal compressive stress = 304,740psi
    - Transverse Tensile Stress = 13,900psi
    - Transverse Compressive Stress = 34,400psi
    - Longitudinal Shear Stress = 16,500psi
    - Transverse Shear Stress = 16,500 psi
- Damage Evolution
    - Fiber Tension = 465 psi-in
    - Fiber Compression = 600 psi-in
    - Matrix Tension = 102 psi-in
    - Matrix Compression = 204 psi-in

Matrix – Defined using Cohesive Interaction Properties
- Normal Behavior: "Hard" Contact (Abaqus defaults to a penalty enforcement)
- Penalty Stiffness
    - Knn = 145,038,000psi
    - Kss = 145,038,000psi
    - Ktt = 145,038,000psi
- Nominal Stress (defines damage initiation)
    - Note: Defined using 90% of matrix (2 direction) properties
    - tn = 12,510 psi
    - ts = 14,850 psi
    - tt = 14,850 psi
- Fracture Energy (Defines Damage Progression) Linear, Energy, B-K
    - Normal = 102psi-in
    - 1st Shear = 354psi-in
    - 2nd Shear =354psi-in
- BK exponent = 1.45

Adhesive (Using 3M AF-191U adhesive)

- Thickness defined using continuum, 3D stress elements
    - Thickness=0.0025in
    - Density=0.041lb/in^3
    - E=415000psi
    - Poisson's Ratio=0.414

- Surface interaction defined using Cohesive Interaction Properties
    - Normal Behavior: "Hard" Contact (Abaqus defaults to a penalty enforcement)
    - Penalty Stiffness
        - Knn = 1.45038E+008psi
        - Kss = 1.45038E+008psi
        - Ktt = 1.45038E+008psi
    - Nominal Stress (defines damage initiation)
        - From 3M AF-191 properties
        - tn = 1050psi
        - ts = 5000psi
        - tt = 5000psi
    - Displacement at Failure (defines damage evolution): 0.0025in (equal to material thickness). Linear displacement evolution

Contact Definitions

- Steel-Carbon Interaction
    - Hard Contact
    - Fric=0.12

- Steel-Steel Interaction
    - Hard Contact
    - Fric=0.5

SS 301

- Isotropic Thermal Expansion 9.78e-6in/in-°F
- Elastic Modulus: 13328000psi
- Poissons Ratio: 0.29
- Density: 0.289lb/in^3
- Ductile Damage: Fracture Strain 0.1875
- Damage Evolution: Linear Displacement at failure 0.008in

- Plasticity

Eng Stress (psi)	Eng Strain	True Stress (Yield Stress) (psi)	True Strain	True Plastic Strain
0	0	0.000	0.00000	0.0000
133400	0.0100093	134735	0.00996	-0.0001
156109	0.0126491	158083	0.01257	0.0007
171922	0.015288	174550	0.01517	0.0021
180497	0.0179284	183733	0.01777	0.0040
185191	0.0205645	188999	0.020355901	0.0062
189742	0.0258438	194646	0.025515514	0.0109
192923	0.0363909	199944	0.035744372	0.0207
194365	0.0469386	203488	0.045870271	0.0306
195372	0.0574912	206604	0.055899296	0.0404
206842	0.2100	250279	0.19062036	0.1718

Hi-Lok Alloy

- Plastic Potential: all values set to 1. (to work with orthotropic expansion)
- Specific heat 0.114
- Thermal expansion: Orthotropic
  - 11 Direction: 0
  - 22 Direction: 0
  - 33 Direction: 7.06e-6in/in-°F
- Elastic Modulus: 30.7e6psi
- Poisson's Ratio: 0.29
- Density: 0.284 lb/in^3
- Plasticity

Eng Stress (psi)	Eng Strain	True Stress (psi)	True Strain	True Plastic Strain
103,000	0.003468	103,4 00	0.003462	0.0000
160,000	0.1320	181,1 00	0.1240	0.1179

17-4PH Stainless Steel (Fixtures)

- Elastic Modulus: 28.5e6psi
- Poisson's Ratio: 0.272
- Density: 0.284 lb/in^3
- Plasticity

True Stress (psi)	True Plastic Strain
110000	0.0000
168000	.1073

Appendix J Shank-Only v. Full Hybrid Tables

Table 53: 18-Ply Single Shear Countersunk Load-Displacement Data: Shank-Only v. Hybrid

	Shank-Only Hybrid			Hybrid					
	Average	Stdev	N	Average	Stdev	N	Diff	% Diff	Stat Sig
Yield Load (kips)	3.662 (3.523-3.801)	0.1325	6	3.862 (3.740-3.985)	0.1533	6	0.2001	5.46	Yes
Offset Load (kips)	4.113 (4.045-4.181)	0.05481	5	4.459 (4.383-4.535)	0.08678	5	0.3458	8.41	Yes
Ultimate Load (kips)	4.234 (4.162-4.306)	0.05778	5	4.667 (4.542-4.791)	0.1099	3	0.4325	10.2	Yes
Strain Energy (in-lb)	215.7 (205.6-225.7)	4.041	3	239.0 (230.0-248.0)	7.937	3	23.33	10.8	Yes

Table 54: 18-Ply Single Shear Countersunk Stress-Strain Data: Shank-Only Hybrid v. Hybrid

	Shank-Only Hybrid			Hybrid					
	Average	Stdev	N	Average	Stdev	N	Diff	% Diff	Stat Sig
Yield Stress (ksi)	108.2 (104.5-111.9)	3.526	6	104.6 (101.3-108.0)	4.168	6	-3.545	-3.277	No
Yield Strain	0.08050 (0.07666-0.08434)	0.003658	6	0.07686 (0.07365-0.08008)	0.0040	6	-0.003635	-4.516	No
Offset Stress (ksi)	121.6 (120.0-123.2)	1.275	5	120.5 (118.2-122.7)	2.574	5	-1.088	-0.8951	No
Offset Strain	0.09798 (0.09377-0.1022)	0.003390	5	0.09631 (0.09338-0.09925)	0.0033	5	-0.001668	-1.702	No
Ultimate Stress (ksi)	125.2 (122.7-127.7)	2.002	5	126.2 (122.7-129.8)	3.156	3	1.082	0.8641	No
Modulus (ksi)	1379 (1339-1419)	37.98	6	1399 (1377-1420)	27.00	6	19.88	1.442	No
Strain Energy Density (in-lb/in^3)	20447 (19294-21599)	463.9	3	20767 (19911-21623)	756.8	3	320.3	1.567	No

Appendix K NDI Ultrasonic Scans

Panels Not Used Due to Erroneous Cure Cycle (Not machined into specimens)

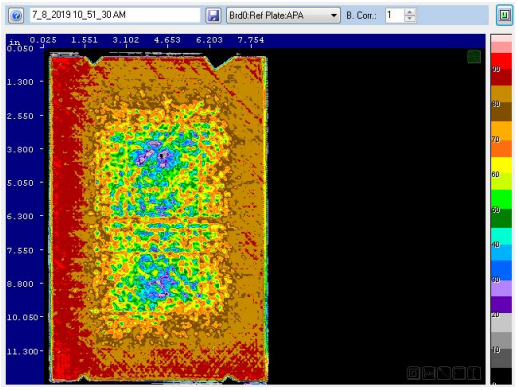

Figure 169: Panel C-01 5dB

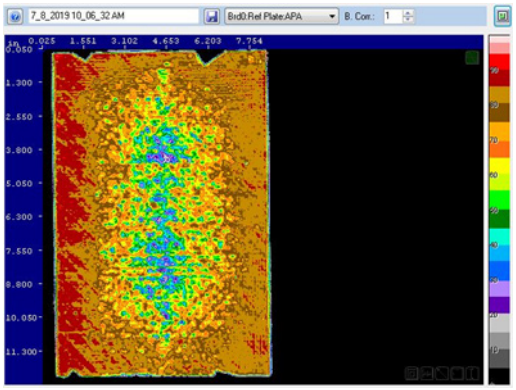

Figure 170:Panel C-02 5dB

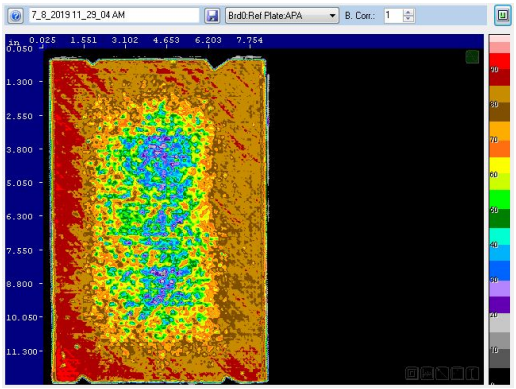

Figure 171: Panel C-03 5dB

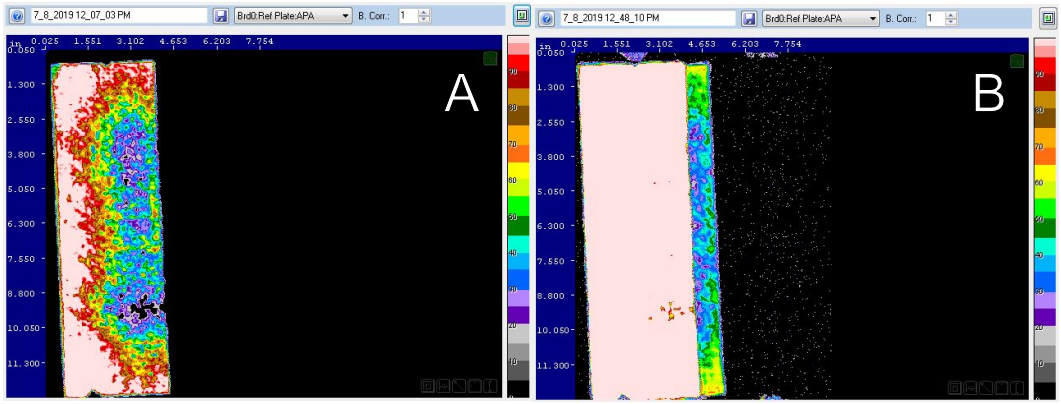

Figure 172: Panel H-01 A) Control Region 15 dB B) Transition Region 35 dB

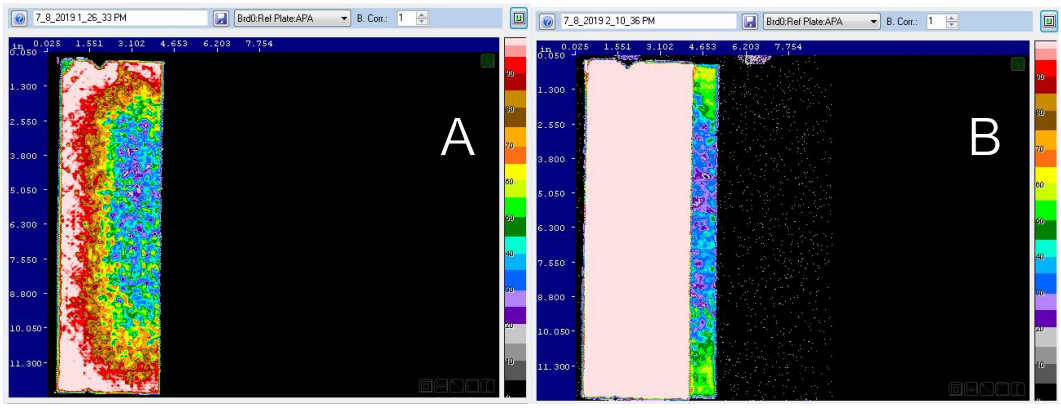

Figure 173: Panel H-02 A) Control Region 15 dB B) Transition Region 35 dB

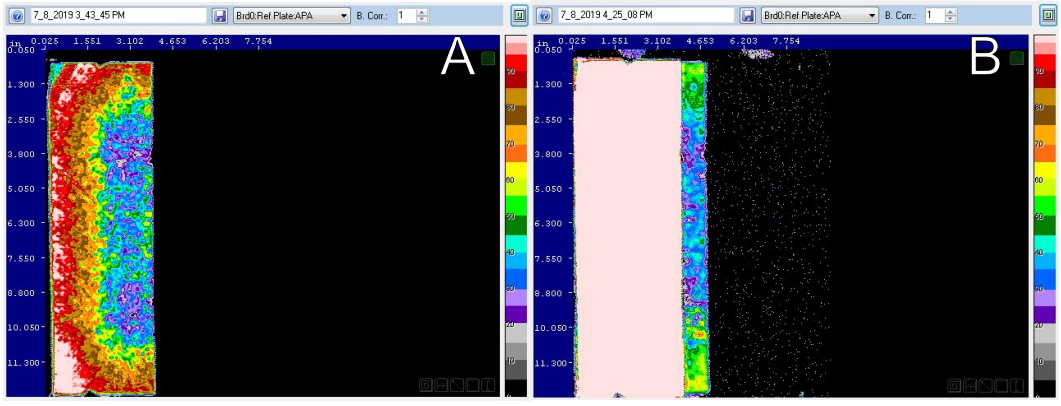

Figure 174: Panel H-03 A) Control Region 15 dB B) Transition Region 35 dB

Not Used Due to Contaminating Polymer Backer

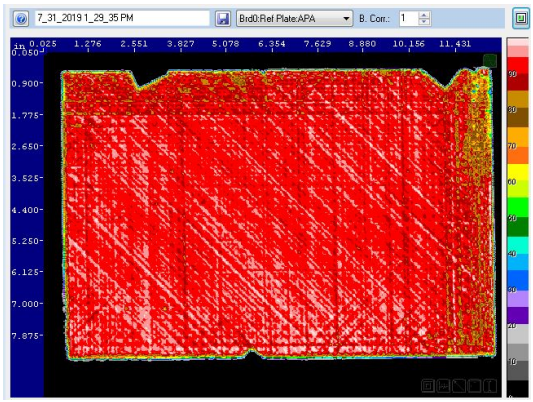

Figure 175: Panel C-11 5dB

Control Panels

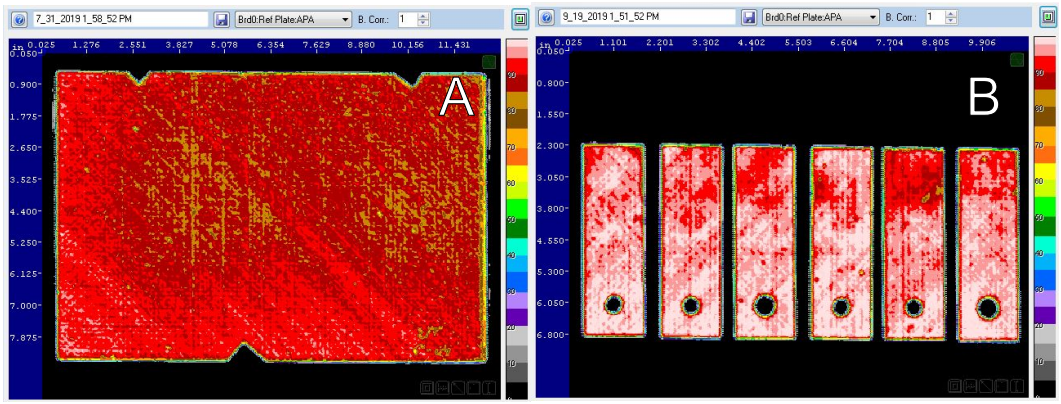

Figure 176: Panel C-04 A) Panel 6 dB B) Coupons 7 dB

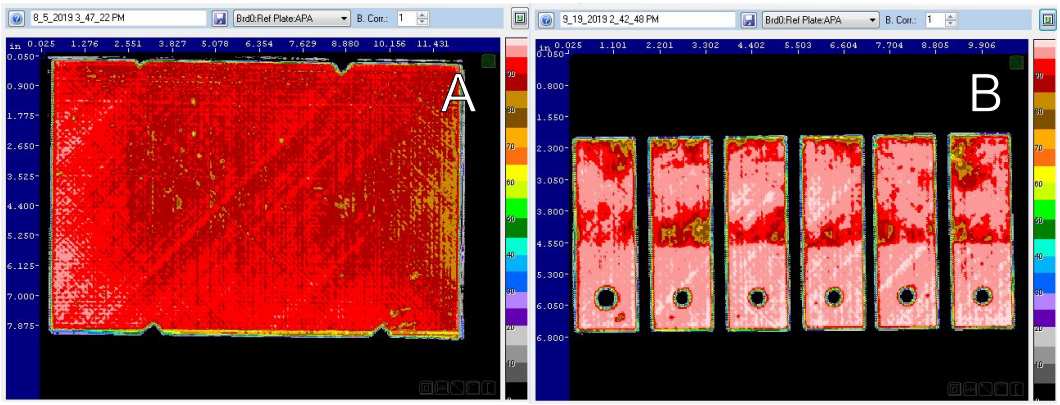

Figure 177: Panel C-05 A) Panel 8 dB B) Coupons 8 dB

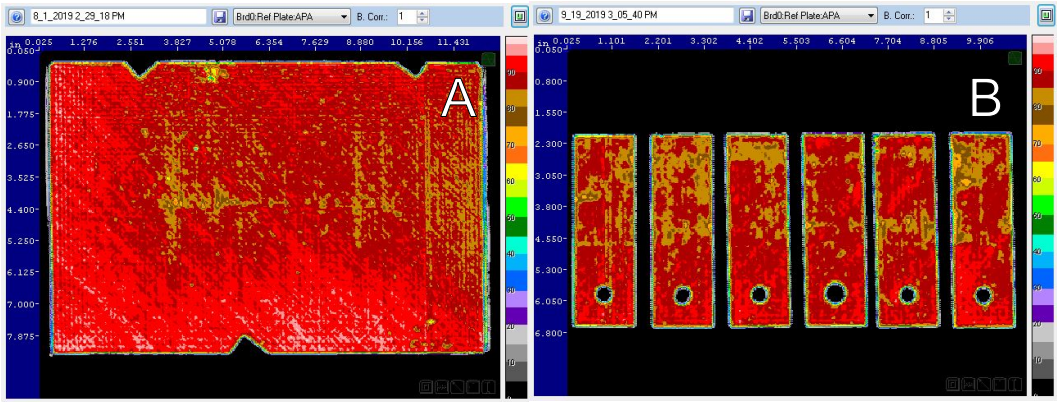

Figure 178: Panel C-06 A) Panel 6 dB B) Coupons 6 dB

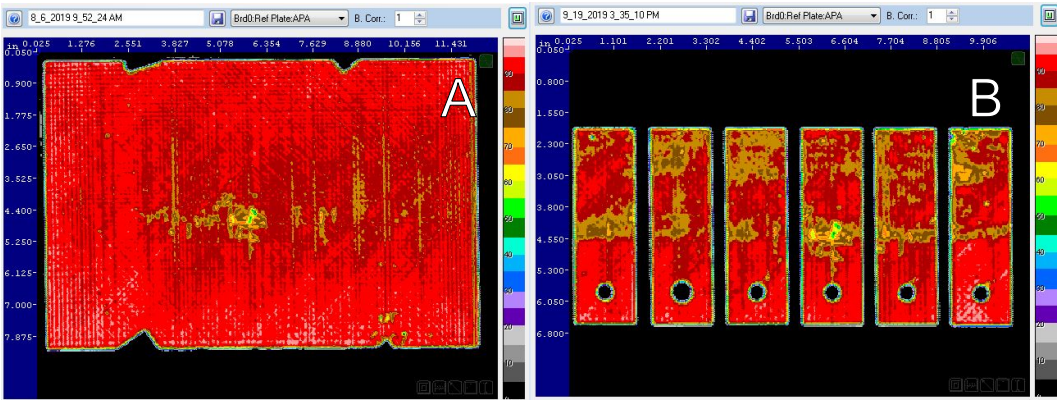

Figure 179: Panel C-07 A) Panel 7 dB B) Coupons 7 dB

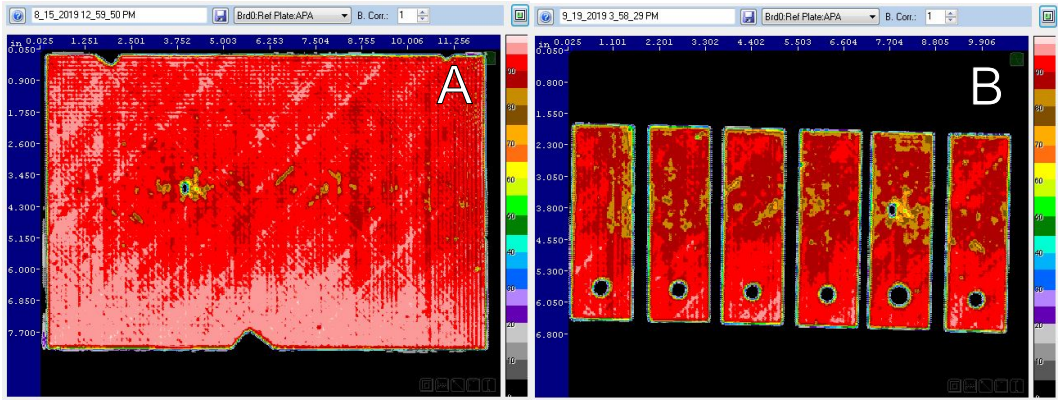

Figure 180: Panel C-08 A) Panel 7 dB B) Coupons 7dB

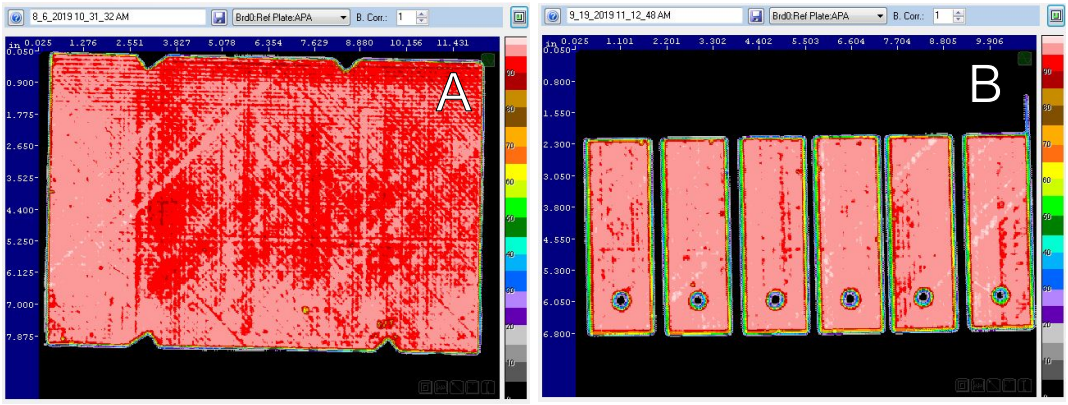

Figure 181: Panel C-12 A) Panel 7 dB B) Coupons 7dB

Hybrid Panels

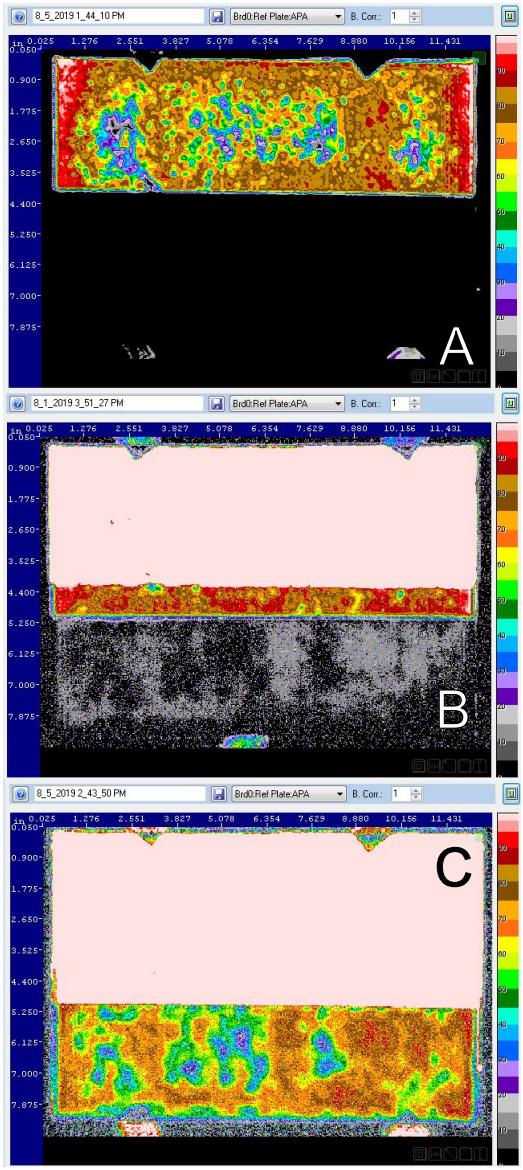

Figure 182: Panel H-04
A) Control Region 17 dB
B) Transition Region 40 dB
C) Bearing Region 50 dB

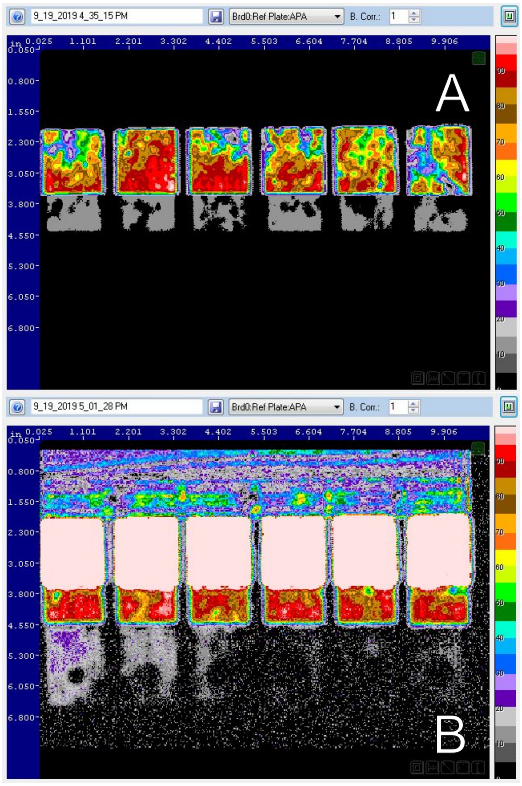

Figure 183: Panel H-04
A) Control Region 18 dB
B) Transition Region 40 dB

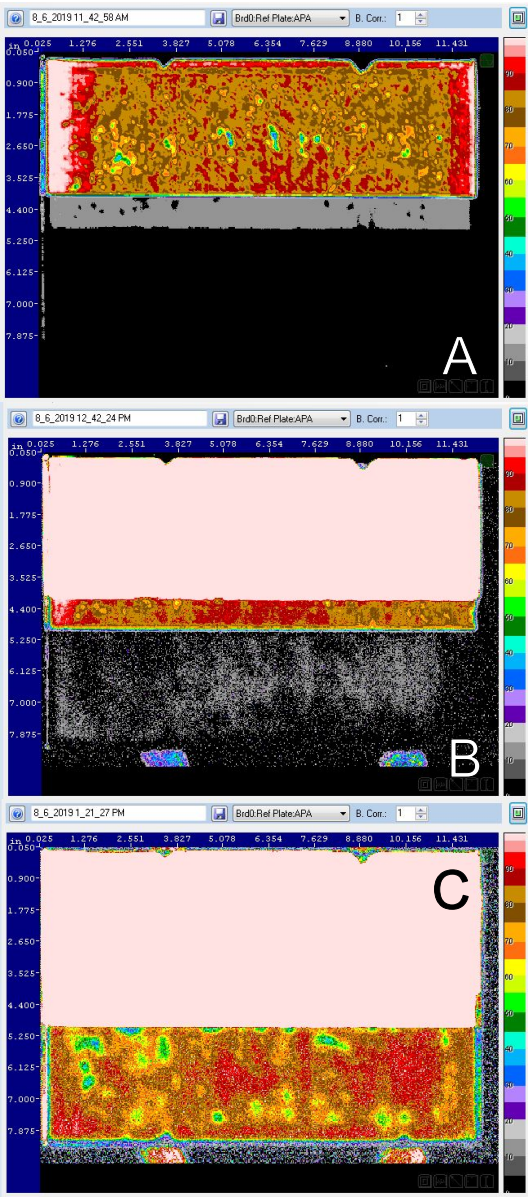

Figure 184: Panel H-05
A) Control Region 18 dB
|B) Transition Region 40 dB
C) Bearing Region 50 dB

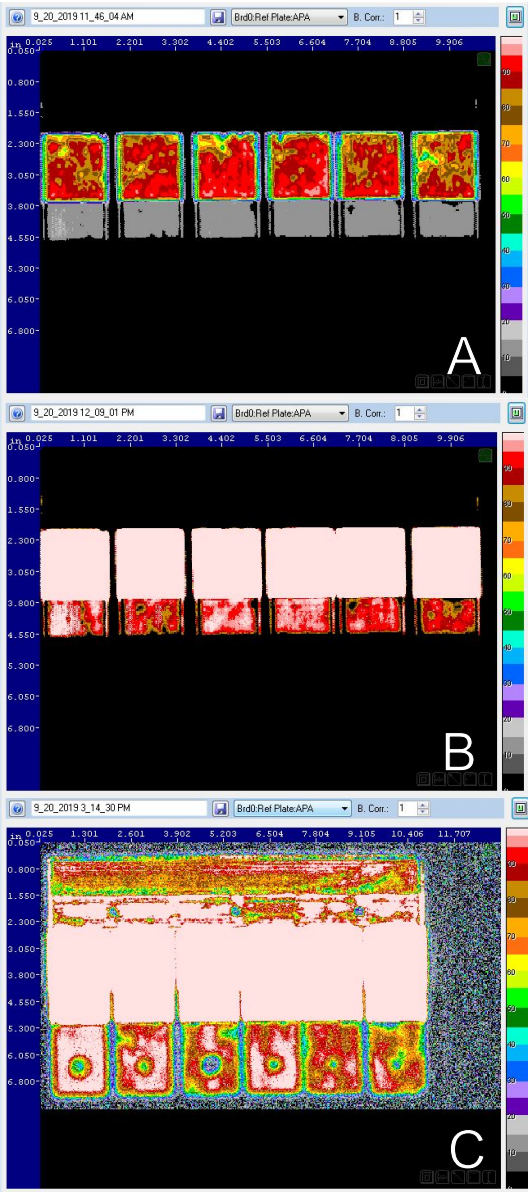

Figure 185: Panel H-05
A) Control Region 19 dB
B) Transition Region 37 dB
C) Bearing Region 50 dB

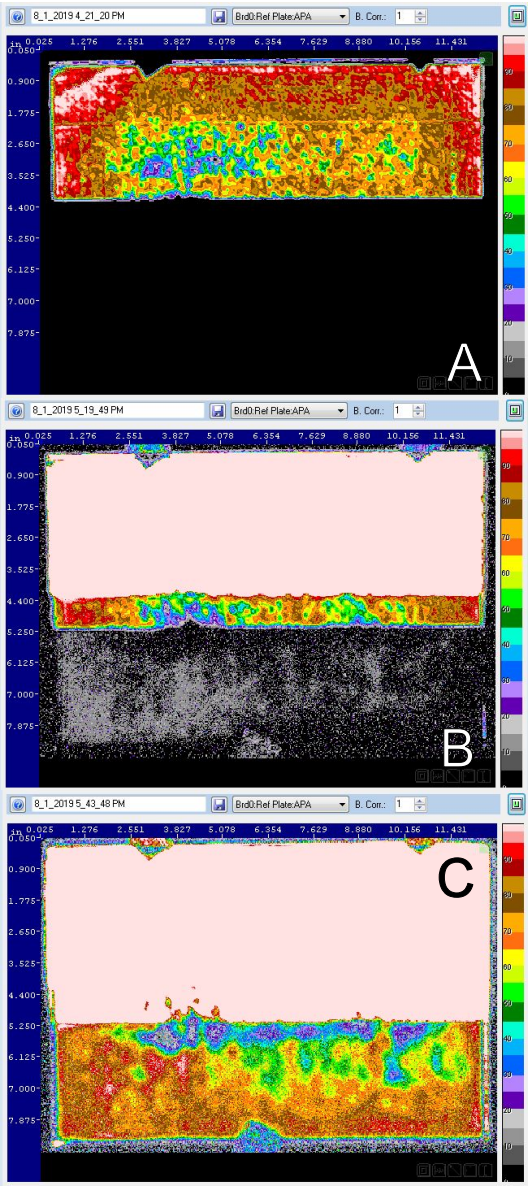

Figure 186: Panel H-06
A) Control Region 15 dB
B) Transition Region 40 dB
C) Bearing Region 50 dB

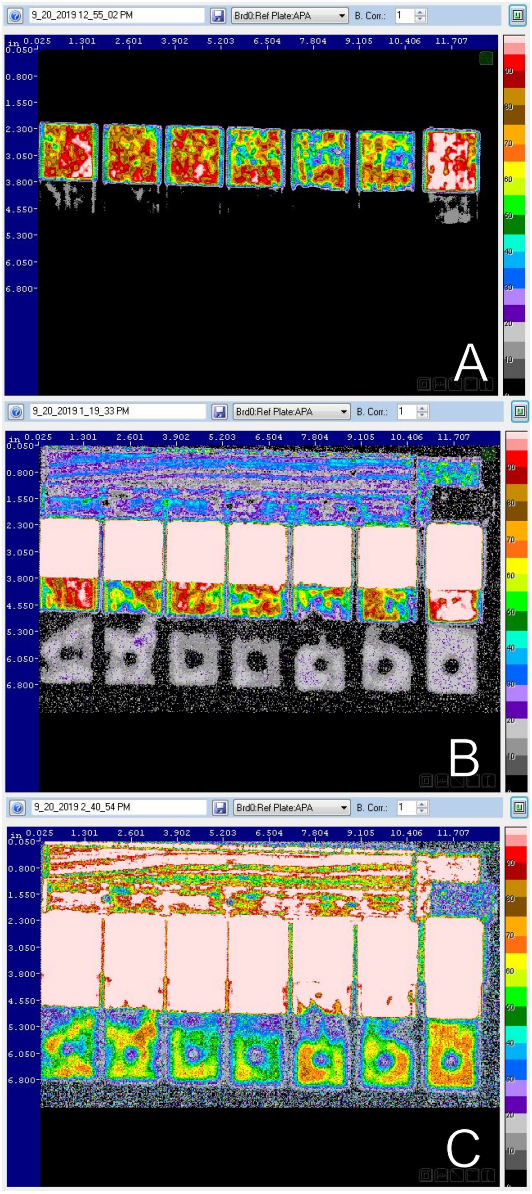

Figure 187: Panel H-06 Coupons
A) Control Region 17 dB
B) Transition Region 38 dB
C) Bearing Region 50 dB

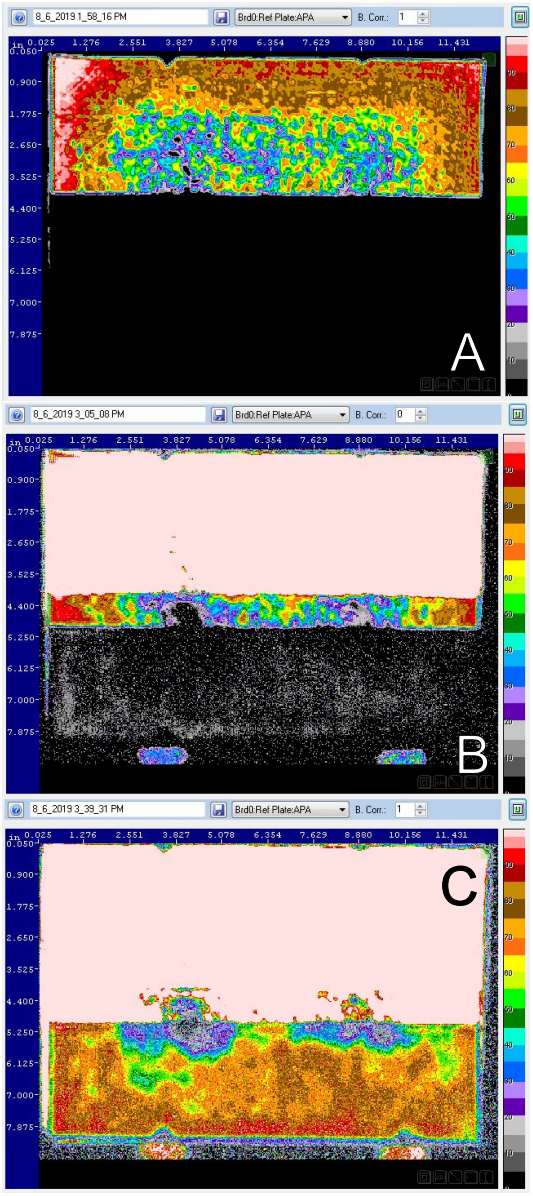

Figure 188: Panel H-07
A) Control Region 15 dB
B) Transition Region 40 dB
C) Bearing Region 50 dB

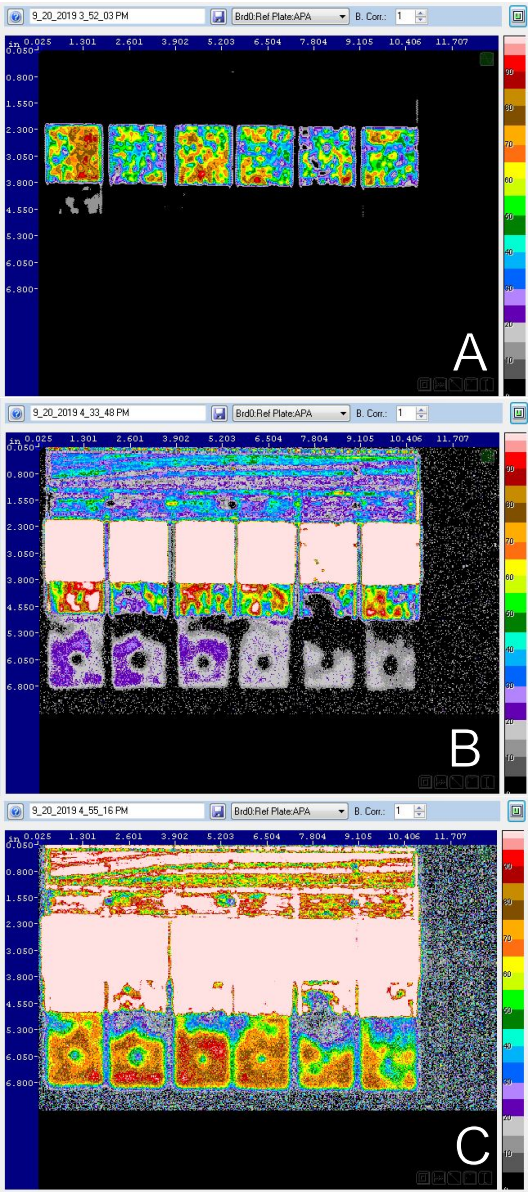

Figure 189: Panel H-07 Coupons
A) Control Region 17 dB
B) Transition Region 40 dB
C) Bearing Region 50 dB

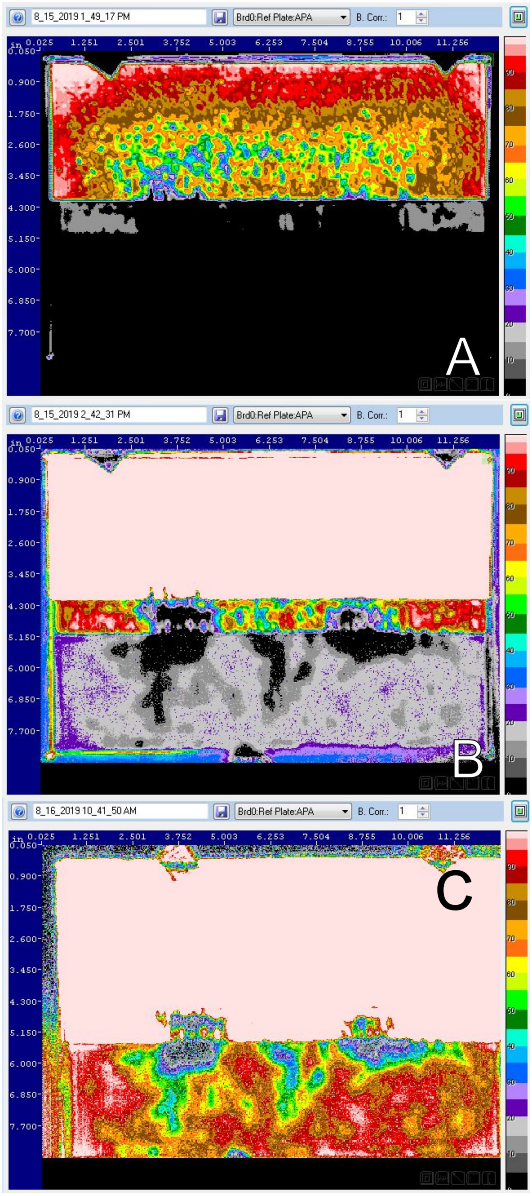

Figure 190: Panel H-08
A) Control Region 16 dB
B) Transition Region 35 dB
C) Bearing Region 49 dB

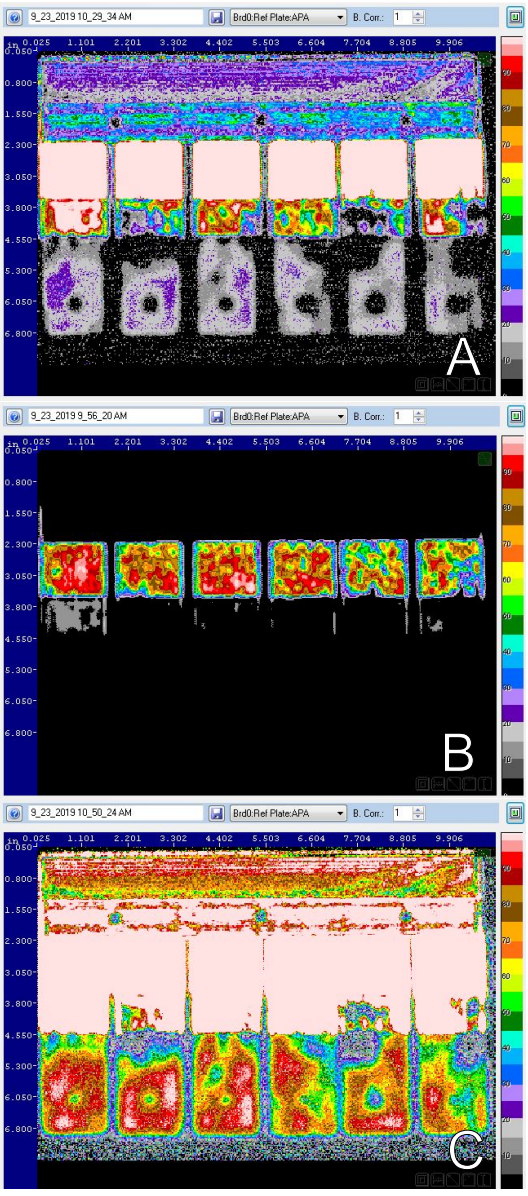

Figure 191: Panel H-08 Coupons
A) Control Region 18 dB
B) Transition Region 39 dB
C) Bearing Region 50 dB

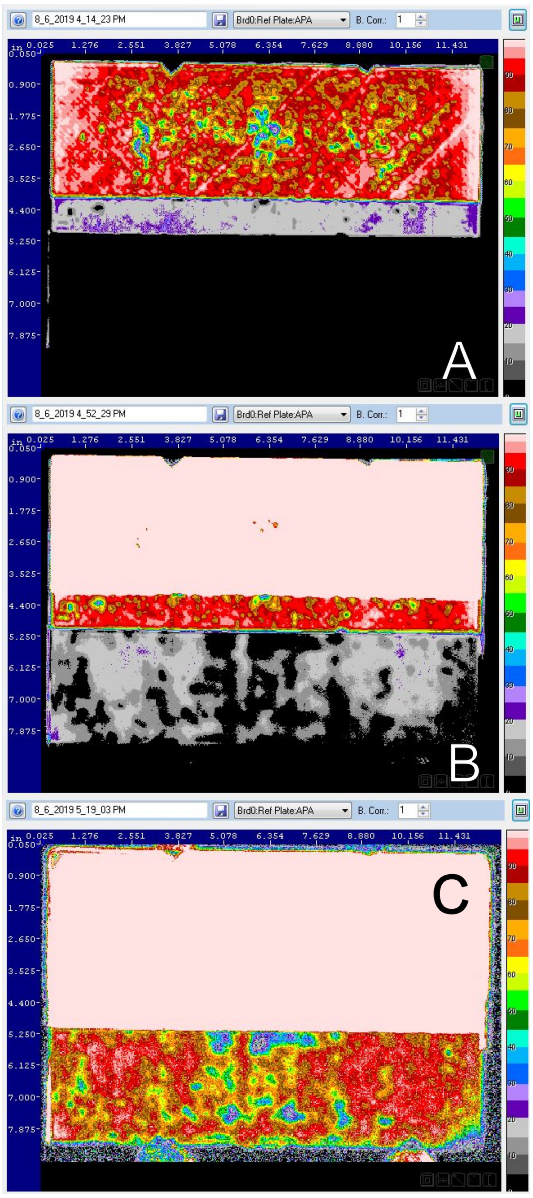

Figure 192: Panel H-11
A) Control Region 13 dB
B) Transition Region 27 dB
C) Bearing Region 50 dB

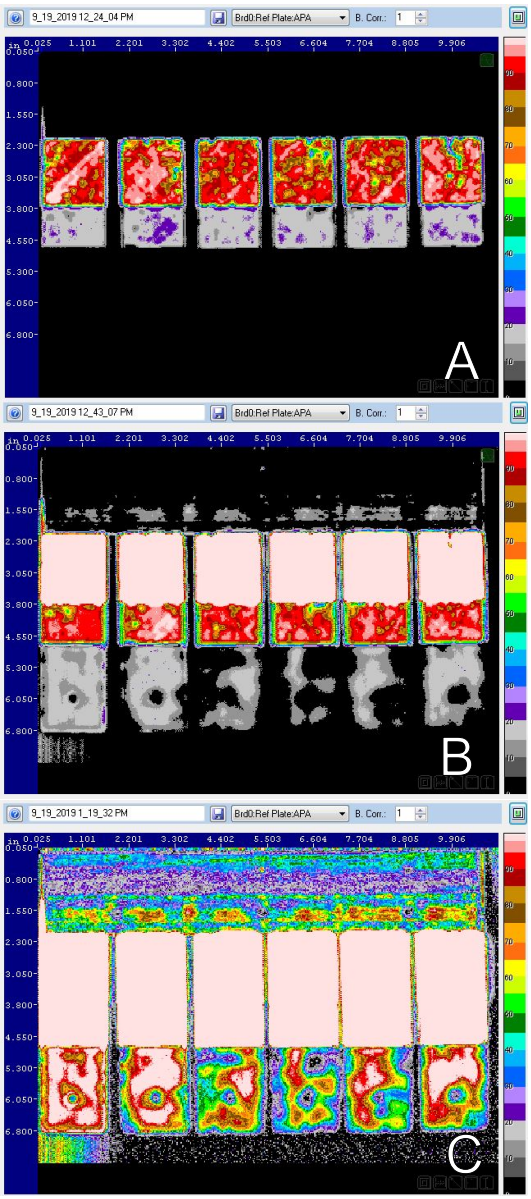

Figure 193: Panel H-11 Coupons
A) Control Region 13 dB
B) Transition Region 27 dB
C) Bearing Region 43 dB

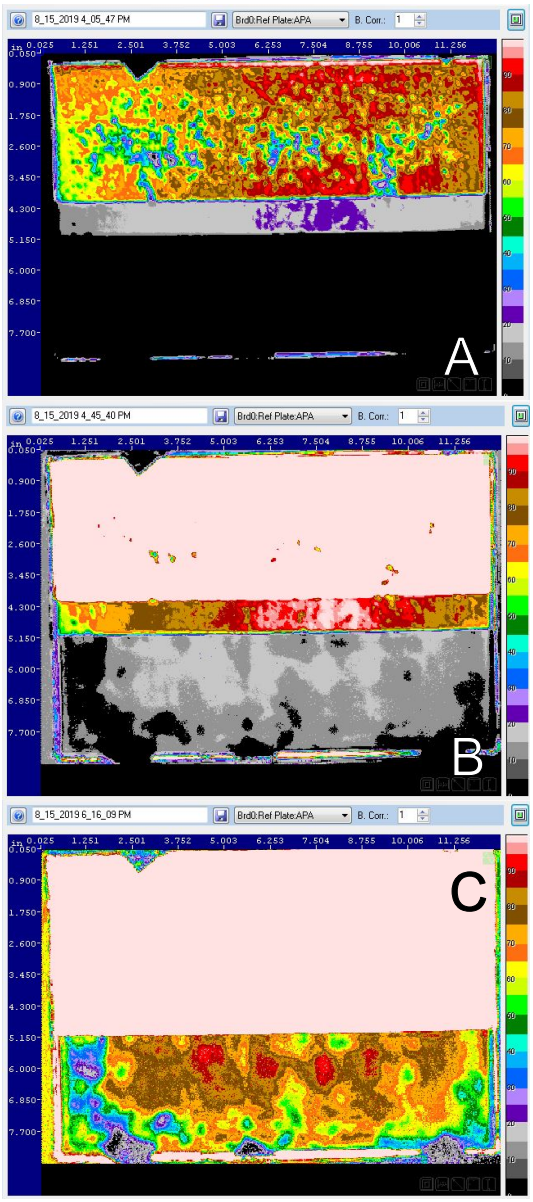

Figure 194: Panel S-01
A) Control Region 13 dB
B) Transition Region 27 dB
C) Bearing Region 42 dB

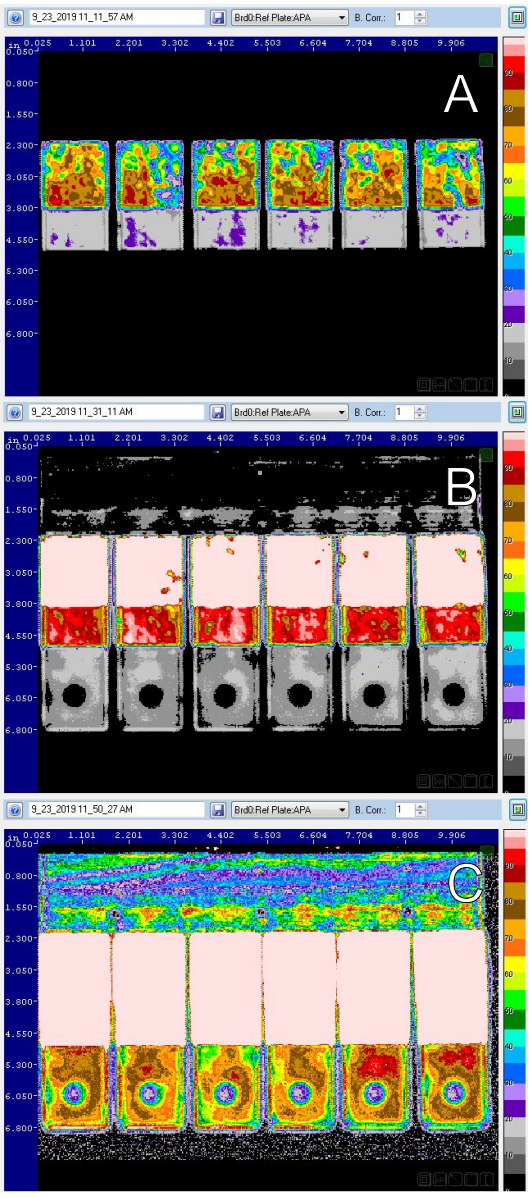

Figure 195: Panel S-01 Coupons
A) Control Region 13 dB
B) Transition Region 27 dB
C) Bearing Region 42 dB

Appendix L Dimensioned Drawings

Dimensioned drawings are included on the following pages.

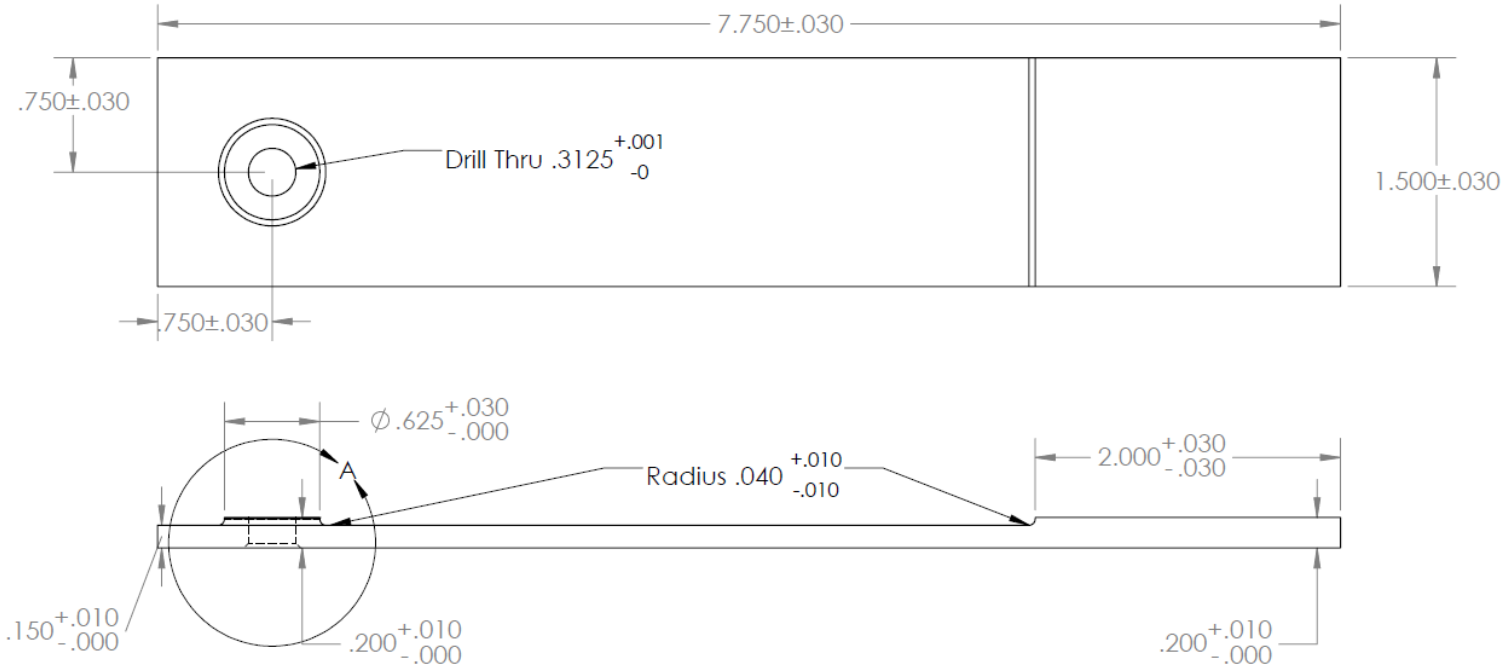

DETAIL A
SCALE 2 : 1

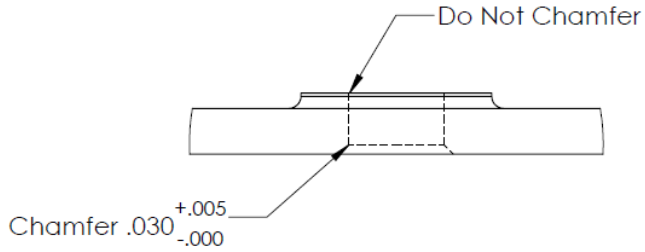

Note:
- 3D CAD model will be provided
- Chamfer accepts .030 radius under hi-lok head

	Approval	Date
Drawn	J. Brewer	26 Jun 19
Checked	B. Smyers	26 Jun 19
Engineer	J. Feie	26 Jun 19
Released	M. Durham	26 Jun 19

Drawing Package: STRATUS Fixtures

Part Name: Fixture, Double Shear, Front

Material: 17-4PH Stainless Steel

Quantity Required: 2

Prepared By: Maj John Brewer
John.Brewer@afit.edu
850-272-7931

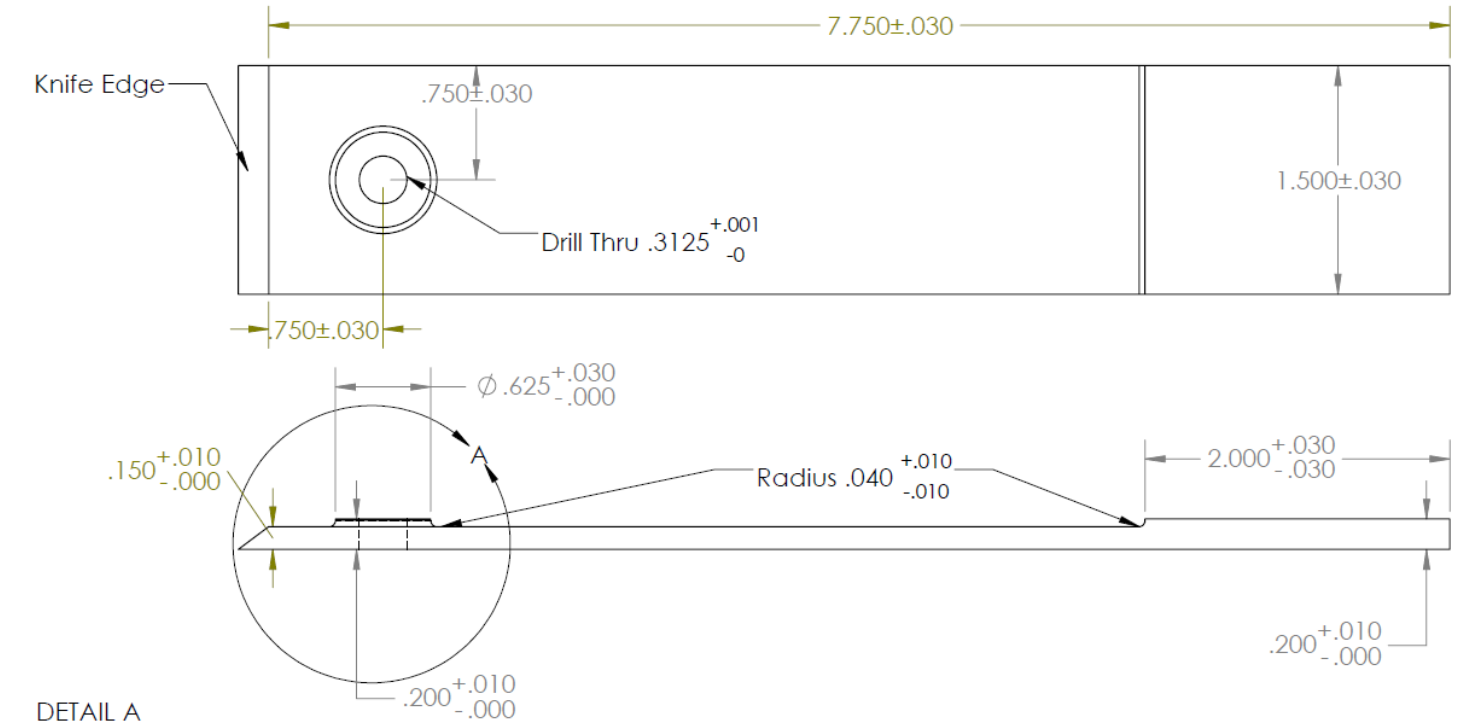

DETAIL A
SCALE 2 : 1

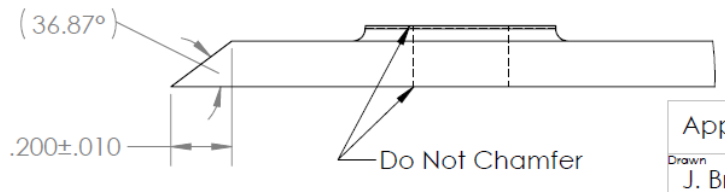

Note: 3D CAD model will be provided

Approval	Date
Drawn J. Brewer	26 Jun 19
Checked B. Smyers	26 Jun 19
Engineer J. Feie	26 Jun 19
Released M. Durham	26 Jun 19

Drawing Package: STRATUS Fixtures
Part Name: Fixture, Double Shear, Rear
Material: 17-4PH Stainless Steel
Quantity Required: 2
Prepared By: Maj John Brewer John.Brewer@afit.edu 850-272-7931

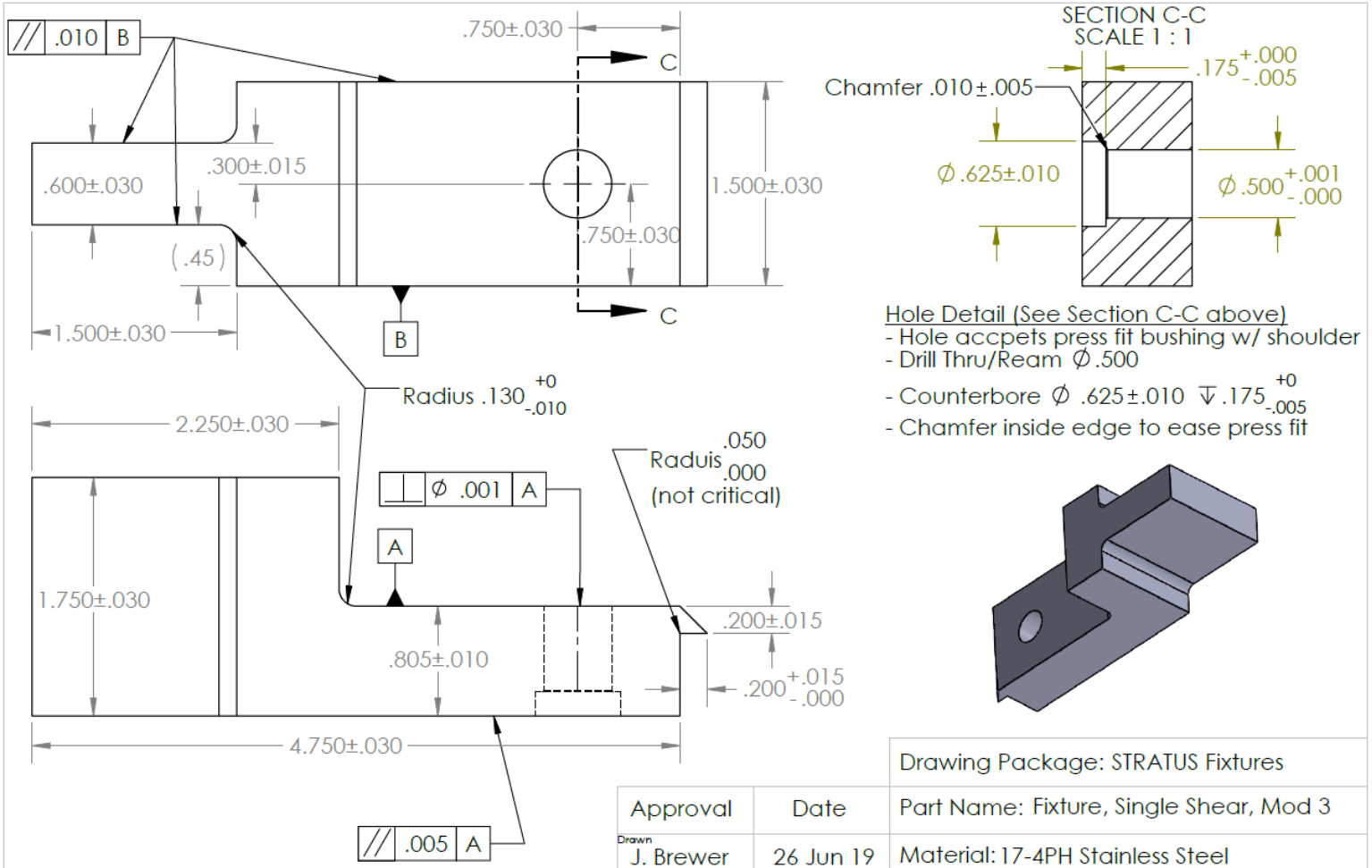

Hole Detail (See Section C-C above)
- Hole accpets press fit bushing w/ shoulder
- Drill Thru/Ream Ø.500
- Counterbore Ø .625±.010 ↧.175 +0 -.005
- Chamfer inside edge to ease press fit

Note: 3D solid model will be supplied

Approval	Date
Drawn J. Brewer	26 Jun 19
Checked B. Smyers	26 Jun 19
Engineer J. Feie	26 Jun 19
Released M. Durham	26 Jun 19

Drawing Package: STRATUS Fixtures

Part Name: Fixture, Single Shear, Mod 3

Material: 17-4PH Stainless Steel

Quantity Required: 2

Prepared By: Maj John Brewer
John.Brewer@afit.edu
850-272-7931

Bushing Modifications

- Begin with Mcmaster pn 8492A159
- Bushing OD and ID are correct from factory
- Dimension length as defined below
- See Single-Shear Fixture Assembly

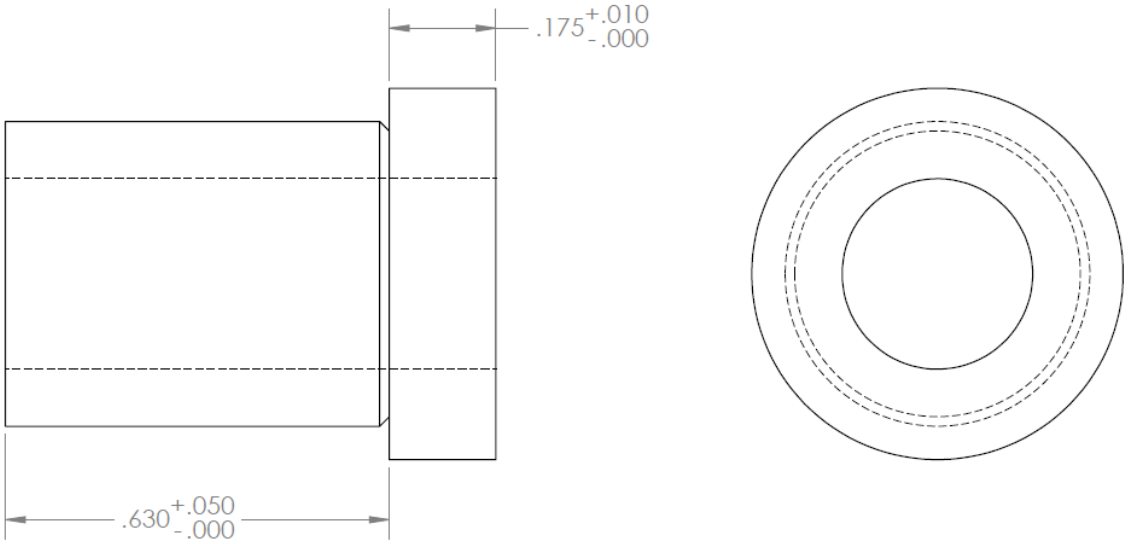

		Drawing Package: STRATUS Fixtures
Approval	Date	Part Name: Bushing, Sing-Shear Fixture
Drawn J. Brewer	26 Jun 19	Material: Steel (as supplied)
Checked B. Smyers	26 Jun 19	Quantity Required: 4
Engineer J. Feie	26 Jun 19	Prepared By: Maj John Brewer John.Brewer@afit.edu 850-272-7931
Released M. Durham	26 Jun 19	

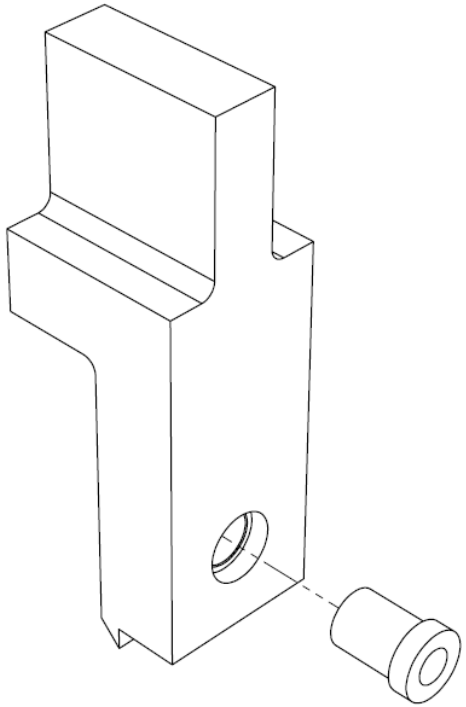

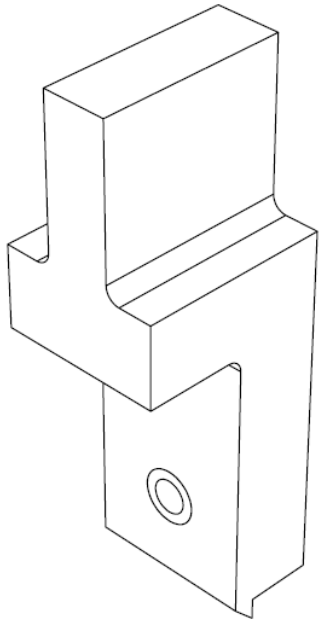

Assembly Procedure

- Machine bushing per "Bushing, Single-Shear Fixture"
- Press modified bushing into fixture
- Grind busing flush with both sides of fixture

		Drawing Package: STRATUS Fixtures
Approval	Date	Part Name: Sing-Shear Fixture Asm
Drawn J. Brewer	26 Jun 19	Material: Stainless Steel/ Steel
Checked B. Smyers	26 Jun 19	Quantity Required: Assemble 2
Engineer J. Feie	26 Jun 19	Prepared By: Maj John Brewer John.Brewer@afit.edu 850-272-7931
Released M. Durham	26 Jun 19	

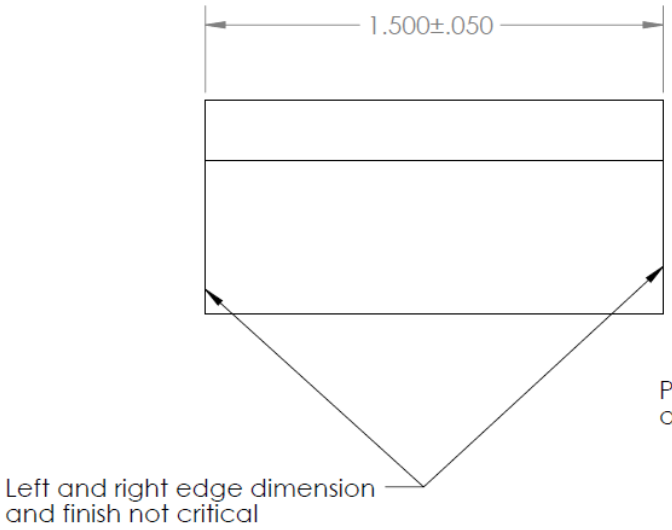

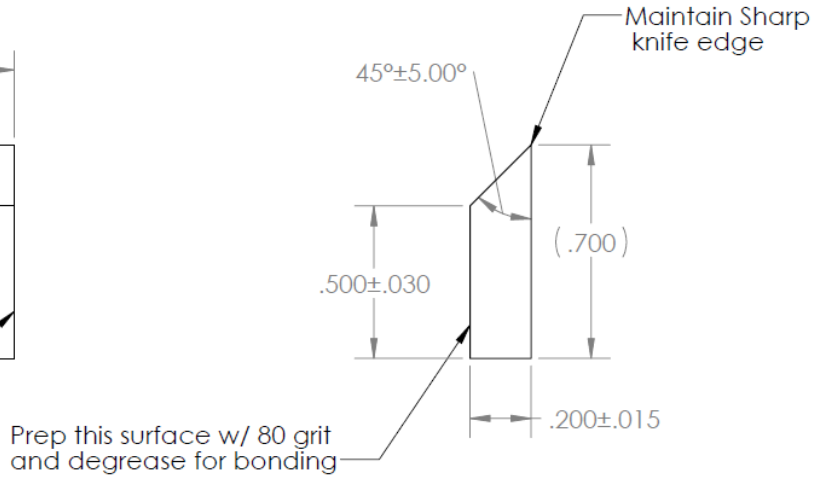

		Drawing Package: STRATUS Fixtures
Approval	Date	Part Name: Clip Gauge Tab
Drawn J. Brewer	26 Jun 19	Material: Al 6061 (or similar)
Checked B. Smyers	26 Jun 19	Quantity Required: 78
Engineer J. Feie	26 Jun 19	Prepared By: Maj John Brewer John.Brewer@afit.edu 850-272-7931
Released M. Durham	26 Jun 19	

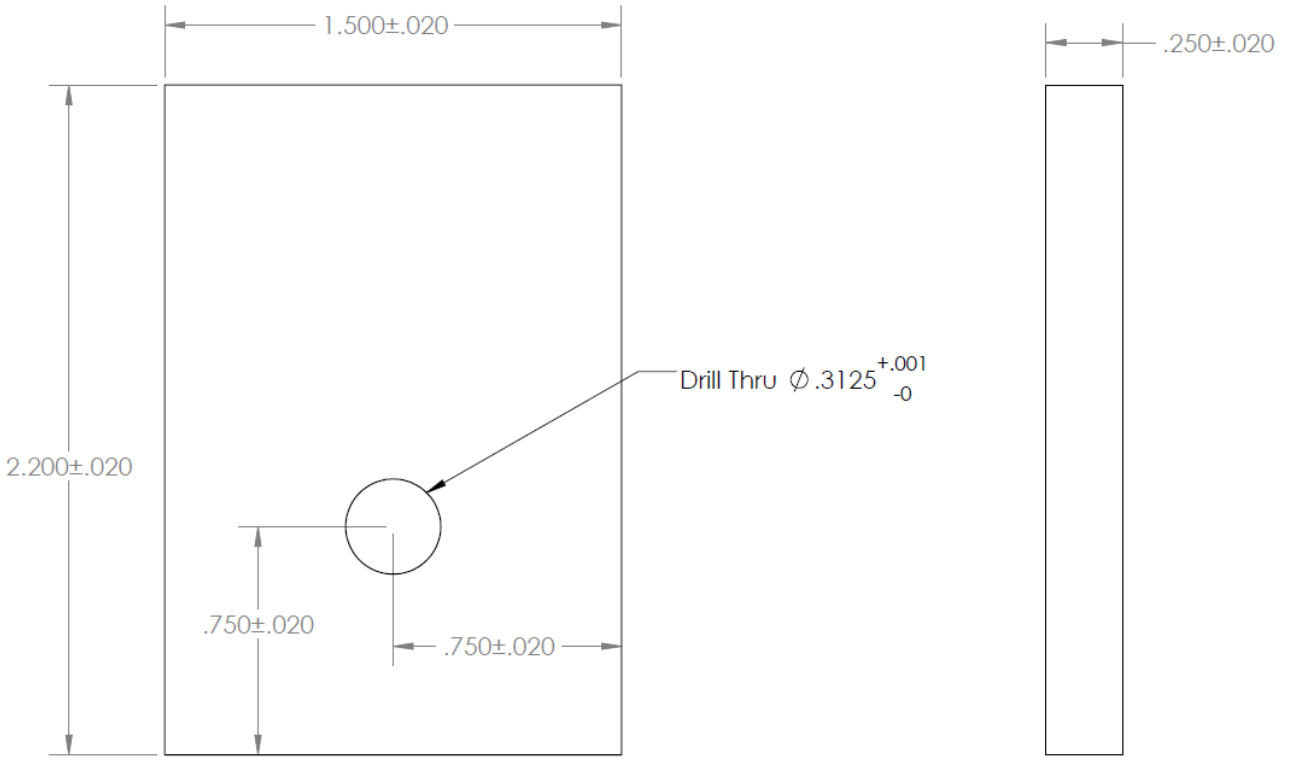

		Drawing Package: STRATUS Fixtures
Approval	Date	Part Name: Jig, Clip Tab Alignment
Drawn J. Brewer	26 Jun 19	Material: Any Aluminum Alloy
Checked B. Smyers	26 Jun 19	Quantity Required: 2
Engineer J. Feie	26 Jun 19	Prepared By: Maj John Brewer John.Brewer@afit.edu 850-272-7931
Released M. Durham	26 Jun 19	

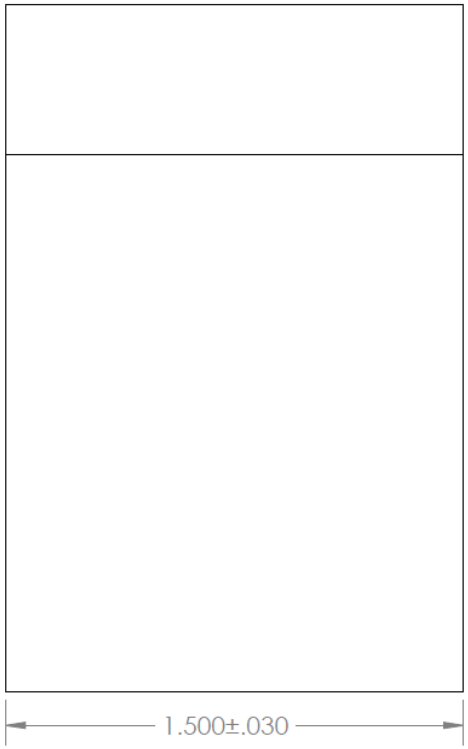

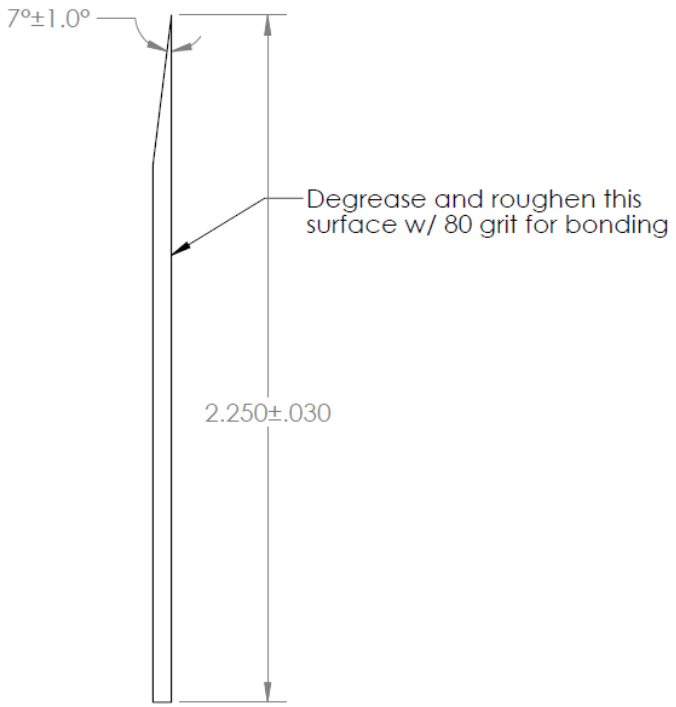

Note:
- Thickness is material thickness as provided (~ .062)
- 324 required

		Drawing Package: STRATUS Fixtures
Approval	Date	Part Name: Grip Tab
Drawn J. Brewer	15 Jul 19	Material: G10 Fiberglass
Checked B. Smyers	15 Jul 19	Quantity Required: 324
Engineer J. Feie	15 Jul 19	Prepared By: Maj John Brewer John.Brewer@afit.edu 850-272-7931
Released M. Durham	17 Jul 19	

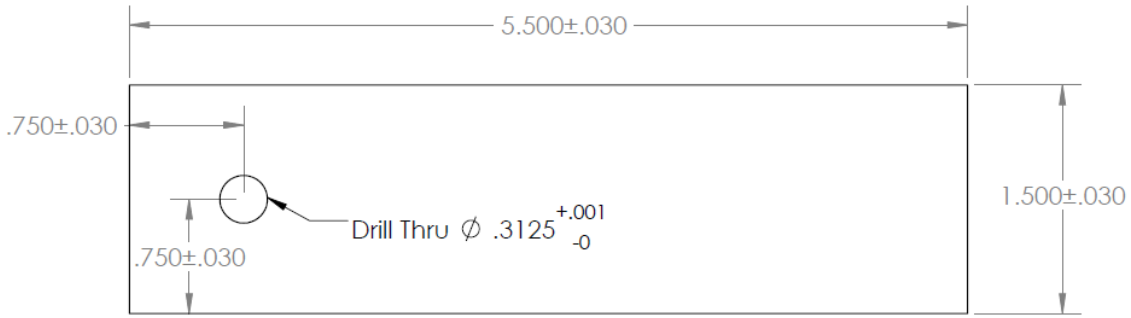

Notes:
- 3D CAD models will be provided
- Thickness governed by composite layup
- This procedure applies to coupons from the following panels: C-01, C-04, H-01,H-04
- 24 total coupons

		Drawing Package: STRATUS Coupons
Approval	Date	Part Name: Coupon, Double-Shear
Drawn J. Brewer	26 Jun 19	Material: Composite/Hybrid Composite
Checked B. Smyers	26 Jun 19	Quantity Required: 24 Coupons
Engineer J. Feie	26 Jun 19	Prepared By: Maj John Brewer John.Brewer@afit.edu 850-272-7931
Released M. Durham	26 Jun 19	

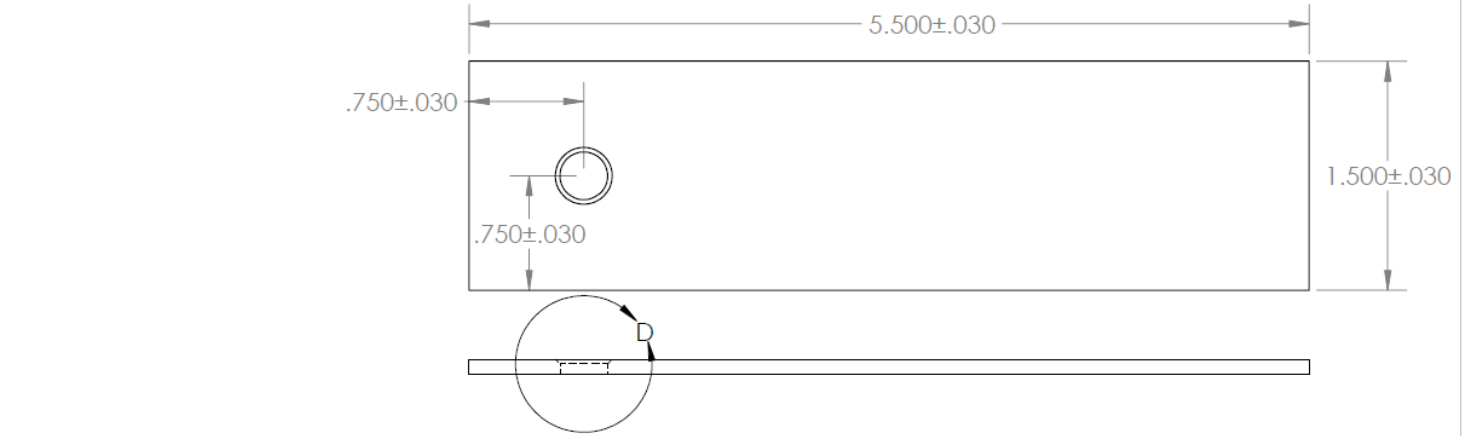

DETAIL D
SCALE 5 : 1

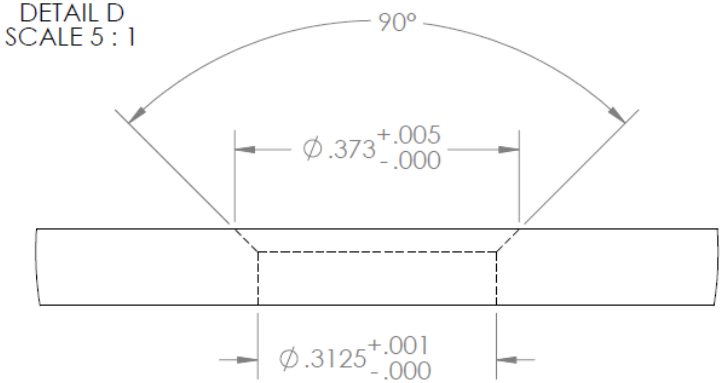

Notes:
- 3D CAD model will be provided
- Thickness governed by composite layup
- Countersink accepts .030 radius under head of hi-lok fastener
- Keep Ply 1 down when countersinking
- This procedure applies to coupons from the following panels: C-02, C-05, H-02, h-05
- 24 Total coupons

Approval	Date	Drawing Package: STRATUS Coupons
Drawn J. Brewer	26 Jun 19	Part Name: Coupon, Single-Shr, Protruding
Checked B. Smyers	26 Jun 19	Material: Composite/Hybrid Composite
Engineer J. Feie	26 Jun 19	Quantity Required: 24 Coupons
Released M. Durham	26 Jun 19	Prepared By: Maj John Brewer John.Brewer@afit.edu 850-272-7931

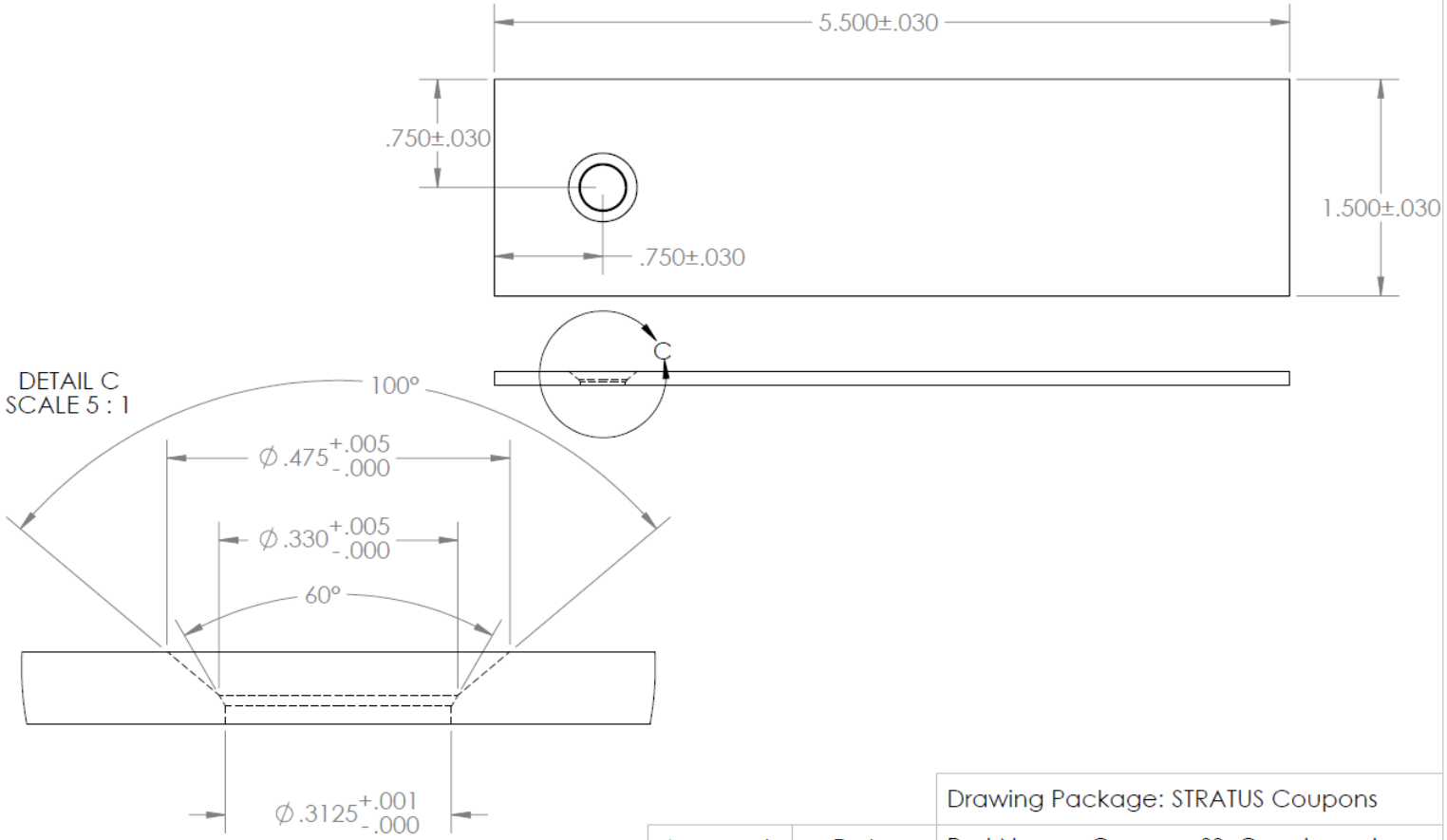

Notes:

- 3D CAD models will be provided
- Thickness governed by composite layup
- 100° csk acceps hi-lok fastener
- 60° chamfer accepts raduis under hi-lok head
- Keep ply 1 down when countersinking
- This procedure applies to coupons from the following panels: C-03, H-03, S-01
- Applies to 18 total coupons

Approval	Date
Drawn J. Brewer	26 Jun 19
Checked B. Smyers	26 Jun 19
Engineer J. Feie	26 Jun 19
Released M. Durham	26 Jun 19

Drawing Package: STRATUS Coupons

Part Name: Coupon, SS, Countersunk

Material: Composite/Hybrid

Quantity Required: 18 Coupons

Prepared By: Maj John Brewer
John.Brewer@afit.edu
850-272-7931

Appendix M SI Equivalent Tables

Table 55: Coupon Thickness (Table 12 SI Units)

Layup Type	Average Thickness (mm)	Thickness Stdev (mm)	Thickness Increase Over Control (mm)	Thickness Increase Over Control %
9-Ply Control	1.202	0.03825	--	--
9-Ply Hybrid	1.537	0.01391	0.3345	27.82
18-Ply Control	2.353	0.04912	--	--
18-Ply Hybrid	2.997	0.03205	0.6449	27.41
18-Ply Shank-Only	2.761	0.01312	0.4072	0

Table 56: Thickness Statistical Analysis (Table 13 SI Equivalent)

	2x 9-Ply Thickness			18-Ply Thickness					
	Average	Stdev	N	Average	Stdev	N	Diff	% Diff	Stat Sig
Control Thickness (mm)	2.405	0.07648	6	2.353	0.04912	33	-0.05156	-2.145	No
Hybrid Thickness (mm)	3.073	0.02781	6	2.997	0.03205	33	-0.07544	-2.454	Yes

Table 57: 9-Ply Double Shear Load Based Data (Table 13 SI Units)

	Control			Hybrid					
	Average (95% CI)	Stdev	N	Average (95% CI)	Stdev	N	Diff	% Diff	Stat Sig
Yield Load (kN)	8.215 (7.759-8.671)	0.4346	6	10.30 (9.854-10.76)	0.4295	6	2.090	25.44	Yes
Offset Load (kN)	9.063 (8.755-9.372)	0.2937	6	12.23 (11.75-12.71)	0.4577	6	3.168	34.95	Yes
Ultimate Load (kN)	9.568 (8.892-10.24)	0.2723	3	13.59 (12.86-14.31)	0.2931	3	4.018	42.00	Yes
Strain Energy (J)	15.93 (13.63-18.23)	0.9248	3	24.07 (22.78-25.35)	0.5178	3	8.135	51.06	Yes

Table 58: 9-Ply Double Shear Stress Based Data (Table 15 SI Units)

	Control			Hybrid					
	Average (95% CI)	Stdev	N	Average (95% CI)	Stdev	N	Diff	% Diff	Stat Sig
Yield Stress (MPa)	864.0 (813.6-914.5)	48.06	6	847.8 (804.4-891.2)	41.34	6	-16.22	-1.877	No
Yield Strain	0.04176 (0.03920-0.04432)	0.002437	6	0.04194 (0.03939-0.04449)	0.002431	6	1.817E-4	0.4350	No
Offset Stress (MPa)	953.1 (924.6-981.5)	27.11	6	1006 (958.3-1054)	45.75	6	53.19	5.581	Yes
Offset Strain	0.05387 (0.05162-0.05613)	0.002150	6	0.0591 (0.05173-0.06648)	0.007025	6	0.005173	9.714	No
Ultimate Stress (MPa)	1028 (926.2-1129)	540.9	3	1121 (1038-1203)	33.27	3	92.96	9.045	No
Modulus (MPa)	21750 (20910-22600)	805.5	6	21320 (20240-22400)	1027	6	-433.9	-1.995	No
Strain Energy Density (MJ/m^3)	216.1 (190.6-241.6)	10.27	3	250.8 (236.9-264.8)	5.624	3	34.74	16.08	Yes

Table 59: 18-Ply Double Shear Load Based Data (Table 16 SI Units)

	Control 18 Ply			Hybrid 18 Ply					
	Average (95% CI)	Stdev	N	Average (95% CI)	Stdev	N	Diff	% Diff	Stat Sig
Yield Load (kN)	16.33 (15.78-16.87)	0.5911	7	18.35 (17.92-18.78)	0.5548	9	2.025	12.40	Yes
Offset Load (kN)	18.03 (17.69-18.37)	0.3241	6	22.73 (22.41-23.05)	0.3508	7	4.702	26.08	Yes
Ultimate Load (kN)	20.08 (18.41-21.75)	0.6735	3	26.42 (26.00-26.84)	0.2657	4	6.339	31.57	Yes
Strain Energy (J)	14.04 (13.06-15.02)	0.3935	3	19.09 (18.88-19.30)	0.1328	4	5.055	36.01	Yes

Table 60: 18-Ply Double Shear Stress-Strain Data (Table 17 SI Units)

	Control 18 Ply			Hybrid 18 Ply					
	Average (95% CI)	Stdev	N	Average (95% CI)	Stdev	N	Diff	% Diff	Stat Sig
Yield Stress (MPa)	883.6 (844.7-922.5)	42.05	7	771.0 (751.0-791.0)	26.01	9	-112.6	-12.74	Yes
Yield Strain	0.04027 (0.03754-0.04300)	0.002956	7	0.03379 (0.03242- 0.03515)	0.001775	9	-0.006481	-16.09	Yes
Offset Stress (MPa)	973.9 (945.1-1003)	27.46	6	956.3 (940.7-971.8)	16.80	7	-17.62	-1.810	Yes
Offset Strain	0.05254 (0.05047-0.0546)	0.001976	6	0.04937 (0.04797- 0.05077)	0.001512	7	-0.003169	-6.031	No
Ultimate Stress (MPa)	1102 (1082-1122)	8.163	3	1112 (1084-1140)	17.46	4	9.745	0.8842	No
Modulus (MPa)	23170 (22680-23670)	643.7	9	24250 (3446-3590)	692.7	10	1080	4.661	Yes
Strain Energy Density (MJ/m^3)	97.40 (91.96-102.8)	2.190	3	101.5 (99.55-103.5)	1.256	4	4.147	4.258	No

Table 61: Control 9-Ply and 18-Ply Load Data (Table 18 SI Units)

	2x Control 9 Ply			Control 18 Ply					
	Average (95% CI)	Stdev	N	Average (95% CI)	Stdev	N	Diff	% Diff	Stat Sig
Yield Load (kN)	16.43 (15.52-17.34)	0.8693	6	16.33 (15.78-16.87)	-0.1040	7	-0.1040	-0.6331	No
Offset Load (kN)	18.13 (17.51-18.74)	0.5875	6	18.03 (17.69-18.37)	-0.09867	6	-0.09867	-0.5443	No
Ultimate Load (kN)	19.14 (17.78-20.49)	0.5446	3	20.08 (18.41-21.75)	0.9445	3	0.9445	4.936	No

Table 62: Hybrid 9-Ply and 18-Ply Load Data (Table 19 SI Units)

	2x Hybrid 9-Ply			Hybrid 18 Ply					
	Average (95% CI)	Stdev	N	Average (95% CI)	Stdev	N	Diff	% Diff	Stat Sig
Yield Load (kN)	20.61 (19.71-21.51)	0.8590	6	18.35 (17.92-18.78)	0.5548	9	-2.260	-10.96	Yes
Offset Load (kN)	24.46 (23.50-25.42)	0.9154	6	22.73 (22.41-23.05)	0.3508	7	-1.733	-7.083	Yes
Ultimate Load (kN)	27.17 (25.72-28.63)	0.5862	3	26.42 (26.00-26.84)	0.2657	4	-0.752	-2.769	No

Table 63: 9-Ply Control Computational v. Experimental Load Data (Table 21 SI Units)

	9-Ply Control Load-Based Data				
	Computational	**Experimental Avg (95% CI)**	**Diff**	**% Diff**	**Comp Falls in**
Yield Load (kN)	8.745	8.215 (7.759-8.671)	-0.5305	-6.458	No
Yield Disp (mm)	0.3340	0.3304 (0.3102-0.3506)	-3.614E-03	-1.094	Yes
Offset Load (kN)	9.506	9.063 (8.755-9.372)	-0.44238	-4.881	No
Offset Disp (mm)	0.4249	0.4262 (0.4084-0.4441)	1.296E-03	0.3041	Yes
Ultimate Load (kN)	9.911	9.568 (8.892-10.24)	-0.3425	-3.580	Yes

Table 64: 9-Ply Control Computational v. Experimental Stress Data (Table 22 SI Units)

	9-Ply Control Stress-Based Data				
	Computational	**Experimental Avg (95% CI)**	**Diff**	**% Diff**	**Comp Falls in**
Yield Stress (MPa)	948.0	864.0 (813.6-914.5)	-84.00	-9.722	No
Yield Strain	0.04221	0.04176 (0.03920-0.04432)	-4.517E-04	-1.082	Yes
Offset Stress (MPa)	1031	953.1 (924.6-981.5)	-77.67	-8.149	No
Offset Strain	0.05372	0.05387 (0.05162-0.05613)	1.517E-04	0.2815	Yes
Ultimate Stress (MPa)	1074	1028 (926.2-1129)	-46.40	-4.515	Yes
Modulus (MPa)	23570	21750 (20910-22600)	-1821	-8.370	No

Table 65: 18-Ply Control Computational v. Experimental Load Data (Table 25 SI Units)

	18-Ply Control Load Based Data				
	Computational	**Experimental Avg (95% CI)**	**Diff**	**% Diff**	**Comp Falls in 95% CI**
Yield Load (kN)	17.02	16.33 (15.78-16.87)	-0.6979	-4.275	No
Yield Disp (mm)	0.3193	0.3196 (0.2979-0.3413)	3.651E-04	0.1142	Yes
Offset Load (kN)	18.17	18.03 (17.69-18.37)	-0.1383	-0.7670	Yes
Offset Disp (mm)	0.4028	0.4157 (0.3993-0.4321)	0.01286	3.093	Yes
Ultimate Load (kN)	18.55	20.08 (18.41-21.75)	1.527	7.605	Yes

Table 66: 18-Ply Control Computational v. Experimental Stress Data (Table 26 SI Units)

	18-Ply Control Stress Based Data				
	Computational	**Experimental Avg (95% CI)**	**Diff**	**% Diff**	**Comp Falls in 95% CI**
Yield Stress (MPa)	922.5	883.6 (844.7-922.5)	-38.91	-4.403	Yes
Yield Strain	0.04036	0.04027 (0.03754-0.04300)	-9.000E-05	-0.2235	Yes
Offset Stress (MPa)	984.6	973.9 (945.1-1003)	-10.69	-1.097	Yes
Offset Strain	0.05092	0.05254 (0.05047-0.0546)	0.001620	3.083	Yes
Ultimate Stress (MPa)	1006	1102 (1082-1122)	96.16	8.725	Yes
Modulus (MPa)	24060	23170 (22680-23670)	-882.6	-3.809	Yes

Table 67: 9-Ply Hybrid Computational v. Experimental Load Data (Table 29 SI Units)

	9-Ply Hybrid Load Based Data				
	Computational	**Experimental Avg (95% CI)**	**Diff**	**% Diff**	**Comp Falls in 95% CI**
Yield Load (kN)	9.679	10.30 (9.854-10.76)	0.6256	6.071	Yes
Yield Disp (mm)	0.3045	0.3318 (0.3116-0.3520)	0.02835	8.223	No
Offset Load (kN)	12.24	12.23 (11.75-12.71)	-0.005881	-0.04808	Yes
Offset Disp (mm)	0.4440	0.4676 (0.4093-0.5260)	0.02365	5.058	Yes
Ultimate Load (kN)	13.19	13.59 (12.86-14.31)	0.3974	2.925	Yes

Table 68: 9-Ply Hybrid Computational v. Experimental Stress Data (Table 30 SI Units)

	9-Ply Hybrid Stress Based Data				
	Computational	**Experimental Avg (95% CI)**	**Diff**	**% Diff**	**Comp Falls in 95% CI**
Yield Stress (MPa)	836.3	847.8 (804.4-891.2)	11.47	1.353	Yes
Yield Strain	0.03849	0.04194 (0.03939-0.04449)	0.003450	8.226	No
Offset Stress (MPa)	1057.0	1006 (958.3-1054)	-50.68	-5.036	No
Offset Strain	0.05612	0.0591 (0.05173-0.06648)	0.002985	5.050	Yes
Ultimate Stress (MPa)	1140	1121 (1038-1203)	-18.94	-1.690	Yes
Modulus (MPa)	22918	21320 (20240-22400)	-1600	-7.503	No

Table 69: 18-Ply Hybrid Computational v. Experimental Load Data (Table 33 SI Units)

	18-Ply Hybrid Load Based Data				
	Computational	**Experimental Avg (95% CI)**	**Diff**	**% Diff**	**Comp Falls in 95% CI**
Yield Load (kN)	19.31	18.35 (17.92-18.78)	-0.9596	-5.230	No
Yield Disp (mm)	0.3021	0.2682 (0.2574-0.2790)	-0.03388	-12.63	No
Offset Load (kN)	23.35	22.73 (22.41-23.05)	-0.6234	-2.742	No
Offset Disp (mm)	0.4183	0.3906 (0.3796-0.4017)	-0.02771	-7.093	No
Ultimate Load (kN)	25.84	26.42 (26.00-26.84)	0.5760	2.180	No

Table 70: 18-Ply Hybrid Computational v. Experimental Load Data (Table 34 SI Units)

	18-Ply Hybrid Stress Based Data				
	Computational	**Experimental Avg (95% CI)**	**Diff**	**% Diff**	**Comp Falls in 95% CI**
Yield Stress (MPa)	834.3	771.0 (751.0-791.0)	-63.24	-8.203	No
Yield Strain	0.03818	0.03379 (0.03242- 0.03515)	-0.004391	-13.00	No
Offset Stress (MPa)	1009	956.3 (940.7-971.8)	-52.44	-5.484	No
Offset Strain	0.05374	0.04937 (0.04797- 0.05077)	-0.004369	-8.848	No
Ultimate Stress (MPa)	1116	1112 (1084-1140)	-4.413	-0.3969	Yes
Modulus (MPa)	23060	24250 (3446-3590)	1197	4.937	No

Table 71: 18-Ply Single Shear Protruding Load Displacement Data (Table 36 SI Units)

	Control			Hybrid					
	Average (95%CI)	Stdev	N	Average (95%CI)	Stdev	N	Diff	% Diff	Stat Sig
Yield Load (kN)	10.48 (9.986-10.97)	0.5342	7	13.76 (13.24-14.27)	0.4128	5	3.277	31.27	Yes
Offset Load (kN)	12.97 (12.71-13.24)	0.2503	6	16.24 (15.74-16.73)	0.3980	5	3.264	25.16	Yes
Ultimate Load (kN)	17.39 (15.97-18.81)	0.5711	3	23.82 (22.10-25.53)	0.6903	3	6.428	36.96	Yes
Strain Energy (J)	28.51 (24.52-32.50)	1.607	3	46.63 (44.21-49.04)	0.9741	3	18.12	63.54	Yes

Table 72: 18-Ply Single Shear Protruding Stress-Strain Data (Table 37 SI Units)

	Control			Hybrid					
	Average (95%CI)	Stdev	N	Average (95%CI)	Stdev	N	Diff	% Diff	Stat
Yield Stress (MPa)	565.3 (535.1-595.6)	32.69	7	582.1 (560.0-604.2)	17.79	5	16.79	2.971	No
Yield Strain	0.03342 (0.03247-0.03436)	0.001024	7	0.03691 (0.03572-0.03810)	9.574E-04	5	0.003496	10.46	Yes
Offset Stress (MPa)	701.8 (681.7-722.0)	19.20	6	687.0 (666.8-707.3)	16.31	5	-14.83	-2.113	No
Offset Strain	0.0488 (0.04788-0.04965)	8.443E-04	6	0.05124 (0.04988-0.05260)	0.001098	5	0.002478	5.083	Yes
Ultimate Stress (MPa)	947.4 (903.2991.5)	17.79	3	1007 (943.9-1070)	25.43	3	59.76	6.308	Yes
Modulus (MPa)	17990 (17360-18620)	683.9	7	16660 (16090-17240)	459.6	5	-1325	-7.364	Yes
Strain Energy Density (MJ/m^3)	196.4 (173.8-219.0)	9.103	3	249.1 (236.3-261.9)	5.146	3	52.74	26.86	Yes

Table 73: 18-Ply Single Shear Countersunk Load-Displacement Data: Control v. Shank-Only (Table 38 SI Units)

	Control			Shank-Only Hybrid					
	Average	Stdev	N	Average	Stdev	N	Diff	% Diff	Stat Sig
Yield Load (kN)	14.88 (14.12-15.63)	0.7194	6	16.29 (15.67-16.91)	0.5895	6	1.413	9.500	Yes
Offset Load (kN)	15.09 (14.71-15.48)	0.3100	5	18.30 (17.99-18.60)	0.2438	5	3.200	21.2	Yes
Ultimate Load (kN)	15.65 (15.37-15.94)	0.1800	4	18.83 (18.52-19.15)	0.2570	5	3.182	20.3	Yes
Strain Energy (J)	19.81 (17.82-21.80)	0.8016	3	24.37 (23.23-25.50)	0.4566	3	4.557	23.0	Yes

Table 74: 18-Ply Single Shear Countersunk Load-Displacement Data: Control v. Hybrid (Table 39 SI Units)

	Control			Hybrid					
	Average	Stdev	N	Average	Stdev	N	Diff	% Diff	Stat Sig
Yield Load (kN)	14.88 (14.12-15.63)	0.7194	6	17.18 (16.46-17.90)	0.6818	6	2.303	15.48	Yes
Offset Load (kN)	15.09 (14.71-15.48)	0.3100	5	19.83 (19.35-20.31)	0.3860	5	4.739	31.39	Yes
Ultimate Load (kN)	15.65 (15.37-15.94)	0.1800	4	20.76 (19.54-21.97)	0.4888	3	5.106	32.62	Yes
Strain Energy (J)	19.81 (17.82-21.80)	0.8016	3	27.00 (24.78-29.23)	0.8968	3	7.193	36.31	Yes

Table 75: 18-Ply Single Shear Countersunk Stress-Strain Data: Control v. Shank-Only Hybrid (Table 40 SI Units)

	Control			Shank-Only Hybrid					
	Average (95% CI)	**Stdev**	**N**	**Average (95% CI)**	**Stdev**	**N**	Diff	% Diff	Stat Sig
Yield Stress (MPa)	797.4 (759.4-835.5)	36.29	6	745.9 (720.4-771.4)	24.31	6	-51.57	-6.467	Yes
Yield Strain	0.07609 (0.07012-0.08206)	0.005687	6	0.08050 (0.07666-0.08434)	0.003658	6	0.004408	5.794	No
Offset Stress (MPa)	807.7 (792.0-823.5)	12.70	5	838.3 (827.3-849.2)	8.794	5	30.52	3.778	Yes
Offset Strain	0.08564 (0.08168-0.08961)	0.003195	5	0.09798 (0.09377-0.1022)	0.003390	5	0.01234	14.41	Yes
Ultimate Stress (MPa)	833.4 (791.0-875.8)	26.66	4	863.0 (845.9-880.1)	13.80	5	29.58	3.549	No
Modulus (MPa)	10800 (10190-11400)	579.5	6	9507 (9232-9781)	261.9	6	-1289	-11.94	Yes
Strain Energy Density (MJ/m^3)	134.5 (122.6-146.3)	4764	3	141.0 (133.0-148.9)	3.198	3	6.520	4.849	No

Table 76: 18-Ply Single Shear Countersunk Stress-Strain Data: Control v. Hybrid (Table 41 SI Units)

	Control			Hybrid					
	Average (95% CI)	**Stdev**	**N**	**Average (95% CI)**	**Stdev**	**N**	Diff	% Diff	Stat Sig
Yield Stress (MPa)	797.4 (759.4-835.5)	36.29	6	721.4 (691.3-751.6)	28.74	6	-76.01	-9.532	Yes
Yield Strain	0.07609 (0.07012-0.08206)	0.005687	6	0.07686 (0.07365-0.08008)	0.0040	6	7.733E-04	1.016	No
Offset Stress (MPa)	807.7 (792.0-823.5)	12.70	5	830.8 (808.7-852.8)	17.75	5	23.01	2.849	No
Offset Strain	0.08564 (0.08168-0.08961)	0.003195	5	0.09631 (0.09338-0.09925)	0.003347	5	0.01067	12.46	Yes
Ultimate Stress (MPa)	833.4 (791.0-875.8)	26.66	4	870.4 (816.4-924.5)	21.76	3	37.04	4.444	No
Modulus (MPa)	10800 (10190-11400)	579.5	6	9644 (9448-9839)	186.2	6	-1152	-10.67	Yes
Strain Energy Density (MJ/m^3)	134.5 (122.6-146.3)	4764	3	143.2 (130.2-156.1)	5.218	3	8.729	6.492	No

Table 77: Double Shear Fatigue Step Test Method Data (Table 43 SI Units)

	Control			Hybrid					
	Average (95%CI)	Stdev	N	Average (95%CI)	Stdev	N	Diff	% Diff	Stat Sig
Fatigue Load (kN)	21.66 (19.84-23.49)	0.7332	3	27.33 (26.30-28.35)	0.4121	3	5.661	26.13	Yes
Fatigue Stress (kPa)	1155 (1139-1171)	6.527	3	1143 (1087-1199)	22.54	3	-12.29	-1.064	No

Table 78: Single Shear Fatigue Step Test Method Data (Table 44 SI Units)

	Control			Hybrid					
	Average (95%CI)	Stdev	N	Average (95%CI)	Stdev	N	Diff	% Diff	Stat Sig
Fatigue Load (kN)	18.36 (17.21-19.52)	0.4646	3	24.28 (24.00-24.55)	0.1112	3	5.912	32.19	Yes
Fatigue Stress (kPa)	990.1 (889.4-1091)	40.53	3	1041 (1030-1053)	4.543	3	51.27	5.178	No

Table 79: 18-Ply Single Shear Countersunk Load-Displacement Data: Shank-Only v. Hybrid (Table 54 SI Units)

	Shank-Only Hybrid			Hybrid					
	Average (95%CI)	Stdev	N	Average (95%CI)	Stdev	N	Diff	% Diff	Stat Sig
Yield Load (kN)	16.29 (15.67-16.91)	0.5895	6	17.18 (16.46-17.90)	0.6818	6	0.8900	5.463	Yes
Offset Load (kN)	18.30 (17.99-18.60)	0.2438	5	19.83 (19.35-20.31)	0.3860	5	1.538	8.407	Yes
Ultimate Load (kN)	18.83 (18.52-19.15)	0.2570	5	20.76 (19.54-21.97)	0.4888	3	1.924	10.21	Yes
Strain Energy (J)	24.37 (23.23-25.50)	0.4566	3	27.00 (24.78-29.23)	0.8968	3	2.636	10.82	Yes

Table 80: 18-Ply Single Shear Countersunk Stress-Strain Data: Shank-Only Hybrid v. Hybrid (Table 55 SI Units)

	Shank-Only Hybrid			Hybrid					
	Average (95% CI)	**Stdev**	**N**	**Average (95% CI)**	**Stdev**	**N**	Diff	% Diff	Stat Sig
Yield Stress (MPa)	745.9 (720.4-771.4)	24.31	6	721.4 (691.3-751.6)	28.74	6	-0.003635	-4.516	No
Yield Strain	0.08050 (0.07666-0.08434)	0.003658	6	0.07686 (0.07365-0.08008)	0.0040	6	-24.44	-3.277	No
Offset Stress (MPa)	838.3 (827.3-849.2)	8.794	5	830.8 (808.7-852.8)	17.75	5	-0.001668	-1.702	No
Offset Strain	0.09798 (0.09377-0.1022)	0.003390	5	0.09631 (0.09338-0.09925)	0.003347	5	-7.503	-0.8951	No
Ultimate Stress (MPa)	863.0 (845.9-880.1)	13.80	5	870.4 (816.4-924.5)	21.76	3	7.457	0.8641	No
Modulus (MPa)	9507 (9232-9781)	261.9	6	9644 (9448-9839)	186.2	6	137.1	1.442	No
Strain Energy Density (MJ/m^3)	141.0 (133.0-148.9)	3.198	3	143.2 (130.2-156.1)	5.218	3	2.209	1.567	No

Bibliography

[1] ASTM International, "D6873/D6873M-08 Standard Practice for Bearing Fatigue Response of Polymer Metrix Composite Laminates," vol. i. ASTM International, pp. 1–9, 2014, doi: 10.1520/D6873.

[2] ASTM International, "ASTM D5961/D5961M Standard Test Method for Bearing Response of Polymer Matrix Composite Laminates," *Annu. B. ASTM Stand.*, vol. i, no. April 2004, pp. 1–18, 2003, doi: 10.1520/D5961.

[3] "Abaqus Unified FEA - SIMULIA™ by Dassault Systèmes®." https://www.3ds.com/products-services/simulia/products/abaqus/ (accessed Jun. 23, 2020).

[4] "Skinning the F-35 fighter," *Composites World*, Oct. 19, 2009. https://www.compositesworld.com/articles/skinning-the-f-35-fighter (accessed Oct. 05, 2020).

[5] "Lockheed Martin Starts F-35 Composite Forward-Fuselage Assembly – NetComposites," *NetComposites*, Jul. 19, 2004. https://netcomposites.com/news/lockheed-martin-starts-f-35-composite-forward-fuselage-assembly/ (accessed Oct. 05, 2020).

[6] "AERO - Boeing 787 from the Ground Up." https://www.boeing.com/commercial/aeromagazine/articles/qtr_4_06/article_04_2.html (accessed Jul. 01, 2020).

[7] "Airbus in Illescas delivers first A350 XWB Wing Lower Cover to Airbus in Broughton," *Airbus Newsroom*. https://www.airbus.com/newsroom/press-releases/en/2011/09/airbus-in-illescas-delivers-first-a350-xwb-wing-lower-cover-

to-airbus-in-broughton.html (accessed Mar. 06, 2019).

[8] "The A350 XWB – Advanced Materials and Design." https://www.azom.com/article.aspx?ArticleID=7858 (accessed Jul. 01, 2020).

[9] "Airbus takes on Boeing with composite A350 XWB - Materials Today," Jan. 05, 2008. https://www.materialstoday.com/composite-applications/features/airbus-takes-on-boeing-with-composite-a350-xwb/ (accessed Jul. 01, 2020).

[10] A. Crosky, C. Grant, D. Kelly, X. Legrand, and G. Pearce, "Fibre placement processes for composites manufacture," in *Advances in Composites Manufacturing and Process Design*, Elsevier Inc., 2015, pp. 79–92.

[11] K. He, H. Nie, and C. Yan, "ScienceDirect The Intelligent Composite Panels Manufacturing Technology Based on Tape-laying Automatic System," 2016, doi: 10.1016/j.procir.2016.10.120.

[12] M. W. D. Nielsen, K. J. Johnson, A. T. Rhead, and R. Butler, "Laminate design for optimised in-plane performance and ease of manufacture," *Compos. Struct.*, vol. 177, pp. 119–128, Oct. 2017, doi: 10.1016/J.COMPSTRUCT.2017.06.061.

[13] B. J. Jensen *et al.*, "Fiber Metal Laminates Made by the VARTM Process," Accessed: Feb. 04, 2019. [Online]. Available: https://ntrs.nasa.gov/search.jsp?R=20090028660.

[14] J. S. Brewer, "Delamination Toughness Characterization of Out-of-Autoclave Vacuum-Bag-Only Polymer Matrix Composites Enhanced by z-aligned Carbon Nanofibers," University of South Alabama, 2015.

[15] E. Milberg, "Scaled Composites Completes Test of Stratolaunch, the World's Largest Composite Aircraft," *Composite Manufacturing Magazine*, 2017.

http://compositesmanufacturingmagazine.com/2017/06/scaled-composites-completes-test-stratolaunch-worlds-largest-composite-aircraft/ (accessed Mar. 06, 2019).

[16] “Having Completed the Stratolaunch SOW, We’re Handing Over the Keys - News | Scaled Composites.” https://www.scaled.com/2019/10/11/having-completed-the-stratolaunch-sow-were-handing-over-the-keys/ (accessed Jul. 01, 2020).

[17] “AIAA SciTech.” https://www.aiaa.org/SciTech/program (accessed Jul. 01, 2020).

[18] J. D. Bartley-Cho *et al.*, “Composite Airframe Life Extension: Project 2, Air Force Research laboratory Aerospace Systems Directorate,” 2018.

[19] N. Kashaev, V. Ventzke, S. Riekehr, F. Dorn, and M. Horstmann, “Assessment of alternative joining techniques for Tiâ€“6Alâ€“4V/CFRP hybrid joints regarding tensile and fatigue strength,” *J. Mater.*, vol. 81, pp. 73–81, 2015, doi: 10.1016/j.matdes.2015.04.051.

[20] P. Lopez-Cruz, J. Laliberté, and L. Lessard, “Investigation of bolted/bonded composite joint behaviour using design of experiments,” *Compos. Struct.*, 2017, doi: 10.1016/j.compstruct.2017.02.084.

[21] J. Bishopp, “13 - Adhesives for Aerospace Structures,” in *Handbook of Adhesives and Surface Preparation*, 2011, pp. 301–344.

[22] B. Kolesnikov, L. Herbeck, and A. Fink, “CFRP/titanium hybrid material for improving composite bolted joints,” *Compos. Struct.*, vol. 83, no. 4, pp. 368–380, 2008, doi: 10.1016/j.compstruct.2007.05.010.

[23] G. Kolks and K. I. Tserpes, “Efficient progressive damage modeling of hybrid composite/titanium bolted joints,” *Compos. Part A Appl. Sci. Manuf.*, vol. 56, pp.

51–63, 2014, doi: 10.1016/j.compositesa.2013.09.011.

[24] S. Zu, Z. Zhou, L. Che, Y. Zhang, and J. Zhang, “Tightening torque and washer size effects on bearing strength of fiber metal laminate bolted-joints.” Accessed: Jan. 18, 2019. [Online]. Available: https://www-matec-conferences-org.afit.idm.oclc.org/articles/matecconf/pdf/2017/22/matecconf_icmaa2017_01010.pdf.

[25] Y. Zhou, H. Yazdani Nezhad, C. Hou, X. Wan, C. T. Mccarthy, and M. A. Mccarthy, “A three dimensional implicit finite element damage model and its application to single-lap multi-bolt composite joints with variable clearance,” 2015, doi: 10.1016/j.compstruct.2015.06.073.

[26] Z. Wu and Z. Wu, “Optimal hole shape for minimum stress concentration using parameterized geometry models,” vol. 37, pp. 625–634, 2009, doi: 10.1007/s00158-008-0253-4.

[27] P. P. Camanho, C. M. L. Tavares, R. De Oliveira, A. T. Marques, and A. J. M. Ferreira, “Increasing the efficiency of composite single-shear lap joints using bonded inserts,” 2005, doi: 10.1016/j.compositesb.2005.01.007.

[28] C. A. J. R. Vermeeren, “An Historic Overview of the Development of Fibre Metal Laminates,” 2003. Accessed: Jan. 24, 2019. [Online]. Available: https://link-springer-com.afit.idm.oclc.org/content/pdf/10.1023%2FA%3A1025533701806.pdf.

[29] R. M. Frizzell, C. T. Mccarthy, and M. A. Mccarthy, “Simulating damage and delamination in fibre metal laminate joints using a three-dimensional damage model with cohesive elements and damage regularisation,” 2011, doi:

10.1016/j.compscitech.2011.04.006.

[30] T. Sinmazçelik, E. Avcu, M. Ö. Bora, and O. Çoban, “A review: Fibre metal laminates, background, bonding types and applied test methods,” 2011, doi: 10.1016/j.matdes.2011.03.011.

[31] Jérôme Pora, “Composite Materials in the Airbus A380-From History to Future.”

[32] F. C. Campbell, *Structural Composite Materials*. ASM International, 2010.

[33] “3M Advanced Technologies for Aerospace Structures 3Innovation • Structural Composites • Structural Adhesives • Protective Products.” Accessed: Apr. 16, 2019. [Online]. Available: http://www.proximatape.com/wp-content/uploads/settori-industriali/3M Aereospace.pdf.

[34] D.-W. Lee and J.-I. Song, “Research on simple joint method using fiber-metal laminate design for improved mechanical properties of CFRP assembly structure,” 2018, doi: 10.1016/j.compositesb.2018.11.081.

[35] “Linear Thermal Expansion Coefficient for Metals.” https://www.amesweb.info/Materials/Linear-Thermal-Expansion-Coefficient-Metals.aspx (accessed Mar. 15, 2019).

[36] T. Yamada, H. Nakatani, and S. Ogihara, “Evaluation of Bearing Damage Behavior in Thin Titanium Films-Cfrp Hybrid Laminate,” 2013.

[37] A. Fink, P. P. Camanho, J. M. Andrés, E. Pfeiffer, and A. Obst, “Hybrid CFRP/titanium bolted joints: Performance assessment and application to a spacecraft payload adaptor,” *Compos. Sci. Technol.*, vol. 70, no. 2, pp. 305–317, 2010, doi: 10.1016/j.compscitech.2009.11.002.

[38] J. M. Hundley, H. T. Hahn, J.-M. Yang, and A. B. Facciano, “Three-dimensional

progressive failure analysis of bolted titanium-graphite fiber metal laminate joints," doi: 10.1177/0021998310391047.

[39] E. Petersen, D. Stefaniak, and C. Hühne, "Experimental investigation of load carrying mechanisms and failure phenomena in the transition zone of locally metal reinforced joining areas," 2017, doi: 10.1016/j.compstruct.2017.09.002.

[40] J. Lopes *et al.*, "Fatigue behaviour of CFRP/steel hybrid composites Stress-Strain," 2015, Accessed: Jul. 01, 2020. [Online]. Available: https://www.researchgate.net/publication/284609619.

[41] M. Falugi and P. Knoth, "Hybrid Laminates for Efficient Composite Bolted Joints," 2017.

[42] B. Egan, M. A. Mccarthy, R. M. Frizzell, P. J. Gray, and C. T. Mccarthy, "Modelling bearing failure in countersunk composite joints under quasi-static loading using 3D explicit finite element analysis," *Compos. Struct.*, 2014, doi: 10.1016/j.compstruct.2013.10.033.

[43] B. Egan, C. T. McCarthy, M. A. McCarthy, P. J. Gray, and R. M. Frizzell, "Modelling a single-bolt countersunk composite joint using implicit and explicit finite element analysis," *Comput. Mater. Sci.*, vol. 64, pp. 203–208, 2012, doi: 10.1016/j.commatsci.2012.02.008.

[44] B. Egan, M. A. McCarthy, R. M. Frizzell, and C. T. McCarthy, "Finite element analysis of catastrophic failure of dynamically-loaded countersunk composite fuselage joints," *Compos. Struct.*, vol. 133, pp. 1198–1208, Dec. 2015, doi: 10.1016/J.COMPSTRUCT.2015.07.004.

[45] "Abaqus Theory Guide 2016." Dassault Systemes.

[46] “Abaqus Analysis User’s Guide 2016.” Dassault Systemes.

[47] R. G. Buentello-Hernandez, “3D Finite Element Modeling of Sliding Wear,” 2013. Accessed: Mar. 26, 2019. [Online]. Available: https://scholar.afit.edu/cgi/viewcontent.cgi?article=1503&context=etd.

[48] B. McGinty, “ContinuumMechanics.org.” http://www.continuummechanics.org/index.html.

[49] A. Mendelson, *Plasticity: Theory and Application*. New York, NY: MacMillan, 1968.

[50] F. Dunne and N. Petrenic, *Introduction to Computational Plasticity*. Oxford University Press, 2006.

[51] R. D. Cook, D. S. Malkus, M. E. Plesha, and R. J. Witt, *Concepts and Applications of Finite Element Analysis*, Fourth. Hoboken, NJ: John Wiley & Sons, Inc., 2002.

[52] K. A. Novak, *Numerical Methods for Scientific Computing*, 1.1. 2017.

[53] J. F. Doyle, *Nonlinear Analysis of Thin-Walled Structures*. New York, NY, 2001.

[54] A. S. Saada, *Elasticity Theory and Applications*, Second Edi., vol. 91. J. Ross Publishing, Inc., 2009.

[55] K. M. Liew, Z. Z. Pan, and L. W. Zhang, “An overview of layerwise theories for composite laminates and structures: Development, numerical implementation and application,” *Compos. Struct.*, 2019, doi: 10.1016/j.compstruct.2019.02.074.

[56] J. N. Reddy, “An evaluation of equivalent-single-layer and layerwise theories of composite laminates,” 1993. Accessed: Feb. 21, 2019. [Online]. Available: https://ac-els-cdn-com.afit.idm.oclc.org/026382239390147I/1-s2.0-026382239390147I-main.pdf?_tid=c6cd2f36-60e4-4f87-9b52-

0fdf470b9287&acdnat=1550774593_3f927be5f294f6dd987462785fe454d7.

[57] R. C. Burk, “Standard Failure Criteria Needed for Advanced Composites,” *AIAA*, vol. 21, pp. 58–62, 1983.

[58] C. T. Sun, B. J. Quinn, and J. Tao, “Comparative Evaluation of Failure Analysis Methods for Composite Laminates,” 1996. Accessed: Feb. 12, 2019. [Online]. Available: www.tc.faa.gov/its/act141/reportpage.html.

[59] and A. R. Hashin, Z., “A Fatigue Criterion for Fiber-Reinforced Materials,” *J. Compos. Mater.*, vol. 7, pp. 448–464, 1973.

[60] Z. Hashin, “Failure Criteria for Unidirectional FibreComposites,” *J. Appl. Mech.*, vol. 47, no. June, pp. 329–334, 1980.

[61] A. P. K. Joseph, P. Davidson, and A. M. Waas, “Open hole and filled hole progressive damage and failure analysis of composite laminates with a countersunk hole,” 2018, doi: 10.1016/j.compstruct.2018.06.120.

[62] F. Paris, “A Study of Failure Criteria of Fibrous Composite Materials,” Hampton, VA, 2001. Accessed: Feb. 12, 2019. [Online]. Available: http://www.sti.nasa.gov.

[63] M. V. Donadon, S. F. M. de Almeida, M. A. Arbelo, and A. R. de Faria, “A Three-Dimensional Ply Failure Model for Composite Structures,” *Int. J. Aerosp. Eng.*, vol. 2009, pp. 1–22, 2009, doi: 10.1155/2009/486063.

[64] S. Lauterbach, C. Balzani, and W. Wagner, “Failure Analysis on Shell-like Composite Laminates Using the Puck Criteria,” *PAMM · Proc. Appl. Math. Mech*, vol. 9, pp. 231–232, 2009, doi: 10.1002/pamm.200910089.

[65] H. M. Deuschle, “3D Failure Analysis of UD Fibre Reinforced Composites: Puck’s Theory within FEA,” Universitat Stuttgart, 2010.

[66] K. Kodagali, “Progressive Failure Analysis of composite Materials using the Puck Failure Criteria,” 2017. Accessed: Feb. 21, 2019. [Online]. Available: https://scholarcommons.sc.edu/cgi/viewcontent.cgi?article=5464&context=etd.

[67] C. Roberts, “Modeling Hybrid Composites Using Tsai-Wu and Hashin Failure Criteria,” Air Force Institute of Technology, 2020.

[68] F. George and J. Langley, “A Study of Failure Criteria Composite Materials of Fibrous,” no. March, 2001.

[69] P. Liu, X. Cheng, S. Wang, S. Liu, and Y. Cheng, “Numerical analysis of bearing failure in countersunk composite joints using 3D explicit simulation method,” 2016, doi: 10.1016/j.compstruct.2015.11.058.

[70] C. Friedrich and H. Hubbertz, “Friction behavior and preload relaxation of fastening systems with composite structures,” *Compos. Struct.*, vol. 110, pp. 335–341, 2014, doi: 10.1016/j.compstruct.2013.11.024.

[71] P. P. Camanho and C. G. Davila, “Mixed-Mode Decohesion Finite Elements for the Simulation of Delamination in Composite Materials,” Hampton, VA, 2002. Accessed: Feb. 28, 2019. [Online]. Available: https://ntrs.nasa.gov/archive/nasa/casi.ntrs.nasa.gov/20020053651.pdf.

[72] R. M. Frizzell, C. T. McCarthy, and M. A. McCarthy, “Predicting the effects of geometry on the behaviour of fibre metal laminate joints,” *Compos. Struct.*, vol. 93, no. 7, pp. 1877–1889, 2011, doi: 10.1016/j.compstruct.2011.01.018.

[73] N. H. Kim, *Introduction to Nonlinear Finite Element Analysis*. New York, NY: Springer International Publishing, 2015.

[74] “Abaqus User’s Guide 6.10.” Dassault Systemes.

[75] A. DeLeon, “Investigation of Several Methods of Evaluating Wear in a High-Speed Environment.” Accessed: Apr. 10, 2019. [Online]. Available: https://apps.dtic.mil/dtic/tr/fulltext/u2/1056558.pdf.

[76] A. I. Ştefancu, S. C. Melenciuc, and M. Budescu, “Penalty based algorithms for frictional contact problems,” *Bull. Polytech. Inst. Iasi - Constr. A*, vol. 61, no. 3, pp. 119–129, 2011.

[77] R. Prussak, D. Stefaniak, E. Kappel, C. Hühne, and M. Sinapius, “Smart cure cycles for fiber metal laminates using embedded fiber Bragg grating sensors,” *Compos. Struct.*, vol. 213, pp. 252–260, 2019, doi: 10.1016/j.compstruct.2019.01.079.

[78] “HexTow ® IM7 Carbon Fiber Product Data Sheet,” 2018. http://www.hexcel.com/contact/salesoffice (accessed Jan. 30, 2019).

[79] “Properties: S-Glass Fibre.” https://www.azom.com/properties.aspx?ArticleID=769 (accessed Mar. 15, 2019).

[80] R. S. Fredell, “Damage Tolerant Repair Techniques for Pressurized Aircraft Fuselages,” Delft, 1994.

[81] H. Hosseini-Toudeshky, M. Sadighi, and A. Vojdani, “Effects of curing thermal residual stresses on fatigue crack propagation of aluminum plates repaired by FML patches,” *Compos. Struct.*, vol. 100, pp. 154–162, 2013, doi: 10.1016/j.compstruct.2012.12.052.

[82] A. A. da Costa, D. F. N. R. da Silva, D. N. Travessa, and E. C. Botelho, “The effect of thermal cycles on the mechanical properties of fiber-metal laminates,” *Mater. Des.*, vol. 42, pp. 434–440, 2012, doi: 10.1016/j.matdes.2012.06.038.

[83] J. Hausmann, P. Naghipour, and K. Schulze, “Analytical and Numerical Residual Stress Models for Fiber Metal Laminates – Comparison and Application,” *Procedia Mater. Sci.*, vol. 2, pp. 68–73, 2013, doi: 10.1016/j.mspro.2013.02.009.

[84] Q. Sun *et al.*, “Failure mechanisms of cross-ply carbon fiber reinforced polymer laminates under longitudinal compression with experimental and computational analyses,” 2018, doi: 10.1016/j.compositesb.2018.12.041.

[85] D. Maxwell and T. Nicholas, “A Rapid Method for Generation of a Haigh Diagram for High Cycle Fatigue,” in *Fatigue and Fracture Mechanics: 29th Volume*, 100 Barr Harbor Drive, PO Box C700, West Conshohocken, PA 19428-2959: ASTM International, 1999, pp. 626–641.

[86] T. Nicholas, *High Cycle Fatigue*. Sandiego, CA: Elsevier Inc., 2006.

[87] E. V. Iarve, K. H. Hoos, Y. Nikishkov, and A. Makeev, “Discrete damage modeling of static bearing failure in laminated composites,” *Compos. Part A Appl. Sci. Manuf.*, vol. 108, pp. 30–40, May 2018, doi: 10.1016/J.COMPOSITESA.2018.02.019.

[88] J. Brewer, A. Palazotto, and M. Falugi, “Optimization of the bearing stress of a hybrid composite,” 2019, doi: https://doi.org/10.2514/6.2019-0779.

[89] “HI-LITE™ and HI-LOK™ Studs - LISI AEROSPACE.” https://www.lisi-aerospace.com/en/product/hi-lite-and-hi-lok-studs/ (accessed Nov. 14, 2019).

[90] J. S. Brewer, A. N. Palazotto, J. Feie, and M. Gran, “Bearing Response Characterization in Bolted Hybrid Composite Joints,” Jan. 2020, doi: https://doi.org/10.2514/6.2020-1928.

[91] “LOCTITE EA 9394/ C-2 AERO Epoxy Paste Adhesive Technical Process

Bulletin."

[92] "Technologies for the Rapid Curing of Composite Parts (PVCI08-007-1) | SBIR.gov." https://www.sbir.gov/sbirsearch/detail/11753 (accessed Apr. 17, 2020).

[93] "CYCOM 977-3 | Solvay." https://www.solvay.com/en/product/cycom-977-3 (accessed Feb. 06, 2019).

[94] "Material Certification: 301 Stainless Steel." .

[95] A. Mehner, A. von Hehl, and H. W. Zoch, "Galvanic corrosion of aluminum wrought alloys in integral hybrid components with carbon fiber reinforced plastics (CFRP) and titanium," *Mater. Corros.*, vol. 69, no. 5, pp. 648–660, 2018, doi: 10.1002/maco.201709658.

[96] J. Whittaker, "Ductility and Use of Titanium Alloy and Stainless Steel Aerospace Fasteners," 2015.

[97] C. Kondash, J. Smith, K. Storage, K. Tienda, and J. Mazza, "Evaluation of alumina grit particulate size and removal procedures on the grit-blast/sol-gel surface preparation process," 2018.

[98] "3M™ Surface Pre-Treatment AC-130-2, 1 gal Kit, 2 kit/case | 3M United States." https://www.3m.com/3M/en_US/company-us/all-3m-products/~/3M-Surface-Pre-Treatment-AC-130-2-1-gal-Kit-2-Kit-Case/?N=5002385+3294568487&rt=rud (accessed Sep. 21, 2020).

[99] "BR 6747-1 | Solvay." https://www.solvay.com/en/product/br-6747-1 (accessed Sep. 21, 2020).

[100] W. S. Johnson, L. M. Butkus, and R. V. Valentin, "Applications of Fracture

Mechanics to the Durability of Bonded Composite Joints," 1998. http://www.tc.faa.gov/its/worldpac/techrpt/ar97-56.pdf (accessed Apr. 16, 2019).

[101] "3M Scotch-Weld Structural Adhesive Film AF 191." Accessed: Jan. 28, 2019. [Online]. Available: https://multimedia.3m.com/mws/media/241227O/3mtm-scotch-weldtm-structural-adhesive-film-af191.pdf.

[102] A. Lanciotti and L. Lazzeri, "Fatigue resistance and residual strength of riveted joints in FML," *Fatigue Fract. Eng. Mater. Struct.*, 2009, doi: 10.1111/j.1460-2695.2009.01389.x.

[103] "Screw Threads - UNJ Profile, Inch Controlled Radius Root with Increased Minor Diameter," *SAE Stand. AS8879D*, [Online]. Available: https://www.sae.org/standards/content/as8879d/.

[104] J. Lv, Y. Xiao, and Y. Xue, "Time-temperature-dependent response and analysis of preload relaxation in bolted composite joints," *J. Reinf. Plast. Compos.*, vol. 37, no. 7, pp. 460–474, 2018, doi: 10.1177/0731684417752082.

[105] "Bolt Torque Calculator." https://www.engineeringtoolbox.com/bolt-torque-load-calculator-d_2065.html (accessed Nov. 13, 2019).

[106] D. C. Montgomery, *Design and Analysis of Experiments*, Eighth Edi. Hoboken, NJ: John Wiley & Sons, Inc., 2013.

[107] ASTM International, "ASTM E122-07 Standard practice for calculating sample size to estimate , with specified precision , the average for a characteristic of a lot or process," *Annu. B. ASTM Stand.*, pp. 1–5, 2009, doi: 10.1520/E0122-09E01.2.

[108] "JMP ®, Version 13." SAS Institute Inc, Cary, NC, 2020.

[109] "HL-18 Product Specification." Lisi Aerospace, Accessed: Jun. 11, 2020. [Online].

Available: https://catalog.lisi-aerospace.com/catalog/_layouts/CentralDocConnector/DCConnector.aspx?id=151&listId=HI-LOK PINS&downloaded=HL18&type=nominal_size_shank.

[110] "HL-19 Product Specification." Lisi Aerospace, Accessed: Jun. 11, 2020. [Online]. Available: https://catalog.lisi-aerospace.com/catalog/_layouts/CentralDocConnector/DCConnector.aspx?id=152&listId=HI-LOK PINS&downloaded=HL19&type=nominal_size_shank.

[111] F. Ghods, "Finite Element Modeling of Single Shear Fastener Joint Specimens: A Study of Clamp-Up, Friction and Plasticity Effects," Wichita State University, 2001.

[112] "ASM Material Data Sheet: AISI 4340 Steel." http://asm.matweb.com/search/SpecificMaterial.asp?bassnum=M434AE (accessed Jun. 10, 2020).

[113] E. J. Barbero, *Finite element analysis of composite materials using abaqus™*. 2013.

[114] Dassault Systèmes, "Analysis of Composite Materials with Abaqus." 2009.

[115] Andrew M. Giles and S. Venkataraman, "Progressive Failure Analysis of Hybrid Composites for Bearing Strength Estimation." 2016.

[116] M. D. Sherburne, C. R. Roberts, J. S. Brewer, T. E. Weber, T. V. Laurvick, and H. Chandrahalim, "Comprehensive Optical Strain Sensing through the Use of Colloidal Quantum Dots," *ACS Appl. Mater. Interfaces*, vol. 12, no. 39, pp. 44156–44162, 2020, doi: 10.1021/acsami.0c12110.

[117] M. D. Sherburne *et al.*, "Strain Sensing Using Colloidal Quantum Dots Integrated

With Epoxy." IEEE Sensors 2020.

[118] "Abaqus/Explicit: Advanced Topics: Quasi-Static Analyses." 2005.

[119] K. Song, F. A. Leone, and C. A. Rose, "Analysis of Progressive Damage in Cross-Ply and Quasi-Isotropic Panels Subjected to Quasi-Static Indentation." Accessed: Jul. 24, 2019. [Online]. Available: https://ntrs.nasa.gov/search.jsp?R=20190000435.

[120] S. Sachin, H. Shivananda Nayaka, B. Santhosh, and P. Krishna, "Experimental study of Mode I and Mode II interlaminar fracture toughness on aerospace structural composite T300/914 ," in *Proceedings*, 2019, vol. 2057, doi: 10.1063/1.5085578.

[121] S.-J. Yoon, K. Arakawa, S.-W. Han, D. Chen, and N.-S. Choi, "Effect of Compaction Treatment on Laminated CFRP Composites Fabricated by Vacuum-Assisted Resin-Transfer Molding Sang-Jae," *Polym. Compos.*, 2015, doi: DOI 10.1002/pc.23578.

[122] " ASC Process Systems: Econoclave EC2X4." http://www.aschome.com/index.php/en/econoclave-ec2x4 (accessed Jun. 18, 2020).

[123] "301 Stainless Steel." http://www.matweb.com/search/datasheet.aspx?matguid=0cf4755fe3094810963eaa74fe812895&ckck=1 (accessed Apr. 07, 2020).

[124] G. A. Schoeppner, D. H. Molenhauer, and E. V. Iarve, "Prediction and Measurement of Residual Strains for a Composite Bonded Joint," *Mech. Compos. Mater.*, vol. 40, no. (2), pp. 119–134, 2004.

REPORT DOCUMENTATION PAGE

Form Approved
OMB No. 0704-0188

1. REPORT DATE *(DD-MM-YYYY)*	2. REPORT TYPE	3. DATES COVERED *(From - To)*
12/24/2020	Doctoral Dissertation	Sep 2017 – Dec 2020

4. TITLE AND SUBTITLE
Experimental and Computational Analysis of Progressive Failure in Bolted Hybrid Composite Joints

5a. CONTRACT NUMBER

5b. GRANT NUMBER

5c. PROGRAM ELEMENT NUMBER

6. AUTHOR(S)
Brewer, John S., Maj, USAF

5d. PROJECT NUMBER

5e. TASK NUMBER

5f. WORK UNIT NUMBER

7. PERFORMING ORGANIZATION NAME(S) AND ADDRESS(ES)
Air Force Institute of Technology
Graduate School of Engineering and Management (AFIT/ENY)
2950 Hobson Way, Building 640
WPAFB OH 45433-8865

8. PERFORMING ORGANIZATION REPORT NUMBER
AFIT-ENY-MS-20-D-057

9. SPONSORING/MONITORING AGENCY NAME(S) AND ADDRESS(ES)
Michael Gran, Aerospace Engineer
Aerospace Systems Directorate, Air Force Research Laboratory
1950 5th St., WPAFB OH 45433-8865
michael.gran@us.af.mil

10. SPONSOR/MONITOR'S ACRONYM(S)
AFRL/RQ

11. SPONSOR/MONITOR'S REPORT NUMBER(S)
Intentionally left blank

12. DISTRIBUTION/AVAILABILITY STATEMENT
APPROVED FOR PUBLIC RELEASE; DISTRIBUTION UNLIMITED.

13. SUPPLEMENTARY NOTES
This material is declared a work of the U.S. Government and is not subject to copyright protection in the United States.

14. ABSTRACT
Composite materials are strong, lightweight, and stiff making them desirable in aerospace applications. However, a practical issue arises with composites in that they behave unpredictably in bolted joints, where damage and cracks are often initiated. To address this problem, a novel hybrid composite material was developed, where thin stainless steel foils were placed between and in place of composite plies in the primary layup to reinforce stress concentrations in bolted joints. Hybridizing the composite material increased yield by as much as 25% and increased ultimate load capacity as much as 42%. The finite element models employed Hashin failure criteria and proved the ability to predict the yield load capacity to within 6.5%.

15. SUBJECT TERMS
Hybrid composites, fiber metal laminates, polymer matrix composites (PMC), finite element analysis (FEA), finite element modeling (FEM)

16. SECURITY CLASSIFICATION OF:			17. LIMITATION OF ABSTRACT	18. NUMBER OF PAGES	19a. NAME OF RESPONSIBLE PERSON
a. REPORT	b. ABSTRACT	c. THIS PAGE			Palazotto, Anthony R CIV AFIT/ENY
					19b. TELEPHONE NUMBER *(Include area code)*
U	U	U	UU	384	(937) 255-6565,ext 4667 Anthony.Palazotto@afit